EVOLUTION OF MICROSTRUCTURE AND CORRELATION WITH PROPERTIES IN WELDMENTS OF 9Cr REDUCED ACTIVATION FERRITIC / MARTENSITIC STEELS

By

THOMAS PAUL V

Enrolment No: ENGG02200804022

Indira Gandhi Centre for Atomic Research, Kalpakkam

A thesis submitted to the
Board of Studies in Engineering Sciences
In partial fulfillment of requirements
For the Degree of

DOCTOR OF PHILOSOPHY

Of

HOMI BHABHA NATIONAL INSTITUTE

August, 2015

Homi Bhabha National Institute

Recommendations of the Viva Voce Committee

As members of the Viva Voce Committee, we certify that we have read the dissertation prepared by V. Thomas Paul entitled **"Evolution of Microstructure and Correlation with Properties in Weldments of 9cr Reduced Activation Ferritic / Martensitic Steels"** and recommend that it may be accepted as fulfilling the thesis requirement for the award of Degree of Doctor of Philosophy.

Chairman + Prof. T. Jayakumar (Dean-Academic) (Retired) Date: 27/04/2016

Convener Prof. Saroja Saibaba. Date: 27/04/2016.

External Examiner Prof. Nithyanand Prabhu Date: 27/04/2016

Member 1 Prof. B. K. Panigrahi Date: 27/4/16

Member 2 UKamachi Mudali Prof. U. Kamachi Mudali Date: 27 Ap/16

Final approval and acceptance of this thesis is contingent upon the candidate's submission of the final copies of the thesis to HBNI.

I hereby certify that I have read this thesis prepared under my direction and recommend that it may be accepted as fulfilling the thesis requirement.

Date: April 27, 2016

Place: Kalpakkam

Guide: Prof. Saroja Saibaba

STATEMENT BY AUTHOR

This dissertation has been submitted in partial fulfillment of requirements for an advanced degree at Homi Bhabha National Institute (HBNI) and is deposited in the Library to be made available to borrowers under rules of the HBNI.

Brief quotations from this dissertation are allowable without special permission, provided that accurate acknowledgement of source is made. Requests for permission for extended quotation from or reproduction of this manuscript in whole or in part may be granted by the Competent Authority of HBNI when in his or her judgment the proposed use of the material is in the interests of scholarship. In all other instances, however, permission must be obtained from the author.

Thomas Paul V

DECLARATION

I, hereby declare that the investigation presented in the thesis has been carried out by me. The work is original and has not been submitted earlier as a whole or in part for a degree/diploma at this or any other Institution/University.

Thomas Paul V

Publications from the thesis

a. Journal Publications:

1. Microstructural characterization of weld joints of 9Cr Reduced Activation Ferritic Martensitic Steel fabricated by different joining methods, ***V. Thomas Paul***, *S. Saroja, S. K. Albert, T. Jayakumar, E. Rajendra Kumar*; Mater. Charact. 96 (2014) 213-224.
2. Influence of alloy content and prior microstructure on evolution of secondary phases in weldments of 9Cr Reduced Activation Ferritic-Martensitic steel, ***V. Thomas Paul***, *C. Sudha, S. Saroja*; Metall. Mater. Trans.A, 46 (8) (2015) 3378-3392.
3. Microstructural variations across a dissimilar 316L austenitic - 9Cr Reduced Activation Ferritic Martensitic steel weld joint: ***V. Thomas Paul****, Karthikeyan T, Arup Dasgupta, Sudha C, Hajra R.N, Shaju K. Albert, S. Saroja and Jayakumar T*, Metall. Mater. Trans.A, 47A (3) (2016), 4432-1168.

b. Conference presentation:

1. Early precipitation of laves phase in the heat affected zone of 9cr RAFM steel weldment; ***V. Thomas Paul****, S. Saroja, T. Jayakumar, E. Rajendra Kumar*, Proc. International Conf. Electron Microscopy, EMSI 2013, (2013) Kolkata p.203.

2. Effect of Tungsten on microstructural evolution and mechanical properties of 9Cr RAFM steel; ***V. Thomas Paul****, Ran Vijay Kumar, V. D. Vijayanand, V. Karthik, C. Sudha and S. Saroja* , 7th International Conference on Creep, Fatigue and Creep Fatigue Interaction (CF-7)

c. Manuscripts under preparation

1. Influence of alloy content and microstructure on mechanical properties of RAFM steel
2. Simulation of HAZ microstructures in INRAFM steel

Dedicated to my late parents and brother

ACKNOWLEDGEMENTS

I would like to express my sincere gratitude to all of them who were supportive for the successful completion of my research work and thesis. First of all, I am extremely grateful to my research guide Dr. Saroja Saibaba for her valuable guidance, scholarly inputs and consistent encouragement that I received throughout the research work. She has been a magnificent mentor with her continual motivation. I would like to express my gratefulness and thanks to Dr. M. Vijayalakshmi, AD, PMG and Dr. Shaju K Albert, Head, MTD for giving confidence to do my research and thereby nurturing me to pursue new avenues.

This feat was possible only because of the unconditional support provided by Dr. T. Jayakumar, former Director, MMG. I am also grateful to the present and all the former Directors of IGCAR who have rendered the academic support and facilities for carrying out research at this Centre. I would also like to thank my Doctoral committee members, Dr. Kamachi Mudali and Dr. B K Panigrahi for their keen interest and encouragement in my research work. I thank Dr. C. Sudha, Dr. V. Karthik and Mr. David Vijayanand for their active research collaborations which resulted in gaining technical information through personal and scholarly interactions. Dr. R. Mythili was kind enough to critically read the thesis and provide useful suggestions. I acknowledge her for the meticulous and timely work.

I would like to thank Mr. E. Mohandas, Head MSSCD and Dr. P. Parameswaran, Program Leader, SPCP for their support provided for the completion of this research study. My colleagues have extended their help in many ways. I thank Dr. T. Karthikeyan, Dr. Arup Dasgupta, Mr. Ran Vijay Kumar, Dr. P.K. Ajikumar, Dr. S. Raju, and Mrs. Jyothi for their timely help in providing me experimental support. I express my sincere thanks to Dr. N. L. Parthasarathy, Dr. Tom Mathews, Manoj Kumar and all the members of PMG for extending their help to me.

I am very much indebted to my wife Silvi, my son Arun and daughter Anusha who supported me in every possible way to achieve the completion of the work.

Finally, I thank the Almighty for supporting me through all my ups and downs. I have experienced your guidance day by day. Thank you, Lord.

CONTENTS

CHAPTER 3 MICROSTRUCTURAL EVOLUTION IN 9Cr RAFM STEEL WITH VARYING TUNGSTEN CONTENT AND ITS CONSEQUENCE ON PROPERTIES

CHAPTER 4 IDENTIFICATION OF MICROSTRUCTURAL ZONES IN WELDMENTS OF RAFM STEEL AND ITS MODIFICATIONS ON THERMAL EXPOSURE

CHAPTER 5 MICROSTRUCTURAL VARIATIONS IN A DISSIMILAR AUSTENITIC - FERRITIC STEEL WELD JOINT

CHAPTER 6 SUMMARY AND SCOPE FOR FUTURE WORK

SYNOPSIS

1. Introduction

The development of 9Cr ferritic/martensitic (F/M) steels as structural materials for the plasma facing components in fusion reactor and more specifically for the International Thermonuclear Experimental Reactor (ITER) stems from their excellent resistance to neutron radiation and their potential use as cladding and wrapper materials in the sodium cooled fast reactors [1]. The Cr-Mo steels commonly used for power plant and fast reactors have a limitation for service in high energy-high flux neutron environment of fusion reactors due to induced radioactivity, which poses difficulties in the storage and disposal of these materials. Hence, a new variant of this class of steel namely the ‘reduced activation’ ferritic/martensitic steel (RAFM) has been developed internationally by (i) substituting W for Mo and Ta for Nb and (ii) minimizing tramp elements with strict control on residual impurities, while keeping the mechanical and thermal properties unaltered [2]. Considering the good toughness, adequate creep strength and weldability, and above all the vast fabrication experience with 9Cr steels in the production of large structures gave preference to the 9Cr-RAFM as a construction material for the Test Blanket Modules (TBM) to be tested in the ITER [3]. As a part of the Indian TBM program, which consists of composition optimization of RAFM steels with varying tungsten and tantalum contents, an India specific 1.4W-0.06Ta steel was produced indigenously. The steel has met with the desired property requirements and has been designated as the Indian RAFM or INRAFM.

The stability of microstructures on prolonged service exposure to high neutron flux and temperature is of serious concern to RAFM steels. Although the physical metallurgy of F/M steels with respect to phase transformations and microstructural evolution on thermal and irradiation exposures, have been extensively studied in literature [5], there are limited studies to understand the effect of W in the degradation of microstructure and hence properties during long term service exposures in this class of steels.

One of the major challenges posed in the fabrication of TBM is the development of reliable joining technologies. Hence, knowledge based design of welding methodologies for the RAFM steel is a thrust area of research [4]. Different welding techniques are being tried out to arrive at a suitable methodology for different specific applications. Weld joints are known to be the weakest regions with respect to mechanical properties and most of the service failures in ferritic steels are reported either in the weld or Heat Affected Zone (HAZ) [6]. Hence an effort has been made to study the microstructural evolution in INRAFM steel, the microstructural and micro-chemical modifications during welding and service exposures, and its impact on mechanical properties.

This thesis aims to present the results of a comprehensive study on the microstructural evolution in wrought and weldments of 1W and INRAFM steel and its effect on the mechanical properties based on a systematic experimental investigation using X-ray Diffraction (XRD) Scanning Electron Microscopy (SEM), Energy Dispersive Spectroscopy (EDS), Electron Back Scattered Diffraction (EBSD), Analytical Transmission Electron Microscopy (ATEM) and Differential Scanning Calorimetry (DSC); mechanical property evaluation by hardness measurements, Impression Creep and Small Punch Tests; Dependence of microstructural evolution on alloy composition, initial microstructure and temperature has also been simulated using JMatpro® softwares and validated by experimental studies.

2. Scope of the Thesis

This thesis titled “EVOLUTION OF MICROSTRUCTURE AND CORRELATION WITH PROPERTIES IN WELDMENTS OF 9Cr REDUCED ACTIVATION FERRITIC / MARTENSITIC STEELS” presents the results of a systematic study on the physical metallurgy aspects of two variants of RAFM steel with different tungsten contents with emphasis on the microstructures that evolve in this steel on heat treatment and welding employing a variety of microstructural and microchemical characterization techniques. The consequence of microstructural variation on the mechanical properties of the steel has been studied using two novel small specimen testing methods namely impression creep and automated ball indentation.

Since welding is a very important fabrication method for the fusion reactor components a critical comparison of the microstructures obtained by three different welding methods namely autogenous TIG, electron beam and laser beam techniques has been made. The conditions for Post Weld Heat Treatment (PWHT) have been optimized for autogenous TIG welding based on the hardness values and the resultant microstructure. The phases that form in the weldment in the three regions namely base metal, weld and heat affected zone due to difference in the initial microstructures and chemistry have been predicted using JMatPro a computational software and the results of the computation have been compared with the experimental results. The microstructure of the weld and the interface structure in an electron beam weld joint has been studied in depth to understand the effects of mixing in a austenitic (316L) – ferritic (RAFM steel) dissimilar joint and the phases that evolve as a result of the composition gradient. The thesis focuses mainly on three themes which are as follows:

- Microstructural evolution in RAFM steels during thermal exposures and its consequence
    - Effect of composition and temperature on evolution of phases
    - Influence of secondary phases on mechanical properties

- Comparison of different welding methods which include:
    - Variation in microstructural parameters in welds prepared by different methods
    - Optimization of Post Weld Heat Treatment (PWHT) for RAFM welds.
    - Role of initial microstructure, alloy composition and temperature on the kinetics of evolution of secondary phases during prolonged thermal exposure – an experimental and computational study.
    - Simulation of weld microstructures

- Characterization of RAFM-316L dissimilar welds joint which include:
    - Identification of zones in the dissimilar weld
    - Evolution of microstructure during PWHT and elevated temperature exposures

An outline of the thesis is consolidated as a flow chart in Figure 1. The results of the studies will be described in the subsequent sections.

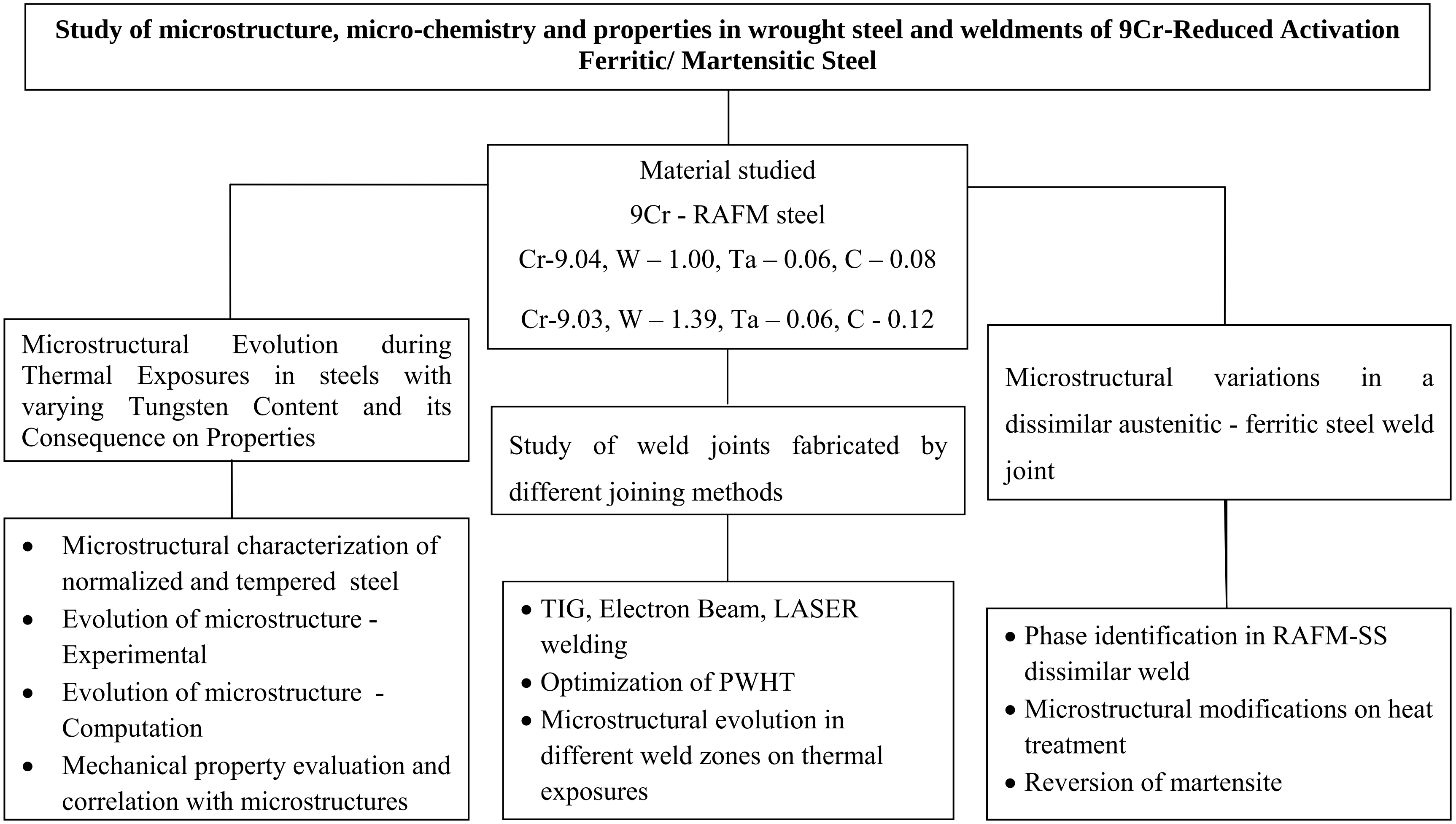

Fig.1. Flow chart of the major themes of the thesis

2.1 *Microstructural evolution in RAFM steels during thermal exposures*

Analytical Transmission Electron Microscopy studies on two variants 1W and 1.4W (INRAFM)) of normalized and tempered RAFM steels showed a tempered martensitic structure with retention of lath structure. The INRAFM steel showed finer laths as compared to 1W steel which is attributed to the higher W content, which resists the recovery/ recrystallisation process. Figure 2 (a) shows the decoration of lath and grain boundaries with precipitates of different morphology and size. Based on electron diffraction and Energy Dispersive Spectroscopy analysis these have been identified as the coarse Cr and W rich $M_{23}C_6$ carbides and fine V/Ta rich inter-lath MX precipitates (Fig.2 (b)). The phase fraction of secondary phases and its composition was calculated by simulation using JmatPro®.

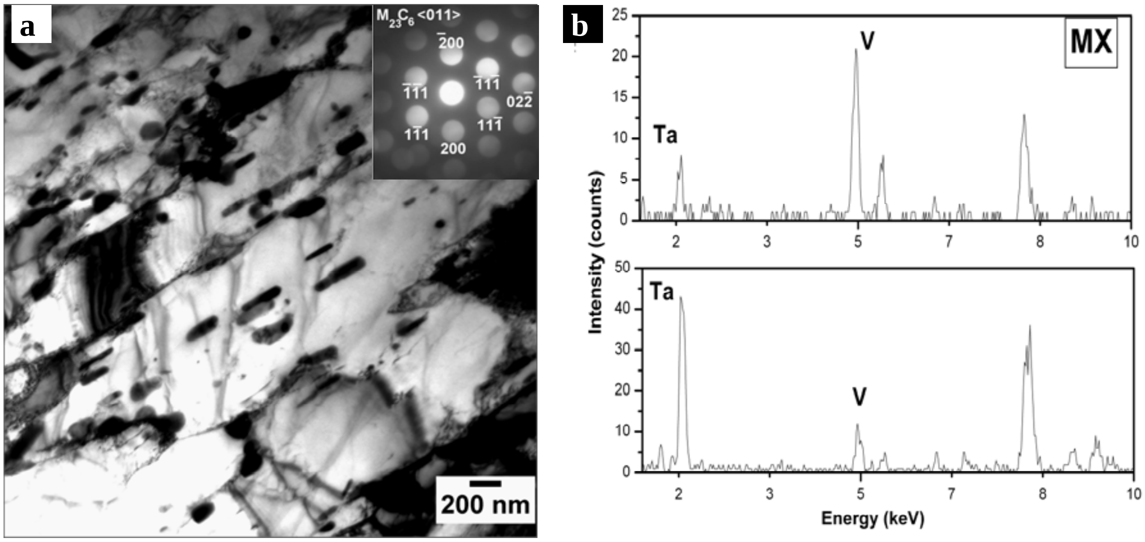

Fig.2: Micrographs from 1W steel showing, morphology and distribution of carbides in normalized and tempered 1W steel, (a) Lenticular inter & intra lath precipitates (inset shows a diffraction pattern from $M_{23}C_6$ along <011>and zone axes (b) EDS from V/Ta MX carbides.

2.1.1 Effect of composition and temperature on evolution of phases

The microstructural changes occurring during long term service exposures of 1 and 1.4 W RAFM steels in the temperature range of 773-873 K have been studied by experiments as well as computation. Hardness values did not show significant changes against the expected softening due to recovery. It is understood that the reduction in hardness due to recovery is compensated by an increase due to precipitation. An increase in the volume fraction, average size and Cr content of carbide was observed in both steel with aging time and temperature. Laves phase (Fe_2W) was found to be present when INRAFM steel is aged at 823 K. An increase in volume fraction of carbide after aging at 823 K for 10000h was justified by the presence of coarse Laves phase, along lath boundaries. Compared to 1W steel, formation of Laves phase occurred early in INRAFM steel due to (i) higher W content and (2) abundant precipitation of carbides that increased the availability of W and reduced the supersaturation of carbon in the region surrounding the carbides. Simulation results also supported the experimental data. The significant differences in the predicted (simulated) behaviour of microstructural evolution between the INRAFM and 1W steels at high temperatures are listed as follows:-

- Early onset of precipitation of MX carbides was observed specifically at 823 and 873 K.
- M_2X carbo-nitrides were stable only up to 4h of heat treatment at 873 K.
- Laves phase formed in both the steels after 1000h of aging at 823 K, and its volume fraction was relatively higher in INRAFM steel as compared to 1W steel.
- Laves phase was quite predominant only next to $M_{23}C_6$ after aging for 5000 h at 873 K.

2.1.2 Influence of secondary phases on mechanical properties

Impression test and small punch tests were carried out to understand the effect of composition and secondary precipitations on creep and toughness behaviour. Figure 3 (a) shows the plot of displacement versus time for both the steels. The values of secondary creep obtained from impression tests were higher as compared to minimum creep rate in the conventional tests, because, the minimum creep rate is obtained in the later stages of creep test. However, it is very clear that an increase in 0.4%W in INRAFM steel decreases the creep rate to nearly half the value shown by 1W steel. This effect is striking and is attributed to the role of W in reducing the diffusion of Fe during the recovery process. The values of DBTT of the normalized and tempered steels measured by Small Punch test showed similar values for the 1W and INRAFM steel. Fig. 3(b) shows the trend in DBTT for variations in aging temperature and time.

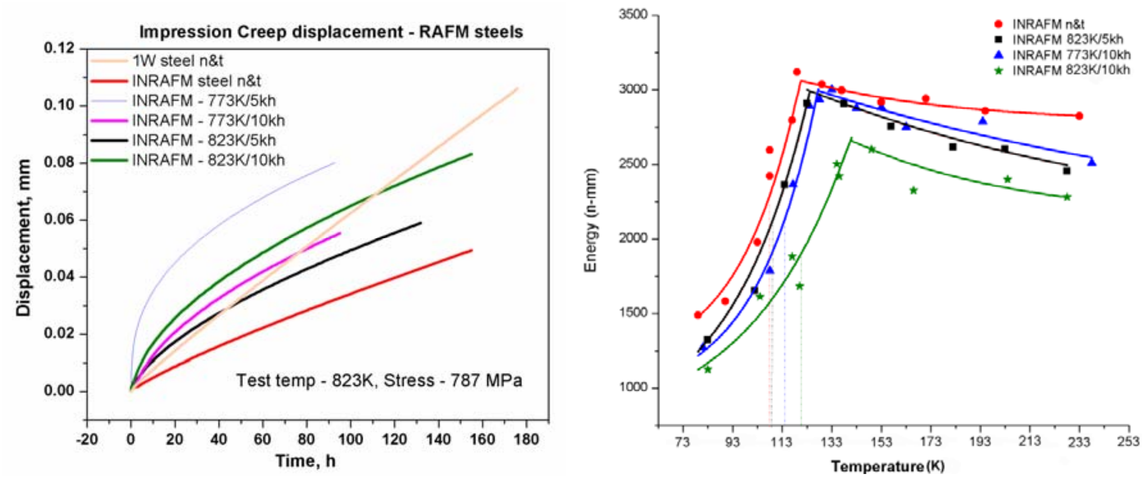

Fig.3: (a) Impression displacement versus time curves (b) Plot of SP fracture energy versus temperature for aged INRAFM steel

A progressive but small increase in DBTT was observed with increase in aging temperature and time. However, a significant change in DBTT is observed after aging for

10000h at 823 K. A discontinuous network of Laves phase mainly along lath boundaries and coarsening of carbides are responsible for the observed increase in DBTT. The test results on aged steel confirmed that the fracture properties are not degraded as long as the Laves phase is fine in nature.

2.2 *Comparison of different welding methods*

This section presents the results on a detailed electron microscopy study on the microstructure of various regions of weldment fabricated by three welding methods namely Tungsten Inert Gas (TIG) welding, Electron Beam (EB) welding and Laser Beam (LB) welding. Experimental results were augmented with computations to effectively study the evolution of microstructures on Post Weld Heat Treatment (PWHT) and long term exposure at service temperatures.

2.2.1 Variation in microstructural parameters in welds prepared by different methods

A martensite structure was obtained in the weld prepared by the three different methods. Orientation imaging microscopy studies using Electron Back Scatter Diffraction showed random micro-texture in all the three welds. However, the prior austenite grain size in the TIG weld was far higher than in EBW and LBW. This is attributed to the higher residence time at temperatures above Ac_3 due to higher heat input in TIG. This also resulted in a higher width of HAZ in TIG weld as compared to narrow HAZ in EBW and LBW. The weld metal exhibited high hardness exceeding 400VHN although the lath sizes were finer in EBW and LBW due to low heat input. Using Rosenthal's steady state solutions to heat transfer equation, the temperature at a point in the plate could be calculated in case of TIG welding. The calculated temperature was plotted as a function of time for different depths from the surface of the plate with each curve depicting the heating/cooling cycles experienced by the point at a particular depth. By assigning peak temperatures, the cooling curve corresponding to different regions of the weld were generated.

Prior austenite grain size and hardness in the HAZ is controlled by the peak temperature and cooling rate in the region. Peak temperature varies as a function of distance from the heat source and this explains for the progressive decrease of hardness in HAZ. Negligible amount of carbides in Coarse Grain HAZ (CGHAZ) of TIG weld is attributed to the complete dissolution of carbides at high temperatures prevailing in the CGHAZ. The higher carbon super saturation in the martensite and the high dislocation density due to high cooling rate explains for the high hardness in this region, despite the large grain size. Although Fine Grain HAZ (FGHAZ) showed a martensitic microstructure, carbides were found to be undissolved to a large extent, due to lower temperature of exposure. It was difficult to distinguish the FGHAZ from Inter Critical HAZ (ICHAZ) where both ferrite and martensite co-exists.

Optimum condition for PWHT is identified as 2h at 1033 K for TIG welds of RAFM steel based on microstructure and hardness values. Holloman-Jaffe parameter which is a function of tempering time and duration has been used to estimate the extent of tempering. The activation energy of the tempering process has been evaluated and found to be in agreement with the activation energy for migration of carbon in ferrite matrix.

2.2.2 Kinetics of evolution of secondary phases

The weld metal which is essentially martensite undergoes a continuous process of tempering on prolonged exposure in the temperature range of 773-823 K, accompanied by a reduction in hardness from ~450 to 300VHN. The JMatPro computation predicted carbides such as $M_{23}C_6$, MX, M_2X and M_7C_3 on thermal exposure. However, TEM analysis from a large number of precipitates has shown only the presence of MX, $M_{23}C_6$ and Laves phase. This can be understood in terms of the kinetics of evolution of the metastable phases which is too rapid or very low fractions which is beyond the limit of detection of the technique.

Experiments carried out for few selected temperature-time combination confirmed the formation of Fe_2W type of Laves phase in both FGHAZ and base metal of INRAFM steel after long durations at temperatures ≥823 K. No evidence was obtained for the formation of Laves phase in weldment of 1W-RAFM steel under identical experimental conditions, which is clearly a manifestation of the lower W content. Enhanced precipitation of Laves phase observed in the FGHAZ of INRAFM steel weldments in comparison to base metal is attributed to the abundant carbide precipitations in this region leading to an increase in W and decrease in C content locally, which is expected to accelerate the nucleation and growth of Laves phase. Due to enhanced kinetics of precipitation of Laves phases, FGHAZ was identified to be the region susceptible for failure during long term service exposures of INRAFM steel weldments.

2.2.3 Simulation of weld microstructures

The INRAFM steel specimens were subjected to thermal cycles in a GLEEBLE thermo-mechanical simulator at four different peak temperatures, namely 1173, 1273, 1373 and 1523 K which are expected to simulate the temperatures of the ICHAZ, FGHAZ, and CGHAZ respectively. The resultant microstructures were correlated with those observed in the HAZ of the TIG weldment. A typical example of the microstructure simulated at 1173 K in Fig.4 (a) shows the co-existence of martensite and tempered martensite, corresponding to ICHAZ. The microstructure obtained by subjecting this simulated ICHAZ specimen to a heat treatment of 1033 K for 1h is shown in Fig.4 (b). A fully tempered martensitic microstructure is observed from the micrograph resembling a structure obtained during PWHT of the ICHAZ region of a weldment.

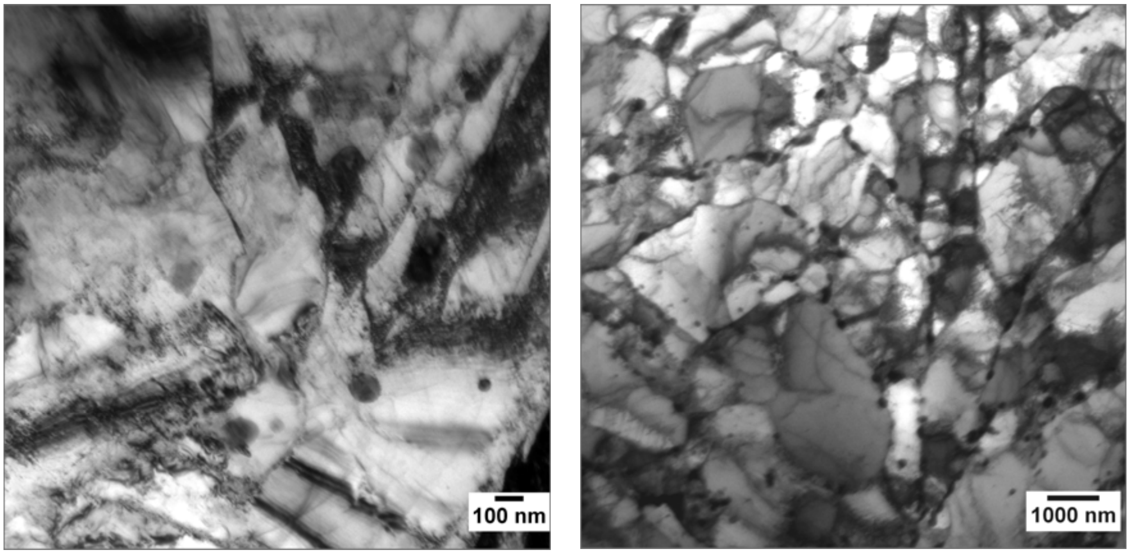

Fig.4: TEM micrograph from Gleeble simulated (1173 K) INRAM steel showing (a) lath martensite and over tempered ferrite corresponding to ICHAZ (b) tempered martensite after heat treatment

2.3 Characterization of RAFM- SS 316L dissimilar weld joint

A study on dissimilar joint of austenitic stainless steel to RAFM steel was carried out to understand the microstructural variations across the weld joint. The metallographic examination of dissimilar weld joint revealed a complex microstructure. The microchemical analysis using EPMA showed a sharp change in composition at the interface, although no zone formation was observed at the interface unlike the joints of 9Cr-1Mo- 21/4Cr-1Mo steel [7]. After carrying out heat treatments the distribution of elements was studied to understand the microchemistry driven phase or microstructural changes. The results of the study are described in the following sections.

2.3.1 Identification of zones in the dissimilar weld

Based on the chemical composition of the two alloys, the fraction of weld dilution from each alloy was calculated by mass balance. By using this dilution value, the effective Cr_{eq} and Ni_{eq} of weld metal was calculated from the base metal compositions. Using the estimated Cr_{eq} (22.0 and 11.2 for SS 316L and RAFM respectively) and Ni_{eq} (16.7 and 3.6 for SS316L and RAFM respectively) values on the Schaeffler-Schneider diagram the phases in the weld metal were predicted. A dilution of 1:3 mixing of two alloys is expected to result in a weld metal with Cr_{eq} and Ni_{eq} of 14.0 and 6.8 respectively. The weld is predicted to have a mixed microstructure of austenite and martensite. Metallographic examination of the weld metal showed a dendritic but fine martensitic microstructure in general, with a high hardness of 480VHN. EBSD studies revealed the presence of austenite phase in the weld. SEM observation showed lenticular features at the austenite interface, which was confirmed as delta ferrite by XRD analysis and 3D EBSD (Fig.5). Although delta ferrite was predicted in the weld, it could not be identified due to the fine intense mixing of ferrite with martensite which possesses similar crystal structures.

2.3.2 Evolution of microstructure during PWHT and elevated temperature exposures

PWHT at 1033 K did not result in any appreciable change in hardness. It is of interest to note that the microstructure was martensitic in the weld region even after PWHT although the microstructure in the CGHAZ of RAFM steel showed signatures of tempering. The Differential Scanning Calorimetry (Fig.6) thermogram obtained by a heating and cooling of the weld region showed a reduction in the transformation temperature to 1076 K of $\alpha \rightarrow \gamma$ as compared to 1104 K reported for the RAFM steel.

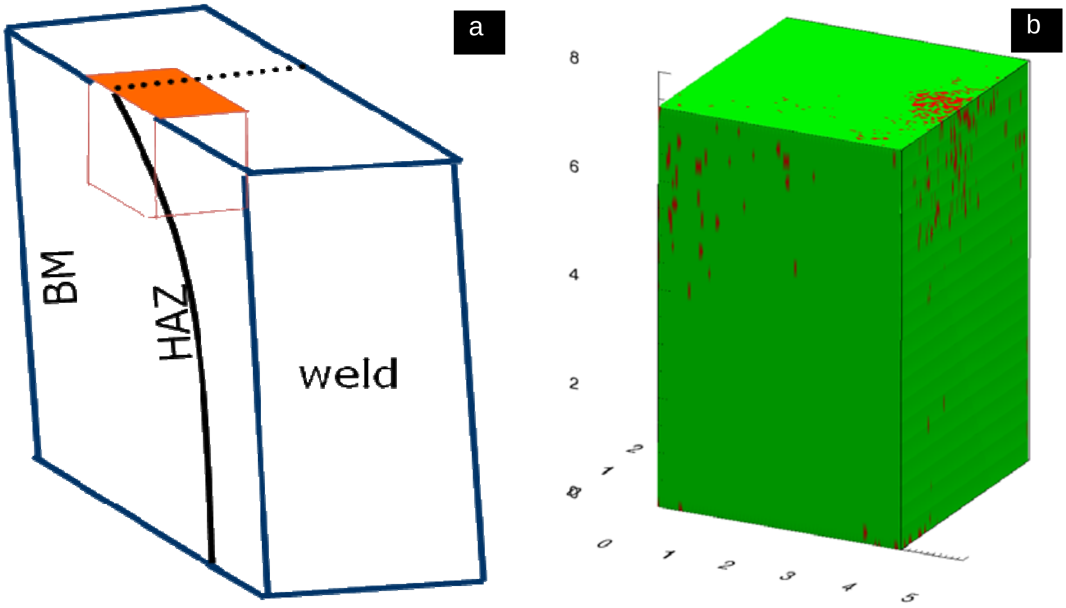

Fig. 5: (a) Location of specimen from weld interface for 3D EBSD and (b) distribution of delta ferrite in 3D showing high volume of delta ferrite at the interface.

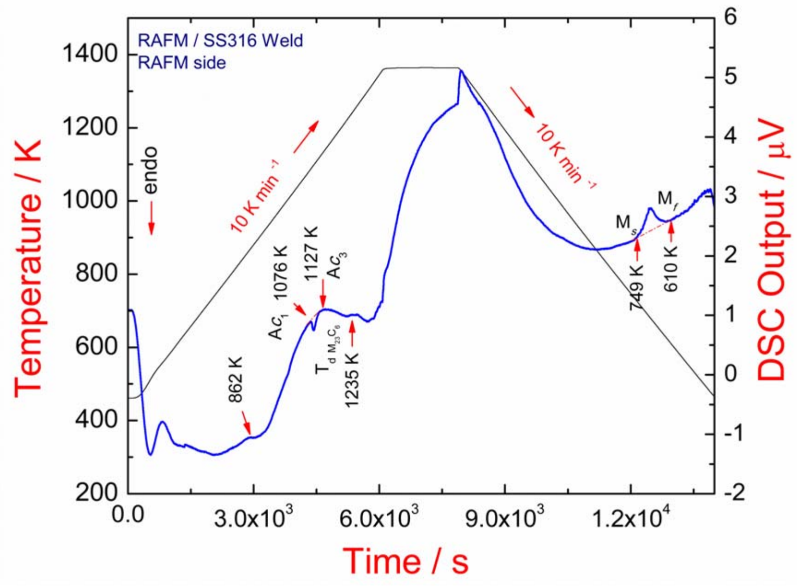

Fig.6: DSC thermogram of RAFM-SS weld metal; critical transformation temperatures are marked

The experimentally measured as well as empirical calculations of Ac_1 temperature of weld metal showed that they were above 1033 K, which is the temperature of PWHT. Hence, the observation of martensite and high hardness after PWHT cannot be correlated to the decrease in Ac_1. Heat treatment of the welds at 873 and 1073 K up to 100h showed a decrease followed by an increase in the hardness suggesting that the onset of austenite is below 1073 K. It is reasonable to expect that the diffusion of nickel into HAZ of RAFM steel is responsible for reduction of Ac_1, resulting in austenite transforming to martensite in this zone.

3. Organization of the Thesis

This thesis consists of six chapters which are organized as follows:-

Chapter 1, **Introduction,** presents a brief survey of available literatures on RAFM steel focusing on the historical development of the steel, the indigenous effort, physical metallurgy and structure- property correlations in this class of steel. It also deals with newer welding methods adopted in the construction of the Test Blanket Module (TBM) and, miniaturized specimen testing methods for mechanical property evaluation.

Chapter 2, titled **Experimental details,** describes the various experimental and analytical techniques used in the study. Details of heat treatments, specimen preparation, operating conditions of the microstructural and microchemical analysis techniques, methodology used for image analysis and possible errors are described. Test procedures of impression creep test and small punch test and a brief description on simulation software JMatPro® are also included.

Chapter 3, titled “**Microstructural evolution in RAFM steels during thermal exposures and its correlation with mechanical properties”,** presents a comprehensive study on microstructural evolution in INRAFM steel during long term elevated temperature exposure and compares the same with that of 1W steel. The main emphasis is on the type, chemistry and volume fraction of the secondary phases that form in the steel. The phases that form as a function of temperature have been predicted using the CALPHAD based simulation software JMatPro® and compared with the experimental results obtained by detailed electron microscopy investigations Creep and toughness property have been evaluated by small specimen testing methods and correlated with the observed microstructures.

Chapter 4, titled ***“Identification of microstructural zones in weldments of RAFM steel and its modifications on thermal exposure”,*** presents the results of a systematic characterization of the microstructure of the distinct zones in the welds prepared by three different welding methods namely autogenous TIG, electron beam and laser beam welding. Optimization of Post Weld Heat Treatment and determination of kinetics of tempering are also described in this chapter. The role of initial microstructure and chemistry on the evolution of phases in each zone is discussed based on extensive microscopy of the different zones of the weldment and simulation studies.

Chapter 5, titled “**Characterisation of RAFM-SS dissimilar weld joint”,** deals with the microstructural characterization of the weld joint and the interface of a RAFM-316L dissimilar joint and its modifications on PWHT and diffusion anneal studies. Possible phases in the weld metal that form due to intermixing or base metal dilution have been predicted based on the Cr and Ni equivalents. The results on microstructural changes that arise due to the local variations in microchemistry, studied using various microscopy techniques are described in this chapter. The possible modification of the phase transformation characteristics due to chemistry changes have been studied using Differential Scanning Calorimetry.

Chapter 6, titled **"Summary and Conclusions"** summarizes the important findings in this thesis and also identifies few areas for study in future.

References

[1] R. L. Klueh, A. T. Nelson. Ferritic/martensitic steels for next-generation reactors. J. Nucl.Mater. 371(2007) 37-52.

[2] M. Tamura, H. Hayakawa, M. Tanimura, A. Hishinuma and T. Kondo. Development of potential low activation ferritic and austenitic steels. J. Nucl.Mater.141-143 (1986) 1067-1073.

[3] N. Baluc, Materials for fusion power reactors, Plasma Phys. Control. Fusion48(2006) B165–B177

[4] H. Tanigawa, T. Hirose *et.al,* Technical issues of reduced activation ferritic/martensitic steels for fabrication of ITER test blanket modules, Fusion Engineering and Design 83 (2008) 1471–1476

[5] R. L. Klueh, D. R. Harries, High-chromium Ferritic and Martensitic Steels for Nuclear applications, ASTM, Monograph 3, 2001

[6] Bell. K (1997) Elevated temperature midlife weldment cracking, Report 597/1997. The Welding Institute, Abington, UK

[7] Sudha C, Thomas Paul. V *et.al.* Microstructure and microchemistry of hard zone in dissimilar weldments of Cr-Mo steels. Welding J. (2006) 85(3):71-s

LIST OF FIGURES

LIST OF TABLES

List of Symbols and Abbreviations

A : Atomic Absorption

ATEM : Analytical Transmission Electron Microscopy

BM : Base Metal

BSE : Back Scattered Electron

CEN : European Committee for Standardization

CGHAZ : Coarse Grain HAZ

DF : Dark Field

DSC : Differential Scanning Calorimetry

EB : Electron Beam

EBSD : Electron Back Scatter Diffraction

EDM : Electro Discharge Machining

EDS : Energy Dispersive Spectrometer

EPMA : Electron Probe Micro Analyzer

E_{SP} : SP fracture energy

F : Atomic Fluorescence

FGHAZ : Fine Grain HAZ

FIB : Focused Ion Beam

HAZ : Heat Affected Zone

IC : Impression Creep

ICDD : International Center for Diffraction Data

ICHAZ : Inter-Critical HAZ

IPF : Inverse Pole Figure

OIM : Orientation Imaging Microscopy

PAGS : Prior Austenitic Grain Size

SAD : Selected Area Diffraction

SE : Secondary Electron

SEM : Scanning Electron Microscopy

SP : Small Punch

T1G : Tungsten Inert Gas

T_{SP} : SP transition temperature

WM : Weld metal

XRD : X-ray diffraction

Z : Atomic number

Chapter 1

Introduction: Selection Criteria and Joining Methods of 9Cr Reduced Activation Ferritic Martensitic steel for Fusion Technology

1.0 Introduction

The projected future demand and supply scenario for energy is an indication of a global energy policy exploiting the potential of all available resources, each technology bestowed with its own inherent challenges. In this scenario nuclear energy is one of the most viable energy options, since it meets several criteria like sustainability, clean source of power and minimum impact on environmental degradation. Nuclear fission based reactors have attained a fairly high level of technological maturity and several countries have a nuclear energy program in place. Although it would fill in the energy demand to a considerable extent, a major breakthrough like launching commercial fusion technology needs to be aimed at in the long term. Nuclear fusion, a safe, clean and proliferation resistant means of energy with abundant fuel availability, with the additional advantages of no risk of long-lived radioactive waste and severe accidents would be a significant leap into the energy security, by end of this century.

Fusion technology is based on deuterium - tritium (D, T) nuclear reactions releasing 14.5 MeV neutrons. Major challenge in the fusion technology is "confinement" of the high temperature plasma. The earliest configuration of plasma confinement is the Tokamak with a doughnut shaped magnetic chamber. The subsequent use of lasers is one of the current challenges in fusion technology. The current international strategy in nuclear fusion is to demonstrate the "technological" feasibility of magnetic fusion energy, before middle of this century. The first reactor, namely International Thermonuclear Experimental Reactor (ITER), is under construction at Cadarache, France [1]. This effort is also expected to evaluate the economic competitiveness and demonstrate the technology to be environmentally friendly. The future project DEMO envisages the demonstration of commercial feasibility of fusion technology [2-3]. For the successful launch into fusion technology through the ITER and DEMO programs, materials play a key role.

The major components of ITER and DEMO are the plasma facing components namely the first wall and breeding blankets, which are subjected to high neutron irradiation, in addition to strong mechanical, thermal, and electromagnetic loadings, under static and transient conditions [4-6]. The materials suitable for plasma facing components are the high temperature materials such as copper based composites and tungsten alloys.

Presently, the ITER project includes feasibility studies on the production of fusion energy and examination of various concepts using Test Blanket Modules (TBM) for tritium breeding. Hence, all the ITER participating members (China, Europe, India, Japan, Korea, Russia and USA) are engaged in the TBM program for testing various types of tritium breeding modules [7-9]. It is important that the alloy design for the structural materials incorporates necessary steps to reduce induced radioactivity and minimize the radioactivity level of the waste for safe disposal and storage [10-11]. The calculated radioactivity of few alloying elements of steel, on exposure to typical fusion neutron spectrum is shown in **Figure 1.1**. It is seen that alloying elements such as Mo, Ni and Nb need to be eliminated to obtain low level of radiation after about 100 years of cooling time. Three major classes of structural materials that can fulfill the “low activation” requirement considered for first wall and breeding blanket concepts designs are ferritic-martensitic steels, vanadium alloys and SiC/SiC ceramic composites. The experience from fast reactors has demonstrated that the ferritic-martensitic steels have excellent resistance to irradiation induced void swelling in addition to adequate strength and

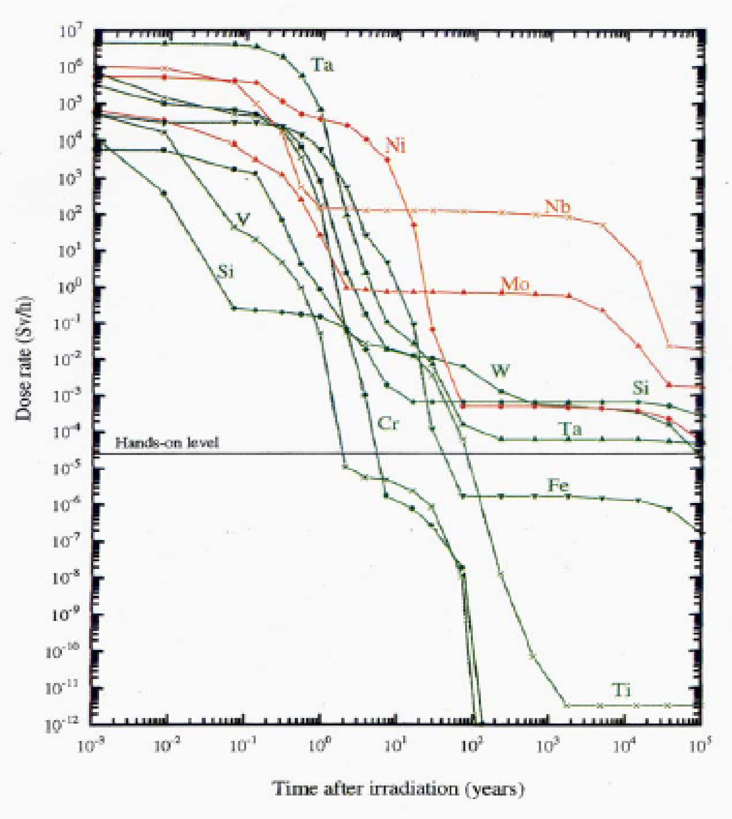

Fig.1.1: Calculated radioactivity on few elements versus time after exposure to typical fusion neutron spectrum [5]

toughness, which makes them a natural choice as structural material for the TBM. The immediate choice of ferritic/martensitic steel is also aided by its technological maturity with respect to industrial production, fabrication and testing methodologies [12-15]. The practical limitation imposed by industry and economic considerations for achieving "low activation" has enabled the development of Reduced Activation Ferritic /Martensitic Steel (RAFM) [16-17].

1.1 Design of Reduced Activation Ferritic/Martensitic steel

The guiding principles for the development of RAFM steel are as follows:

(i) Replacement of radiologically undesirable elements such as Mo, Nb and Ni in the existing commercial P91 (modified 9Cr-1Mo ferritic martensitic) steels by elements such as W, V, Ta, which have equivalent or similar effects on the constitution and structure but less prone to induced radioactivity upon prolonged neutron irradiation.

(ii) Removal of impurities like B, Cu, Ni, Al, Co and Ti, which are prone to transmutation on neutron irradiation.

(iii) Strict control on tramp elements such as S, P, As, Sb, Sn, Zr and O which promote embrittlement [18-19].

Cr is an important alloying element to offer high oxidation resistance and for formation of carbide precipitates which provide stability to the microstructure. The optimum Cr content is considered as 9% on the basis of (i) the longest creep life and (ii) lowest increase in DBTT (**Figure 1.2**) on irradiation [20-21]. In order to avoid the formation of undesirable δ- ferrite, the Cr content is restricted to 9%.

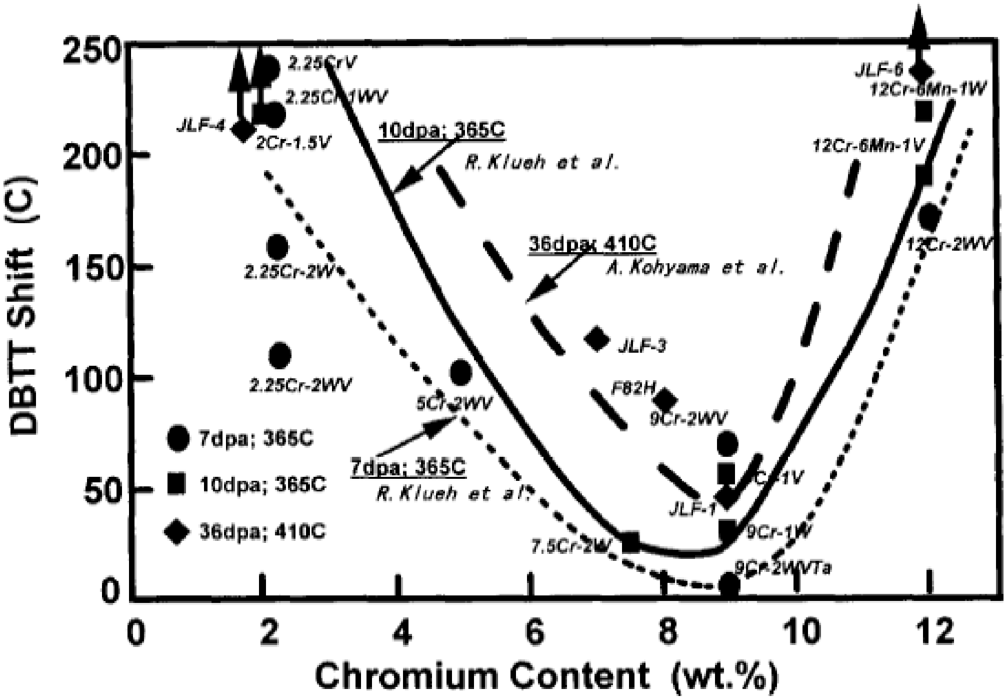

Fig.1.2: Effect chromium content on shift in DBTT of RAFM steels [21]

Tungsten is beneficial as it produces a more stable microstructure as well as slows down the recovery of martensite by stabilizing the substructure. It is reported that in 9Cr steels, tungsten refines the martensitic lath size and resists its coarsening on creep exposure [22-23]. Additionally, the presence of tungsten in carbides reduces its coarsening kinetics by retarding iron self-diffusion [24].

Tungsten improves the high temperature strength by increasing the binding force among the atoms in solid solution. But formation of Laves phase (Fe_2W) on long time service temperatures may deteriorate the toughness properties [25-26]. V and Ta are added to form MX type of carbonitrides which imparts significant increase in creep strength. Like Cr, Si also improves oxidation resistance of the steel, but it also enhances the precipitation of Laves phase [27-28]. Several variants of RAFM steels have been developed by various countries such as F82H, JLF-1 (Japan), Eurofer 97 (Europe), ORNL-9Cr2WVTa (US) and INRAFM (India) and extensive research is underway [29-30]. The composition of the steels is compared in **Table 1**.1.

Table 1.1: Nominal compositions of the RAFM steels

Steel	Element (wt%)										
	C	**Si**	**Mn**	**Cr**	**W**	**V**	**Ta**	**N**	**B**	**Fe**	**Ref.**
EUROFER	0.10-0.12	0.05 max	0.4-0.6	8.0-9.0	1.0-1.2	0.20-0.30	0.06-0.10	0.02-0.04	0.004-0.006	Bal.	[21]
F82H	0.10	0.20	0.50	8.0	2.0	0.20	0.04	<0.01	0.003	Bal.	[31]
JLF-1	0.10	0.08	0.45	9.0	2.0	0.20	0.07	0.05		Bal.	[32]
9Cr-2WVTa	0.10	0.30	0.40	9.0	2.0	0.25	0.17			Bal.	[33]

Besides meeting the nuclear properties such as good resistance to void swelling, helium embrittlement, and mechanical properties, 9Cr RAFM steels have good thermal conductivity, low thermal expansion coefficient and good compatibility with wide range of liquid and gaseous coolants.

1.2. Physical Metallurgy of 9Cr RAFM steels

The Cr rich part from the phase diagram of Fe-Cr-C alloy containing 0.1%C is shown in **Figure 1.3**. It can be seen that 9Cr steels are fully austenitic at austenitizing temperatures in the range of 850-1150°C. The austenite phase transforms to martensite for a wide range of cooling rates due to high *Ms* (martensite start) temperatures (~673 K). The steels are subsequently tempered to obtain a good combination of strength, ductility and toughness. The solutionizing and tempering temperatures are decided based on the Ac_1 and Ac_3 transformation temperatures. An elaborate calorimetry study on 9Cr-1W steel has established the Ac_1 and Ac_3 transformation temperatures as 1104 K and1144 K respectively [34-35]. The steel normalized at 1253 K showed martensite start (M_s) at 714 K and finish (M_f) at 618 K. The effect of holding time at solutionising temperature has significant effect on martensitic transformation characteristics [36-37]. The typical microstructure of RAFM steel is tempered martensite consisting of martensite laths with high dislocation density and precipitates distributed along grain and lath boundaries. The normalizing treatment leads to formation of hard and brittle martensite phase, which on tempering leads to the formation of inter and intra grain/lath carbides such as $M_{23}C_6$ (M= Fe, Cr and W) and MX (M=V, Ta and X = C, N) carbonitrides.

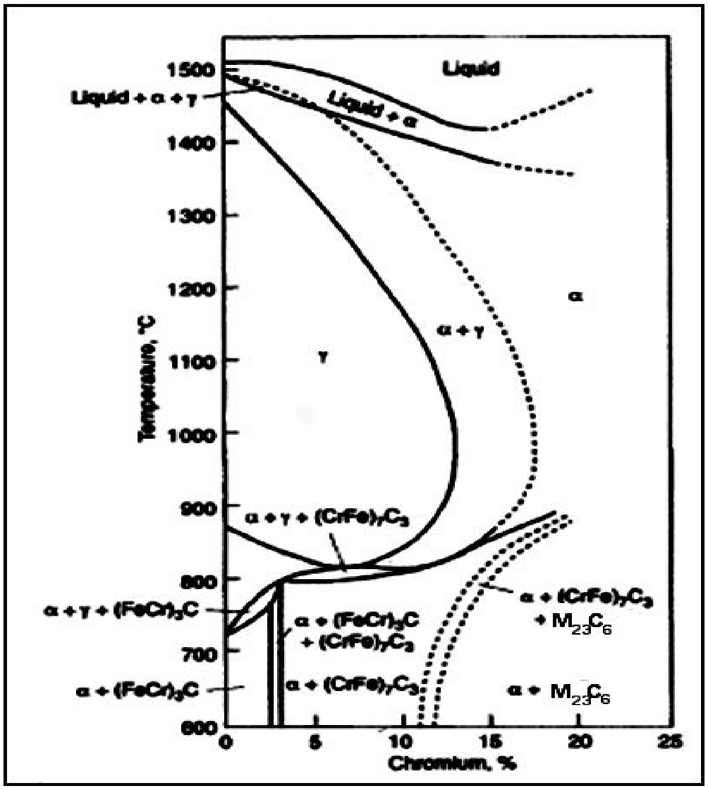

Fig.1.3: Section of Phase diagram of Fe-Cr-C alloys containing 0.1%C

These precipitates interact with moving dislocations and arrest the migration of lath boundaries thus pinning the dislocations and subgrain boundaries. The subgrain boundaries provide hindrance to dislocation motion during creep deformation [38]. The carbide stabilized subgrain boundaries also are known to reduce the creep rate considerably [39]. A tempered martensitic structure thus provides the combination of high strength and toughness and it is well established that the ferritic martensitic steels derive their strength from the tempered martensite lath structure.

The prolonged thermal exposure of the tempered martensite structure is of serious concern due to continuous evolution of microstructure in RAFM steel. Microstructural evolution in these steels includes coarsening of precipitates, reduction in dislocation density, changes in microchemistry, and formation of new phases. Although the principal carbide in this steel is $M_{23}C_{6,}$ small quantities of carbo-nitrides of V and Ta formed during tempering. Further precipitations, coarsening and spheroidization of carbides occur during aging or under creep. Prolonged exposure to high temperature produce Laves phase (Fe_2W) and its volume fraction depends on W content in the steel. 9Cr-1Mo steels and its variants being a workhorse of petrochemical and energy industries, above aspects of evolution have been studied by several research groups all over the world [40-42]. However, alloying elements such as W and Ta exert a profound influence on the kinetics of different processes like formation and dissolution of precipitates, coarsening and substructure changes. The role of W and Ta in refining the prior austenite grain size in 9Cr RAFM id reported [43]. It is reported that W is more effective in resisting the recovery of martensite than Ta.

1.3. Properties of 9Cr RAFM steels – A comparison

Extensive literature is available on the development of RAFM steels, in the last three decades, which have primarily addressed the issues related to the optimization of composition to obtain the required mechanical properties, weldability, fabricability as well as gaining experience under irradiation in the Tokamak facilities. Although, the composition of the Eurofer and F82H vary with respect to Cr, W and Ta contents, the steels have similar microstructure, tensile, impact and creep properties [7, 44]. These two steels are considered as reference material for the first wall applications. At temperatures above 573 K the RAFM steels are expected to exhibit a good resistance to swelling (1 vol.% per 100 dpa as compared to 1 vol.% per 10 dpa in austenitic stainless steels) [45]. The mechanical properties of F82H, ORNL 9Cr2WTAV, JLF 1 and Eurofer 97 have been evaluated and found to meet the acceptable values for the intended application of

TBM [46]. It has been reported that RAFM steels have a moderate tensile strength (~700MPa) at room temperature, which reduces beyond about 873 K [47]. A strong reduction in creep strength at temperatures above 873 K and a significant stress softening in low cycle fatigue tests is also reported [45].

The RAFM steels possess a bcc structure and like other materials of this type, they exhibit a ductile-to-brittle transition temperature (DBTT). In the unirradiated state, the DBTT of F82H, OPTIMAX A and EUROFER 97 alloys lies well below room temperature, which is between 193 K and 183 K [48]. An extensive research with 72 compositions by Chun et.al brought out the effect of normalizing temperature and addition of trace amounts of Zr on creep and impact strength of RAFM steels [49]. Their results show that lower normalizing temperature provides better resistance to cleavage crack propagation, thus reducing DBTT. Creep-rupture experiments between 723 and 923 K until 30000 h showed satisfactory results, indicating long-term stability and predictability. Aging the steel up to 10000 h between 773 and 873 K does not significantly influence the tensile and impact properties, confirming high microstructural stability [48]. A study on stress relaxation revealed that an optimum composition of W and Ta is necessary to have the best creep–fatigue interaction life [50]. At high temperatures, it is reported that the RAFM steels lose their creep strength and at lower temperature undergo embrittlement [51-52]. This restricts the usage of RAFM steel to a narrow range of 623 to 823 K for long term industrial applications. Efforts are in progress to expand this limit by oxide dispersion (for enhancing the high temperature limit) and reducing tramp elements (for lowering the low temperature limit). The data on irradiation response of the steels to fusion service conditions is very scarce. Although extrapolating the data from fast reactors to fusion may have uncertainties, with limited or no data from fusion reactor it is necessary to understand the behavior of the material from the fast reactor data. Although the response to irradiation depends on temperature and neutron fluence, experience in fast reactors indicate that F/M steels show excessive radiation induced hardening, embritlement and loss of creep strength under irradiation [53-55]. For irradiation above 425–723 K, properties are generally unchanged. However, depending on fluence radiation-enhanced softening occur [56-57]. Irradiation at temperatures below 623 K leads to strong hardening and loss of ductility [58]. The reason for the observed embritlement is formation of irradiation- induced dislocation loop in the microstructure. These experiments have been repeated under hydrogen and helium environment that would prevail in the fusion reactor. The studies show increased tendency for hydrogen and helium embrittlement [54].

Irradiation campaigns of EUROFER in the temperature range 573–598 K did not show any saturation of hardening effect on yield strength or any substantial shift in DBTT up to 40dpa [59]. To obtain a better understanding of the evolution of microstructure in bcc RAFM steels on irradiation, modeling studies using molecular dynamics calculations, Monte Carlo (MC) simulations and dislocation dynamics are being studied [60-61].

The effect of radiation on toughness is characterized by an increase in DBTT and a decrease in upper-shelf-energy (USE), which is detected using Charpy test. The shift in DBTT varies inversely with irradiation temperature. Irradiation induced hardening and embrittlement at temperature below 623 K are the most critical issues for ferritic/martensitic steels [62]. In general, EUROFER exhibits superior irradiation resistance to conventional FM steels. The RAFM steels also have resistance to high pressure water circulation loops and flowing Pb-Li coolant. Intense R&D on development of coatings on RAFM for protecting them against the first wall conditions of corrosion is in progress [63-64].

1.4 Fabrication and Joining Technologies for RAFM steels

The complexity of the design of components in the fusion reactor has invoked severe challenges for development of innovative technologies for fabrication. The TBM, which is to be fabricated using RAFM steel has a complex shape. Figure 1.4 shows the schematic of the components to be integrated to the Indian TBM. It can be seen that several locations have complex geometries with shapes in the form of ‘pancakes’ or ‘boxes’. Hot Isostatic Pressing (HIP) is one method which has been used for fabrication of complex shapes of TBM with RAFM steel under selected conditions [29, 65]. It is basically a powder metallurgical process to densify powders or cast and sintered parts in a furnace at high pressure and temperatures. This can be extended as a diffusion welding process to manufacture near shape components. As a part of the development of Helium Cooled Ceramic Breeder (HCCB) for Chinese TBM, a high quality HIP joint was obtained at 150MPa/1423 K on discs of CLF-1 RAFM steel of diameter of 120mm and thickness of 35 mm. The HIP joint subsequently subjected to Post Weld Heat Treatment (PWHT) consisting of normalizing and tempering treatments [66]. Technologies for inspection and quality assurance of the integrity of the HIP joint have been successfully demonstrated. Torsion and Charpy properties of F82H HIP joints made for first wall with cooling channels of the blanket system showed a reduction of the absorption energy, and the reason was diagnosed as oxide present at the HIP interface [67].

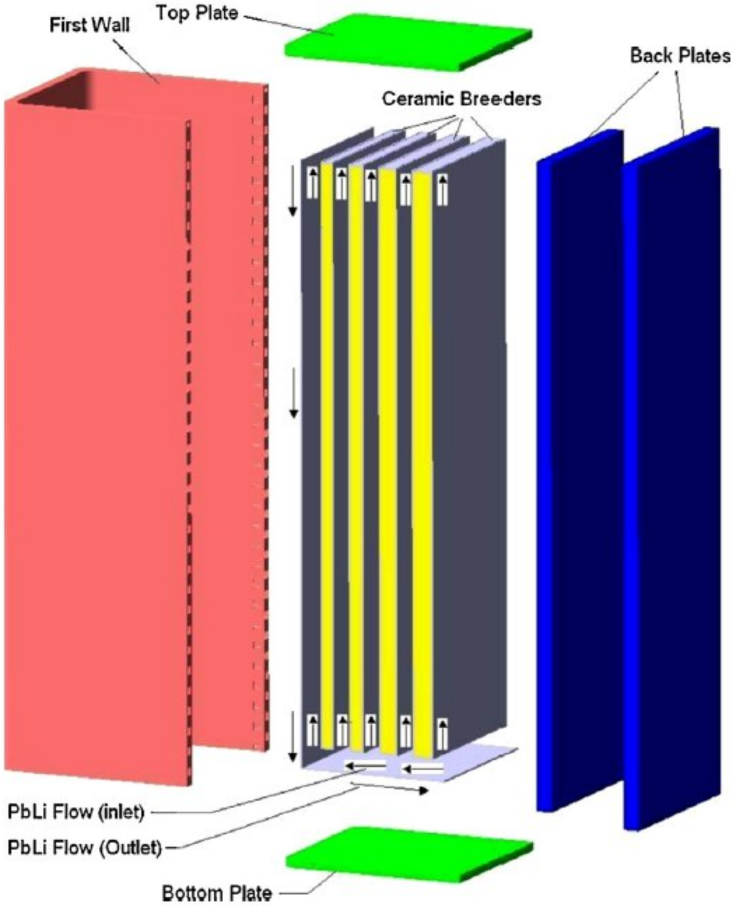

Fig.1.4: A Schematic of exploded view of Indian TBM

In recent years, the complexity of the shapes, rigid tolerance and difficulty in quality assessment have led the researchers to resort to additive manufacturing methodology ("3D printing"), to arrive at the most optimum fabrication procedure. In this process, the digital 3D design data is used to build up a component in layers by depositing material. This field is in its infancy for fabrication of components at an industrial scale.

There has been a plethora of research activities world-wide for knowledge based design of welding methodologies to be adopted for the TBM using variants of the RAFM steel [68-72]. The structure of TBM needs to withstand a helium pressure of 8 MPa with F/M steel which is susceptible to hot cracking. Hence, a thorough knowledge in fabricability and weldability is required to fabricate a defect free component. Electron beam welding, laser welding and gas tungsten arc welding (GTAW or TIG) methods were evaluated, due to the advantage of minimum quantum of weld metal and HAZ. Weld qualification procedures and post weld heat treatment (PWHT) for all the welding methods have also to be finalized. It is reported that inspection is possible even for the narrowest welds in some parts of TBM [71]. TIG, narrow gap TIG and Laser hybrid welding are being developed for integration of various components such as first wall, back plate, bottom plate breeder assembly and flow dividers in TBM.

In fusion welding, the solidified metal as well as base metal undergo a number of thermal cycles depending on the distance from the heat source and number of passes employed resulting in a highly heterogeneous microstructure consisting of martensite, tempered martensite and ferrite [73-76]. The failures during creep testing and long term service exposures are found to occur in the Heat Affected Zone (HAZ) region of the weld [77-78]. Advanced welding techniques with low heat input such as Electron Beam (EB) welding and Laser Beam (LB) welding are alternate methods to reduce the HAZ width, thereby minimizing the soft zone[79]. A review on welding of F82H has raised concern about the presence of a weakest region at the over-tempered HAZ region near the transformation line, and its impact properties [70]. The above feature could cause localized deformation, which may expand on irradiation of the weld joint. It recommends avoiding weld joints at locations of stress concentration.

In addition to welding methodologies, PWHT play a crucial role in minimizing embrittlement of the weld due to uncontrolled martensite formation. Extensive literature is available, on the effect of different combinations of PWHT conditions on microstructure and mechanical properties, which in turn dictate the in-service behavior [69, 79-81]. A careful combination of temperature and duration in PWHT is required to ensure high strength and ductility, by controlled tempering of the martensite. There are extensive structure-property correlation studies available in the literature in the development of PWHT of different types of ferritic steel joints [82-85]. Wang et.al demonstrated that high quality EB and TIG welding joints in CLF-1 RAFM steel of 15mm thickness with a PWHT at 101 K for 3 h without any preheating during welding [66]. Similarly hybrid, laser and NGTIG (Narrow Gap Tungsten Inert Gas) processes have been carried out on the EUROFER-97 steel (thickness up to 40 mm) and found that it has excellent weldability. The most promising joining techniques are EB, high power laser with less distortion levels and hybrid welding depending on section size.

Since it is the microstructural stability that decides the soundness of the weld joint, many experimental studies are focused on the change in structure and property during long term service exposures of the weldment [78, 86]. So an understanding of microstructural evolution including coarsening of precipitates, change in microchemistry and formation of any detrimental phases in various regions of the weldments are important for ensuring the desired life of the component and the joint. Like any other F/M steel, the high temperature creep strength of cross weld sample of RAFM is significantly lower as compared to base metal and creep failures occur at HAZ more precisely at intercritical heat affected zone (ICHAZ). Microstructural and mechanical property studies by Chandravati *et.al* on intercritically heat treated samples showed a decrease of prior austenite grain size, hardness and tensile strength [87]. A substantial reduction of dislocation density was also observed in ICHAZ.

Though RAFM steel is the primary candidate material for fabrication of Test Blanket Module in ITER, 316L (N) austenitic steel is the material selected for the vacuum vessels and several other components. Hence, dissimilar weld joints between RAFM and austenitic stainless steels are inevitable for fabrication of the structures in the fusion reactor. Fabrication of dissimilar weld joints between ferritic and austenitic steel is very challenging because of differences in structural, chemical and mechanical properties of the two base metals which may result in joints of inferior performance [88]. For making dissimilar joints of ferritic steel to austenitic steel by arc welding, usually austenitic (SS309) or Ni based welding consumables are used to ensure a desirable weld metal microstructure. However, for the TBM, irradiation embrittlement being of major concern, a joining process that would result in minimum volume of weld metal and HAZ needs to be employed. Such a process will also meet the requirement of minimum distortion. Hence EB or LASER welding is preferred. EB welding between RAFM and SS316L (N) resulted in retention of delta ferrite, which in turn affected the brittle transition temperature of the weld metal [89]. The improper mixing of the two base metals in the fusion zone of the dissimilar welds was evidently noticed.

A dissimilar weld joint between a ferritic steel and an austenitic contains a complex interface with a sharp change in composition as well as microstructure. When the thermal properties are different for these alloys, thermal stresses arise during fabrication and service. Further, during PWHT or service exposure, diffusion of carbon across the weld interface from ferritic steel to austenitic steel can lead to a carbon depleted layer in ferritic side and carbon enriched layer in austenite side [90]. This enriched carbon in the austenite side precipitates as carbides at the expense of Cr, which results in the reduction of Cr in the austenite matrix. Diffusion of carbon due to the activity gradient has also been reported in a 2.25Cr-1Mo/ 9Cr-1Mo steel joint [76, 91]. As a result, microstructural and microchemical stability of the weld joint on long term service at high temperature is of major concern in dissimilar weld joints.

1.5 Indigenous Development of India specific RAFM steel

Being a participating member, ITER India has a detailed and comprehensive program to fabricate Indian Test Blanket Module (TBM) to be tested in ITER. Towards this an elaborate R&D effort was taken up at IGCAR in collaboration with Institute of Plasma Research (IPR), Gandhinagar and the Indian industry namely Mishra Dhatu Nigam (MIDHANI), Hyderabad, India to develop the India specific RAFM steel. In the first stage of this development, pilot scale melt of RAFM steel with composition of 1 weight % W and 0.06 wt. % Ta with minimum trace elements, was made in order to establish the capability of the Indian steel industry for producing the steel with the specified chemistry which would result in the required physical and mechanical properties [92-93]. In the second stage of the development, tungsten and tantalum in the RAFM steel were varied in the range of 1-2 wt% and 0.06-0.14 respectively and steels with four different compositions were developed (**Table 1.2**). Based on successful in house R&D on structure property correlations the composition (1.4W-0.06Ta) with optimum combination of strength and toughness was identified and designated as India-specific RAFM (INRAFM) [71, 94-96].

Presently in the third phase, commercial melts have been produced based on these specification and detailed investigations on microstructure, mechanical properties, aging behavior and effect of irradiation are in progress.

Table 1.2: Chemical composition of RAFM steels studied for the optimization of INRAFM

Steel	Element (wt%)										
	Cr	**C**	**Mn**	**V**	**W**	**Ta**	**N**	**O**	**P**	**S**	**Fe**
1W-0.06Ta	9.04	0.08	0.55	0.22	1	0.06	0.023	0.0057	0.002	0.002	Bal.
1.4W-0.06Ta	9.03	0.126	0.56	0.24	1.38	0.06	0.03	0.002	<0.002	<0.001	Bal.
2W-0.06Ta	8.99	0.12	0.65	0.24	2.06	0.06	0.02	0.0024	0.002	0.0014	Bal.
1W-0.14Ta	9.13	0.12	0.57	0.22	0.94	0.135	0.033	0.0041	<0.002	0.0015	Bal.

As a part of the development of Indian RAFM steel, evaluation of the various welding techniques with respect to the mechanical properties and microstructure of the weld joint are being studied. Mock up fabrication of various components using this steel is also being pursued. Towards this, welding of INRAFM steel using potential processes that would be used in TBM fabrication and evaluation of the properties of the weld joints have been initiated. Procedures for hot isostatic pressing, electron beam welding, laser and laser-hybrid welding for making similar and dissimilar joints using INRAFM have been developed. The complex nature and limited access available for inspection in TBM has also led to the development of innovative inspection procedures using phased array ultrasonic and C-scan imaging [71].

1.6 Objective of the thesis

The objective of this thesis is to obtain an in-depth understanding into the evolution of microstructure on thermal exposure in indigenously developed 9Cr RAFM steels with two different tungsten contents and to study its influence on creep and toughness property. The microstructural changes in the RAFM steel on subjecting to three different welding processes namely Tungsten Inert Gas, electron beam and laser beam have also been studied in detail. The resultant microstructures have been correlated to the thermal cycles following the Rosenthal's steady state solutions to heat transfer equation as well as by GLEEBLE simulation. The solidification structure and the activity gradient driven phase transformations have been studied in a dissimilar weld of 9Cr RAFM steel and 316L stainless steel. The thesis highlights the effect of composition and thermal cycles on microstructure and microchemistry by a systematic experimental and computational study using JMatPro software. A variety of analytical techniques like electron probe microanalysis and analytical transmission electron microscopy has been used along with state of the art techniques like Focused Ion Beam – Scanning Electron Microscopy and Electron Back Scattered Diffraction technique for the structural and microchemical studies. Novel testing methods like impression creep and small punch technique have been employed to obtain the mechanical properties.

1.7. Scope of the thesis

This thesis presents the results of a systematic study on the physical metallurgy aspects of two variants of RAFM steel with different tungsten contents with emphasis on the microstructures that evolve in this steel on heat treatment and welding, employing a variety of microstructural and microchemical characterization techniques. The consequence of microstructural variation on the mechanical properties of the steel has been studied using two novel small specimen testing methods namely impression creep and small punch techniques.

The thesis focuses mainly on three themes which are as follows:

- Microstructural evolution in RAFM steels during thermal exposures which includes:
    - Effect of composition and temperature on evolution of phases
    - Influence of secondary phases on mechanical properties
- Comparison of different welding methods which include:
    - Variation in microstructural parameters in welds prepared by different methods
    - Optimization of Post Weld Heat Treatment (PWHT) for RAFM welds.
    - Role of initial microstructure, alloy composition and temperature on the kinetics of evolution of secondary phases – an experimental and computational study.
    - Simulation of weld microstructures
- Characterization of RAFM-316L dissimilar welds joint which include:
    - Identification of zones in the dissimilar weld
    - Evolution of microstructure during PWHT and elevated temperature exposures

1.8 Organization of the Thesis

This thesis consists of six chapters which are organized as follows:-

Chapter 1, **Introduction: Selection Criteria and Joining Methods of 9Cr Reduced Activation Ferritic Martensitic Steel for Fusion Technology,** presents a brief survey of available literatures on RAFM steel focusing on the historical development of the steel, physical metallurgy and structure- property correlations in this class of steel and the indigenous effort on development of the steel. It also deals with newer welding methods adopted in the construction of the Test Blanket Module (TBM).

Chapter 2, titled **Experimental and Computational Techniques,** describes the various experimental and analytical techniques used in the study. Details of heat treatments, specimen preparation, operating conditions of the microstructural and microchemical analysis techniques, methodology used for image analysis and possible errors are described. Test procedures of impression creep test and small punch test and a brief description on simulation software JMatPro® are also included.

Chapter 3, titled *"***Microstructural evolution in 9Cr RAFM steel with varying Tungsten Contents and its influence on properties",** presents a comprehensive study on microstructural evolution in INRAFM steel during long term elevated temperature exposure and compares the same with that of 1W steel. The main emphasis is on the type, chemistry and volume fraction of the secondary phases that form in the steel. The phases that form as a function of temperature have been predicted using the CALPHAD based simulation software JMatPro® and compared with the experimental results obtained by detailed electron microscopy investigations. Creep and toughness property have been evaluated by small specimen testing methods and correlated with the observed microstructures.

Chapter 4, titled **"Identification of Microstructural Zones in Weldments of RAFM steel and its Modifications on Thermal Exposure",** presents the results of a systematic characterization of the microstructure of the distinct zones in the welds prepared by three different welding methods namely autogenous TIG, electron beam and laser beam welding. Optimization of Post Weld Heat Treatment and determination of kinetics of tempering are also described in this chapter. The role of initial microstructure and chemistry on the evolution of phases in each zone is discussed.

Chapter 5, titled *"***Microstructural variations in a Dissimilar Austenitic – Ferritic Weld Joint",** deals with the microstructural characterization of the weld interface of RAFM-316L dissimilar joint and its modifications on PWHT and diffusion anneal studies. Possible phases in the weld metal that form due to intermixing or base metal dilution have been predicted based on the Cr and Ni equivalents. The results on microstructural changes that arise due to the local variations in chemistry, studied using various microscopy techniques are described in this chapter. The possible modification of the phase transformation characteristics due to chemistry changes have been studied using Differential Scanning Calorimetry (DSC).

Chapter 6, titled **"Summary and Scope for future work"** summarizes the important findings in this thesis and also identifies few areas for study in future.

Chapter 2

Experimental and Computational Techniques

2.0 Introduction

This chapter presents the experimental and computational schemes followed in the thesis. Details on the chemical composition of steels studied, welding parameters, heat treatment, specimen preparation and various techniques employed for characterization of microstructure and evaluation of mechanical properties are discussed. Experimental techniques like Optical Metallography, Electron Probe Micro Analyzer (EPMA), X-ray diffraction, Scanning Electron Microscopy and Analytical Transmission Electron Microscopy were used to determine the microstructural and microchemical changes that take place on thermal exposures or welding. The operating conditions of the instruments, calibration, procedure for data analysis and sources of errors are also discussed. The mechanical properties were evaluated using novel miniaturized testing methods like Impression Creep and Shear Punch. The physical simulation of HAZ was carried out by GLEEBLE® thermo mechanical simulator. In order to determine changes in phase constitution as a function of composition and temperature, a commercial soft computation package JMatPro® was used. The details of the above mentioned methods and procedures are discussed in the following sections.

2.1 Weld preparation, Heat treatment and Specimen preparation

2.1.1 Composition of the steel studied:

Two variants of 9Cr–W–Ta–0.2V-0.1C RAFM steel with different tungsten contents of 1 and 1.4wt.% supplied by M/s MIDHANI, Hyderabad in the form of 12 and 6mm thick plates respectively has been used in the present study. Chemical compositions of the steels are shown in **Table 2.1**. Of the two steels 1W–0.06Ta and 1.4W–0.06Ta, the latter one has been designated as India Specific RAFM (here after INRAFM) based on the elaborate studies carried out at IGCAR to optimize the composition with respect to mechanical properties. The steels were produced by selection of proper raw materials, employing vacuum induction melting and vacuum arc refining routes with stringent control over the thermo-mechanical processing parameters during forging, rolling and heat treatment. Strict control has also been exercised on the amount of elements (Mo, Nb, B, Cu, Ni, Al, Co and Ti) that can induce radioactivity and on the tramp elements that promote embrittlement (S, P, As, Sb, Sn, Zr and O). These elements have been restricted to ppm levels, as given in **Table 2.1**. The plates were supplied in the normalized (1253 K/1 h) and tempered (1033 K/1 h) condition. Wrought and TIG welded plates of both 1W RAFM and INRAFM steel were used for the long term microstructural studies. Similar weldments of INRAFM steel plates were prepared by both Electron Beam (EB) and LASER Beam (LB) welding. For the preparation of dissimilar weld joint, solution annealed SS316L plate (12 mm thick) was welded to 1W RAFM steel. The chemical composition of SS316L is given in Table 2.2.

Table 2.1: Chemical composition of two RAFM steels used in this study (wt %)

Steel	Cr	C	Mn	V	W	Ta	N	O	P	S	Ti	Ni	Mo	Nb	Fe
1W	9.04	0.08	0.55	0.22	1.0	0.06	0.022	0.005	<0.002	<0.002	0.005	0.005	0.001	0.001	Bal.
INRAFM	9.03	0.12	0.56	0.24	1.39	0.06	0.029	0.002	<0.002	<0.001	0.005	0.005	0.002	0.001	Bal.

Table 2.2: Chemical composition of the SS316L used in this study (wt %)

Steel	C	Cr	Ni	Mn	Mo	P	S	Si	V	Co	Cu	N	Al	Ti	Fe
SS316L	0.027	17.2	12.0	1.7	2.5	0.03	<.005	0.45	0.09	0.22	0.03	0.1	<0.034	<0.08	Bal.

2.1.2 Weld preparation

The plates of 1W and INRAFM steel were machined to 1800 x 700 x 12mm size and autogenous bead-on-plate weldments were fabricated by Tungsten Inert Gas (T1G) welding to simulate conditions similar to Electron Beam (EB) and Laser Beam (LB) Welding, where filler material is not used. The purpose of the autogenous TIG welding was to generate the microstructural variations associated with thermal cycles, at the same time avoid the dilution effects and compositional changes in the weld metal as well as reheating effects due to multiple thermal cycles. Welding parameters used in the present study are listed in **Table 2.3**.

Table 2.3: Welding parameters used in the present study

Welding technique	Voltage & Current			Welding speed (m/minute)	Heat input (kJ/mm)	Gas Flow (L/minute)
TIG	Voltage	Current	Arc gap	0.15	0.9	10
	15 V	150 A	1.5 mm			
EB	Gun voltage	Gun current		0.6	0.36	--
	120 kV	30 mA				
LASER	LASER Power			1	0.21	30
	3.5 kW					

A schematic of the TIG weld geometry is shown as **Fig.2.1**.Various regions of the weldment were classified as weld metal (WM), HAZ1 (Heat Affected Zone (HAZ) near to fusion line), HAZ2 (HAZ near to base metal) and base metal (BM) for simplicity. EB and LB similar weld joints of INRAFM steel were fabricated using 6 mm plate based on conditions optimized [97] to obtain high quality welds. The dissimilar weld joint between 1W RAFM and SS316L was prepared by EB welding.

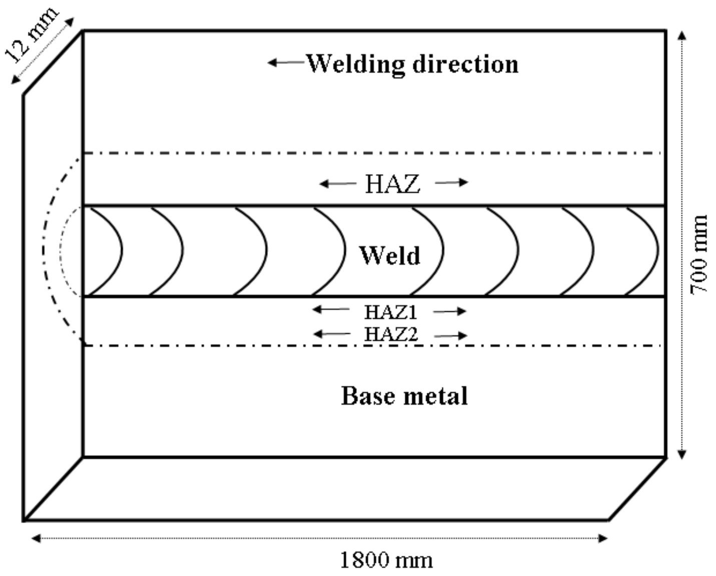

Fig. 2.1: Schematic of the TIG weld geometry

2.1.3 Simulation of HAZ microstructures

The simulation of HAZ microstructures was carried out using a GLEEBLE 3800C Themo-mechanical simulator at Institute for Plasma Research Institute, Gandhinagar, India. GLEEBLE 3800C is an integrated digital closed-loop controlled thermal and mechanical system. It uses windows based computer software with an array of powerful processors with a user friendly interface to run and analyze the data from physical simulation programs. GLEEBLE 3800 system uses direct resistance heating system to heat the specimens at rate of maximum up to 10,000˚C/s. With quenching systems it can provide a maximum cooling rate of maximum up to 10,000˚C/s.

Samples are placed between two sets of jaws that are part of a high current circuit. As current passes through the sample, it is resistively heated. A thermocouple welded to the center of the sample is used in a feedback loop to monitor temperature and control current. A schematic of the jaws, sample and thermocouple wire is shown in **Figure 2.2**. The temperature to which the sample is heated can be controlled manually or automated by a computer program. The jaws and transformer are cooled by water circulation, to keep the system from overheating and also to help in heat removal from the sample during cooling. Temperature distribution in the sample between the jaws is parabolic in nature with a peak temperature at the center of the sample. Using jaws of different geometry and conductivity can alter the temperature distribution. The distance between the jaws (free span) also control the thermal gradient experienced in the sample. In this equipment, the middle portion of a BM specimen is subjected to a thermal cycle similar to that experienced by a specific region of the HAZ that forms in a weldment. Exposure to a uniform peak temperature zone of few millimeters width can be achieved in the center of the specimen, which can be used for microstructural and property evaluation.

In the present study, INRAFM steel specimens were subjected to thermal cycles in the GLEEBLE simulator at four different peak temperatures, namely 1173 K to simulate the inter-critical HAZ (ICHAZ), 1273 K for the fine grain HAZ (FGHAZ), 1373 K and 1523K for the coarse grain HAZ (CGHAZ). In addition, a high temperature (1573 K) test

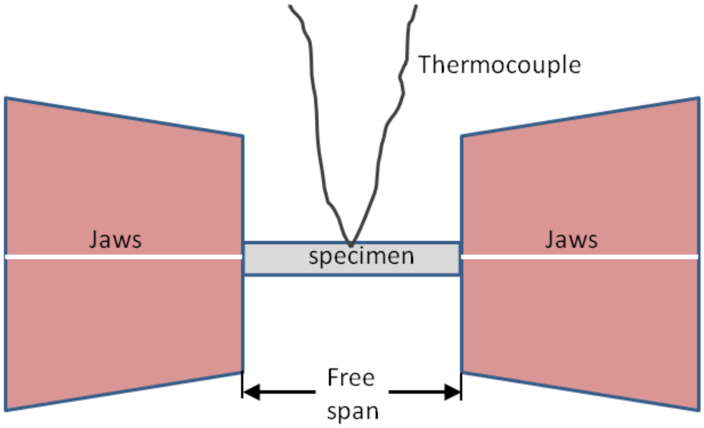

Fig. 2.2: Schematic of the specimen held in jaws with thermocouple welded at the centre

with higher holding time was conducted to examine the possibility of formation of delta ferrite in this steel.

2.1.4. Heat treatments

TIG welded joints were heat treated at three different temperatures in the range of 873 - 1033 K for durations of 0.25 -2 h to optimize the PWHT condition for the indigenous steels. EB and LASER weld joints were subjected to the optimum PWHT at 1033 K for 1 h. TIG weldment specimens encompassing all the three regions namely WM, HAZ and BM were aged at 773 and 823 K for durations of 5000 and 10000 h, to study the long term microstructural behavior. All the heat treatments were carried out in vacuum sealed quartz tubes. The details of the heat treatment schedules are given **Table 2.4**.

Table 2.4: Heat treatment schedules followed - wrought steel, similar and dissimilar welds

Steel	**PWHT**			**Aging**			
	873 K	**973 K**	**1033 K**	**773 K**	**873 K**	**973 K**	**1073 K**
	Time / h			**Time / h**			
N &T 1W & INRAFM				**5000 10000**	**5000 10000**		
Autogenous TIG (1W & INRAFM)	**0.25 0.50 1 2**	**0.25 0.50 1 2**	**0.25 0.50 1 2**	**5000 10000**	**5000 10000**		
Gleeble Simulated INRAFM			**1**				
Electron Beam Welding (INRAFM)			**1**				
LASER Beam Welding (INRAFM)			**1**				
Dissimilar -Electron Beam Welding (SS316-1W RAFM)			**1**		**10 20 50 100**	**10 20 50 100**	**10 20 50 100**

In addition to the above the Gleeble simulated HAZ specimens were subjected to a heat treatment for 1h at 1033 K equivalent to PHWT.

2.1.5 Specimen preparation

The samples for optical microscopy, hardness measurements and scanning electron microscopy (SEM) from wrought and weld were prepared by mounting the cut samples in suitable mounts. Standard polishing and etching techniques (Table 2.5) were used for metallographic preparation of specimens [98].

Transmission Electron Microscopy (TEM) specimens were prepared by sectioning the specimen parallel to fusion line with a precision cutting device. Thin foils were prepared from these samples by jet thinning method as per the details given in **Table 2.5**. In order to understand the structural and chemical changes in austenite during aging as a function of distance from interface, the state of art Focused Ion Beam (FIB) technique in a FEG SEM has been used to prepare TEM sample adjacent to austenite weld interface.

Table 2.5: Specimen preparation methods

Investigation technique	Preparation methods	Etchant/ electrolyte	Details
Optical microscopy Hardness SEM	Conventional metallographic methods	Vilella's reagent	1g picric acid 5ml HCl 100 ml methanol
Transmission Electron Microscopy	Thin foil (Jet thinning)	10% Perchloric acid in Methanol	T= -30°C V = 20V Current density = 40 mA/cm^2
	Carbon extraction replica	Vilella's reagent	• Polishing & light etching • Carbon coating on etched surface • Removal of carbon film by additional etching
EBSD	Electro Polishing	20% Perchloric acid in Methanol	T= -40°C V = 15V

Additionally, carbon extraction replica were prepared using polished cross sectional samples to identify the type, chemistry of the secondary phases [99-100]

2.2 Experimental Techniques for microstructural characterization

2.2.1 Optical microscopy

Optical microscopy was carried out in the bright field mode using a Leica MeF4A microscope fitted with a Leica digital camera along with image analysis software Leica QWin and MW Workstation. The magnification calibration of the objective lenses was carried out with a standard micrometer stage insert with 1000 lines/mm.

2.2.2 X-ray diffraction

X-ray diffraction (XRD) spectra of the specimens were recorded at room temperature with INEL XRG-3000 diffractometer using Cu Kα1 (wavelength=1.54056 Å) radiation and CPS 590 curved position sensitive detector in the angular range of 20–95˚ (2θ). The intensity and 2θ values were calibrated with a standard Si pellet, prior to acquisition of the spectra on the specimens. In the present study, XRD spectra were recorded from flat specimens. Phase identification in XRD was carried out by comparison with JCPDS data [101]. The peak positions were identified at 2θ <±0.3° from the expected values of different phases.

2.2.3 Electron Probe Micro Analyzer

Microchemical characterization was carried out using EPMA (CAMECA SX50 of M/s CAMECA, France) at an accelerating voltage of 20 kV and current of 20 nA. Analyzing crystals used were LiF for FeKα, CrKα and NiKα. Chemical composition of each element was obtained by comparing the X-ray intensities generated from the specimen to that of X-ray intensities generated from pure elemental standards under identical experimental conditions. ZAF correction procedure was incorporated on relative X-ray intensities for atomic number (Z), absorption (A) and fluorescence (F) for determination of chemical composition of the elements within the accuracy of ±1% [102].

2.2. 4 Scanning Electron Microscopy and Orientation Imaging Microscopy

Scanning Electron Microscopy was carried out using a Philips XL-30 SEM on etched and gold coated specimens for microstructural observations in the Secondary Electron (SE) and Back Scattered Electron (BSE) imaging modes. Energy dispersive analysis of X-rays was carried out using an Energy Dispersive Spectrometer (EDS) attached to the SEM, for identification of elements with atomic number >10 and a qualitative analysis to establish relative changes in concentration level of any element across different regions.

Micro-texture evolution during solidification or during transformation has been studied on longitudinal cross section close to the weld surface (face side) in the three types of joints (similar joints) using Electron Back Scatter Diffraction (EBSD) technique in the Philips XL-30 SEM. The scan area is 390 pixels horizontal X 306 pixels vertical with a step size of 0.6 μm. EBSD analysis has been carried out on PWHT samples to obtain high value of indexing. In SS316L-RAFM dissimilar joints, the two dimensional phase map and inverse pole figure (IPF) were obtained from austenite-weld interface using EBSD technique.

For carrying out three dimensional EBSD on dissimilar weld joint, the sample was polished by electro-chemical method. The sample was glued onto a 36° pre-tilted stub which can be tilted 16° toward the focused ion beam (FIB) or rotated 180° and tilted 34° towards the EBSD detector for data collection. The serial sectioning by FIB and EBSD measurements were carried out by using FEI make Helios Nanolab 600i FEG-SEM.

Fiducial markers were milled into the samples. They were used to align the area of interest during the automated EBSD data collection and subsequent milling. It is very essential that the samples should be well-aligned so that amount of material milled away in each step is consistent and controlled. Alignment is also important to ensure that the EBSD maps are being collected from the same region of interest in subsequent steps. An accelerating voltage of 30kV was used for milling the surface at an ion current of 9.3nA for rough-cut and 0.23nA for cleaning the cut surface. The Kikuchi diffraction patterns produced from the sample surface were detected by an EDAX-TSL camera and analysed using commercially available TSL-OIM software. **Fig.2.3** shows the sketch of the sample and the area of interest from where EBSD data is collected. The slice thickness between subsequent serial sections was 200nm and step size during EBSD scan was also 200nm. The scan area was 4µm × 4µm and EBSD data were collected up to 70 µm depth. The EBSD patterns were binned at 4 × 4.

2.2.5 Analytical Transmission Electron Microscopy

Analytical Transmission Electron Microscopy (ATEM) was carried out using a Philips CM 200 microscope at an operating voltage of 120-200kV equipped with Oxford X-max SDD detector for microstructural and microchemical analysis from both thin foils and carbon extraction replicas of the steels. The images were acquired by a bottom mounted ‘on axis’ TVIPS camera of 2048 X 2048 pixel resolution.

Magnification calibration was carried out with a cross grating of 2160 lines/mm with a separation of 469 nm between two lines. Camera length for diffraction analysis was calibrated at 200kV for different camera lengths with polycrystalline ring diffraction patterns of standard nanocrystalline gold islands in holey carbon film. The rotation

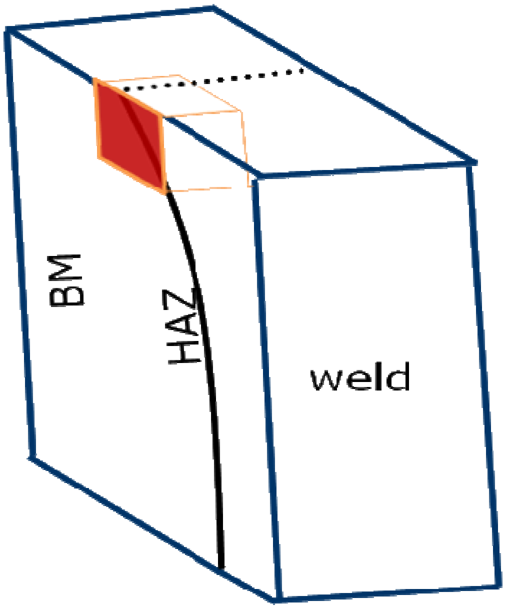

Fig. 2.3: Schematic of the SS316L -1W RAFM dissimilar weld indicating region of interest for EBSD analysis

calibration of SAD patterns with respect to magnification was carried out using MoO_3 crystals.

Thin foil imaging in TEM was carried out on specimens from each region of the weldment prepared by sectioning parallel to fusion line to study the change in microstructure and subgrain size as a function of distance from the fusion line. Identification of secondary phases was carried out by analyzing the Selected Area Diffraction (SAD) and micro diffraction patterns [103-104]. Microdiffraction was especially carried out on fine precipitates of size 10nm and below. In this case, as the incident beam is not parallel, the diffraction spots appear as discs instead of points as in case of SAD. For indexing electron diffraction patterns, the angles and d-spacings were measured with an accuracy of <1° and <10% respectively. The measured d-spacing values were compared with the standard ICDD [101, 105] and measured angle between planes matched with calculated values. In addition, Dark Field (DF) images using specific reflections of the SAD pattern of the phase of interest were acquired for confirmation, wherever possible [106].

Low magnification micrographs from extraction replica were used for finding out the volume fraction and size distribution of secondary phases from each region of the weld cross section by employing image analysis software 'ImageJ'. The size of the precipitate is quoted in terms of normalized diameter, which was calculated from the projected area of the particle assuming it as globular in shape. In general, $M_{23}C_6$ carbide showed a wide range of size, but MX was found to be fine in nature. Due to this wide variation, size of the precipitate is presented as frequency distribution plot. However, for volume fraction analysis no distinction between the two types of carbides could be made, due to very low fraction and size of MX. The volume fraction of the precipitates has been calculated based on area fraction analysis of several regions from a large number of images from the extraction replica. The standard deviation of several readings is considered as the error. However, it is worth to mention that the microscopic undulations in the etched surface cause errors in the analysis, which is due to extraction of stray precipitates from planes below the surface of the specimen [107].

Microchemical analysis of secondary phases with size ranging from 10 to 500nm was carried out on carbon extraction replica of the specimens prepared as per the details given in Table 2.5. Electron beam with different spots sizes were used for collecting characteristic X-rays of the constituent elements of the secondary phases. A low background single/double tilt holders were used to reduce the background noise in the x-ray spectrum. In-hole spectra were obtained periodically to ensure the absence of any spurious x-rays generated inside the column of the microscope. The conditions used to carry out Energy Dispersive Spectroscopy (EDS) analysis is given in **Table 2.6**.

Table 2.6 Conditions for quantification of EDS spectra

Operating voltage	120-200kV
Angle of tilt	30-35°
Beam diameter	30-50nm
Thickness of the sample	100nm
Density	7.5g/cc
Collection time	100s

A large number of X-ray spectra (>25) were collected from each phase from various regions of interest to obtain a statistically reliable data. The performance and reliability of the detector was ensured by carrying out periodical checking of energy calibration with pure Al and Cu standards and energy resolution with MnKα. Composition analysis was carried out assuming a thin foil criterion, which holds true if the intensity difference between in hole spectrum and specimen spectrum is less than 10%. Quantification was carried out by Cliff-Lorimer method by taking FeKα, CrKα, VKα, WMα and TaLα peaks as regions of interest [108]. As per Cliff-Lorimer equation

$$C_A/C_B = K_{AB} I_A/I_B$$

(2.1) where C_A and C_B refer to the concentration of A and B in an alloy AB.

I_A and I_B refer to the intensity of characteristic X-rays from A and B, respectively and K_{AB} refer to Cliff-Lorimer constant. For this study the library values of K_{AB} were used for quantification and verified with samples of known composition. By increasing the collection time to 100s ‘live time’ the error is minimized. Depending upon the size of the precipitate, an appropriate spot size is used for collection of X-rays. However, in some cases it was difficult to avoid the overlap of two closely spaced precipitates or to contain the beam within the precipitate. Considering this, the composition of each carbide was calculated from average of more than 25 measurements. The statistical error for 99% confidence limit in the composition analysis was ±3 wt%.

2.2.6 Simulation of phase transformation – JMatPro®

JMatPro® was used extensively to determine change in phase constitution as a function of composition and temperature. JMatPro® employs a CALPHAD based database for the computation of thermodynamic properties. The '*General steel*' module available in JMatPro® version 7 was used in this study. Equilibrium phases were identified by thermodynamic calculations using Gibb's energy minimization routines proposed by Kattner *et.al.* and Lukas *et.al.* [109-110]. Based on equilibrium calculations phase stability, phase fraction and composition of each phase were determined for different temperature domains. The evolution of precipitates on thermal aging was predicted based on the Johnson-Mehl-Avrami equation [111]. The kinetic simulation of phases is largely influenced by initial conditions of the alloy which decides the microstructure. Accordingly, the inputs for the calculations require composition of steel, temperature of austenitisation and prior austenite grain size along with aging temperature. Correctness of the underlying thermodynamic data was checked by comparing the predicted (using JMatPro) phase transformation temperatures with that of experimental calorimetry measurements [112].

Computation of the phase evolution took into consideration the difference in composition between the two RAFM steels and the thermal cycle undergone by different regions of the weldment during TIG welding [76]. The computed results were correlated with experimental observations. JMatPro® calculations of phase fraction in equilibrium and kinetic simulations are given in weight %.

2.3 Property evaluation techniques and analysis procedures

2.3.1 Differential Scanning Calorimetry

Differential Scanning Calorimetry (DSC) measures the difference in heat flow between the sample and the reference (an empty alumina crucible usually) which are heated at a preset heating/cooling rate. The absorption or evolution of heat associated with a phase change induces a change in differential heat flow between sample and reference. This uncompensated difference in temperature (ΔT) results in a differential signal in the base line. Thermal analysis experiments were carried out using *Setaram Setsys 1600*® heat-flux type differential scanning calorimeter [113]. A typical signal of Heat flow vs Temperature for a phase transformation is given in **Figure 2.4**. The transformation temperature is found out from the intersection points of the tangents drawn from base line and inflection points. The base line calibration is carried out by subtracting an empty (no sample) run signal from the actual run with test sample in position. Other instrumental related errors were minimized by using identical pair of crucibles, gas flow rate and scan rate etc.

The temperature scale is calibrated using the melting points of standard pure metal samples such as Al, Zn, Sn, Cu, Au and Fe. To determine the equilibrium onset temperature at different heating rates, the start of the melting point of pure metals like Al, Zn, Sn is determined and extrapolated for a hypothetical 0 K/min cooling rate. The accuracy in the measurement of temperatures was found to be ± 2 K. The calibration was

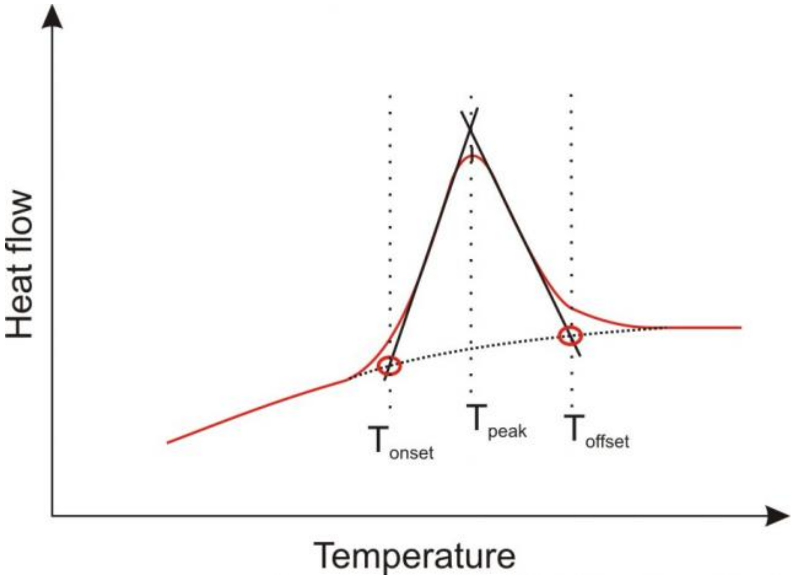

Fig. 2.4: A typical DSC thermogram showing a phase transformation

carried out only in heating cycle and not during cooling cycle due to the large under cooling associated with cooling cycle.

Samples of mass ~60 mg in the form of ≈2 mm × 2 mm × 2 mm thin cubes were used for calorimetry experiments. The entire span of calorimetry experiments were performed under flowing (50 mL min^{-1}) high-purity argon atmosphere. Three independent heating and cooling runs at 10 K/min were performed and the average values of the recorded transformation temperatures have been reported as the typical measured value and reproducibility of the measured temperatures was ± 2 K.

2.3.2 Hardness testing

The Vickers micro hardness measurements were carried out using a Leitz Miniload-2 microhardness tester at a load of 100g, which lies in the load independent region of the load vs diagonal length plot to evaluate the hardness profile of the weldment after different heat treatments. A standard test block of known hardness with prescribed load of 100g was used for calibration. Vickers Hardness number was evaluated after roughly 20 measurements on every sample to get reproducible and reliable values. The possible sources of error could be measurement error w.r.t diagonal length estimation, flatness of the specimen, presence of more than one phase with different hardness within the volume of indentation. The scatter was found to be within ±2% which is nearly same as the 2σ values of 99% confidence limits. In addition to this, bulk hardness measurements were also carried out to evaluate the change in the hardness of the weld metal after aging.

2.3.3 Impression Creep test

In Impression Creep (IC) test, a constant load is applied to the test specimen of thickness 10 mm through a flat bottomed cylindrical indenter of 1 mm diameter, made of tungsten carbide. An illustration of an impression test rig is shown in **Figure 2.5**.

The fundamental equipment of an impression creep test rig consists of:

- Loading system
- Data recovery system
- Heating and temperature system
- Deformation measurement system

The sample is machined parallel to surface and ground with emery sheets of 1000 grit size. The experiment is carried out at a vacuum level of 10^{-6} mbar in order to avoid oxidation of the indenter and the specimen. The temperature is controlled within ±1 K. A pre-test load is applied on the sample for keeping the specimen under compression before the actual load is applied. The punch penetration depth was recorded as function of test time using a LVDT which is attached to load cell. Depth measurement could be carried out with an accuracy of ±1 μm.

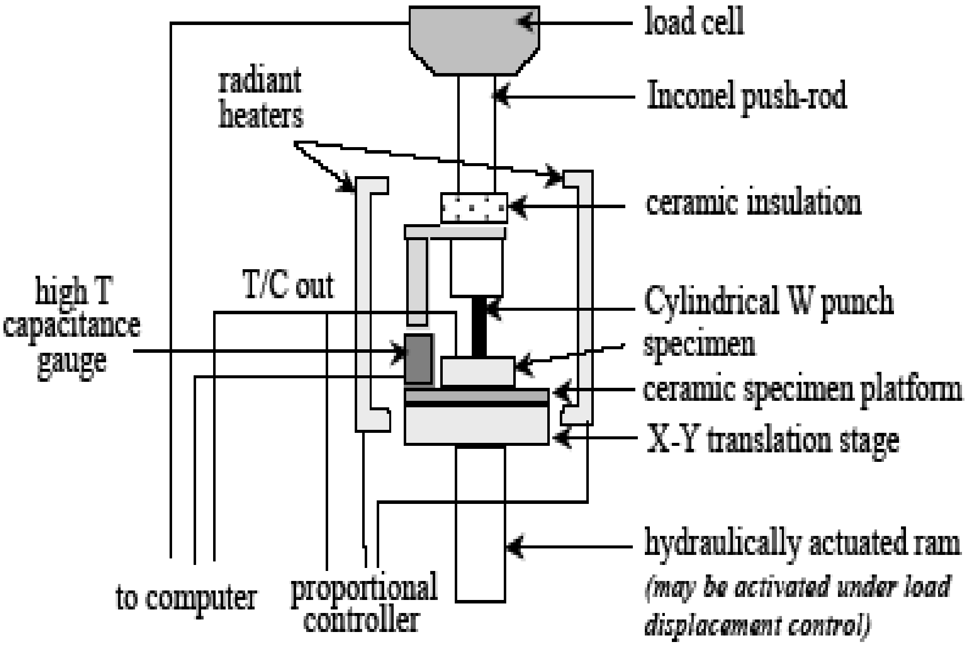

Figure.2.5: A schematic of experimental set up for Impression Creep test [114]

In an impression creep test if a constant load L is applied to the test specimen by a cylindrical punch of diameter d, then the punching stress is given by

$$\sigma_{imp} \quad = \quad 4L/\pi d^2 \qquad (2.2)$$

The punching stress σ_{imp} produces a penetration depth of h in time t. Then rate of penetration or the impression velocity is given by

$$v_{imp} = \mathrm{d}h/\mathrm{d}t \qquad (2.3)$$

Studies on impression testing have shown that the steady state impression velocity σ_{imp}, was found to be proportional to the punching stress σ_{imp} and a stress exponent n_{imp} and obeyed a power law, i.e.

$$v_{imp} /\mathrm{d} \propto \sigma^{n}{}_{imp} \qquad (2.4)$$

Thus σ_{imp} and impression velocity v_{imp} /d in impression creep test can be directly correlated to uniaxial stress (σ_{uni}) and uniaxial creep rate ($\grave{\varepsilon}_{\mathrm{uni}}$) [115]. The material during impression creep test is reported to exhibit the same stress and temperature dependence as the stress in a conventional tensile creep test [116-117]. Impression Creep tests can therefore be used to produce reliable creep strain rates, equivalent to those obtained from a normal creep test [118-120].

2.3.4 Small Punch Test – Toughness evaluation

The Small Punch (SP) test technique involves deforming a small disc specimen (typically 8 mm diameter and 0.5 mm thick) clamped between a set of dies using a spherical tipped punch (typically 2.5 mm diameter) and analysing the resulting load-displacement curve. **Figure 2.6** illustrates a schematic of cross-sectional view of the specimen holder with a hemispherical penetrator and the test specimen. Specimens were cut by Electro Discharge Machining (EDM) to a thickness of 0.55 mm and further carefully polished by emery sheets (1000 grit size) to obtain a uniform thickness of 0.5±01mm. Prior to the test, the holder is forced to clamp the specimen gently and the deformation is limited to the region of the hole of the lower die. A screw driven universal testing machine with a fixed cross head speed was used in SP tests. Load was monitored with a standard load cell of 1 kN ± 0.5%. The displacement of the punch was controlled and measured from the cross head movement. The small punch tests were performed at a constant cross head speed of 1 mm/min. The test performed for this study conforms to the standard codes provided by European Committee for standardization (CEN) by the work shop agreement CWA 15627 for “Small Punch Test Method for Metallic Materials” [115].

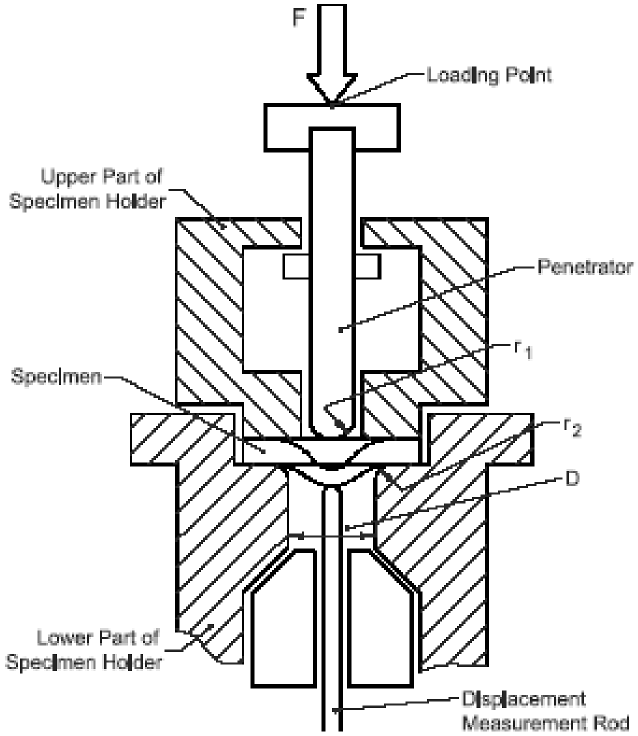

Figure.2.6: Cross- sectional view of the specimen holder for small punch test

According to CWA 15627, the SP fracture energy is defined by the area under the load punch displacement curve up to the displacement at onset of fracture/failure (u_f), which is defined as the punch displacement at 20% load drop after maximum load $F_f = 0.8F_m$. The SP test is carried out at different temperatures from ambient to liquid nitrogen temperature. The test temperatures were controlled within ± 2 K using a PID controller. As the test temperature decreases E_{SP} (SP fracture energy), d_m and P_m values show a transition similar to the Charpy Impact test curve. The objective of the test is to develop a load-displacement record which contains information about the elasto-plastic deformation and strength properties of the material. A typical load-displacement curve for ductile material is given in Figure 2.7. For determination of DBTT the area under the load-displacement up to fracture load is calculated.

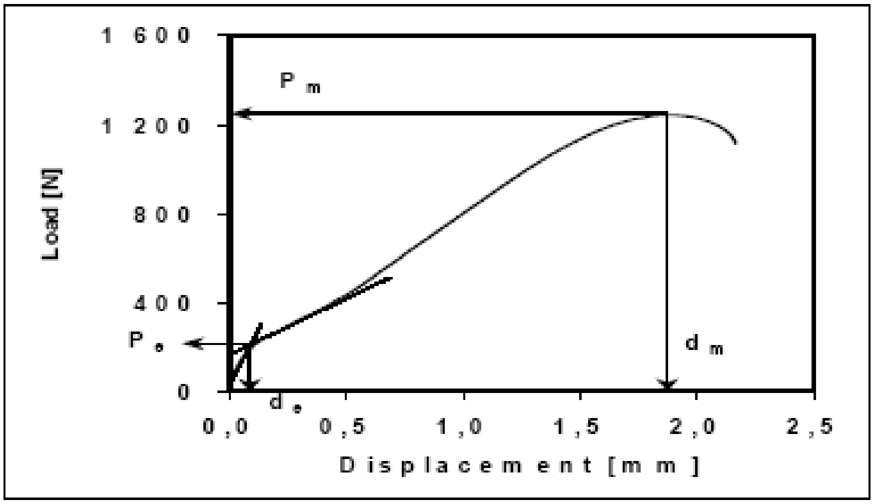

Figure.2.7: Load – displacement curve recorded during small punch test [115]

The evaluation of transition behaviour of ferritic steels is based on the temperature dependence of SP-related parameters [121]. T_{SP} (SP transition temperature) is determined as the temperature corresponding to the mean E_{Sp} value of highest and lowest in the transition region. DBTT is obtained from the SP test results using empirical correlations between T_{SP} (SP transition temperature), determined from the temperature dependence of fracture energy E_{SP}, and DBTT determined from the results of Charpy V Impact tests [115]. Empirical correlations are based on the fact that steels exhibiting standard Charpy V impact ductile to brittle transition behaviour also show this behaviour during a small punch test, but usually at a lower temperature. The principal difference between SP testing and conventional Charpy Impact test lies in the fact that the penetration test is carried out without any notch at slow strain rates, while the Charpy Impact tests are performed at high strain rates on a notched specimen. Hence the transition temperature in SP tests is shifted to lower temperatures. But the attraction of the SP test lies on the merit that a quick comparative study is possible with limited amount material.

Chapter 3

Microstructural Evolution in 9Cr RAFM steel with varying Tungsten Content and its Consequence on Properties

3.0 Introduction

In this chapter the microstructural evolution in the indigenously developed steels with varying tungsten content namely the 1W RAFM and INRAFM steels during prolonged thermal exposure to near service temperatures (773 and 823 K for durations up to 10000 h) has been studied in detail by a combination of simulations and experiments. The microstructural and microchemical changes were studied using Analytical Transmission Electron Microscopy techniques. The formations of various phases and their weight percentages have been evaluated using the JMatPro software for the two steels and compared with experimental results.

On prolonged thermal exposure, the RAFM steel undergoes structural and chemical changes at microscopic level due to competing effects like softening of the matrix, coarsening of precipitates and nucleation of new phases, which have a direct bearing on the mechanical properties such as tensile strength, toughness, creep strength etc. that are crucial to the service life of components. Increase in DBTT and deterioration of creep properties under irradiation are of prime concern in RAFM steels, for the intended application. Hence, emerging techniques like Small Punch and Impression Creep are gaining importance due to their capability for carrying out rapid tests on small specimen, essential to study irradiated specimens. However, in order to assess the degradation of these properties due to irradiation, knowledge of these properties of the steel prior to irradiation is necessary. Accordingly, in the present work, these techniques have been employed to evaluate DBTT and Creep properties of the normalized and tempered as well as aged steels. An attempt has been made to correlate the changes in impression creep behavior and shift in DBTT with the observed microstructures.

This chapter is organized in the following sequence. **Section 3.1** presents a comprehensive characterization of the 1W RAFM and INRAFM steels in normalized and tempered condition. The equilibrium phases in the normalized and tempered steel have been obtained using JMatPro software and compared with experimental results in **Section 3.2.** Microstructural evolution in the two steels on prolonged thermal exposures is described in **Section 3.3** and is compared with the computed results in **Section 3.4.** Results of impression creep tests is correlated with microstructural features and described in **Section 3.5.** The changes in toughness behavior including shift in DBTT with respect to W content and thermal history are given in **Section 3.6**. **Section 3.7** summarizes the results of this chapter.

3.1. Microstructural characterization of normalized and tempered steels

Optical micrographs of 1W and INRAFM steels in the normalized and tempered condition are shown in **Fig.3.1 (a)** and **Fig.3.1 (b)** respectively. Both the steels possess a typical tempered martensitic structure. SEM micrographs from 1W and INRAFM steel are given in **Fig.3.2 (a)** and **Fig.3.2 (b)** respectively. The 1W and INRAFM steels show microstructures with average prior austenitic grain size (PAGS) of 14 and 10 μm respectively. Earlier investigations have also reported that an increase in W content decreases the PAGS [122-123]. Average hardness of 1W steel (~230 VHN) and INRAFM (~240 VHN) is in agreement with the normalized and tempered ferritic-martensitic steels [122, 124-125] with a slightly higher value in INRAFM due to higher W content. **Figure 3.3** shows the TEM thin foil micrographs of normalized (1253 K for 30 minutes) and tempered (1033 K for 90 minutes) steels, which is the condition in which the steel was supplied. It is well known that martensite with high dislocation density

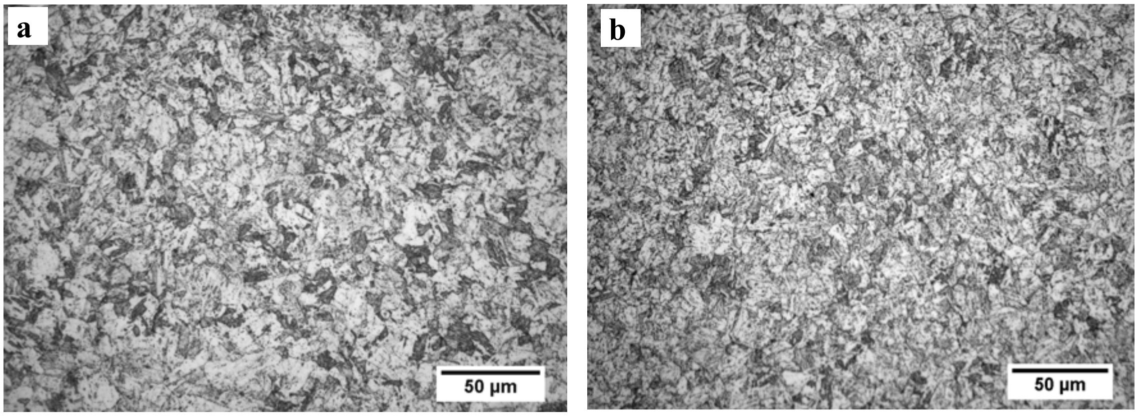

Fig.3.1: Optical micrograph of showing tempered martensitic microstructure in normalized and tempered (a) 1W and b) INRAFM steel.

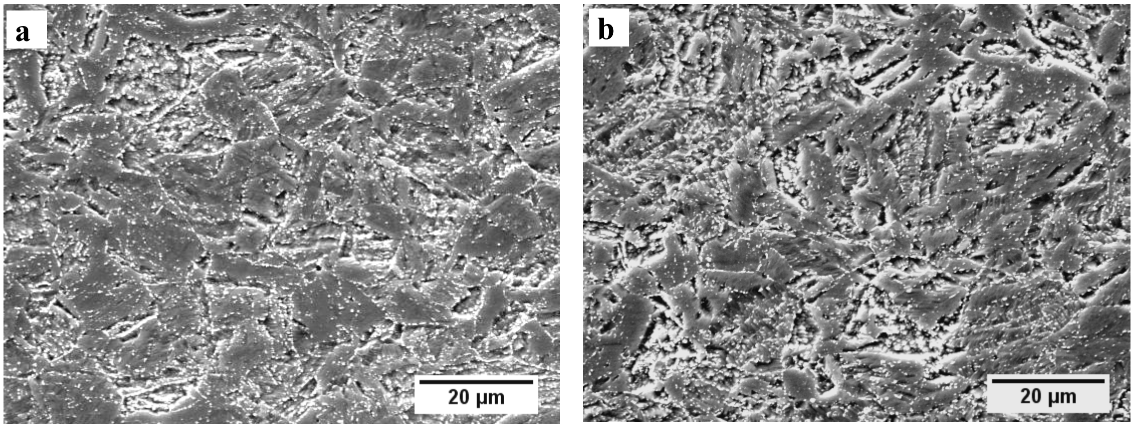

Fig.3.2: SEM micrograph showing tempered martensitic structure revealing the decoration of precipitates in normalized and tempered (a) 1W and (b) INRAFM steel.

forms in normalized 9Cr F-M steel. Tempering is carried out to attain optimum level of strength and toughness. A large number of dislocations and retention of lath morphology, in the prior austenite grains (with characteristic boundary triple point - arrow marked) [76, 126-127] are clearly seen from **Fig.3.3 (a)**. However, the average lath size reduced from 600-700 nm for 1W steel to 400-500 nm for the INRAFM steel (**Fig.3.3 (b)** and **Fig.3.3(c)**).

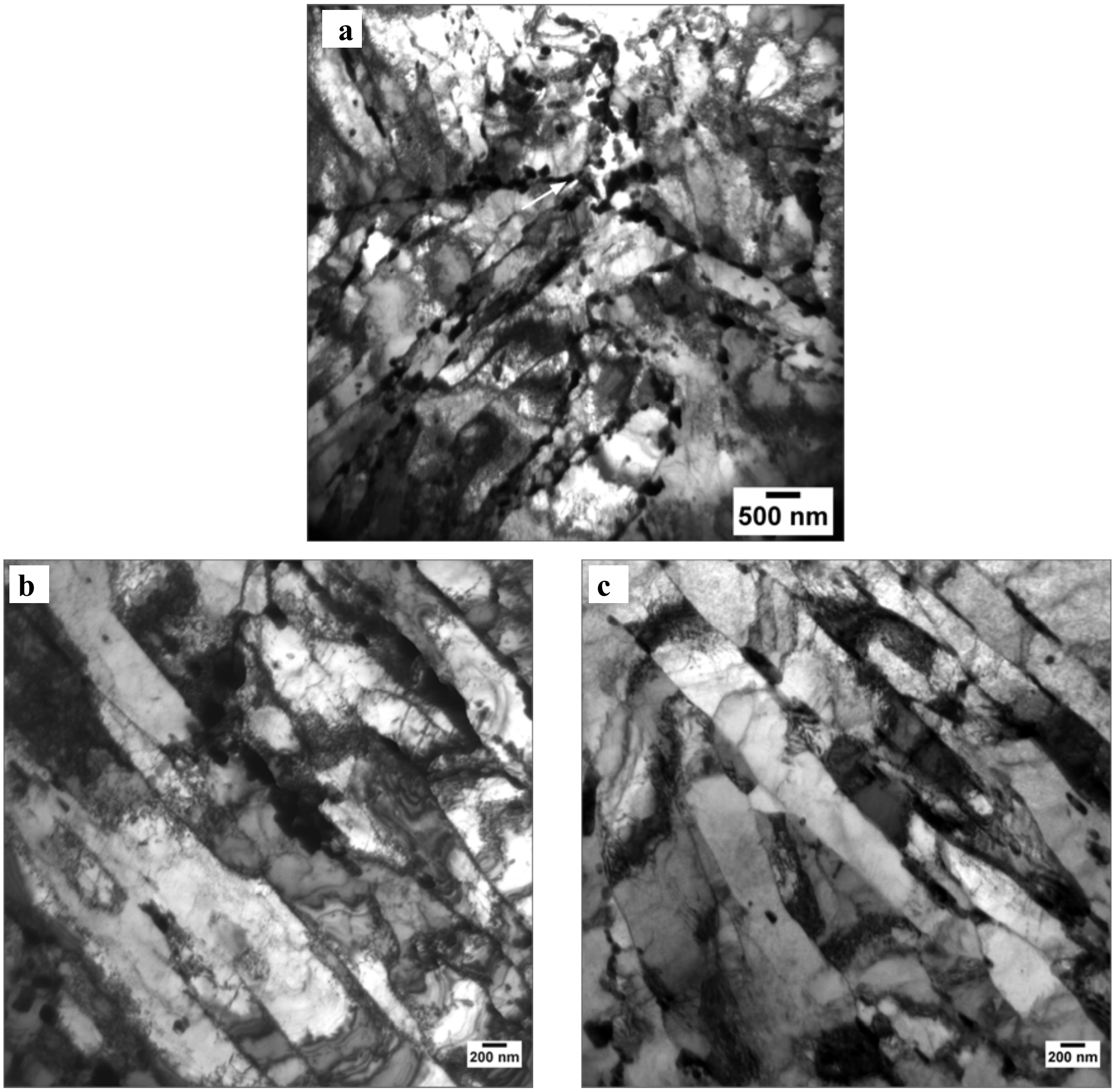

Fig.3.3: Bright Field TEM micrograph from thin foil of normalized and tempered (a) 1W steel showing a triple point (arrow marked) of prior austenite grain boundaries and substructures in different orientations (b) and (c) showing similar lath structure in 1W and INRAFM steel respectively.

The tempering of martensite results in decrease in dislocation density and precipitation of secondary phase. The lower width of laths in 1.4W steel is mainly attributed to the reduced self diffusion of iron in presence of W, since recovery proceeds mainly by self diffusion of iron [24]. It is worth mentioning that both the steels had been subjected to a normalizing treatment at 1253 K which is inadequate for complete dissolution of carbides [35]. Studies on RAFM steel with varying W content showed that dissolution temperature of $M_{23}C_6$ increases with W content [23, 112]. Due to high volume fraction of undissolved carbides in INRAFM steel pinning of grain boundaries is more effective during solution treatment as compared to 1W steel, which in turn restricts the grain growth in the former. Similarly W retards tempering by reducing the self diffusion rate of Fe [32], which is responsible for the fine lath size. The laths are decorated with carbides of various sizes, predominantly of lenticular morphology, as seen in **Fig.3.4 (a)**. However, few regions of ferrite with low dislocation density are also observed (**Fig.3.4 (b)**). Interestingly, the carbides present in the regions of lower dislocation density, were found to be globular and coarser in size than in other regions. In order to evaluate the size, type & chemistry of the carbides without interference from matrix, microscopy was carried out on carbon extraction replicas.

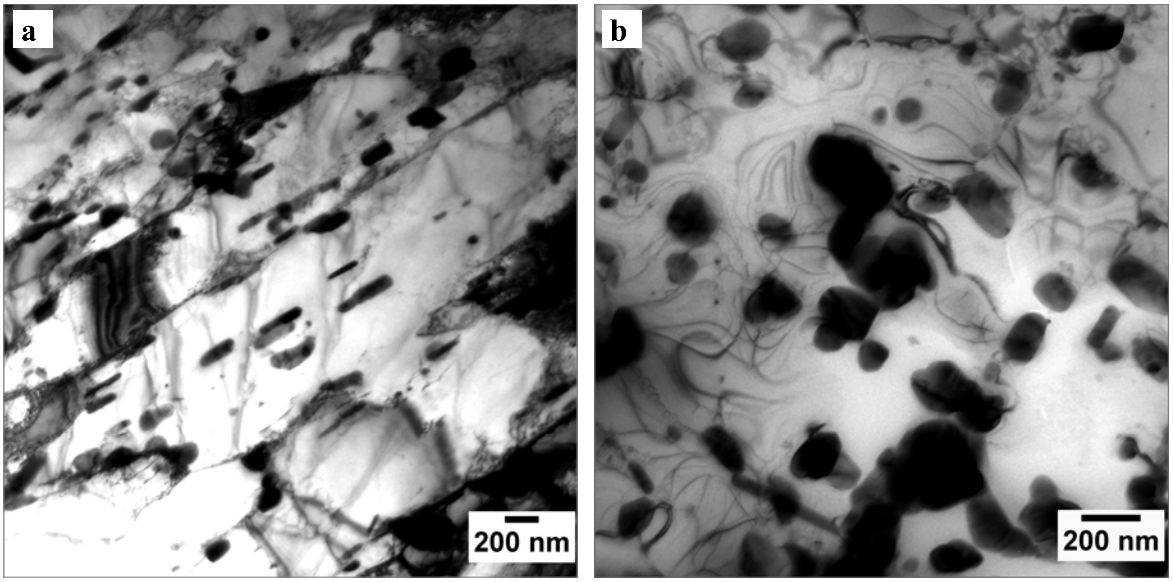

Fig.3.4: Micrographs from thin foil showing, morphology and distribution of carbides in normalized and tempered 1W steel, (a) Lenticular inter & intra lath precipitates and (b) Coarse globular precipitates in a well recovered region.

Figures 3.5 and **3.6** show the microstructural details from carbon extraction replica of the 1W and INRAFM steels respectively. The distribution of precipitates is seen in **Fig. 3.5(a)** and **Fig.3.6 (a)**. Micro-diffraction patterns from two typical precipitates are shown in **Fig.3.5 (b)** and **(c)** and **Fig.3.6 (b)** and **(c)** (diffracting planes are marked). Analyses of these patterns from different zone axis and comparison with standard values of d-spacings ($M_{23}C_6$: ICDD File No: 00-035-07-83, VC: ICDD File No: 01-073-0476 and TaC: ICDD File No: 01-035-0801), the phases were identified as $M_{23}C_6$ and MX type of precipitates (M stands for metal atoms and X stands for C or N).

Although M_2X is reported in this class of steels, it forms in the early stages or low temperature of tempering, and is replaced by $M_{23}C_6$ carbides [124-125] as tempering proceeds. **Fig.3.5 (d)** & **Fig.3.6 (d)** shows the EDX spectrum of $M_{23}C_6$ carbide which is found to be rich in Cr, while **Fig. 3.5(e)** & **Fig.3.6 (e)** shows the V and Ta rich nature of MX. Analysis of a number of carbides showed that the $M_{23}C_6$ contains Cr ~55-60 wt%, W ~ 10-12 wt% and Fe~ 30-35 wt%. However, the W content in the $M_{23}C_6$ carbide from INRAFM steel varied in the range of 10-15%. In fact, composition served as a unique signature to distinguish $M_{23}C_6$ and MX types of precipitates. Analysis of carbon extraction replica showed a higher volume fraction of carbides in INRAFM (0.035 V_f) as compared to 1W steel (0.018 V_f), which is attributed to the higher carbon content in the steel (**Table 2.1**). A typical distribution of the precipitate sizes in 1W and INRAFM steel is given in **Fig.3.7.** Size distribution of $M_{23}C_6$ carbides showed a Gaussian distribution with the average size ranging from 50-130 nm in both the steels.

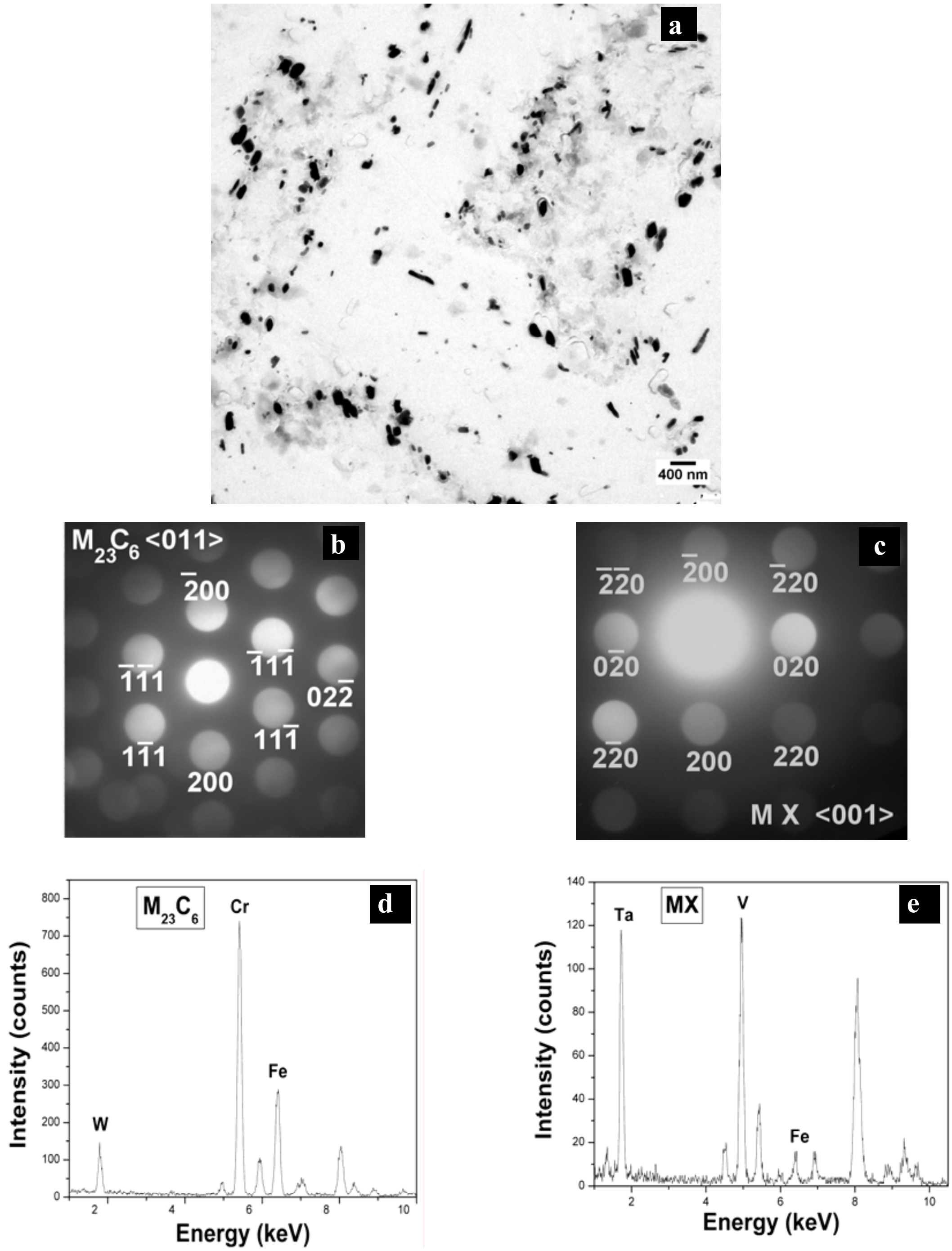

Fig.3.5: TEM micrograph of carbon extraction replica of normalized and tempered 1W RAFM steel showing (a) inter and intra lath boundary carbides in steel (b) and (c) diffraction patterns from $M_{23}C_6$ and MX along <011> and <001> zone axes respectively (d) and (e) EDX spectrum from $M_{23}C_6$ and MX phases showing Cr and V / Ta rich nature respectively.

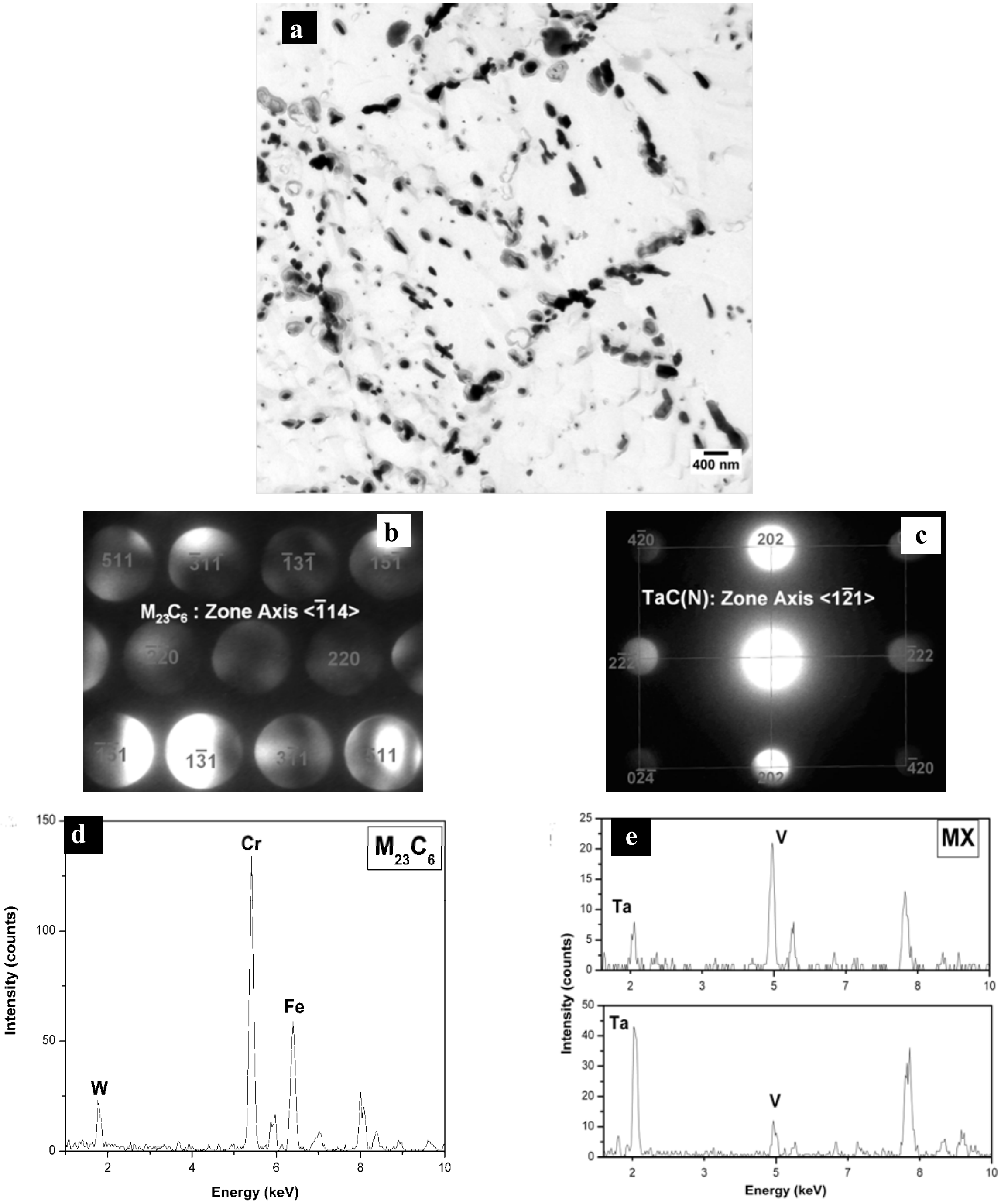

Fig.3.6: TEM micrograph of carbon extraction replica of normalized and tempered INRAFM steel showing (a) inter and intra lath boundary carbides (b) and & (c) diffraction patterns from $M_{23}C_6$ and MX along $<\bar{1}14>$ and $<1\bar{2}1>$ zone axes respectively (d) and (e) EDX spectrum from Cr rich $M_{23}C_6$ and V or Ta rich MX respectively.

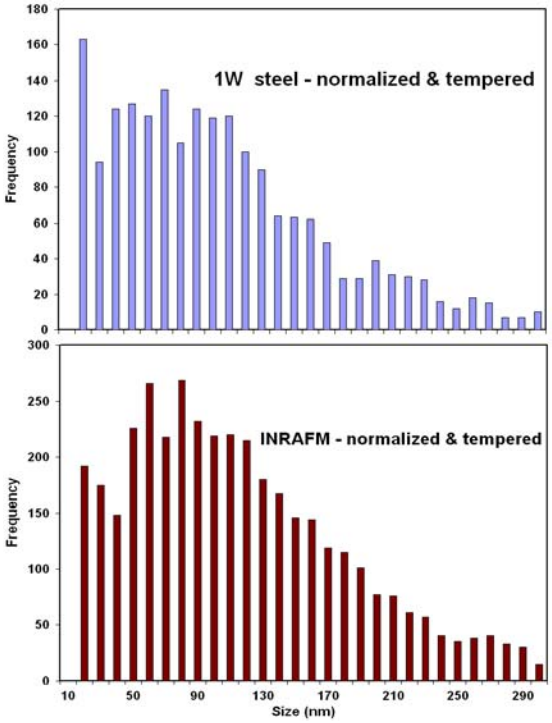

Fig.3.7: Size distribution of carbides in n&t 1W and INRAFM steels

In general, the presence of $M_{23}C_6$ was more dominant than MX. In contrast, MX carbides were few and of very fine size in the range of 10-15 nm.

3.2. Microstructure of normalized and tempered steel – Computation

To understand the precipitation characteristics like volume fraction, size and microchemistry of secondary phases on thermal exposure, simulations were carried out. The change in phase fraction as a function of temperature until melting point was computed using ‘JMatPro’ for the two steels and the results of INRAFM steel is depicted in **Fig. 3.8(a)**. It is seen that M_2X and Laves phases were stable only up to 763 and 923 K respectively for the given steel composition. The equilibrium phases predicted in the temperature range of interest (1000-1253 K) showed the formation of $M_{23}C_6$, MX, ferrite and austenite. Dissolution temperature of $M_{23}C_6$ was found to be higher in INRAFM than in 1W steel.

Change in phase fraction with time at a temperature of 1033 K for INRAFM steel is given in **Fig. 3.8(b)**. It is seen from the plot that tempering for 1h results in the precipitation of predominantly $M_{23}C_6$ with few MX carbides, which is in agreement with the experimental observation (**Fig. 3.6(b)** and **(c)**). The computed concentration of major alloying elements, Fe, Cr and W in $M_{23}C_6$ carbide is shown in **Fig.3.8(c)** (for both 1W and INRAFM) also is in agreement with the values obtained by EDS analysis (**Fig. 3.5(d)** & **Fig. 3.6(d)**). A similar comparison could not be made for the MX precipitates since both Ta and V rich MX carbides with wide range of mutual solubility were identified. Similarly computations showed that the expected size of $M_{23}C_6$ and MX carbides were 218 and 16 nm respectively after tempering for 1 h at 1033 K, whereas experimental measurements showed a wide range of size distribution (**Fig. 3.7**) with a Gaussian behavior peaking at 50-100 and 50-125 nm for 1W and INRAFM steel respectively, with a minor peak at around 200-250nm for few coarse $M_{23}C_6$ carbides. The size of MX varied between 10 and 15 nm.

The partitioning of W and Ta among various phases in INRAFM steel is shown in **Fig. 3.9(a) & (b)** respectively. Presence of W in both ferrite and $M_{23}C_6$ phases suggests that unlike Cr, W not only acted as ferrite stabilizer but also provided enhanced solid solution strengthening and precipitation hardening. Tungsten also has a tendency to promote Laves phase formation as reported in literature [128]. Laves phase is not expected at the tempering temperature (1033 K), which is in agreement with the experimental results. In contrast, Ta has a higher affinity for carbon and gets precipitated as carbides (**Fig. 3.9(b)**) with a maximum of only 2-3 wt% solubility in the ferrite matrix.

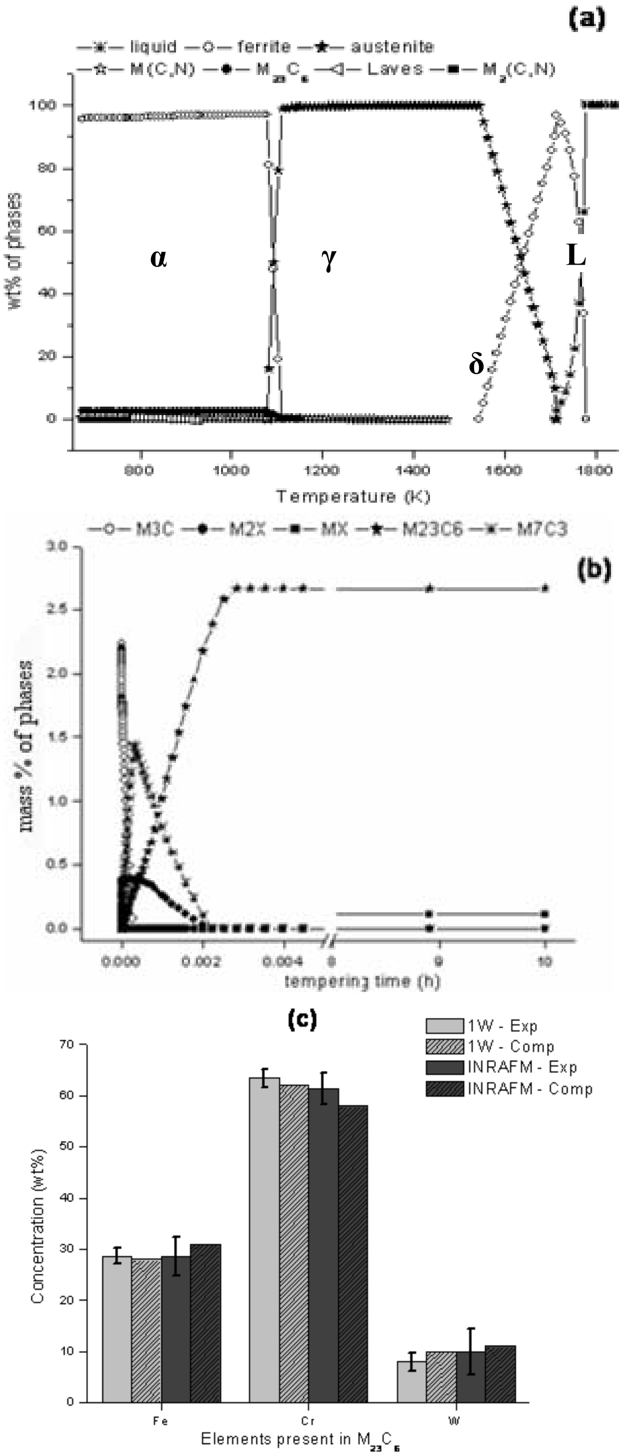

Fig.3.8: Computation of equilibrium phases using 'JMatPro' (a) distribution of various phases as a function of temperature (b) change in phase (weight) percentage as a function of tempering time at 1033 K for INRAFM steel and (c) comparison of experimental and computed concentration of $M_{23}C_6$ carbides in both 1W and INRAFM steels

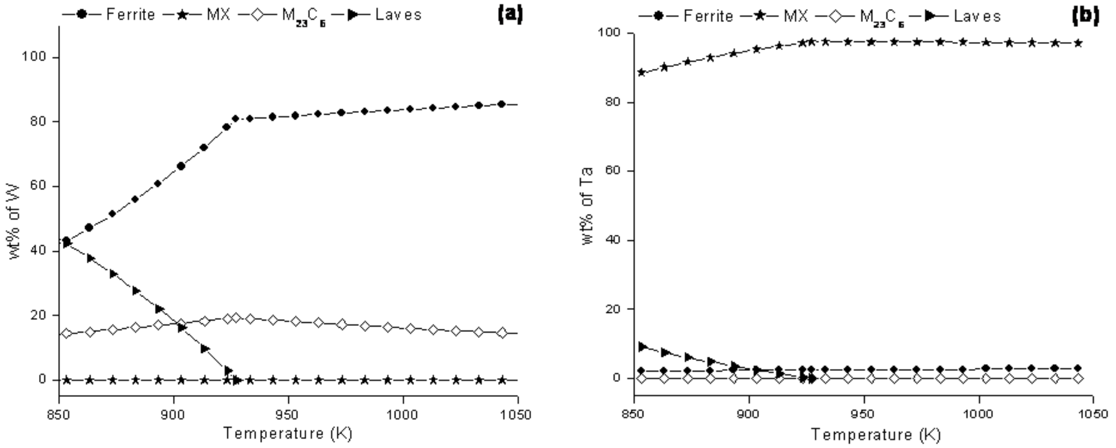

Fig.3.9: Relative distribution of (a) W and (b) Ta in different phases in INRAFM steel as a function of temperature, by computation

Below 923 K, percentage of Ta present in Laves phase increased with decrease in temperature, while in MX, Ta concentration increases with temperature. V was found to be predominantly associated with the MX phase with limited solubility in the $M_{23}C_6$ carbide.

3.3 Thermal exposure induced microstructural evolution in RAFM steel

A detailed microstructural and microchemical characterization of the phases that form on long term exposure of RAFM steels (5000 and 10000 h) in the range of 773-873 K has been carried out. The sequence of precipitation secondary phases, their mole fraction and coarsening rate have also been computed using JMatPro in both the steels. The average hardness values of the two steels after aging for different durations of time and temperature are tabulated in **Table 3.1**. Hardness values did not show any prominent changes contrary to the expected softening due to recovery. It is possible that the reduction in hardness due to recovery is compensated by an increase due to precipitation, which will be established in this section.

Table 3.1: Hardness (VHN) of RAFM steels after aging at 773-823 K

Steel	n & t	773K/5000 h	773K/10000 h	823K/5000 h	823K/10000 h
1W steel	221 ± 5	220 ± 5	226 ± 5	223 ± 5	225 ± 5
INRAFM	230 ± 5	225 ± 5	225 ± 5	226 ± 5	224 ± 5

Analysis of volume fraction and microchemistry of the $M_{23}C_6$ precipitates is presented in **Fig.3.10**. A systematic increase in the volume fraction of carbides (**Fig.3.10a**) is observed as a function of time and temperature in both the steels. A relatively higher amount of precipitates in INRAFM in comparison to 1W steel is clearly due to higher C content of the steel. A progressive increase in the Cr and W content in $M_{23}C_6$ is observed, with time in both the steels from **Fig. 3.10(b).** It is also noted that with aging time there is significant increase in Cr in 1W steel, as against increase in W in INRAFM steel. There is also a large variation in the Cr and W content, which is attributed to the simultaneous coarsening and fresh nucleation of carbides during thermal exposure.

Figure 3.11 (a) shows the micrograph of extraction replica of 1W steel aged at 773 K for 5000 h, revealing a uniform distribution of carbides. An increase in carbide size is observed in 1W steel (50-150 nm), which attained a maximum 200-250 nm (**Fig.3.11 (b)**), but was found to be negligible in INRAFM steel. **Figure 3.12** gives typical micrographs of INRAFM subjected to the same aging treatment. The volume fraction analysis in **Fig. 3.10(a)** and low magnification micrographs in **Fig. 3.11(a)** & **Fig. 3.12(b)** clearly show that the volume fraction of carbides is high in INRAFM steel after aging at 773 K, though there no measurable difference in the maximum size of the carbide between the two steel.

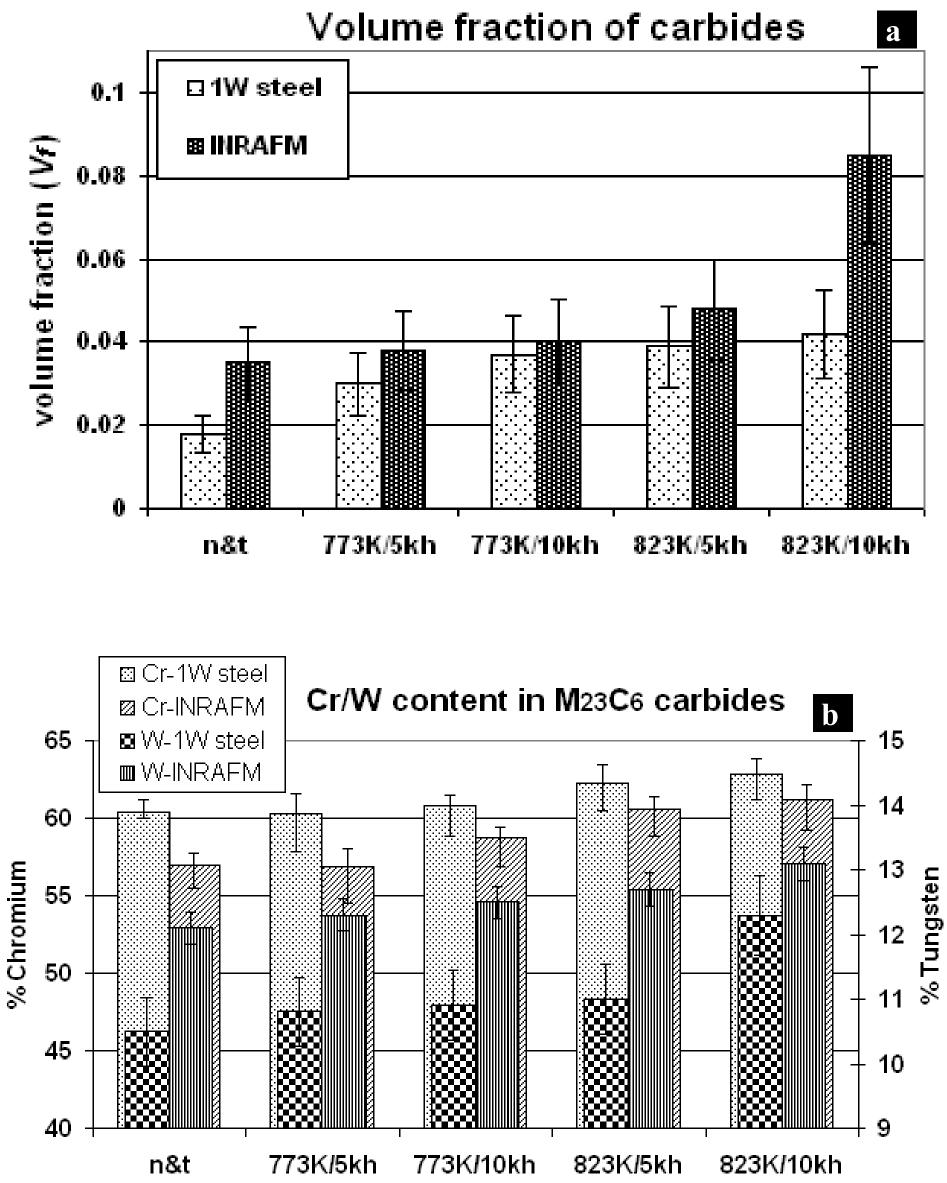

Fig.3.10: (a) Volume fraction of carbide and (b) change in Cr and W content in $M_{23}C_6$ carbide on aging

Increasing the duration of aging to 10000 h at 773 K (**Fig.3.13 (a)**), retained the lath morphology which is comparable to that of normalized and tempered steel (**Fig.3.2 (d)**). However, few regions of low dislocation density and coarser precipitates is observed as compared to n&t steel **(Fig.3.7**) typical of well recovered regions (**Fig. 3.13(a)** and **(b)**).

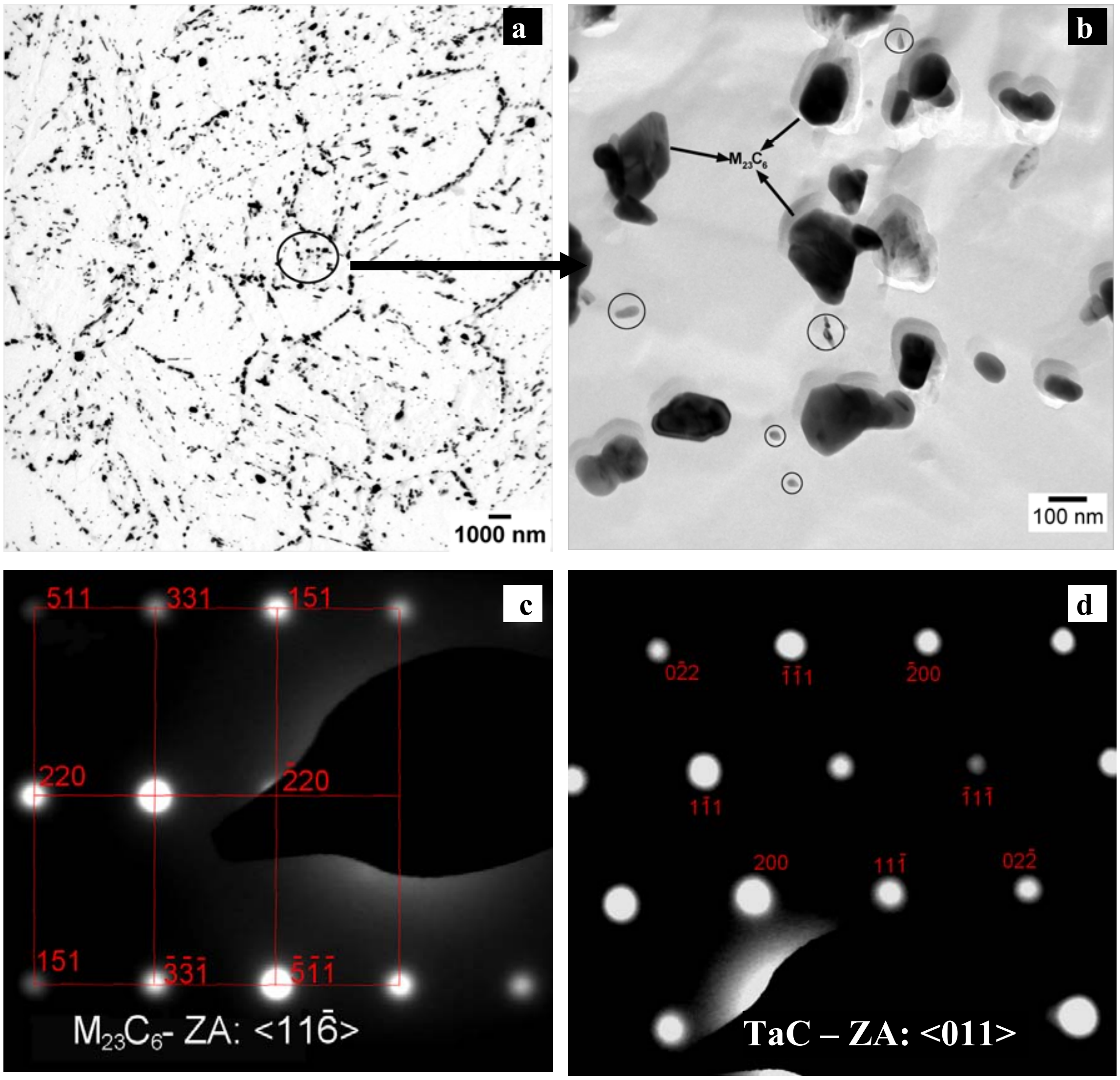

Fig.3.11 (a) TEM micrograph from extraction replica of 1W steel aged at 773 K/5000 h, showing the distribution of carbides (b) High magnification micrograph showing coarse $M_{23}C_6$ and fine MX (circled) carbides (c & d) Diffraction patterns from $M_{23}C_6$ and TaC along <11$\bar{6}$> and <011> zone axes respectively.

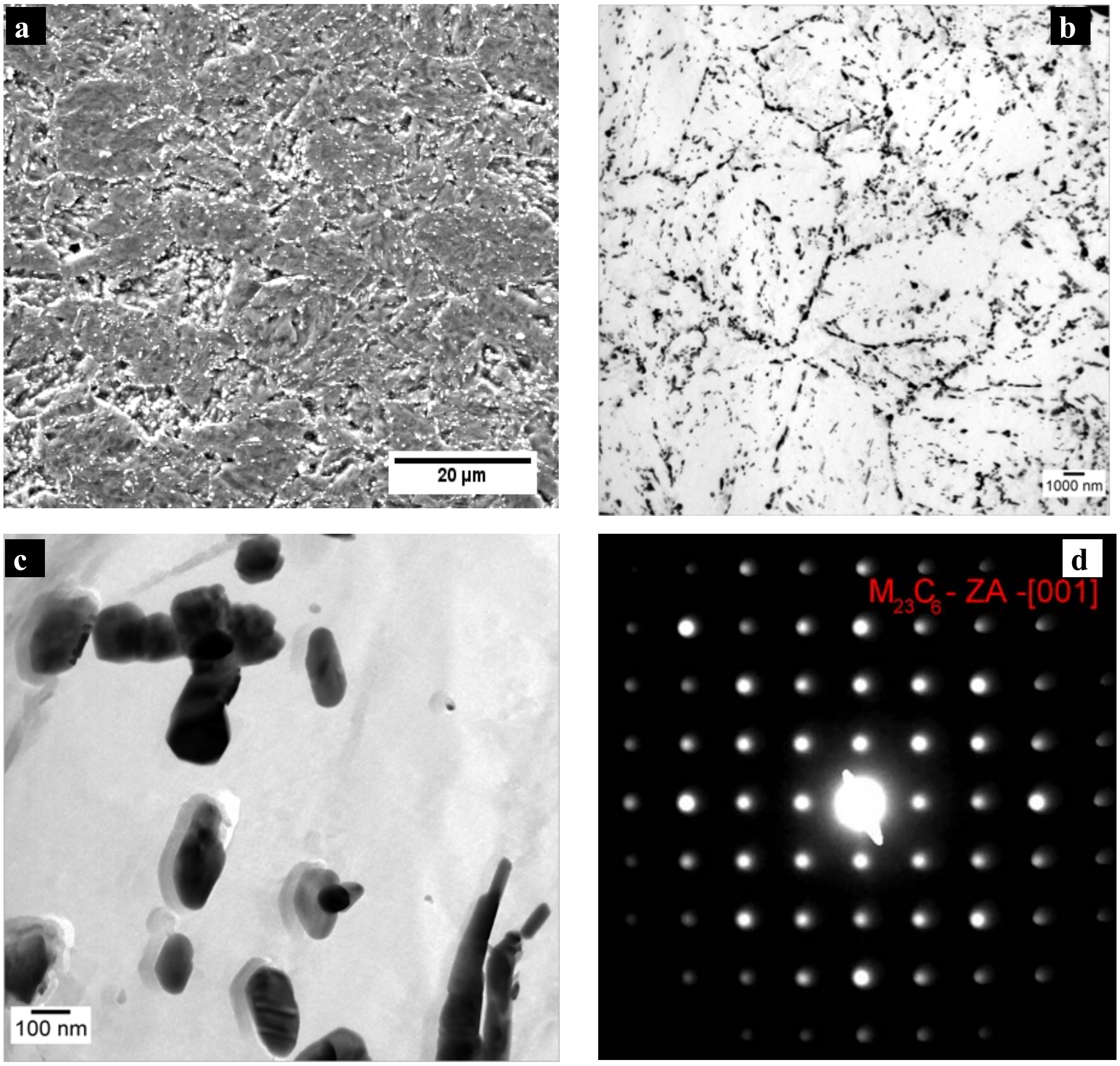

Fig.3.12: Microstructure of INRAFM steel after aging at 773 K for 5000 h (a) SEM micrograph showing tempered martensite (b) Extraction replica micrograph showing distribution of carbides (c) Inter and intra lath precipitates at higher magnification and (d) diffraction pattern from $M_{23}C_6$ carbide along <001> zone axis.

Comparison of the average size of carbide evaluated by image analysis procedures showed only a negligible change as a function of time in both the steels, but size of the carbides in the well recovered regions was estimated to be as high as ~350 nm. Coarsening of $M_{23}C_6$ was more prominent in the 1W steel than in INRAFM steel with higher W content, although the volume percentage of carbides was lower, as compared to INRAFM steel. This is in line with the role of W, which resists the coarsening of $M_{23}C_6$ precipitates, which is also well reported [129-130].

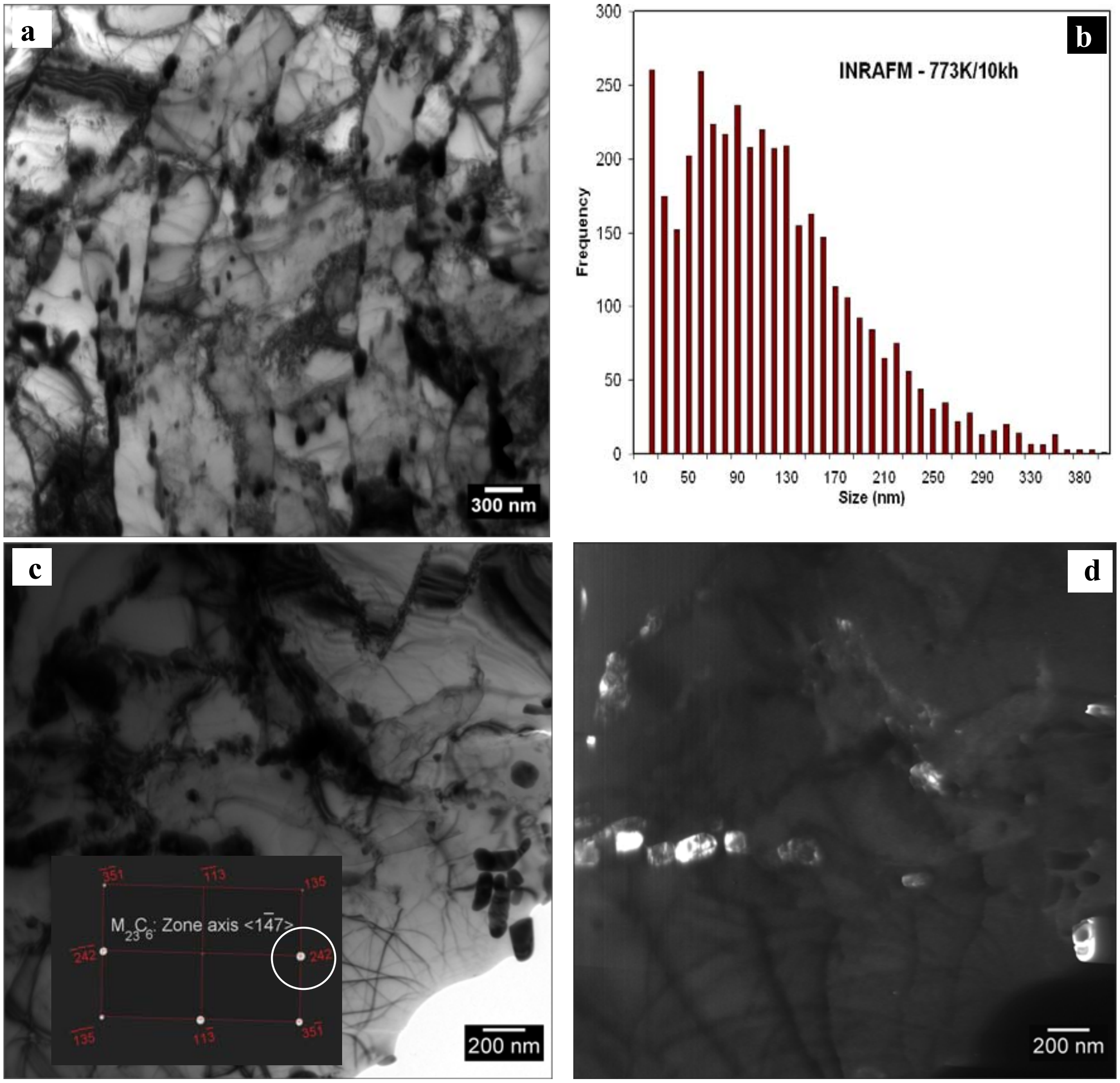

Fig. 3.13: TEM micrographs of INRAFM steel aged at 773 K for 10000 h showing (a) retention of lath structure (b) distribution of carbide size (c) recovered regions of low dislocation density and carbides (inset shows diffraction pattern from $M_{23}C_6$ carbide along <1$\bar{4}$7> zone axis) (d) dark field image for (2 4 2) reflection highlighting coarse carbides along PAG boundary.

As the aging temperature was increased to 823 K, the rate of recovery as well as coarsening was found to increase. **Figure 3.14** shows the microstructural details of INRAFM steel aged for 5000 h hours at 823 K. The size distribution of carbides followed a Gaussian behavior with an average size range of 50-150 nm (**Figure 3.15**) in both steels. TEM at high magnification confirmed that the maximum size was of the order of 350 nm. Analysis of a diffraction pattern (inset of **Fig. 3.14(a)**) showed the presence of an additional phase identified as AB_2 type of Laves phase. The TEM dark field micrograph (**Fig. 3.14(b)**) taken using one of the (001) reflections (marked in **Fig. 3.14(a)**) shows that these are very fine (~20nm) in size.

A typical EDS spectrum (**Fig.3.14(c)**) from the fine phase clearly shows that it is rich in W and Fe with some solubility for Cr, confirming that it is $(Fe,Cr)_2W$ type of Laves phase. The average composition was found to be 59% W, 32% Fe and 9% Cr. **Figure 3.14(d)**, shows that the Laves phase nucleated along the lath boundaries as a thin layer surrounding the coarse boundary carbides. Sawada *et.al* reported that the lath boundaries are the preferential site of nucleation of Laves phase in W containing steel because of which the number density of precipitates in lath boundary increases [131]. The nucleation of fine Laves phases after aging for 5000 h at 823 K also manifested as a slight increase in the average microhardness value to 245 VHN.

This high density of precipitates is considered to be responsible for the delayed recovery of lath structure in W containing steels. It is understood that the increase in Cr/Fe and Cr/W ratio with aging as the carbide tends towards attaining equilibrium composition of $Cr_{23}C_6$ depletes the surrounding matrix of Cr and C resulting in a localized increase in W, which favors the nucleation of Laves phase,

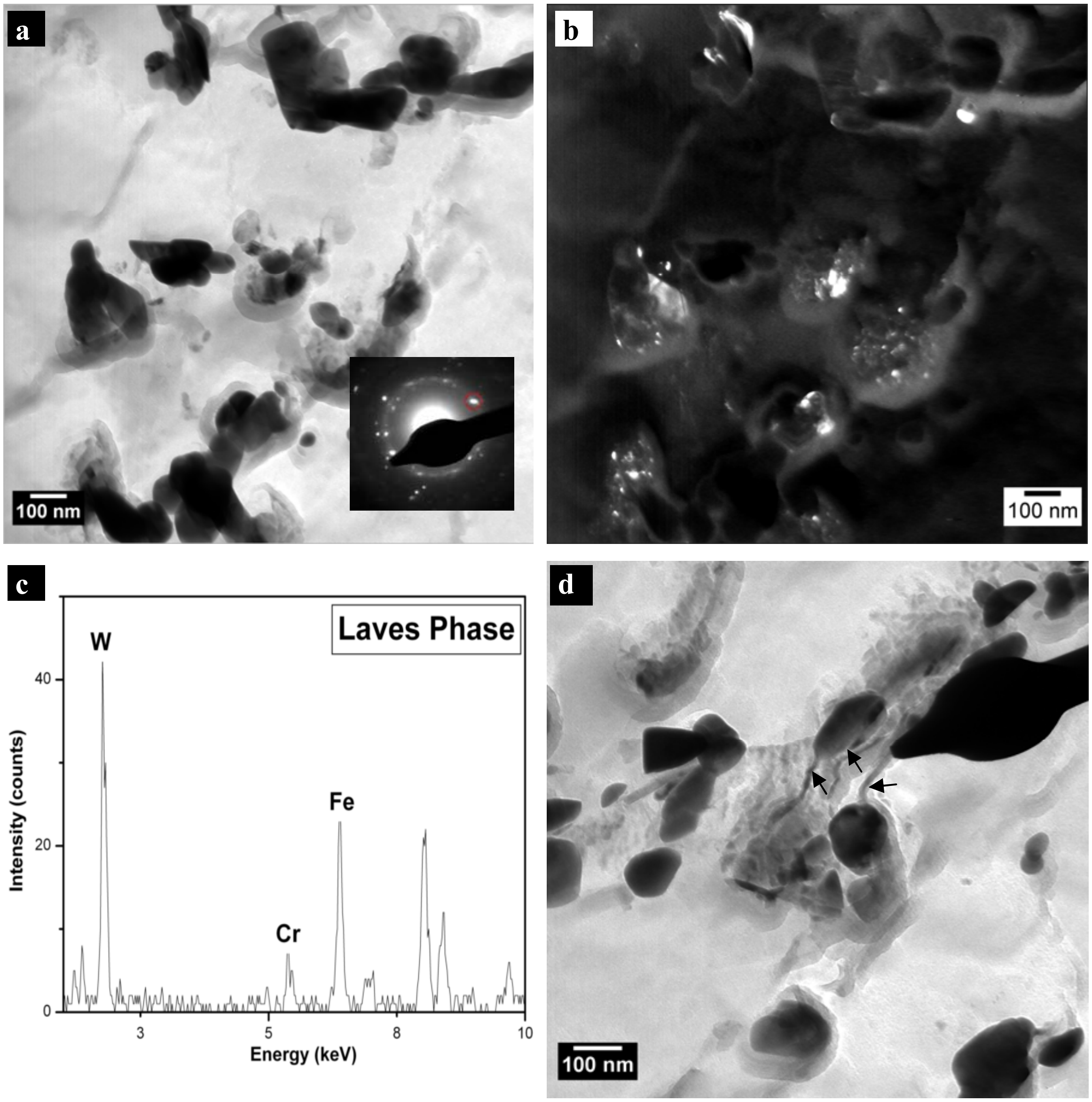

Fig. 3.14: TEM images from INRAFM steel after aging at 823 K for 5000 h (a) bright field images of extraction replica showing carbides along with fine Laves phase; inset shows a spotty ring SAD pattern confirming the presence of nano sized Laves phase (b) dark field image corresponding to one of the (001) reflections of the SAD pattern in (a) (c) EDX spectrum revealing the enrichment of W and Fe in Laves phase (d) formation of Laves phase (arrow marked) surrounding the carbides along lath boundary.

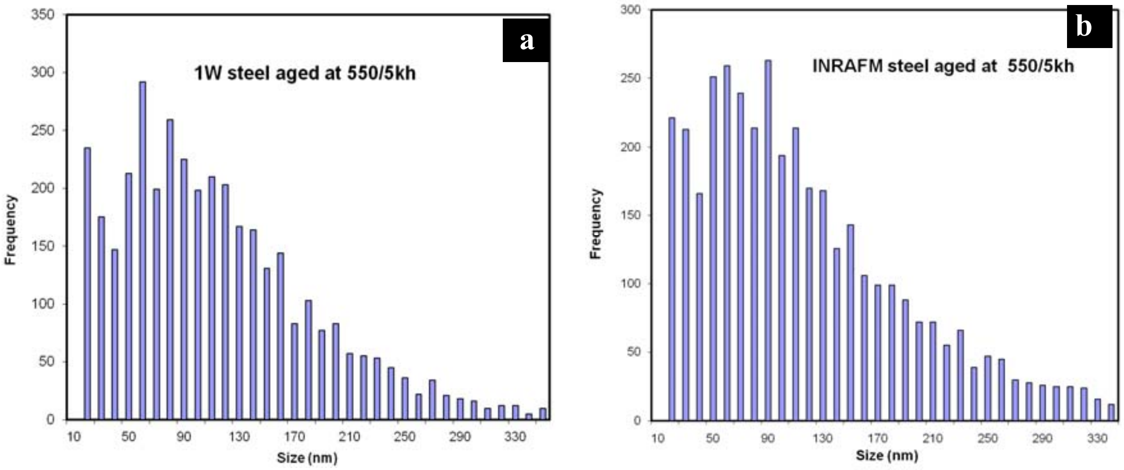

Fig. 3.15: Size distribution of carbides in (a) 1W and (b) INRAFM steel after aging for 5000 h at 823 K.

provided there is enough thermodynamic driving force for its formation. No evidence for Laves phase was found in the 1W steel although $M_{23}C_6$ carbides showed a high enrichment of Cr as compared to INRAFM steel.

When the aging time was increased to 10000 h at 823 K, the microstructure of INRAFM steel (**Fig.3.16**) showed considerable changes. Although few regions maintained the lath morphology (**Fig. 3.16(a)**) with broader laths ((~650 nm) and partially recovered grain structure, several other regions (**Fig. 3.16(b)**) showed a high degree of recovery, partial recrystallisation and abundant precipitation. The distribution of $M_{23}C_6$ carbides along lath boundaries is maintained during coarsening of laths as shown in **Fig.3.13 (a)** and **Fig.3.16 (a)**. This suggests that dissolution and re-precipitation of carbides at lath boundaries take place in a cyclic manner during advancement of lath boundaries by boundary migration. **Figure 3.16(c)** and **3.16(d)** show the presence of carbides and Laves phase at a sub-grain boundary which is almost free of dislocations. The streaking diffraction pattern from Laves phase shows the presence of inherent stacking faults associated with it. From the comparison of **Fig. 3.14** and **3.16(c)**, it is understood that the

Laves phase nucleates in the vicinity of lath boundary carbides after aging for 5000 h at 823 K and grows in size to 30-40 nm on prolonged aging for 10000 h.

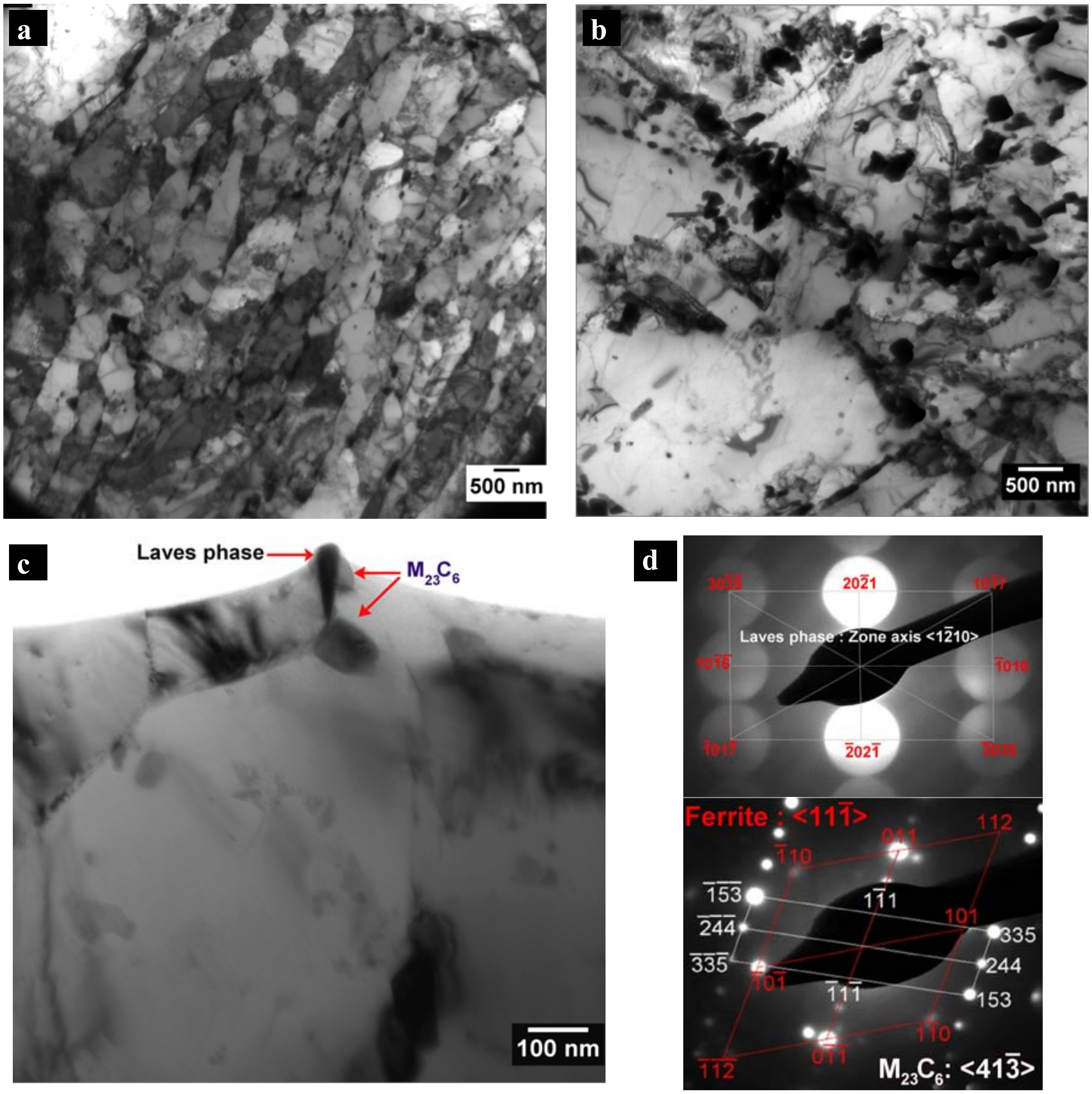

Fig. 3.16: Microstructure of INRAFM steel (thin foil) after aging at 823 K for 10000 h showing a) retention of lath structure b) well recovered regions with coarse precipitates c) presence of $M_{23}C_6$ carbide and Laves phase on a grain boundary d) diffraction patterns obtained from Laves phase, $M_{23}C_6$ carbide marked in (c) and ferrite (matrix) along $<1\bar{2}10>$, $<41\bar{3}>$ and $<11\bar{1}>$ zone axes respectively.

Murata *et.al* and John Hald *et.al* have determined the interfacial energy of Laves phase in similar systems and report that fine Laves phase has low interfacial energy (0.1 J/m^2) which increases to 0.8 J/m^2 as it grows, which indicates that high interfacial energy of the order of 0.8 J/m^2 or above is characteristic of incoherent interface between Laves phase and ferrite [132-133]. Also, they report a morphological change of the Laves phase from fine coherent to granular precipitates with increase in aging time for a typical W content of 0.5 mol % equivalent to 1.4 wt%. Comparison of the observed morphological change in **Fig.3.16(c)** in the present study with the above literature reports, suggests the incoherent nature of the Laves phase. The bright and dark field images (**Fig.3.17 (a)** & **(b)**) of Laves phase and the diffraction pattern from a typical precipitate reveal that the Laves phase encapsulates the existing carbides. Size distribution of carbides in 1W and INRAFM steel aged for 10000 h at 823 K is shown in **Fig.3.17(c)** and **3.17(d)** respectively. Although the average size is around 50-150 nm, a large number of coarse precipitates with Cr (~65 wt. %) characteristic of $M_{23}C_6$ carbides was observed in INRAFM steel. The average size of the V or Ta rich MX phase remained stable at 30-40 nm even after aging for 10000 h, which therefore continue to provide creep strength to the steel.

No evidence for Laves phase was found in 1W steel at 823 K, and $M_{23}C_6$ carbides showed similar enrichment of Cr. An overestimation of size and volume fraction of carbides in INRAFM steel at 823 K cannot be ruled out as the carbides are encapsulated by Laves phase. The observed precipitation behavior in the indigenous steels is in agreement with the reports of Abe *et.al* on the Japanese Low-Activation Ferritic

Martensitic steel [27-28, 32, 134]. The X-ray maps in **Fig.3.18** clearly distinguish the W and Fe rich Laves phase from the Cr rich carbides.

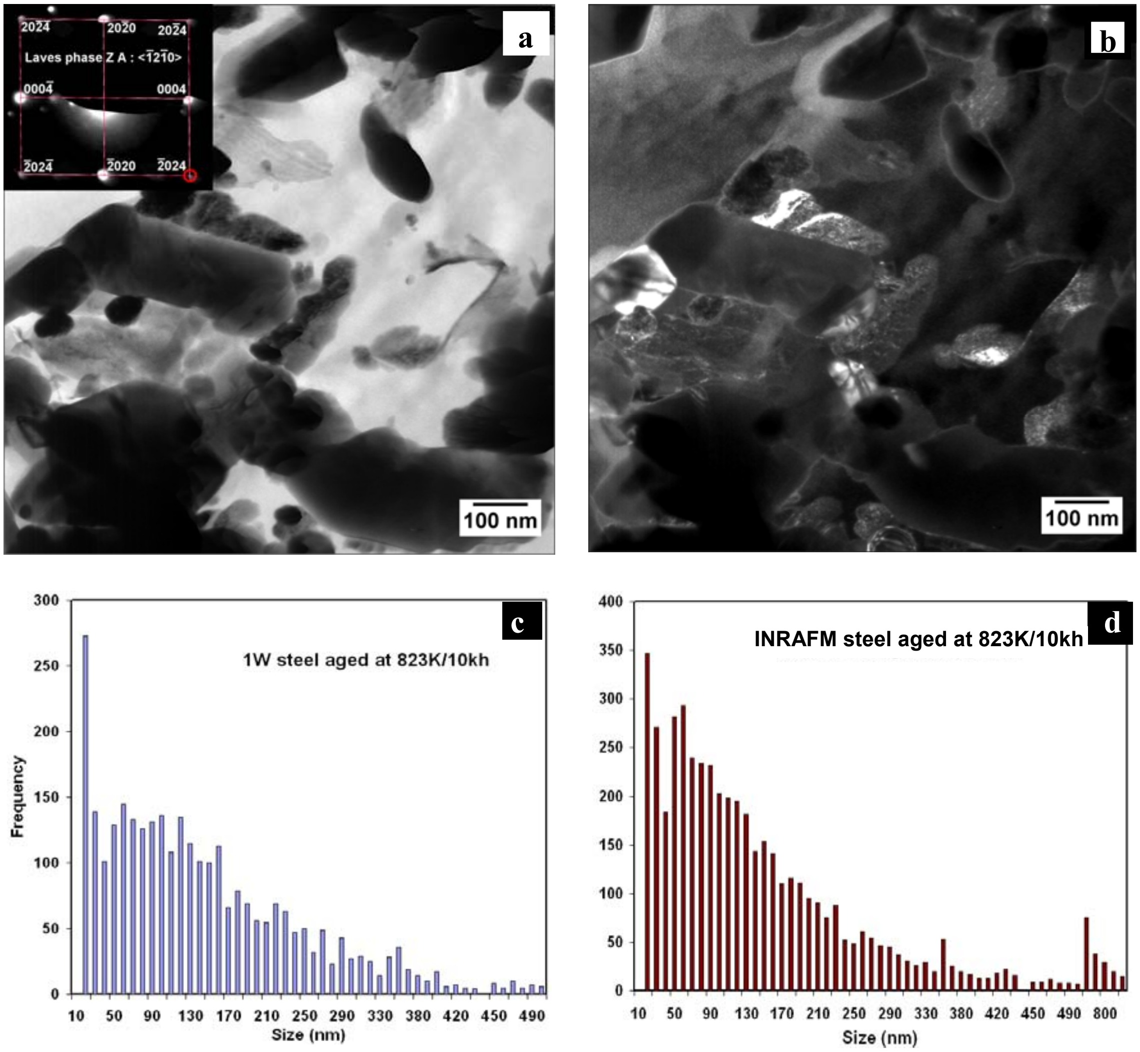

Fig. 3.17: a) Bright field image of carbides and Laves phase in INRAFM steel with inset showing diffraction pattern from Laves phase along $<\bar{1}2\bar{1}0>$ zone axis) aged at 823 K for 10000 h b) Dark field image highlighting the distribution of Laves phase using ($\bar{2}024$) reflection marked in the diffraction pattern in (a) c and d) Size distribution of carbides in 1W and INRAFM steel aged at 823 K for 10000 h respectively.

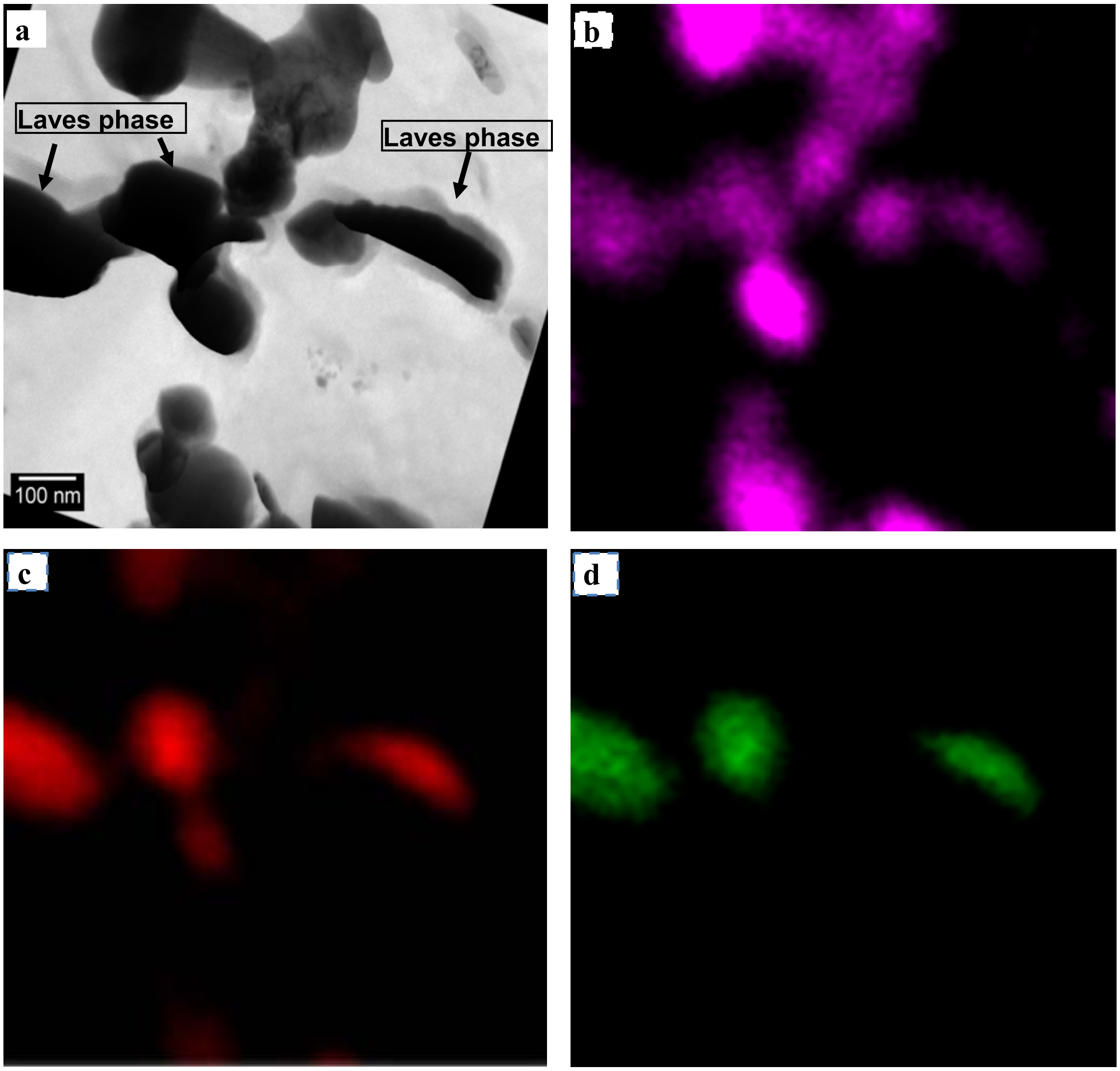

Fig. 3.18: X-ray mapping of constituent elements in the precipitates a) Bright field image of carbides and Laves phase b, c & d) Mapping of Cr Lα , Fe Lα and W Lα respectively.

3.4. Simulation of equilibrium phases in thermally exposed RAFM steels

The sequence of evolution of secondary phases in 1W and INRAFM steel as a consequence of thermal aging at 773, 823 and 873 K for durations in the range of 1-10000 h has been computed using JMatPro simulation software. The type and weight fraction of the different phases that form as a function of aging time at different temperatures have been determined. The predicted equilibrium phases at different temperatures are listed in **Table 3.2**. The calculated weight fraction of carbides is given in **Table 3.3**.

Table 3.2: Simulated sequence of precipitation of secondary phases in 1W and INRAFM steels at different temperatures

Time (h)	**1W**			**INRAFM**		
	773 K	**823 K**	**873 K**	**773 K**	**823 K**	**873 K**
1	M_7C_3, $M_{23}C_6$, M_3C, M_2X	$M_{23}C_6$, M_2X, M_7C_3	$M_{23}C_6$, M_2X	M_7C_3, $M_{23}C_6$, M_3C, M_2X	$M_{23}C_6$, M_2X, M_7C_3	$M_{23}C_6$, M_2X
2	M_7C_3, $M_{23}C_6$, M_2X	$M_{23}C_6$, M_2X	$M_{23}C_6$, M_2X	M_7C_3, $M_{23}C_6$, M_2X	$M_{23}C_6$, M_2X	$M_{23}C_6$, M_2X, MX
10	$M_{23}C_{6,}$ M_2X	$M_{23}C_6$, M_2X	$M_{23}C_6$, MX, M_2X	$M_{23}C_{6,}$ M_2X	$M_{23}C_6$, M_2X, MX	$M_{23}C_6$, MX
100	$M_{23}C_{6,}$ M_2X	$M_{23}C_6$, MX	$M_{23}C_6$, MX	$M_{23}C_{6,}$ M_2X	$M_{23}C_6$, MX	$M_{23}C_6$, MX, Laves
1000	$M_{23}C_6$, MX	$M_{23}C_6$, MX, Laves	$M_{23}C_6$, MX, Laves	$M_{23}C_6$, MX	$M_{23}C_6$, MX, Laves	$M_{23}C_6$, MX, Laves
5000	$M_{23}C_6$, MX	$M_{23}C_6$, MX, Laves	$M_{23}C_6$, MX, Laves	$M_{23}C_6$, MX	$M_{23}C_6$, MX, Laves	$M_{23}C_6$, Laves, MX
10000	$M_{23}C_6$, MX	$M_{23}C_6$, MX, Laves	$M_{23}C_6$, Laves, MX	$M_{23}C_6$, MX	$M_{23}C_6$, MX, Laves	$M_{23}C_6$, Laves, MX

Though the experimentally determined values (Fig 3.10(a)) are relatively higher due to reasons explained in Chapter 2, the trends are consistent. As seen from the computation results the weight percent of carbides in 1W steel increased up to 5000 h of aging at all temperatures, which is in agreement with the experimental results. The difference in amount and size between computed and experimental results in INRAFM steel on aging for 10000 h at 823 K is mainly due to the additional precipitation of Laves phase surrounding the carbides.

Table 3.3: Weight percentage of carbides in aged 1W and INRAFM steel

Temperature (K)	**Time (h)**	**$M_{23}C_6$**		**MX**	
		1W steel	**INRAFM**	**1W steel**	**INRAFM**
773	1	0.245	0.378	-	-
	5000	1.676	2.706	0.068	0.080
	10000	1.676	2.706	0.068	0.080
823	1	1.525	2.355	-	-
	5000	1.708	2.703	0.078	0.086
	10000	1.708	2.703	0.078	0.086

Following are the significant differences in the predicted behavior of microstructural evolution between the INRAFM and 1W steels at high temperatures:

- Higher fraction of secondary phases in INRAFM steel than 1W steel at all temperatures and times.
- Early onset of precipitation of MX carbides specifically at 823 and 873 K.
- M_2X carbonitrides showed stability only up to 4 h of heat treatment at 873 K.
- Formation of Laves phase in both the steels after 1000 h of aging at 823 K, with relatively higher weight percentage (V_f^{LP}) in INRAFM steel (V_f^{INRAFM} = 0.003) than in 1W steel (V_f^{1W} = 0.001).

- Formation of Laves phase after 100 h of aging itself at 873 K, however of very low weight percentage (V_f^{LP} ~ 0.001) as compared to $M_{23}C_6$ (2.7) and MX (0.091) carbides.
- Laves phase was the second most predominant phase ($V_f^{LP} = 0.228$) next to $M_{23}C_6$ ($V_f^{M_{23}C_6} = 2.7$) after aging for 5000 h at 873 K.

Higher fraction of carbides and Laves phase in INRAFM steel than in 1W steel has been already explained in terms of the higher amounts of carbon and W. The computed change in the size of $M_{23}C_6$ and MX carbides is plotted as a function of aging time for various temperatures in **Fig. 3.19 (a and b)** for the two steels. The increase in mean size of $M_{23}C_6$ carbides during aging follows the Ostwald ripening mechanism, since the super-saturation of carbon in the martensite is relieved by precipitation primarily during tempering or early stages of aging. This is consistent with the observed increase in size of the carbide with no increase in weight percentage as seen from **Table 3.3**. In INRAFM

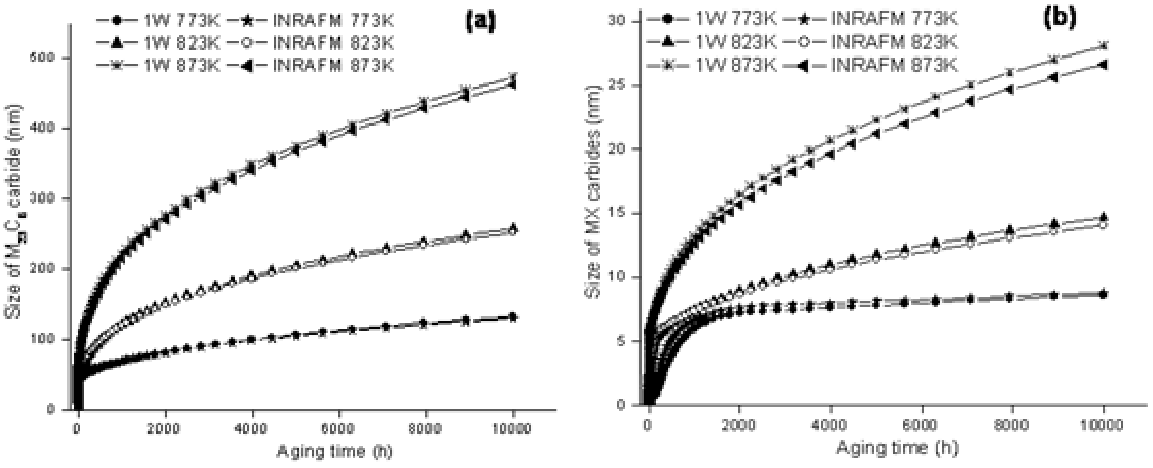

Fig.3.19: Precipitate size as a function of aging time and duration. a) $M_{23}C_6$ and b) MX carbides in INRAFM steels calculated using 'JMatPro'

steel, the $M_{23}C_6$ carbides with high W concentration show a slower kinetics of coarsening on aging and the apparent increase in size is due to the encapsulation of Laves phase on carbide. It is well known that the carbides on lath boundaries resist the coarsening of laths, whose effect reduces as the carbides coarsen.

As expected, coarsening rate of MX carbides in both the steels was found to be much lower than that of $M_{23}C_6$. In addition, the average size of the MX precipitates in INRAFM steel was lower than that in 1W steel. The computation was carried out by adopting a uniform composition of the steel, which is true for a martensite structure as in normalized condition. The effect of tempering is not incorporated in the computation due to the limitation of the software. Computation gives the maximum attainable size of the carbide at a particular temperature where as the actual experimental values reflect a wide distribution.

Even though JMatPro computations indicated the formation of low amounts of Laves phase in 1W steel no experimental evidence was obtained for its presence due to the following reasons: only the equilibrium phases that form for a given alloy composition are predicted by the JMatPro software which does not incorporate the kinetic contribution to phase formation such as: (a) enhanced diffusivity of alloying elements in grain/lath boundaries (b) interaction of a diffusing species with other alloying elements (c) effect of grain/lath size variation and (d) simultaneous dissolution and precipitation of $M_{23}C_6$ carbides leading to local concentration fluctuations in its vicinity, which may promote the formation of Laves phase.

Precipitation of Laves phase has been reported earlier in the HAZ of F82H (8Cr-2WVTa) steel after thermal aging at 823 K for 3000 h [135]. Compared to 1W steel formation of

Laves phase occurred early in INRAFM steel due to higher W content and abundant precipitation of carbides that increased the availability of W and reduced the super-saturation of carbon.

The role of alloy content, temperature and time on the microstructural evolution in RAFM steel was presented in the preceding sections. In the ferritic-martensitic steels which derive their strength from the substructure and precipitation apart from solid solution strengthening, it is necessary to understand the influence of microstructure on high temperature properties, which is discussed in the subsequent sections.

3.5 Studies on creep behavior of RAFM steel by Impression Creep tests

The creep behavior of RAFM steels has been studied using impression creep (IC) test. In this section, the results of the IC tests are discussed and correlated with conventional creep data reported in literature. Creep properties of two steels with different W contents are compared with respect to steady state creep. Further, effect of microstructural degradation due to thermal aging on creep is also evaluated.

3.5.1 Effect of W on creep strength

Impression test was carried out on 1W and INRAFM steel at 823 K under a punching stress of 787 MPa. **Fig. 3.20(a)** shows the plot of displacement versus time for both the steels. Testing of the normalized and tempered steels showed a negligible primary creep region. Primary creep is predominantly transient creep, in which the resistance to deformation of the material increases due to work hardening giving rise to a decreasing creep rate. The initial microstructure is tempered martensite, which undergoes a limited amount of work hardening during creep deformation.

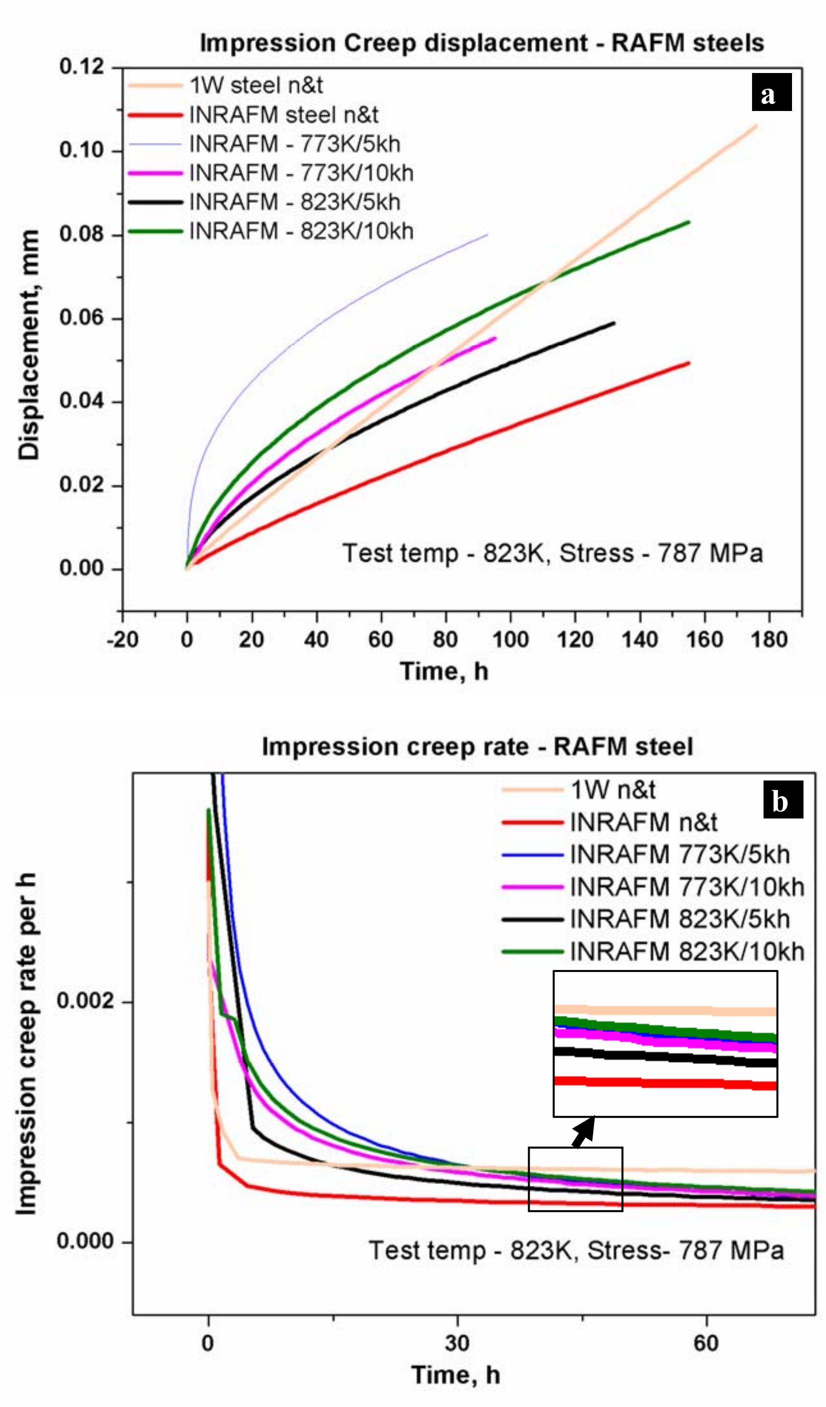

Fig.3.20: a) Impression displacement versus time curves and b) impression creep rate for 1W and INRAFM steels

In the secondary creep region, both work hardening and recovery are in balance resulting in a steady state creep. Unlike austenitic steel, ferritic steel does not show a steady state creep in the conventional creep test due to its bcc crystal structure. So a minimum creep rate is exhibited for this class of steel. **Table 3.4** gives the comparison between the steady state creep of 1W and INRAFM steels in normalized and tempered condition.

Table 3.4: Comparison of creep rate evaluated by uniaxial creep test [136] **and impression test**

Steel used (n & t)	***Uniaxial creep test*** **T = 823K & Stress = 220MPa**	***Impression creep test*** **T = 823K & Stress = 787MPa**
1W	6.018×10^{-5} h^{-1}	5.86×10^{-4} h^{-1}
INRAFM	1.8×10^{-5} h^{-1}	2.97×10^{-4} h^{-1}

The higher values of secondary creep rates obtained from impression tests than those obtained from conventional tests is understood in terms of the minimum creep rate obtained in the later stages of creep test, just before onset of tertiary creep after which recovery dominates in the conventional case. However, it is very clear that an increase in 0.4% W in INRAFM steel decreases the creep rate to nearly half the value of 1W steel. Since, dislocation climb plays a major role in creep deformation, as it aids the recovery of excess dislocations and requires diffusion of vacancies and interstitials, the rate controlling step is atomic diffusion. The role of W on diffusivity is very well known. The effect of W on substructure is already discussed in **Section 3.1**. Presence of W not only reduces the lath size but also resists the coarsening of laths. Coarsening of laths is associated with recovery of dislocations and coarsening of carbides. Studies on Fe-Cr-W alloys showed that W strikingly reduces the rate of self diffusion of Fe, while effect of Cr is not significant [32, 137]. Recovery of dislocation involves self diffusion of Fe and coarsening of carbides depends on its stability. Hence, in both ways W resists recovery process, which is reflected by the higher creep strength. It is reported that for a 9Cr-0.5Mo-W steel, both tensile and creep rupture strength increases with increasing W content [138].

3.5.2 Effect of aging on creep strength

The displacement and creep rate of heat treated INRAFM steel are shown in **Fig.3.20 (a)** & **(b)** respectively. All thermally aged steels showed a distinct primary creep stage unlike normalized and tempered steel. This phenomenon can be attributed to the softening caused by recovery. The softening is primarily a result of the coarsening or dissolution of the carbides, which in turn result in recovery of dislocation substructures. During creep test, the softer matrix undergoes work hardening to a greater extent as compared to the normalized and tempered steel which has a microstructure with optimum creep strength. The INRAFM steel which is aged at 773 K for 5000 h showed the highest depth of penetration as well as highest creep rate. **Figure 3.13** showed that aging for 5000 h at 773 K, resulted in dislocation recovery by lath broadening, coarsening and decrease in number density of carbides. The increase in creep rate or decrease in creep strength in the steel aged at 773 K can be understood on the basis of above mentioned reasons. The impression creep rate remained almost the same in the steel aged for longer times of 10000 h. This can be understood in terms of the nearly same amount of precipitation with time of aging (**Fig.3.10 (a)** (experimental) and **Table 3.2** (simulation)). On the contrary, the INRAFM steel aged at 823 K for 5000 h showed the lowest creep rate or highest creep strength among all the aged steel despite the higher substructure changes expected on exposure to higher temperature. This is clearly ascribed to the existence of the Laves phase that formed at 823 K (**Fig. 3.14**, **Fig. 3.8(a)** & **Fig. 3.9(a)**). The presence of this uniformly distributed nano sized particles of Laves phase are responsible for the increase in creep strength. This is in agreement with earlier studies carried out by other researchers in similar steels [128, 131]. However, an increase in aging time (10000 h) at 823 K increased the creep rate to nearly that at 773 K/5000 h. The precipitation of Laves phase leads to a depletion of W in the matrix and to a reduction of the solid solution hardening effect in alloys [26, 139-140]. On the other hand, Laves phase precipitation can contribute to precipitation hardening and a resultant increase in the creep strength before it coarsens. The Laves phase during aging at 823 K for 10000 h not only coarsens but also forms as a discontinuous net work along the lath and grain boundaries. This network of a brittle phase reduces the strength of the interface, which is well reflected in the results of impression creep tests. It is predicted that further exposure at this temperature may result in a continuous network of Laves phase along the boundaries. Hence the increased creep rate of the INRAFM steel at 823 K after 10000 h is attributed to the higher extent of recovery and the coarsening of Laves phase.

3.5.3 Change in substructure of region under indentation

The evolution of substructure during indentation was studied using optical, SEM and Orientation Imaging Microscopy (OIM). The samples which showed a high (aged at 773 K for 10000 h) and low (normalized and tempered) creep rate were chosen for this study. The impression creep tested specimen was sectioned along the diameter of the indentation using a diamond cutting machine and polished metallographically followed by electro polishing for OIM studies. Microhardness measurements were made on the sectioned surface beneath the impression creep indentation.

Figure 3.21 shows typical micrograph of normalized and tempered INRAFM steel after impression creep test. Three distinct regions (marked I, II and III) with curved lines in the optical micrograph (**Fig. 3.21(a)**) are observed just beneath the indentation mark. The region I which is immediately under the punch did not show any significant change in the morphology of the grain. This shows that the impression creep deformation is localized in nature. Region II (**Fig. 3.21(b)**) exhibited approximately a hemispherical shape and showed signatures of extensive shear deformation. Region III (**Fig.3.21(c)**) far away from the indenter showed little change in the shape of the grains.

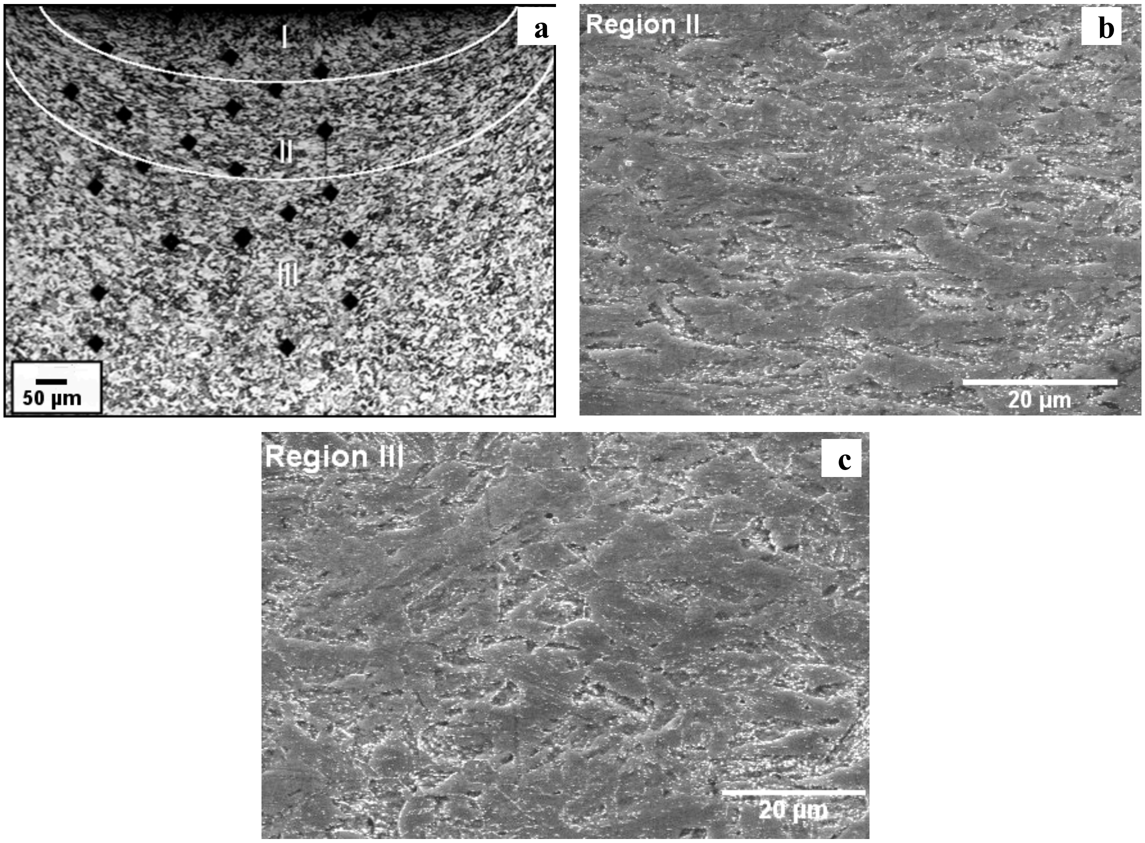

Fig. 3.21: Typical microstructure of cross section below the indentation showing three distinct regions, I & III - no significant change in grain shape and region II– experienced extensive deformation (b &c) magnified view of region II & III respecively

Further, Electron Back Scattered Diffraction (EBSD) analysis was carried out in the three regions in order to study the change in orientation of the ferrite grains due to the deformation process. For a better resolution, EBSD scan was carried out in an area of 800 µm X 400 µm with a step size of 0.6 µm. **Figure 3.22 (a) and 3.22 (b)** shows the Inverse Pole Figure map (along horizontal-Y) of the region below the indentor in n&t and 823 K/10000 h aged INRAFM steel. The orientation of grains along different crystallographic directions as per the legend indicates that there is no preferred orientation.

As observed in the optical micrograph, EBSD also showed three distinct regions. Region II which had undergone extensive deformation also showed two discrete features; namely (i) elongated grains and (ii) fine grains. In region II, it is seen that the elongated (deformed) grains were found to be predominantly oriented along <111> and <100>. It is worth mentioning that in bcc, <111> is the close packed direction. The microharness measurements across top to bottom showed a small increase of 20 VHN in region II, due to work hardening. The onset of recovery and recrystallisation is evident from the fine the grains observed in **Fig.3.22**. Region II was found to be at a depth of ~200 µm for normalised and tempered steel, while for aged steel elongated regions appeared at a depth of ~ 400 µm. Also the spread of this region II was found to be more in the case of aged steel. The above observations have been understood on the basis of the relatively soft structure of aged steel with coarse carbides. Further detailed studies are being planned to study the deformation mechanism.

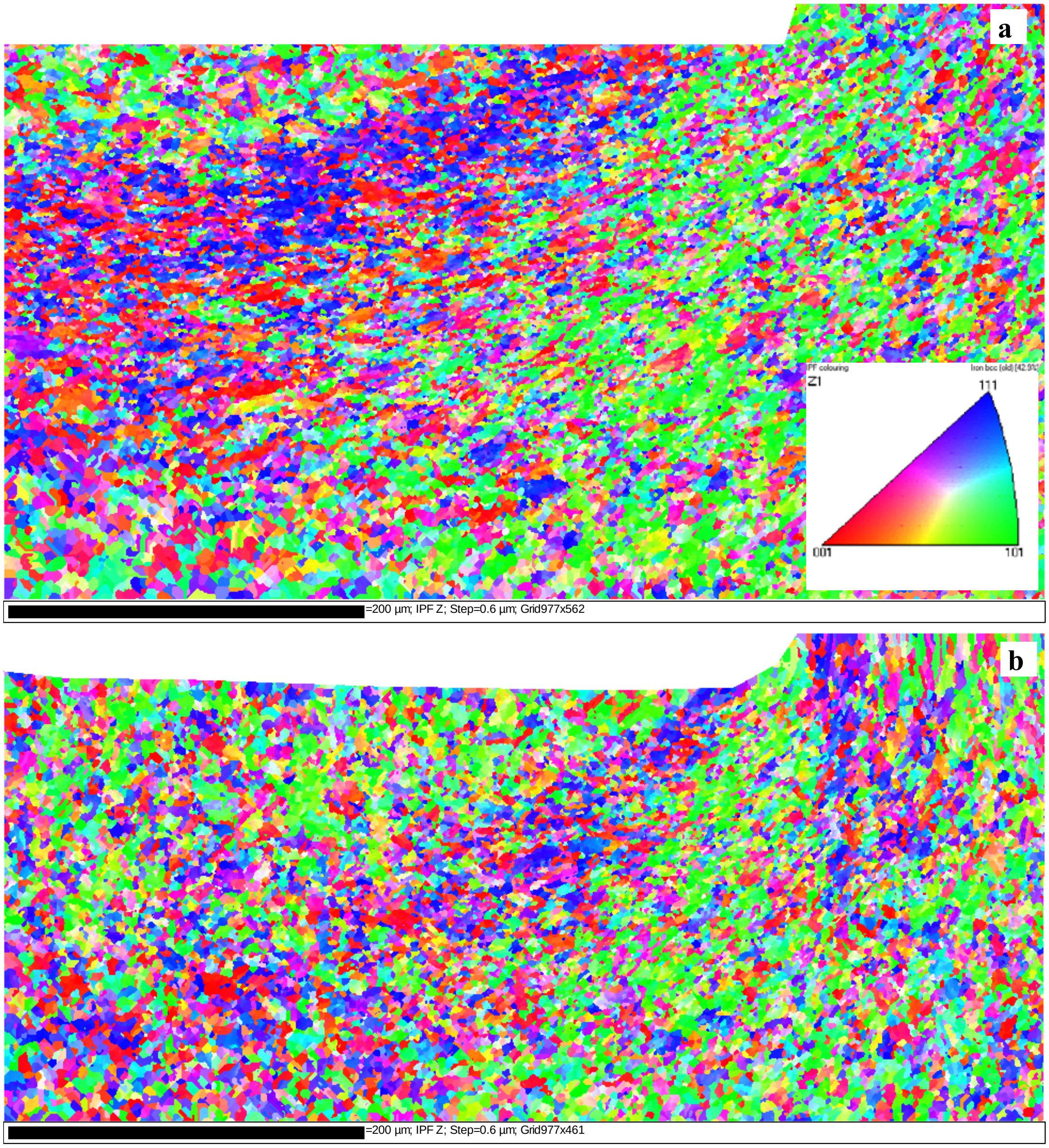

Fig.3.22: EBSD crystal orientation maps (standard IPF) from region below indention of impression tested INRAFM steel showing deformed grains (a) normalised and tempered (b) aged for 10000 h at 773 K

3.6 Effect of aging on Ductile to Brittle Transition Temperature – by small punch test

In the previous section, it is found that the creep properties of RAFM steel are improved by increasing W content from 1 to 1.4 weight %. Additionally, the microstructural changes that occur in RAFM steel on exposure to service temperature and its effects on creep properties are also described. Results showed that creep properties are not severely affected when the steel is exposed to 823 K up to 10000 h. But it is well known that coarsened precipitates such as $M_{23}C_6$ and Laves phase (Fe_2W) forming during thermal or irradiation exposures degrade the fracture toughness of the steel [141-144].

The currently standardized Charpy test requires relatively large volume of test material. For testing a specific region of a weld or an irradiated specimen, normal Charpy tests are not suitable due to size limitations. Considering these aspects, a widely used Small Punch (SP) test was selected and in this section an attempt has been made to correlate the test results with change in chemistry as well as the microstructure of RAFM steel.

SP test was performed on 1W and INRAFM steel for a range of temperatures from room temperature to 78 K. A universal testing machine at a crosshead speed of 1mm/s was used for the experiments. For better statistics three tests were conducted at each temperature and the average value of fracture energy E^{SP} (area under curve) is calculated. **Fig.3.23** shows the typical load – displacement curve obtained from normalized and tempered INRAFM steel tested at 233 & 79 K. Fracture occurs at different regimes depending on the toughness of the material. Since the material at low temperature (79 K) has low toughness, region of plastic instability is absent. **Fig.3.24** shows the smoothened plot of SP fracture energy versus test temperature for both the steels. The typical morphology of plastic bulging (stretching) and crack propagation in 1W RAFM steel is shown as an inset to **Fig.3.23**. At lower temperature, brittle cracks propagate in radial direction due to poor toughness and show less bulging. But at higher temperature plastic bulging is high and ductile cracks propagate along the circumference where the stretching is maximum. Typical SEM fractographs from cracked regions of SP specimen (INRAFM n &t) tested at 233 K and 79 K is shown in **Fig.3.25**. From the fractographs, it is clear that at 233 K the steel is completely ductile but a mixed (ductile & brittle) mode of fracture is observed at 79 K. The fraction of brittle fracture was found increase with decreasing test temperature. Cleavage (intra-granular) type of brittle fracture shows that weaker regions are not prior austenite boundaries but lath boundaries. A transition temperature of 108 K was obtained for normalized and tempered INRAFM steel by SP test in the present study. This value is significantly lower as compared to DBTT values obtained by conventional Charpy impact tests. The same steel showed a DBTT (41J absorbed energy TT) of -93°C (180 K) in Charpy tests [122]. This large difference is due

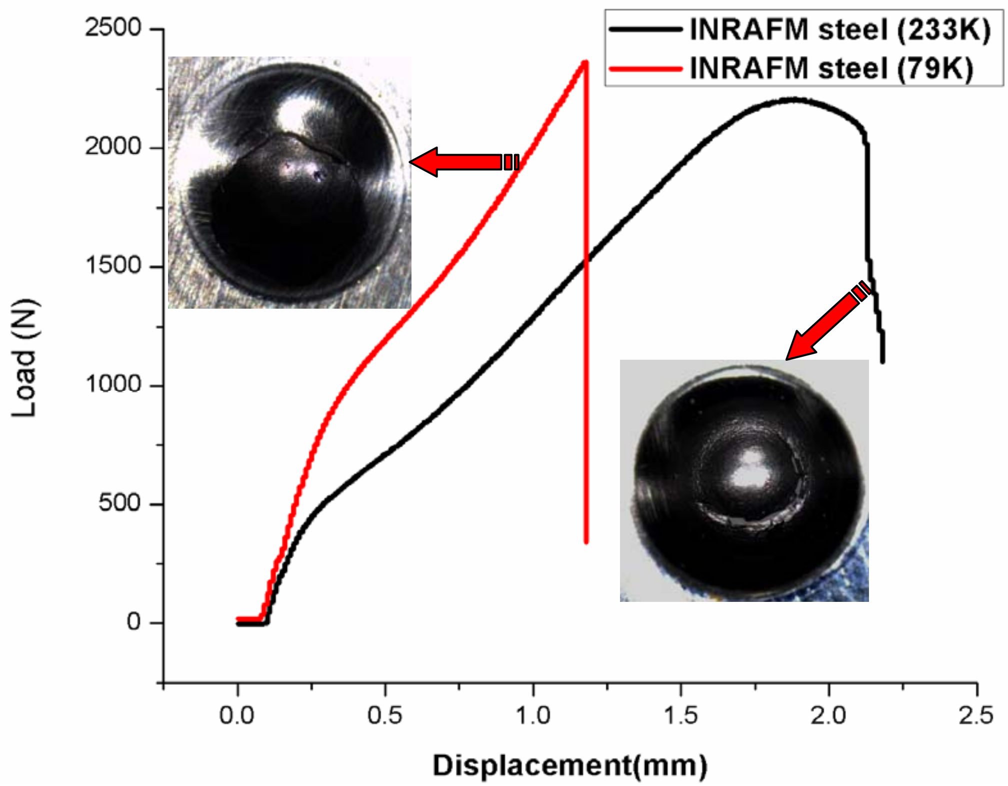

Fig. 3.23: Load - displacement curve of normalized and tempered INRAFM steel SP tested at 233 K and 79 K , with insets showing image of the tested specimens

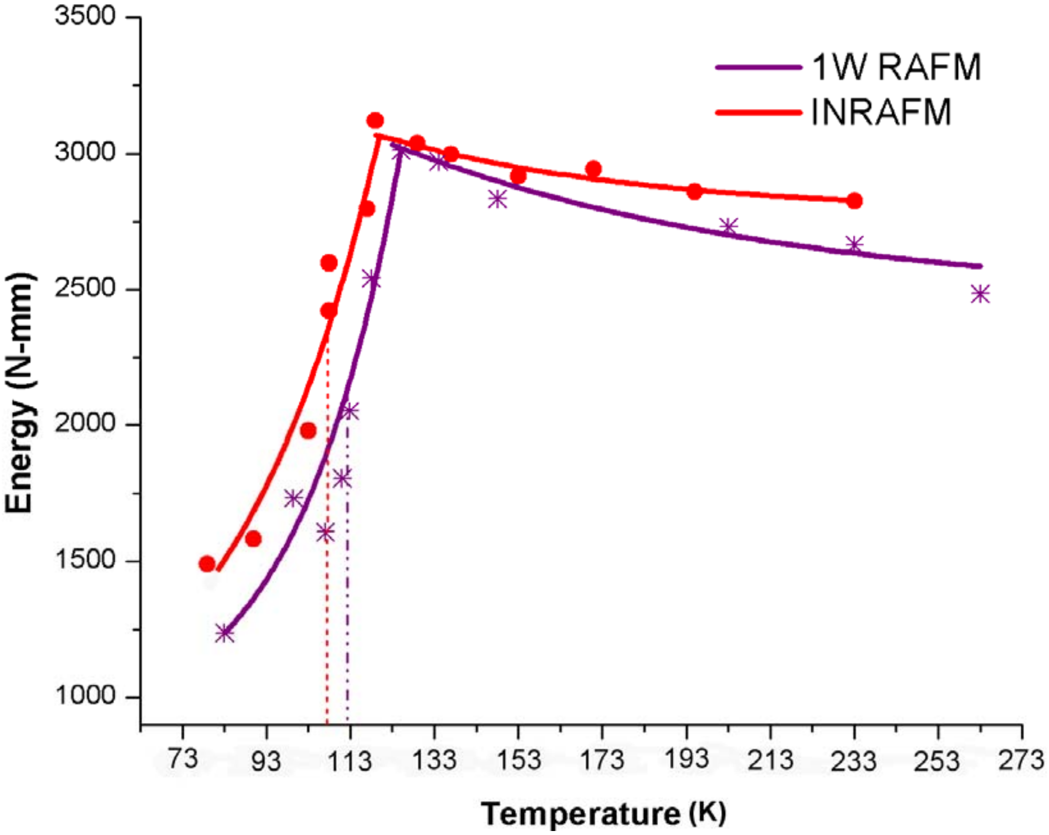

Fig.3.24: SP fracture energy – temperature plot for INRAFM steel and 1W steel.

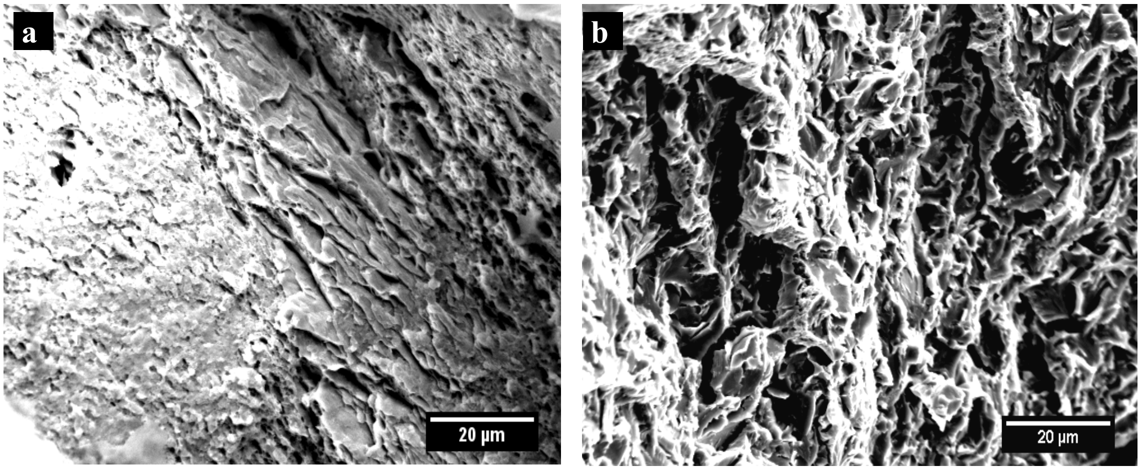

Fig.3.25: Fractographs of n & t INRAFM steel after SP test at a) 233 K and b) 79 K

to the difference in mode of loading. In SP tests, a static load is applied in a biaxial state which is not a favorable condition for a brittle fracture; whereas in a Charpy test an impact load is used in plain strain condition. However, a linear correlation between SP-DBTT and Charpy DBTT has been established theoretically and experimentally by J. Kameda *et.al*. [145] and it is accorded with CEN workshop agreement. The method of determination of DBTT (41 J absorbed energy Transition Temperature) is empirical i.e. by correlation between standard Charpy test values and small punch transition temperature (T_{sp}). SP-DBTT is correlated by the following equation [115],

$$\text{SP-DBTT} = \alpha * \text{Charpy DBTT (K)} \tag{3.4}$$

where α is the correlation coefficient

By correlating (eqn 3.4) with SP-DBTT value, α value was calculated as 0.6. Assuming this value is appropriate to 1W steel, DBTT of normalized and tempered 1W steel is calculated as 188 K. In contrast to this Charpy impact test showed a lower value of DBTT for 1W steel compared to INRAFM steel.

Considering the inherent scatter associated error in fracture toughness values this difference of 8 K is insignificant. However, earlier studies on RAFM steels with varying W contents (0, 1, 2, & 4W) showed that an increase in W content results in an initial decrease in DBTT followed by an increase [146]. It is reported that 1W steel exhibited a minimum value of DBTT. Addition of W to 9Cr steels in small quantities refines the carbides during tempering, thereby reducing DBTT. Size distribution of carbides from extraction replica in the present study showed a similar trend in 1W and INRAFM steel (**Fig.3.7**). However, higher DBTT at high concentration of W (2 wt %) was found to be due to the presence of δ- ferrite. TEM investigation on INRAFM steel did not show any traces of delta ferrite in the normalized and tempered steel. In view of above mentioned findings and reasons, it can be assumed that the DBTT value obtained by SP test is reasonable and can be used for a comparative purpose.

The effect of aging on DBTT was studied using SP technique. **Fig. 3.26** compares SP energy versus test temperature for aged INRAFM steel. A progressive but small increase in DBTT with aging was observed. Typical SEM fractographs of INRAFM steel aged at 823 K for 5000 and 10000 h followed by SP testing at 120 K are given in **Fig.3.27**. It is worth mentioning that the test temperature (120 K) is close to transition temperature (**Fig.3.26**) of both steels. While the steel aged for 5000 h showed a predominantly ductile fracture, the steel aged for 10000 h showed predominantly brittle fracture. It points out that the transition temperature of 5000 h aged steel lies below 120 K and for 10000 h steel lies above 120 K. This is in agreement with the results of the plot given **Fig.3.23**.

The steel aged for 10000 h at 823 K and tested at a lower temperature (83 K) showed a completely brittle fractured surface **(Fig.3.27)**. No intergranular fracture is observed in any of the tested specimen. It is worth mentioning here that INRAFM steel is melted through vacuum induction melting and vacuum arc refining routes with strict control over the radioactive tramp elements and on the elements that promote embrittlement. Hence, it is less likely that the brittle fracture is related to the cleanliness of the steel, but more due to microstructural degradation.

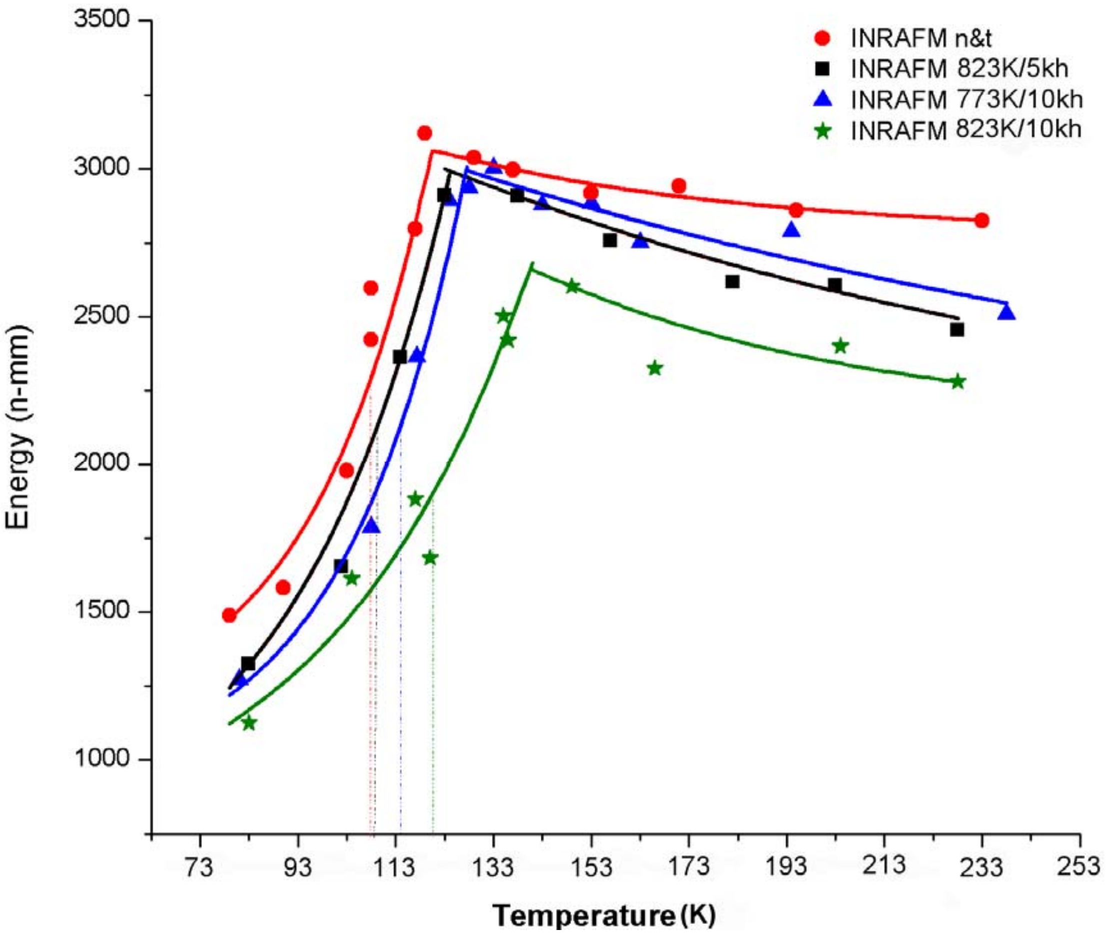

Fig.3.26: Plot of SP fracture energy versus temperature for aged INRAFM steel

As explained earlier in **Section 3.3**, prolonged aging leads to recovery of martensite and evolution of carbides. Recovery of martensite enhances softening, but coarsening of carbides at interfaces has a negative effect on toughness. By looking at the change in DBTT, it is understood that the effect of coarsening of carbide offsets the effect of matrix softening. Aging at 823 K for 5000 h showed only a marginal increase in DBTT. But change in DBTT after aging for 10000 h at 823 K was substantial and is in agreement with literature [113, 141, 147]. A network of Laves phase mainly along lath boundaries and coarsening of carbides (**Fig.3.16**) are responsible for the observed increase in DBTT. The test results on steel aged for 10000 h at 823 K confirms that the fracture properties are not degraded as long as the Laves phase is fine in nature.

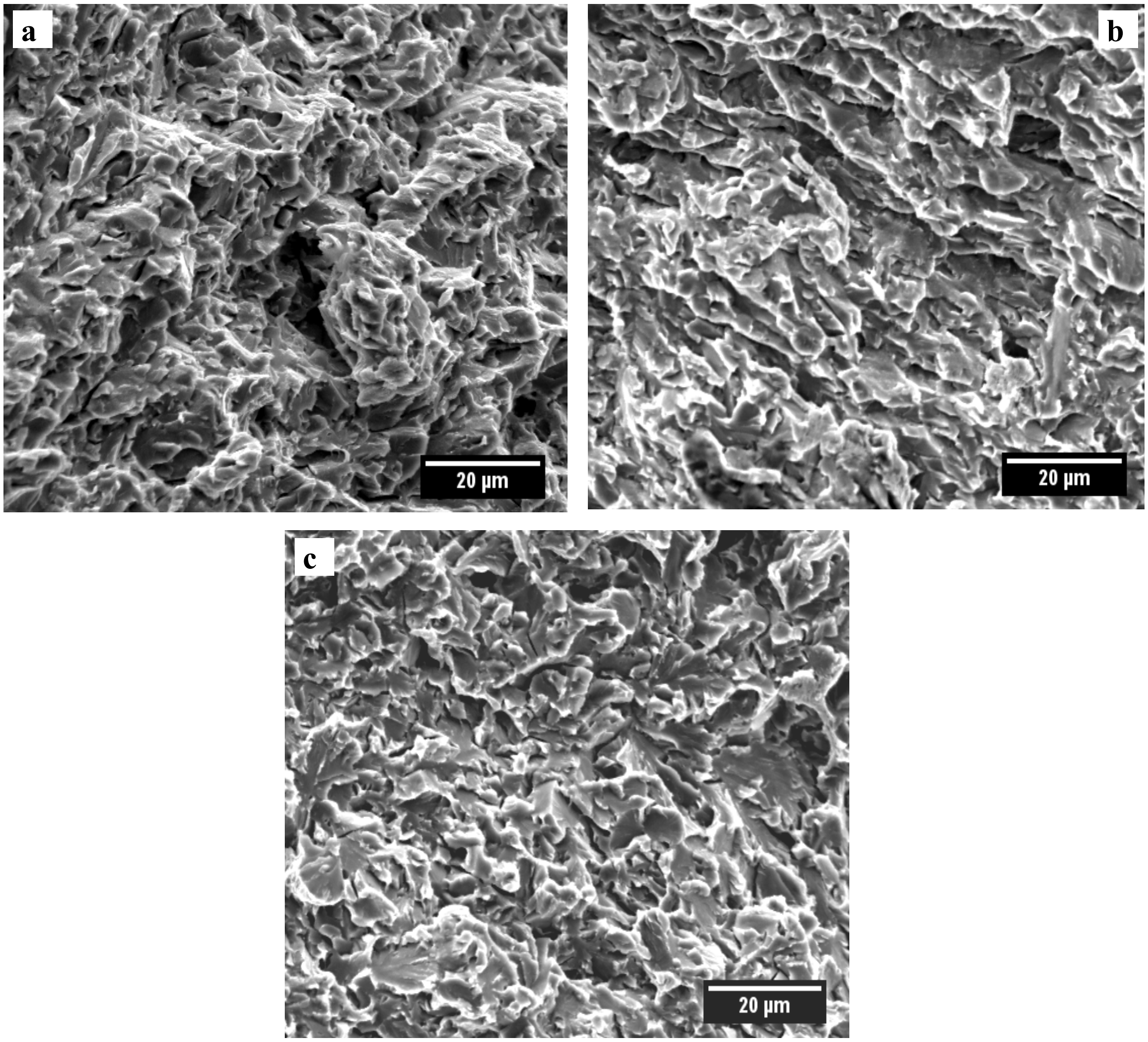

Fig.3.27: Fractographs of aged INRAFM steel after SP test a) aged at 823 K/5000 h & tested at 120 K b) aged at 823 K/10000 h & tested at 120 K and c) aged at 823 K/10000 h & tested at 83 K

3.7 Conclusions

A detailed microstructural characterization of normalized and tempered RAFM steels with two different W contents has been carried out. Microstructural features determined by experiments and computation are compared. Evolution of microstructure was studied with respect to coarsening of carbides and formation of Laves phase. Impression creep and small punch tests have been tried to evaluate differences in the creep strength and DBTT in the two steels. The important results are summarized as below:

- Normalized and tempered RAFM steel possess a tempered martensitic structure consisting of ferrite and carbides, retaining lath morphology of the martensite
- Carbides were identified as Cr rich $M_{23}C_6$ and V/Ta rich MX carbides
- Higher W content in the resisted the coarsening of $M_{23}C_6$ carbides INRAFM steel
- Coarsening of MX was negligible
- A progressive enhancement of Cr is observed in the $M_{23}C_6$ upon aging, supported by computation on equilibrium phases.
- Though computation predicts the nucleation of Laves phase during at 773 K in 1W steel, no experimental evidence could be obtained even after 10000 h of aging which is due to kinetic factors.
- Laves phase nucleates at temperatures of 823 K in INRAFM steel; and above and a discontinuous network of Laves phase forms around 10000 h of aging. Creep properties of two RAFM steels in n & t condition are compared using impression creep test.
- DBTT measurement using small punch test has been attempted for RAFM steel. INRAFM showed a DBTT comparable to 1W RAFM steel.
- The change in creep rate and increase in DBTT upon aging is estimated and correlated with microstructure.

Chapter 4

Identification of microstructural zones in weldments of RAFM steel and its modifications on thermal exposure

4.0 Introduction

A major challenge posed in the fabrication of test blanket module for ITER is the availability of reliable joining technologies. Hence, there is a world-wide impetus to carry out research on knowledge based design of welding methodologies for the RAFM steel variants [68-70, 96]. As a part of the indigenous development of Indian RAFM steel, assessment of welding technologies including evaluation of mechanical properties and microstructural characterization of the weld joints is currently being studied.

In fusion welding, the solidified metal as well as base metal are subjected to a series of thermal cycles which depend upon various parameters like the distance from the heat source and number of passes employed during the process, resulting in microstructural heterogeneities. In case of ferritic- martensitic (F/M) steels these structures vary from martensite, tempered martensite and ferrite [73-76]. The failures during creep testing and long term service exposures in F/M steels are reported to occur in the Heat Affected Zone (HAZ) region of the weld [78, 86]. Advanced welding techniques with low heat input such as Electron Beam (EB) welding and LASER Beam (LB) welding are alternate methods to reduce the width of HAZ thus minimizing the soft zone [79].

In addition to welding methodologies, the selection of conditions for Post Weld Heat Treatment (PWHT) is crucial to obtain improved toughness of the weld joint [82]. A careful combination of temperature and duration is required to ensure adequate strength and ductility, by controlled tempering of the martensite, and has been widely dealt with in literature for different types of ferritic steel joints [82-85]. There is extensive literature available for the effect of PWHT on microstructure, properties and in-service behavior [69, 80-81, 148]. Since, the soundness of the weld and the microstructural stability of the weld joint dictate the performance of welded components, an understanding of microstructural evolution including coarsening of precipitates, change in microchemistry and formation of any detrimental phases in various regions of the weldments are important. Hence, many experimental studies are focused on the change in structure and property during long term service exposures of the weldment [77-78], to assess the performance and ensure the desired life of the component.

This chapter presents the results of a detailed study on the microstructural modifications that take place in the indigenously manufactured INRAFM steel during fusion welding. The microstructural modifications in different regions of the weldment are based on the thermal cycle experienced by the region, which has been computed using Rosenthal's steady state solutions to heat transfer equation. Additionally, the microstructures of different regions of the weldment have been simulated using GLEEBLE thermo mechanical simulator.

The microstructural characteristics of the weldment obtained by conventional Tungsten Inert Gas (TIG) welding are compared with high power-density EB and LB welding processes. The microstructural changes during subsequent PWHTs have also been analyzed employing conventional and electron microscopy techniques. The tempering of martensite in various regions of the weldment during PHWT is discussed in detail to evaluate the mechanism and kinetics of the tempering process. The PWHT conditions have been optimized based on minimization of hardness and microstructural variations across the fusion zone. JMatPro was used to predict the formation of various phases and their relative amounts in different regions of the RAFM steel weldments during tempering and on long term thermal exposures. Comparison of the precipitation behavior of INRAFM and 1W-RAFM steels, clearly demonstrates that tungsten plays an important role in the kinetics of precipitate evolution and formation of intermetallic phases such as Laves phase in different regions of the weldment.

A comprehensive microstructural characterization of normalized and tempered steel (base metal) has been described in **Chapter 3**. The microstructural modifications that arise during welding and PWHT in three different welding methods are discussed and compared in **Section 4.1**. **Section 4.2** presents the results on optimization of PWHT and the kinetics of tempering of martensite. Microstructural evolution in the weldment during prolonged thermal exposure is discussed in **section 4.3**. All the results are summarized in **Section 4.4**.

4.1 Microstructural characterization of weldment – 'As welded' state

The microstructural, micro-chemical changes and micro-texture in different zones due to welding by three techniques have been studied, which will be described sequentially in this section.

4.1.1. Characterization of the autogenous TIG weldment

The micro-hardness profile across the autogenous TIG weldment of two RAFM steels is shown in **Fig.4.1 (a)**. The plot depicts all the regions of the weldments namely weld metal, HAZ and base metal. The average hardness of weld metal was measured as 465 and 490 VHN for 1W and INRAFM steel respectively. The hardness values were found to be higher in the weld zone and HAZ closer to fusion zone, beyond which a steady decrease in hardness was observed. In **Fig.4.1 (b)**, a hardness profile is superimposed on the micrograph obtained from 1W steel weldment. The extent of HAZ was ~1.6mm for a

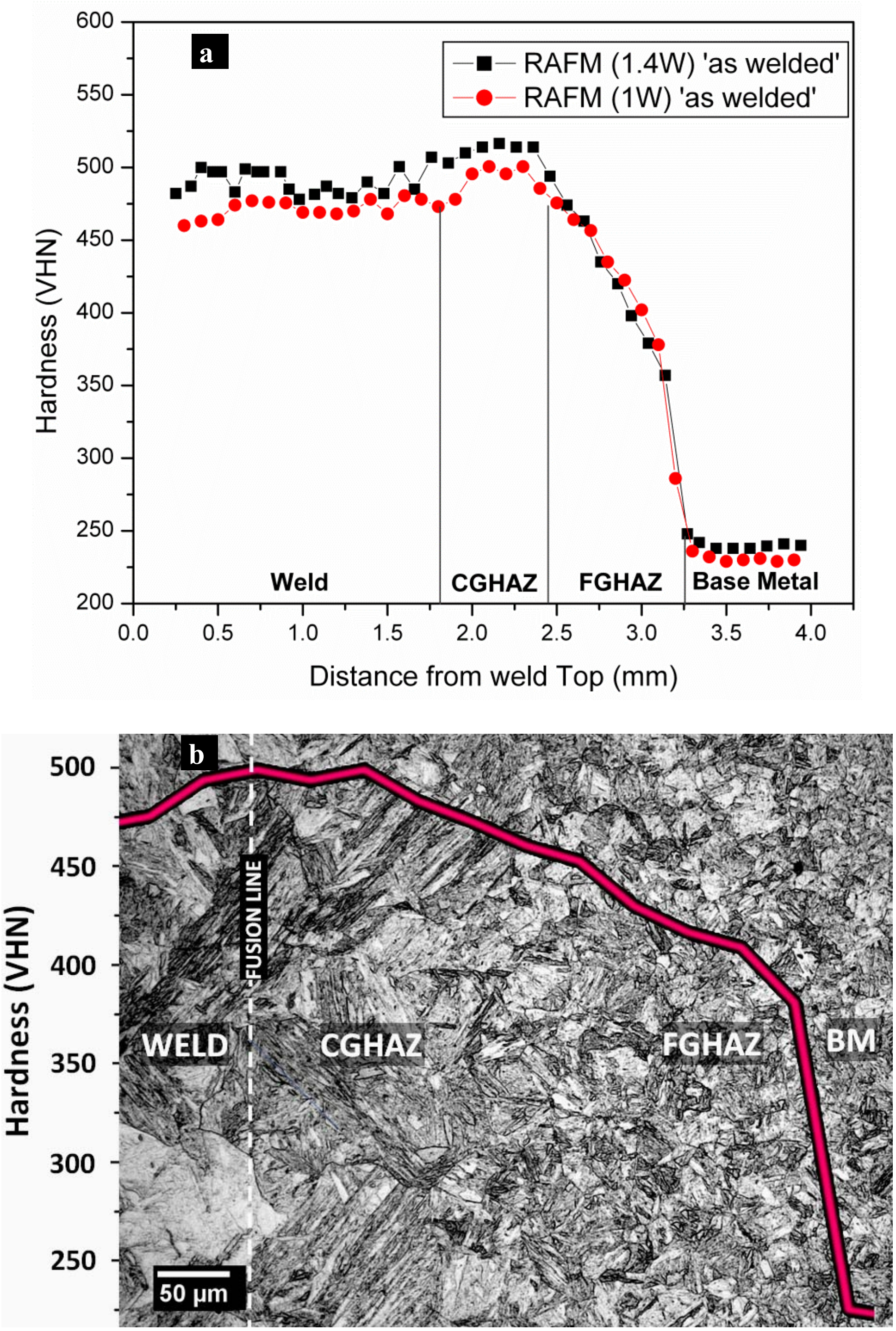

Fig.4.1: (a) Hardness plot across the autogeneous TIG weldment of 1 and 1.4W steel and (b) Optical micrograph showing the Weld, CGHAZ, FGHAZ and Base Metal regions of the weldment of 1W steel, with hardness plot superimposed.

weld bead of thickness 2 mm. The weld region of both the steels exhibited a complete martensitic structure, as seen in **Fig. 4.2 (a and b)**. It reveals a solidification structure with elongated prior austenite grains. The TEM micrograph (**Fig.4.2 (c and d)**) revealed the lath martensite structure with high density of dislocations in the weld region, which is responsible for the high hardness. The lath size of martensite in the weld metal was estimated to be in the range of 400-500 nm that is slightly lower than that of 1W base metal (600-700 nm), which is also reported in literature in similar kind of steels [69]. The fine lath size is due to the higher cooling rate of the welding process compared to normalizing treatment. A typical diffraction pattern from weld metal of 1W steel is shown as an inset in **Fig.4.2(c)**, which corresponded to α-ferrite. The diffraction patterns from martensitic weld metal of both the steels corresponded to α-ferrite, which is in agreement with the low carbon content of the two steels. The carbon extraction replica taken from this region was analyzed by TEM and no precipitates were observed. It is evident that all the carbides have dissolved in the fusion zone and the high cooling rate during solidification and subsequent solid state transformation results only in a fine lath martensite.

The EBSD crystal orientation map from the weld region of INRAFM steel is shown in **Fig.4.3 (a)**, which shows a random microtexture, while **Fig.4.3 (b)** clearly confirms the large size of the columnar prior austenite grain in the weld region. No evidence was obtained for the presence of δ-ferrite in the weld metal, in contrast to reported literature for TIG welded China Low Activation Martensitic (CLAM) steel [149]. Formation of martensite in the weld and HAZ is understood from the Continuous Cooling Transformation (CCT) diagram reported for modified 9Cr-1Mo steel [31].

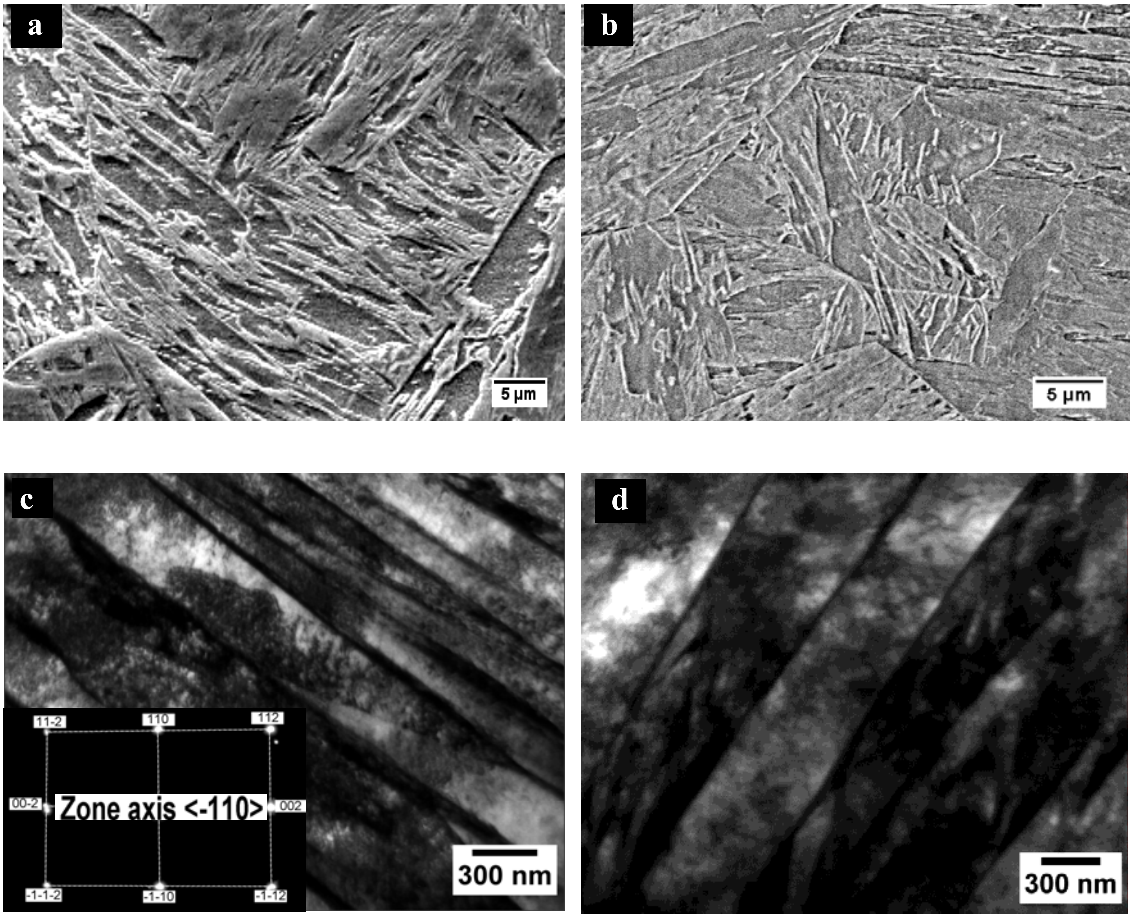

Fig.4.2: Microstructure of weld metal of the TIG weldment showing (a and b) typical martensitic structure in 1W and INRAFM steel; (c and d) lath martensite with high dislocation density (inset in (c) showing SAD pattern from α-ferrite along $\langle\bar{1}10\rangle$ zone axis)

The constitution of the steels at ambient temperature after cooling from solidification temperature can be predicted from the Schaffler-Schneider diagram using the following chromium and nickel equivalents [13] of the alloying elements.

$$Cr_{eq}\ (\text{wt }\%) = \%Ni + \%Co + 0.5(\%Mn) + 0.3(\%Cu) + 30(\%C) + 25(\%N) \qquad (4.1)$$

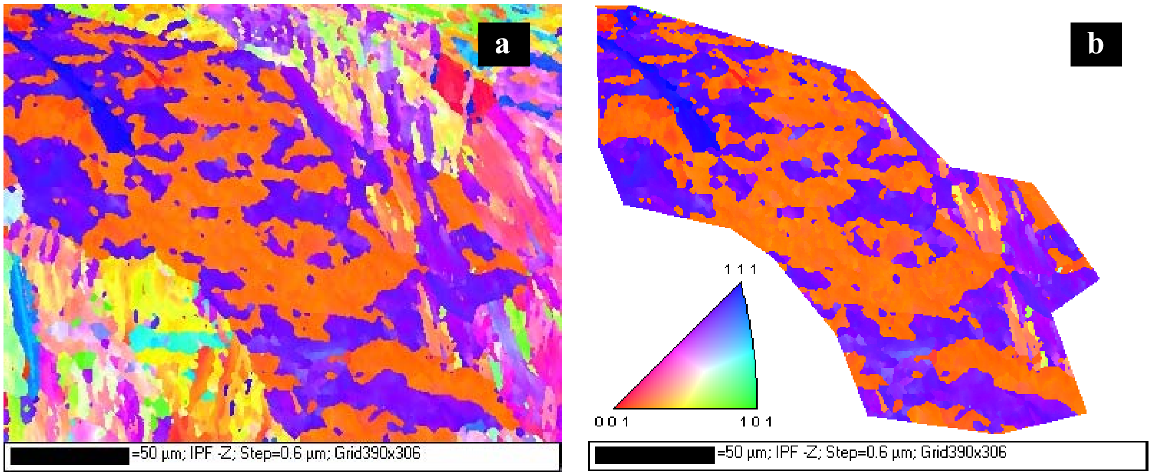

Fig.4.3: EBSD Crystal Orientation map (standard IPF Z colouring) from the weld region of INRAFM steel showing (a) random texture and (b) coarse columnar prior austenite grain with martensite substructure.

$$\begin{aligned} Ni_{eq}\ (\text{wt }\%) = {} & \%Cr + 2(\%Si) + 1.5(\%Mo) + 5(\%V) + 1.75(\%Nb) \\ & + 0.75(\%W) + 5.5(\%Al) + 1.2(\%Ta) + 1.2(\%Hf) \\ & + 1.0(\%Ce) + 0.8(\%Zr) + 1.2(\%Ge) \end{aligned} \tag{4.2}$$

Cr and Ni equivalents of 1W and INRAFM steels were evaluated as (11.4, 3.9) and (11.5, 4.8) respectively. Superimposing these values on Schaffler-Schneider diagram showed that martensite is the only constituent that forms in the weld metal at ambient temperature.

HAZ, the region of base metal immediate to fusion zone, undergoes a variety of solid state transformations depending upon the distance from the heat source. The microstructure of HAZ in F/M steel weldment is highly heterogeneous and its severity depends on welding technique and cooling rate [127, 150]. **Figure 4.4(a)** shows the SEM micrograph of the region close to fusion line. A martensite microstructure with an average

Prior Austenite Grain Size (PAGS) of ~26μm is observed, which is designated as the Coarse Grained HAZ (CGHAZ). The values of hardness were measured as 490 and 515 VHN for 1 W and INRAFM steel respectively, which shows that this region possessed the highest hardness in the weldment.

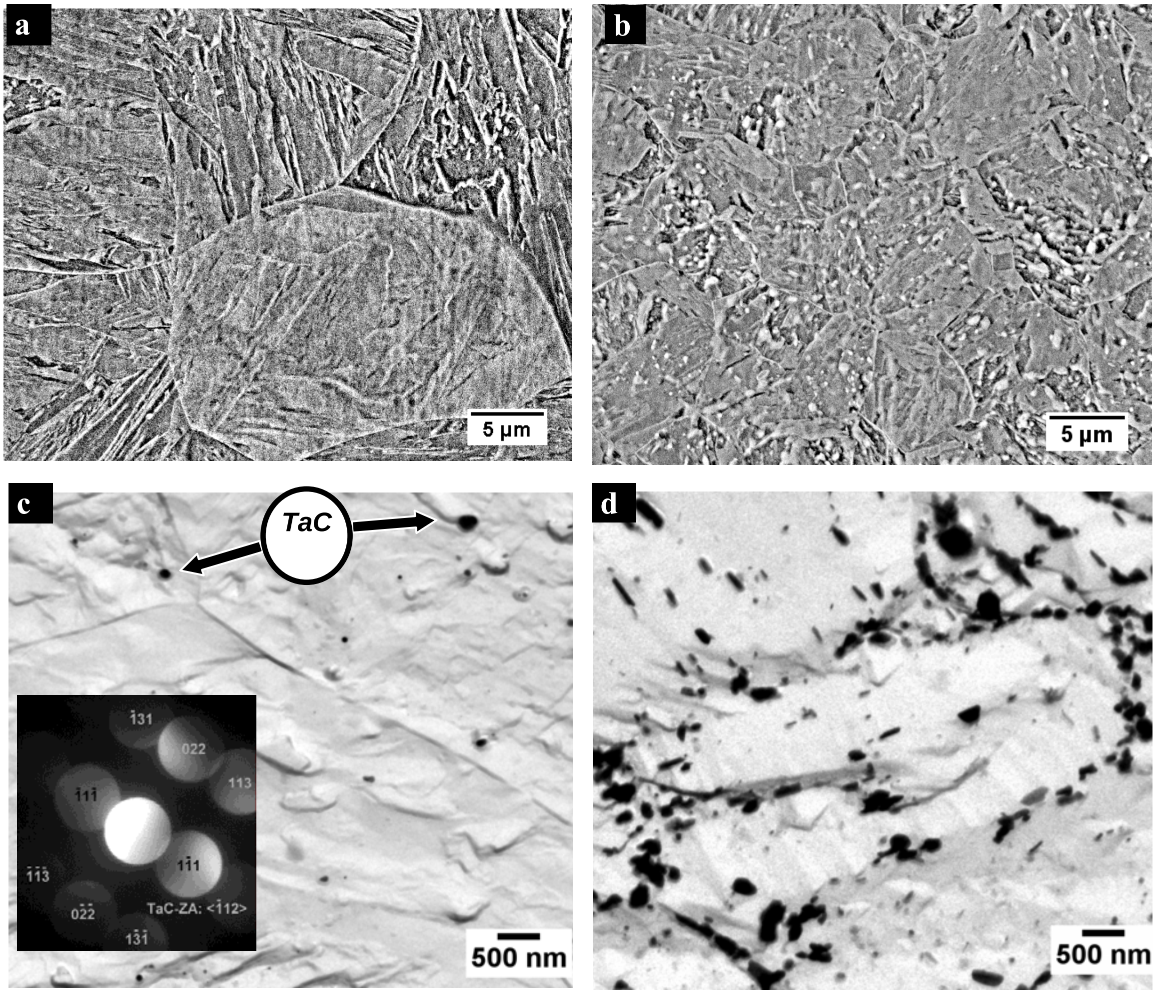

Fig.4.4: Microstructural details of HAZ region in 'as welded' INRAFM steel (a) martensitic structure of CGHAZ, (b) FGHAZ showing fine PAGS, (c) TEM micrographs of carbon extraction replica showing dissolution of carbides in the CGHAZ (inset: diffraction pattern from undissolved TaX along $<1\bar{1}1>$ and (d) high number density of carbides in FGHAZ.

The region adjacent to CGHAZ is characterized by fine prior austenite grains of average size of only ~10 µm (**Fig.4.4 (b)**). This region termed as Fine Grained HAZ (FGHAZ) corresponds to temperatures exceeding Ac_3 during heating part of the weld thermal cycle which transformed completely to martensite. The difference in PAGS is clearly a manifestation of the peak temperature attained by the region as it is a function of distance from the heat source. TEM extraction replica micrographs (**Fig.4.4(c and d)**) showed a few Ta rich precipitates (primary TaC) in CGHAZ but a high number density of carbides in FGHAZ regions due to incomplete dissolution of precipitates at these temperatures.

Figure 4.5 is taken from a narrow zone between FGHAZ and base metal. The PAGS in this zone is similar to that in FGHAZ but the microstructure is duplex consisting of tempered martensite and martensite. The presence of few ferrite grains with lower defect density amidst lath indicates a mixed microstructure typical of regions exposed to temperatures between Ac_1 and Ac_3. This region is termed as intercritcal HAZ (ICHAZ), which arises due to the microscopic region witnessing a temperature regime corresponding to the inter critical temperature of $Ac_3 > T > Ac_1$ for this steel. The presence of duplex structures having extreme differences in properties is account for the reported failures in ICHAZ of ferritic steel weld joints [151-152].

Figure 4.6 (a) compares the volume fraction of extracted carbides in the carbon replica from different regions of the weld for both the steels. The size distribution of carbides present in FGHAZ and CGHAZ of 1W steel weldment is compared in **Fig.4.6 (b)**. It is very clear that the volume fraction of carbide (**Fig.4.6 (a)**) is higher in the FGHAZ as compared to CGHAZ region, in both the steels, the amount being higher in INRAFM steel due to its high carbon content. From **Fig.4.6 (b),** it is observed that the size of the

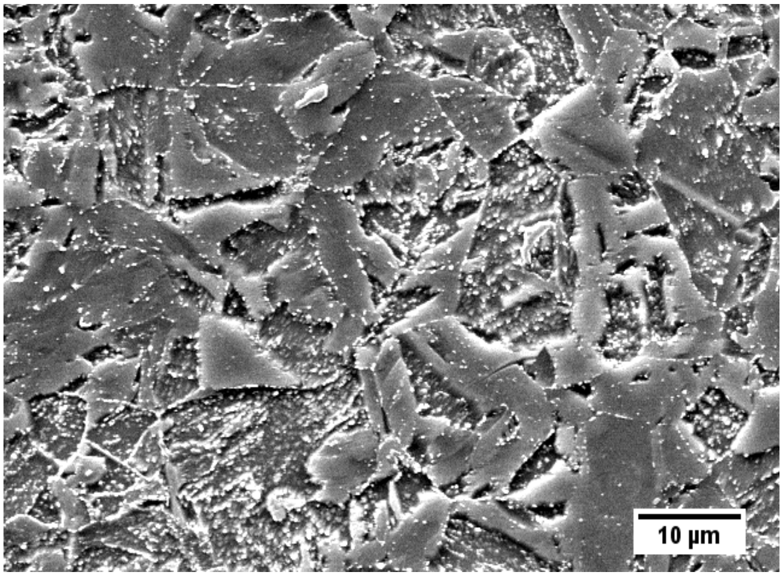

Figure 4.5: Inter-critical HAZ of 1W RAFM steel weldment showing a duplex microstructure consisting of martensite and ferrite

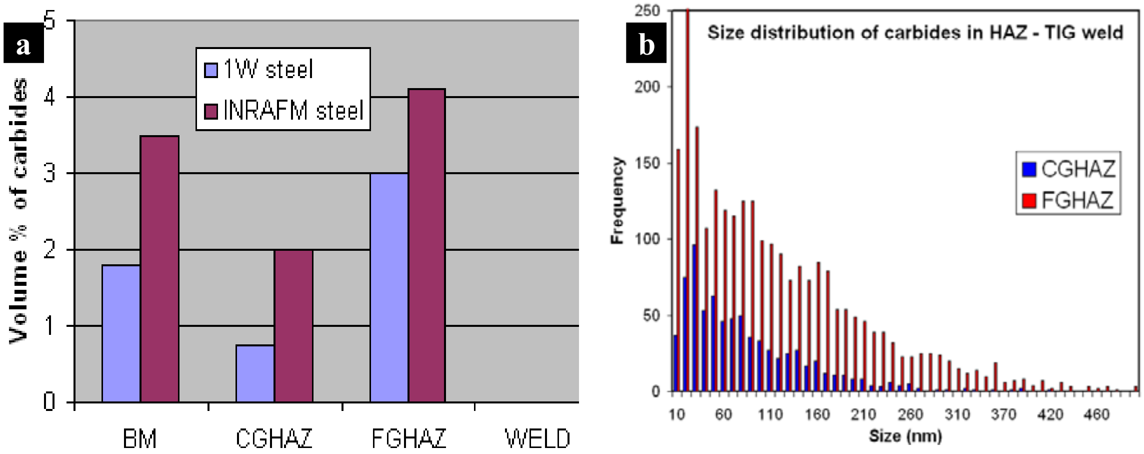

Fig.4.6. (a) Volume fraction of carbides in different regions of the weld for 1 and 1.4W steels (b) Carbide size distribution in CGHAZ and FGHAZ of 1W steel weldment.

carbide varied from 20 to 250 nm in CGHAZ, it varied from 20-350 nm in FGHAZ. The observed high hardness and PAGS in the CGHAZ is attributed to the high carbon super-saturation of the martensite due to the complete dissolution of carbides on exposure to high temperature i.e. above 1500 K [35] and unrestrained grain growth. On the other hand, low hardness and PAGS in FGHAZ is the consequence of incomplete dissolution of precipitates, which pins the grain boundaries thus restraining their growth due to exposure to relatively lower temperature.

4.1.2. Prediction of Thermal Cycles

It is known that these microstructural changes are due to the different thermal cycles experienced by various regions of the weldment. The important parameters of the thermal cycle closely associated with phase transformations are (i) maximum temperature (T_{max}) experienced by each region, (ii) stay time at that temperature and (iii) cooling time (t_{8-5}), which also control the stability of carbide or in other words the carbon content in the transformed austenite phase [153]. Using Rosenthal's steady state solutions to heat transfer equation [154], an attempt has been made to calculate the temperature experienced at a point in the plate when the welding torch is moved at a uniform speed. To validate the application of solution to this equation, it is assumed that an autogenous weld is made on a large plate using a point source. The temperature at a point (x,y,z) is given [155] by

$$T = T_0 + \left(\frac{q_0}{2\pi\lambda R}\right) e^{-\left(\frac{v}{2a\left(R+x\right)}\right)} \tag{4.3}$$

where,

$R = (x^2 + y^2 + z^2)^{1/2}$

V = Voltage (15 V)

I = Current (150 amps)

η = arc efficiency (0.6 for GTAW)

q_0 = heat input = $V \times I \times \eta$

λ = thermal conductivity (25.2 W/m.K)

ρ = density (7665kg/m^3)

c = heat capacity (536 J/kg .K)

v = welding speed (0.0025 m/s)

a = heat diffusivity = $\lambda/\rho c$

T_0 =Pre-heat temperature (473 K)

Temperature as a function of time was calculated for different z (depth) as shown in **Figure 4.7**, with each curve depicting heating/cooling experienced by a point at a particular depth. Generally the different regions of the base metal, which undergo modifications, experience a temperature maximum between T_m and 1033 K. The curves for which maximum temperature (T_{max}) corresponds to critical temperatures have been drawn, such that each curve represents the thermal cycle experienced by a particular region of the weldment. The lowest temperature of concern is the tempering temperature 1033 K below which no transformation is possible.

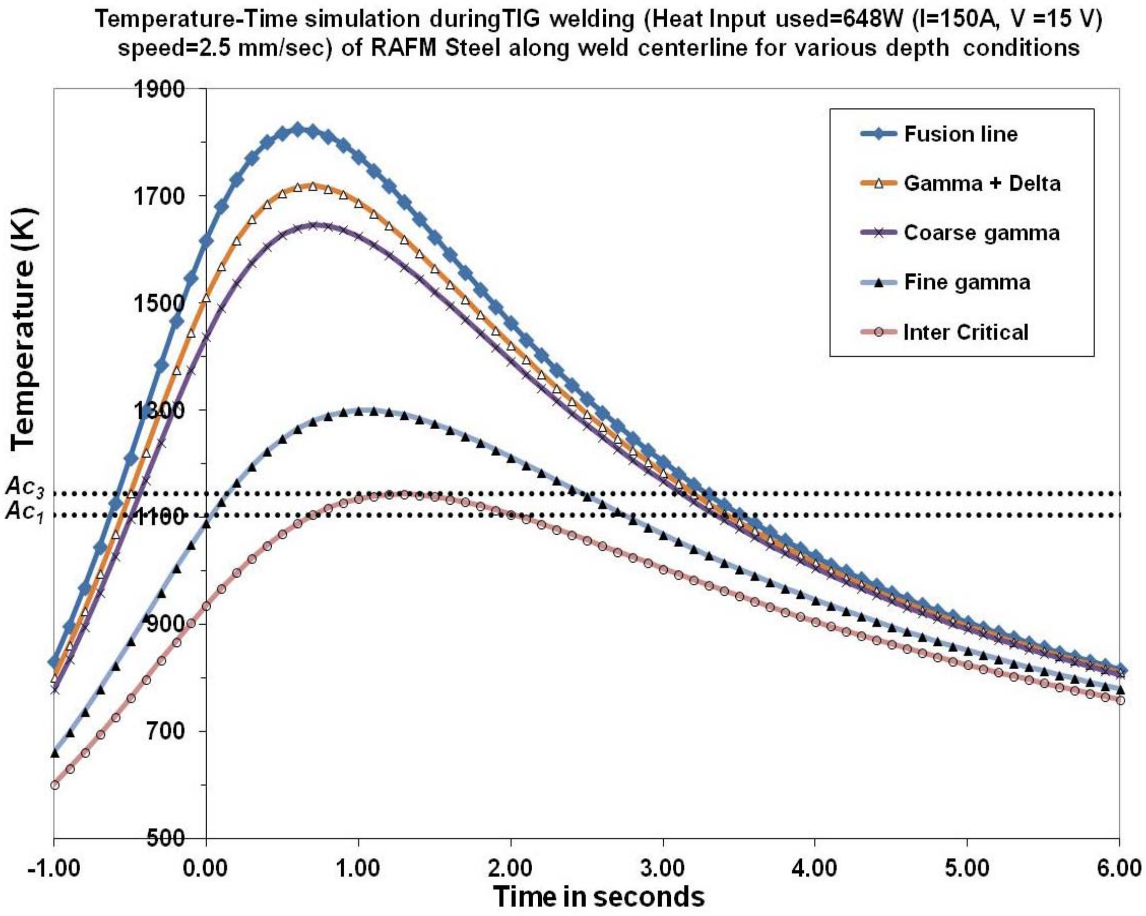

Figure 4.7: Temperature profile during GTAW welding at different regions of weldment

The temperatures corresponding to the different regions are as follows:

- Curve ‘1’ stands for the region of fusion line, where $T_{max} = T_m$.
- Curve ‘2’ represents the region, which has not liquefied but heated to $\gamma + \delta$ region.
- Curve ‘3’ corresponds to high austenitization temperature resulting in coarse prior austenite grains.
- Curve ‘4’ represents a temperature just above Ac_3, the region of fine-grained prior austenite.
- Curve ‘5’ depicts the ICHAZ region where the temperature is between Ac_3 and Ac_1.

Regions far away, where the temperature is below tempering temperature are not expected to undergo any microstructural changes.

4.1.3. Microstructural Analysis of the electron beam and laser beam weldments

Preparation of electron beam (EB) and laser beam (LB) weld joints was carried out on normalized and tempered INRAFM steel. SEM and TEM micrographs of the base metal of the weldments in **Fig.4.8 (a and b)** respectively, show a typical tempered martensitic structure having lath morphology with inter and intra lath precipitates, similar to the wrought steel which had been discussed in detail in Chapter 3.

Macrostructure and hardness profile of EB weld are shown in **Fig.4.8 (c and d)**. The average hardness of weld metal is estimated as 474VHN. The width of the HAZ is about 1-1.5 mm, which is lower than that of TIG weld and the hardness reduced across the HAZ and reached the level of base metal hardness (~225VHN). **Figure 4.9 (a–f)** shows the microstructures of weld metal and HAZ of the weldment prepared by EB welding.

SEM micrograph (**Fig.4.9 (a)**) from weld metal shows a columnar morphology with lath martensitic (**Fig.4.9 (b)**) microstructure. EBSD crystal orientation maps of weld metal from LB weld is given in **Fig. 4.9 (c)**. No evidence of preferred orientation is observed. A typical prior austenite grain from the weld is shown in **Fig.4.9 (d)**.

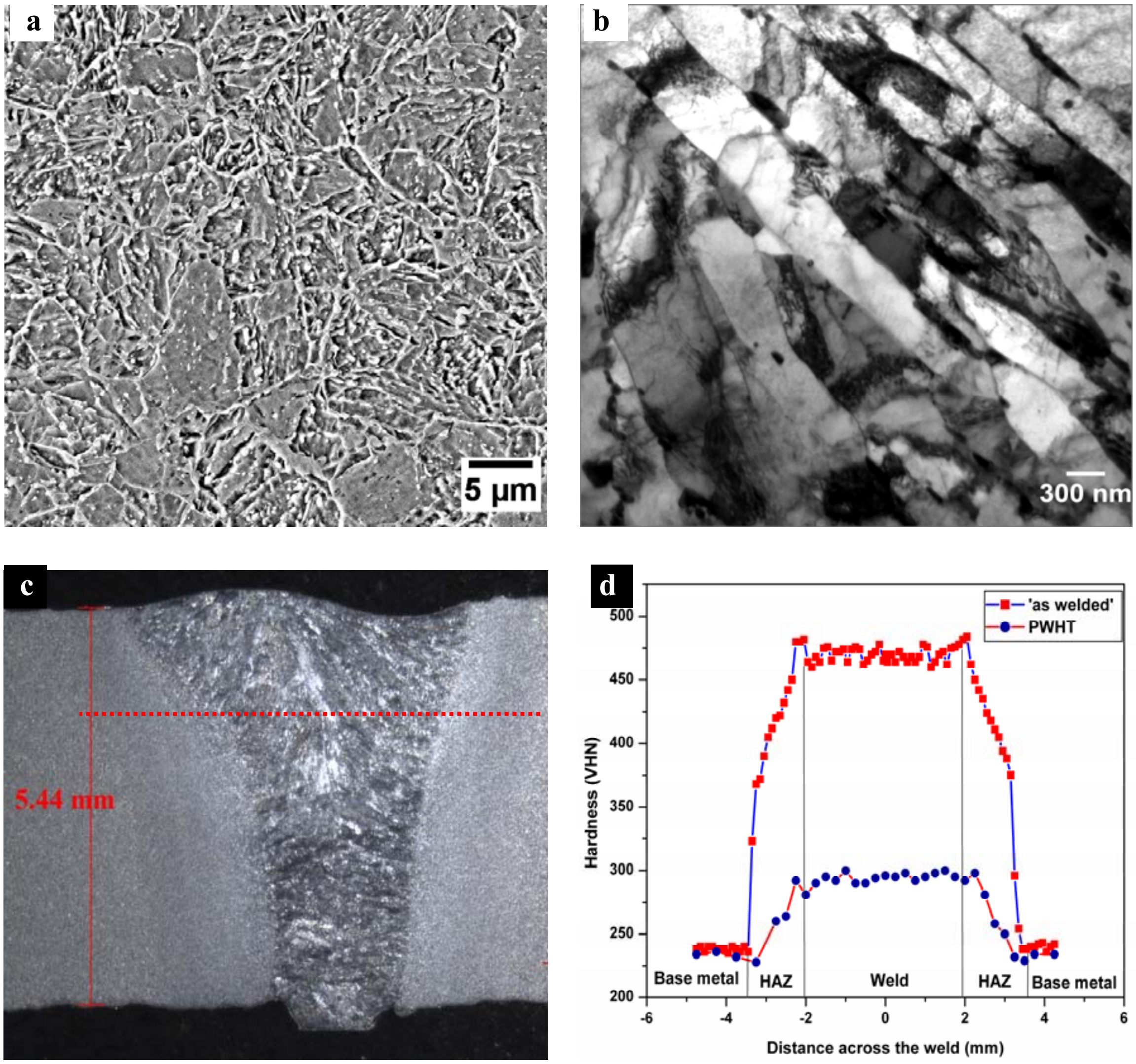

Fig.4.8: Microstructure of electron beam welded INRAFM steel, (a) Base metal showing tempered martensitic structure with (b) lath morphology (c and d) Macrostructure and microhardness profile (along dotted line shown in (c) across the weldment.

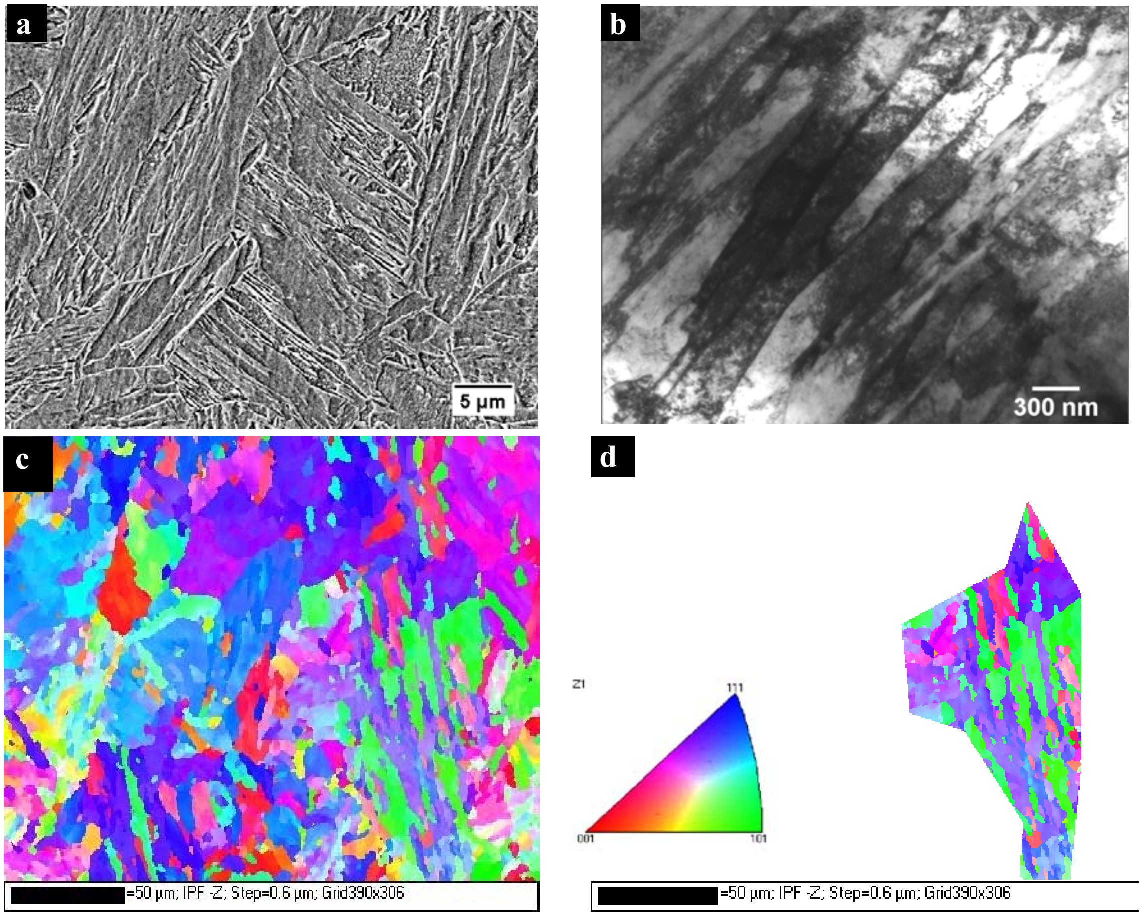

Crystal orientation map – Std. IPF Z coloring

IPF map from a subset prior austenite region

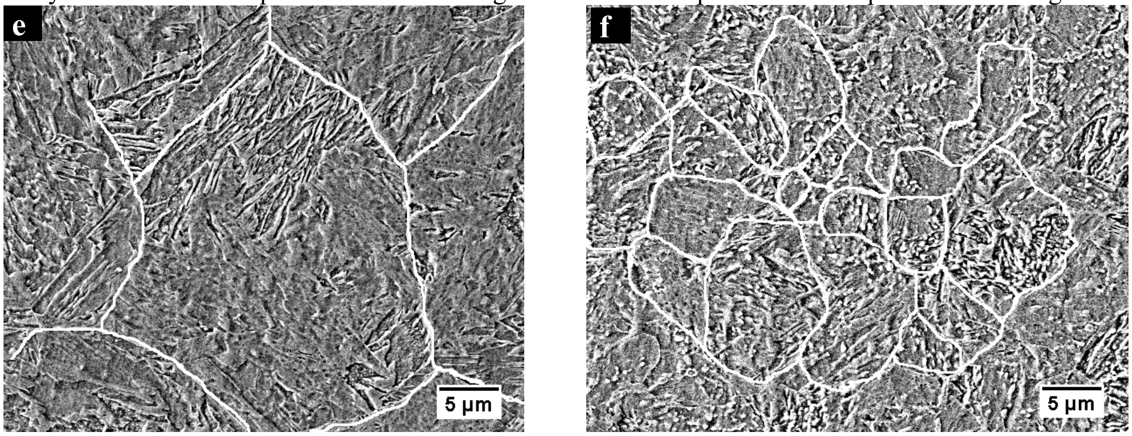

Fig.4.9: Microstructural map of electron beam weldment in 'as welded' condition (a) columnar microstructure in the weld, b) weld metal showing martensitic structure (c and d) EBSD crystal orientation map from weld region and a typical IPF map from a prior austenite grain, (e) CGHAZ with typical martensitic structure and (f) FGHAZ with signatures of large number of precipitates (PAG boundaries are marked).

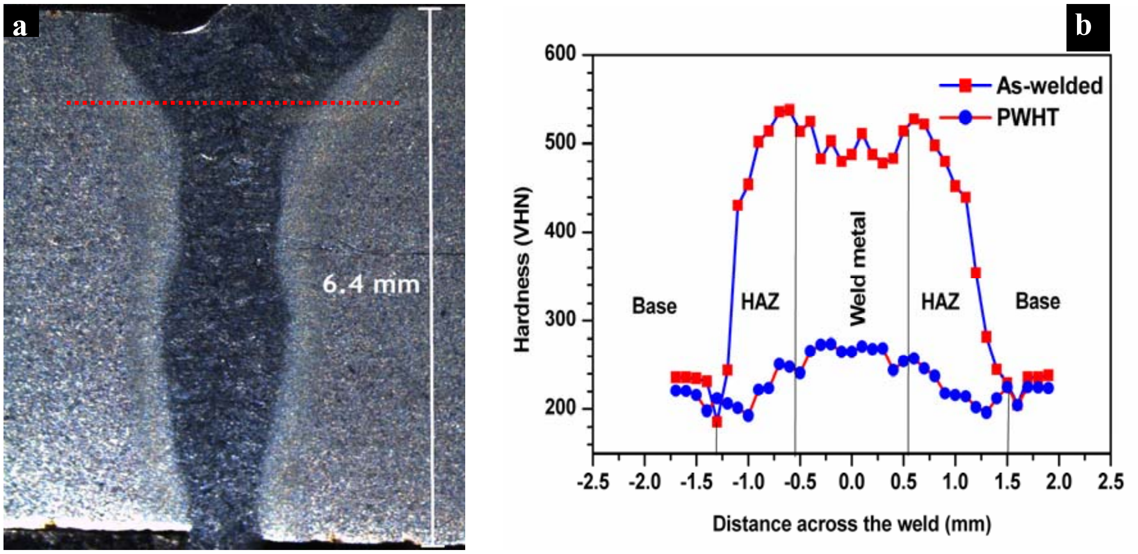

Fig.4.10: (a and b) Macrostructure and microhardness profile (along dotted line) across LB weld of INRAFM steel.

The microstructure of CGHAZ which possessed the highest hardness in the weldment is given in **Fig.4.9 (e),** which showed that the PAGS of CGHAZ was comparable to that of the base metal. **Fig. 4.9 (f)** shows the typical microstructure of FGHAZ from EB weld. The FGHAZ exhibited martensitic or duplex (martensite plus ferrite) structure with finer PAGS.

Macrostructure and hardness profile of LB weld are shown in **Fig. 4.10 (a)** and **Fig.4.10 (b)** respectively and the average hardness is estimated as 497VHN. In both the welding methods, weld metal showed martensitic but columnar structure, which is characteristic of liquid to solid transformation. The width of the HAZ in laser beam weld was measured as ~0.7mm, which is far lower than the TIG (1.6mm) bead on plate welds. Constricted HAZ in electron and laser beam welds has been reported in literature [69, 156], which is understood in terms of the higher energy density offered by these welding methods. The SEM and TEM micrographs from weld metal of LB weld are shown in **Fig.4.11.**

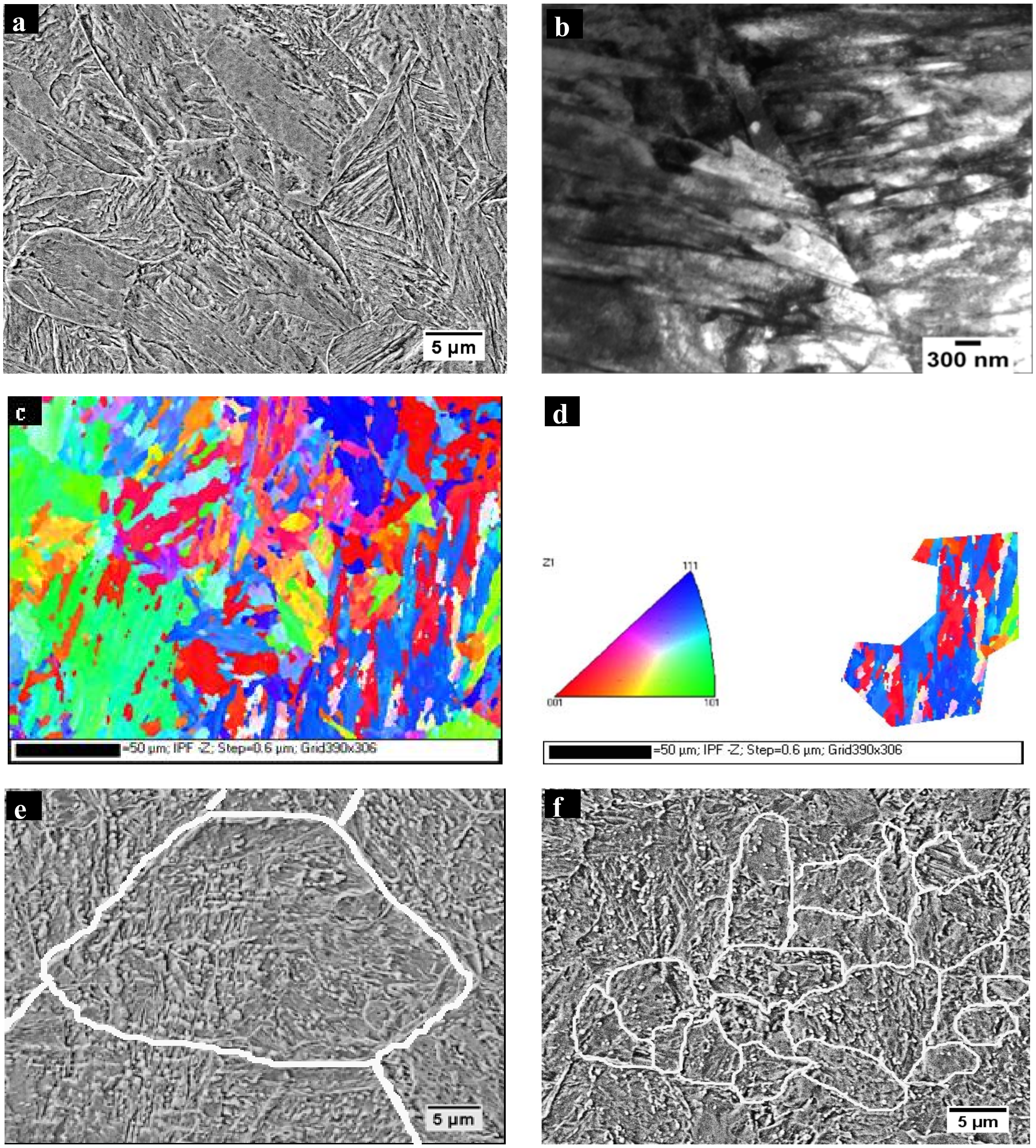

Fig.4.11: Microstructural map of LASER weldment in as welded condition (a) Fully martensitic structure in the weld b) sub structure showing lath martensite in weld metal (c and d) EBSD crystal orientation map from weld region and a typical prior austenite grain (e) martensite within coarse prior austenite grains in CGHAZ and (f) FGHAZ microstructure consisting of martensite and carbides within fine grains of prior austenite grains (prior austenite grain boundaries are marked).

It is clear that the lath martensitic structure is finer in both the EB and LB welds (**Fig. 4.9 (b)** and **4.11(b)**) in comparison with TIG welding (**Fig.4.2(c and d)**).

EBSD crystal orientation maps of weld region along with the IPF map of prior austenite grain from LB weld are given in **Fig.4.11 (c**) and **(d)** respectively, which suggests no preferred orientation of the martensite laths. It is observed that the prior austenite grains are distinctly smaller in the EB and LB welds as compared to TIG weld (**Fig.4.3**).

The microstructure of CGHAZ of LB weldment is given in **Fig.4.11 (e),** showing a fully martensitic structure. Though the PAGS of CGHAZ was comparable to that of the base metal, it possessed the highest hardness in the weldment. **Fig.4.11 (f)** shows the typical microstructures of FGHAZ from LB weld, which exhibits martensitic or duplex (martensite plus ferrite) structure with finer PAGS.

Figure 4.12 (a and b) shows the micrograph of extraction replica obtained from CGHAZ and FGHAZ respectively of EB weld. A higher amount of undissolved carbides is observed in CGHAZ of EB weld, as compared to TIG weld (**Fig.4.4 (c)** and **Fig.4.12 (a)**. However, it is clear from the micrograph that CGHAZ is lean in carbides as compared to FGHAZ, as was also the case in TIG welds. The distribution of size of carbides present in CGHAZ and FGHAZ are compared in **Fig.4.12 (c)**. The carbide size varied from 10-200nm in CGHAZ and between 20 to 300 nm in FGHAZ. The above observations can be understood in terms of the lower residence time at high temperature due to lower heat input in EB welding. Similar results were obtained in the case of LB weld.

The high energy density of the laser and electron beams allows the vaporization of the material at the location of interaction of beam and material (keyhole formation) and subsequent condensation of the vapor as beam moves forward.

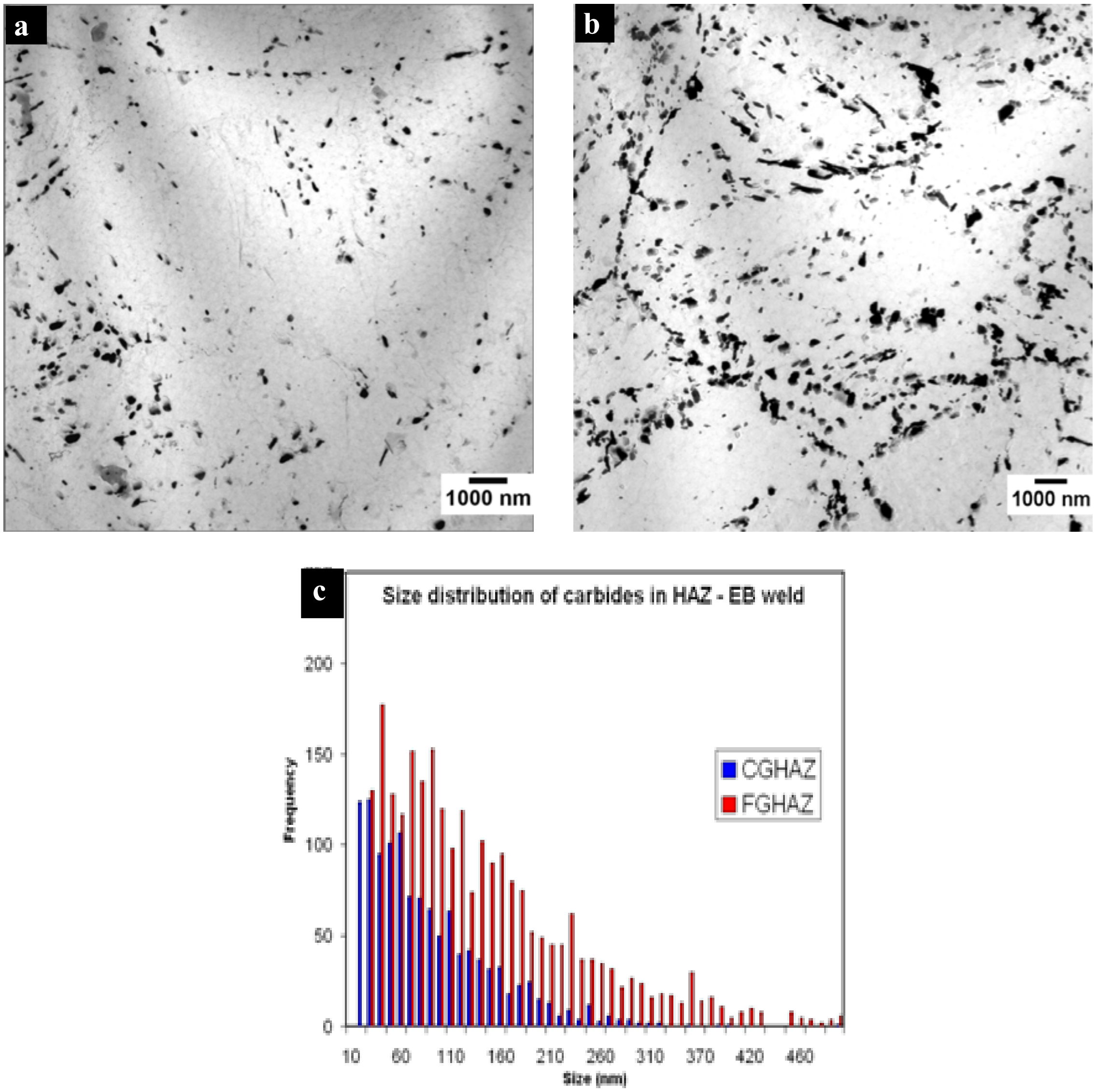

Fig.4.12: Extraction replica micrograph taken from HAZ of electron beam weldment of INRAFM steel showing (a and b) presence of few fine carbides in CGHAZ and large number of coarse carbides in FGHAZ respectively and (c) Comparison of size of the carbides present in CGHAZ and FGHAZ regions

High energy density of the beam necessitates high welding speed and this limits the interaction time of the beam with the material and results in fast cooling of the weld. As a result the high power density welding methods result in small heat-affected zones which ensure good integrity of the weld. The lower PAGS in the weld as well as in CGHAZ exhibited by high energy density welding methods of laser and electron beams is also understood against this background. The variation in hardness in weld metal is not significant for the three welding methods despite a finer substructure in laser and electron beam welds as compared to TIG welds. This is understood in terms of lower solute content of martensite resulting from incomplete dissolution of carbides due to shorter dwelling time in the austenite phase field in HAZ which compensates the effect due to finer substructure.

The microstructural parameters in the three welding methods are compared in **Table 4.1**. The important differences in the microstructures laser and electron beam welds as compared to TIG welding are highlighted below:

- A lower width of weld and a narrow HAZ
- Smaller PAGS of the weld metal in electron beam and laser beam welds.

Shorter dwelling time at peak temperature and high cooling rates are also manifested in finer lath size in electron beam and laser beam welds.

4.2 Optimization of Post Weld Heat Treatment Conditions

4.2.1. Variation of hardness with temperature and time

It is known that PWHT is necessary in ferritic/ martensitic steels to remove residual stresses, to improve toughness and to obtain a relatively stable homogeneous microstructure across the weldment [79, 157-158]. In order to optimize the same, heat treatments at 873, 973 and 1033 K for durations ranging from 0.25 to 2 h were carried out on representative TIG welds of 1W RAFM steel followed by hardness measurements and microstructural investigations. **Figure 4.13 (a)** shows the microhardness profiles across the weldment of 1W steel, heat treated at 873, 973 and 1033 K for 1 and 2 h durations.

Table 4.1: Microstructural parameters of the fusion and HAZ regions of INRAFM steel welds produced by three welding methods

Parameters		TIG weld	EB weld	LB weld
Thickness of weld metal (mm)		6	4.0	1.2
Width of HAZ (mm)		1.6	1.4	0.7
Hardness (VHN)	weld	490 ± 10	474 ± 10	497 ± 10
	CGHAZ	515 ± 10	484 ± 10	520 ±10
	FGHAZ	275-300	280-300	280-300
PAGS (um)	BASE METAL	10 ± 2	18 ± 4	19 ± 4
	Weld	41 ± 4	19 ± 4	20
	CGHAZ	26 ± 5	21 ± 4	19 ± 4
	FGHAZ	10 ± 2	10 ± 2	7 ± 2
Lath size (weld) (nm)		~ 300-500	~150-350	~200-400

The hardness in general showed a reduction with respect to temperature and duration of tempering in all regions of the weldment. Further, there was a pronounced reduction in hardness at ICHAZ region. A lower value of hardness in ICHAZ than that of base metal on PWHT in ferritic steel is reported in literature [159]. **Figure 4.13 (b-d)** shows the SEM micrographs of weld region heat treated at 973 K/2 h, 1033 K/1 h and 1033 K/2 h respectively. The lath morphology of martensite is evident in the specimen treated at 973 K, due to a lesser extent of tempering.

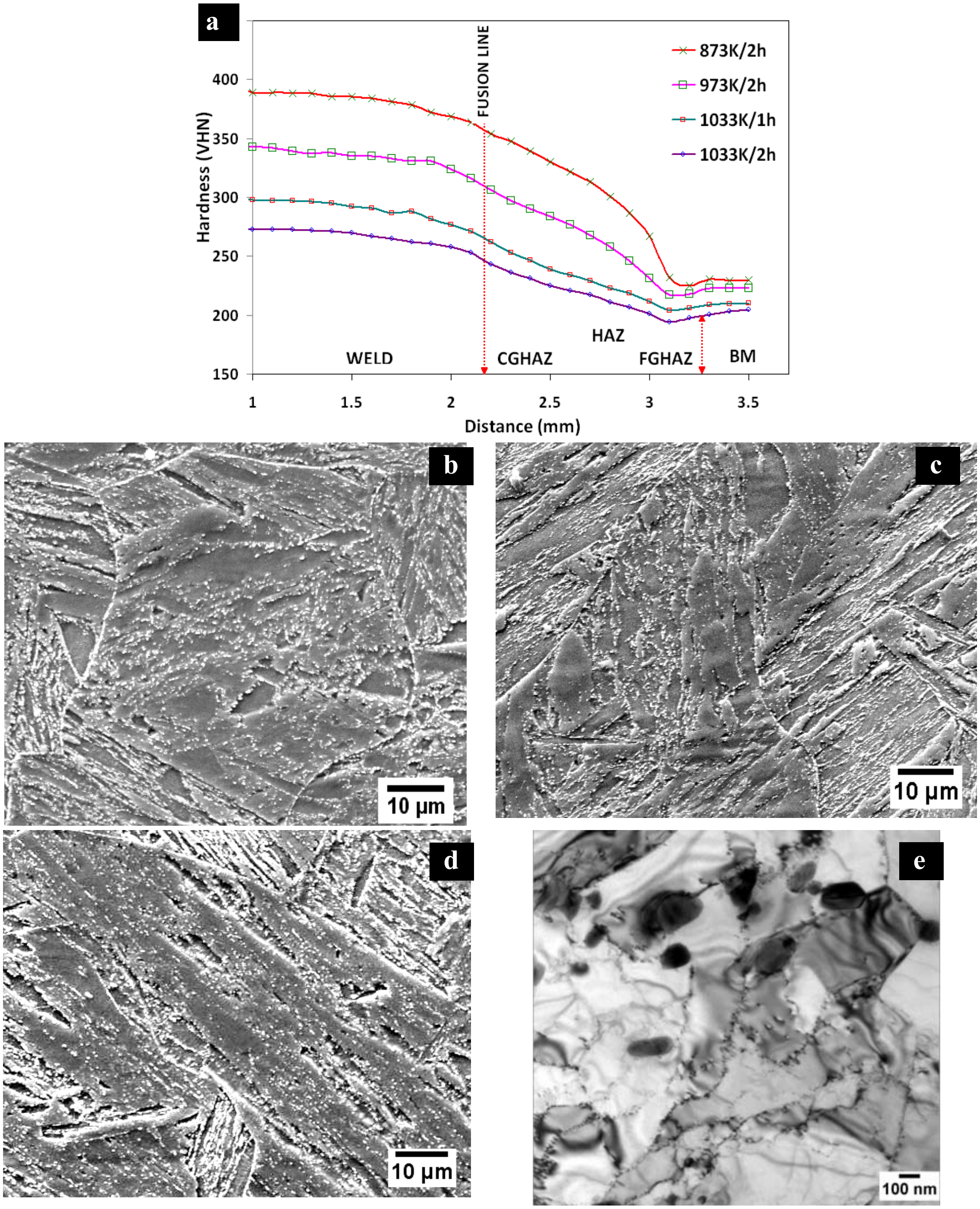

Fig.4.13: Microhardness profile of TIG weldment of 1W RAFM steel after various PWHTs (b, c and d) Micrographs of weld metal after PWHT of 973 K/2 h, 1033 K/1 h and 1033 K/2h respectively showing tempering to different extents (e) TEM micrograph of weld metal after 1033 K/2h showing recovery, partial recrystallisation and precipitation of carbides

It is evident that temperature exerts a pronounced effect on hardness reduction than the duration of treatment at any temperature. From the microstructural features and hardness profile, it is concluded that 873 K is not adequate for tempering.

Reduction in hardness after 2h of heat treatment at 973 K was also not substantial (339 VHN). However, the average hardness after 1 and 2h of treatment at 1033 K reduced to 298 and 272 VHN respectively. Supporting this data, the weld showed a well tempered martensitic structure after treatment for 2 h at 1033 K (**Fig.4.13 (d)**) as compared to 1 h (**Fig.4.13(c)**). Heat treatment of martensite resulted in a variety of microstructures and marked change in the microchemistry of the phases. Analysis of carbon extraction replicas showed that the number density of carbides did not change significantly after short durations of heat treatment. It is evident that the observed reduction in hardness is due to coarsening of the precipitates.

It is clear from **Fig.4.13 (d)** that 2 h of PWHT at 1033 K results in a well tempered structure with uniformly distributed precipitates as compared to treatments that carried out at low temperatures or short durations. The TEM micrograph in **Fig.4.13 (e)** confirms the formation of tempered martensite with low dislocation density and inter and intralath precipitates. Comparison of microstructure (**Fig.4.13 (d)**) and average hardness of the weld after PWHT at 1033 K for 1 and 2 h shows that microstructure and microhardness (272VHN) after PWHT for 2h compares well with the N & T steel and hence considered optimum. However, in actual industrial practice an intermediate time of 90 minutes is considered adequate based on toughness values [96].

Figure 4.14 (a) represents the hardness of the weld region as a function of time at each temperature. The observed exponential decrease with time is represented by the following Holloman – Jaffe parameter [160] combining the effect of temperature and time.

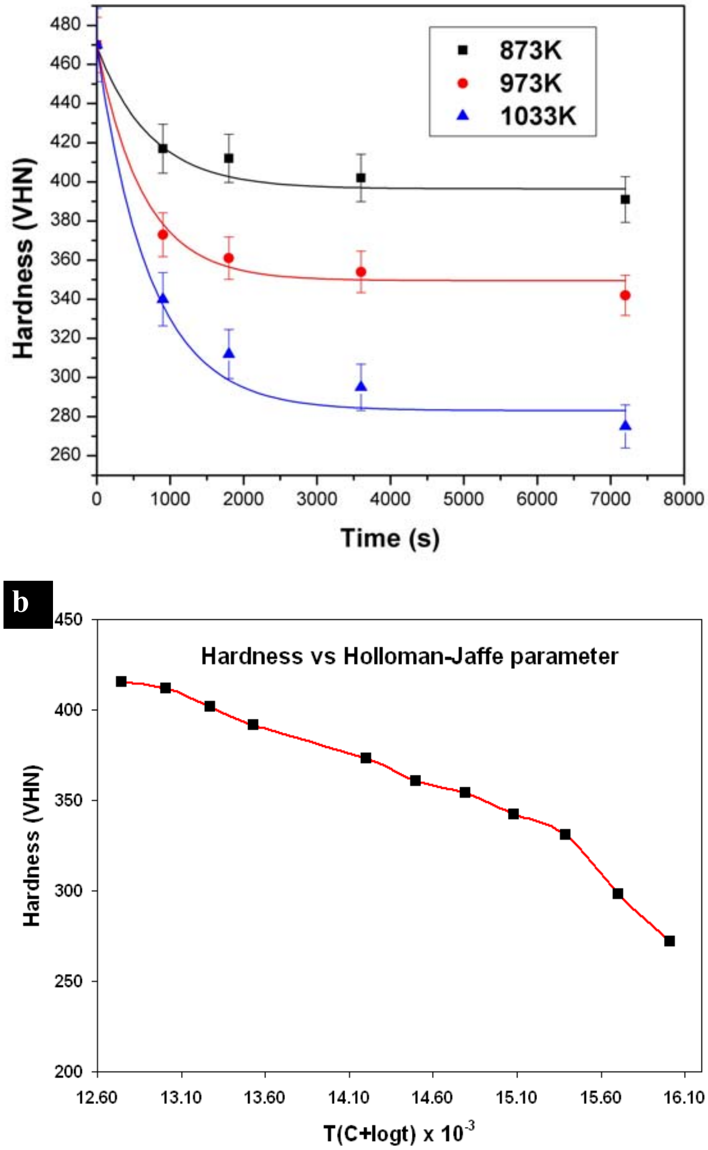

Fig.4.14: (a) Variation of hardness of weld zone (1W RAFM) with time and temperature (b) Hardness vs Holloman-Jaffe parameter: T- temperature in K and t- time in h

$$P = H = T\,(C + \log t) \tag{4.4}$$

where P is Holloman- Jaffe parameter, H is Hardness value (VHN), T is Temperature (K), t is Time (h) and C is a constant which depends on the composition of the steel and thermal history. From **Eq. (4.4)**, it is possible to obtain the same value of hardness by appropriate selection of tempering temperature and time. The value of C has been evaluated as 15.2 by an appropriate combination of temperature and time of tempering. A plot of hardness vs Holloman – Jaffe parameter is given in **Fig.4.14 (b)**.

4.2.2. Kinetics of Tempering of Martensite

The kinetics of tempering has been studied by monitoring the temperature dependence of a kinetic parameter, in this case the rate of change in hardness of the weld. The rapid reduction in initial hardness in 1W steel (**Fig.4.14 (a)**) followed by saturation confirms that major part of tempering occurs within the initial few minutes and thereafter, recovery is sluggish. Hence, recovery rate is calculated from the slope of the initial segment of the curve for each temperature. **Figure 4.15** shows the plot of ln (ΔVHN/Δt) as a function of 1/T. The linear behavior with a negative slope suggests that the process follows an Arrhenius behavior. The activation energy estimated from the slope is 0.65 eV. This value is comparable to the activation energy for interstitial diffusion of carbon in α-ferrite [161] which is ~0.80 eV. The lower value of activation energy of carbon diffusion in the present study is attributed to the high defect density associated with martensite which formed at a high cooling rate as compared to annealed ferrite matrix. This confirms that the interstitial diffusion of carbon in α-ferrite is the rate controlling step in the tempering process [162].

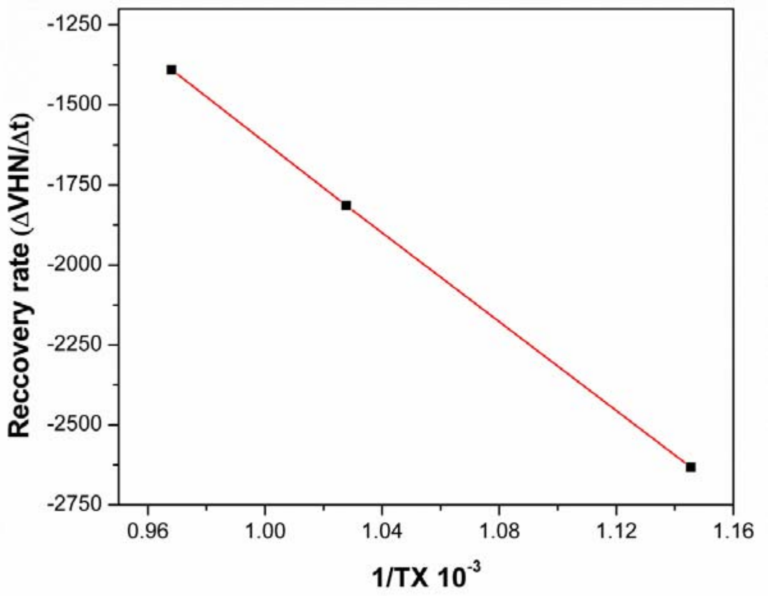

Fig.4.15: Arrhenius plot of the rate of recovery of weld region of 1W RAFM steel

4.2.3. Microstructural changes during PWHT in EB and LB weldment

In the previous section, an optimum temperature (1033 K) of PWHT was arrived at, based on the microstructural and hardness changes. Considering the lower thickness (6mm) of the plate used in EB and LB welding, a PWHT at 1033 K for 1h was carried out and the microstructural changes in the EB/LB weldment is described in this section.

The microstructural variations in three different regions of EB weld (INRAFM) namely weld metal, CGHAZ and FGHAZ has been discussed in detail. The hardness profiles of the EB weld joints of INRAFM subjected to PWHT treatment for 1h at 1033 K is shown in **Fig.4.8 (d)**. The weld metal showed an average hardness of 475VHN which reduced to 300VHN after PWHT. SEM micrographs from different regions of EB weldment in PWHT condition are shown in **Fig.4.16 (a-d)**. The fully martensitic structure of weld (**Fig.4.9 (a and b)**) shows considerable extent of tempering (**Fig.4.16 (a and b)**), within the columnar prior austenite grains. The martensitic CGHAZ (**Fig.4.9 (e)**) with few

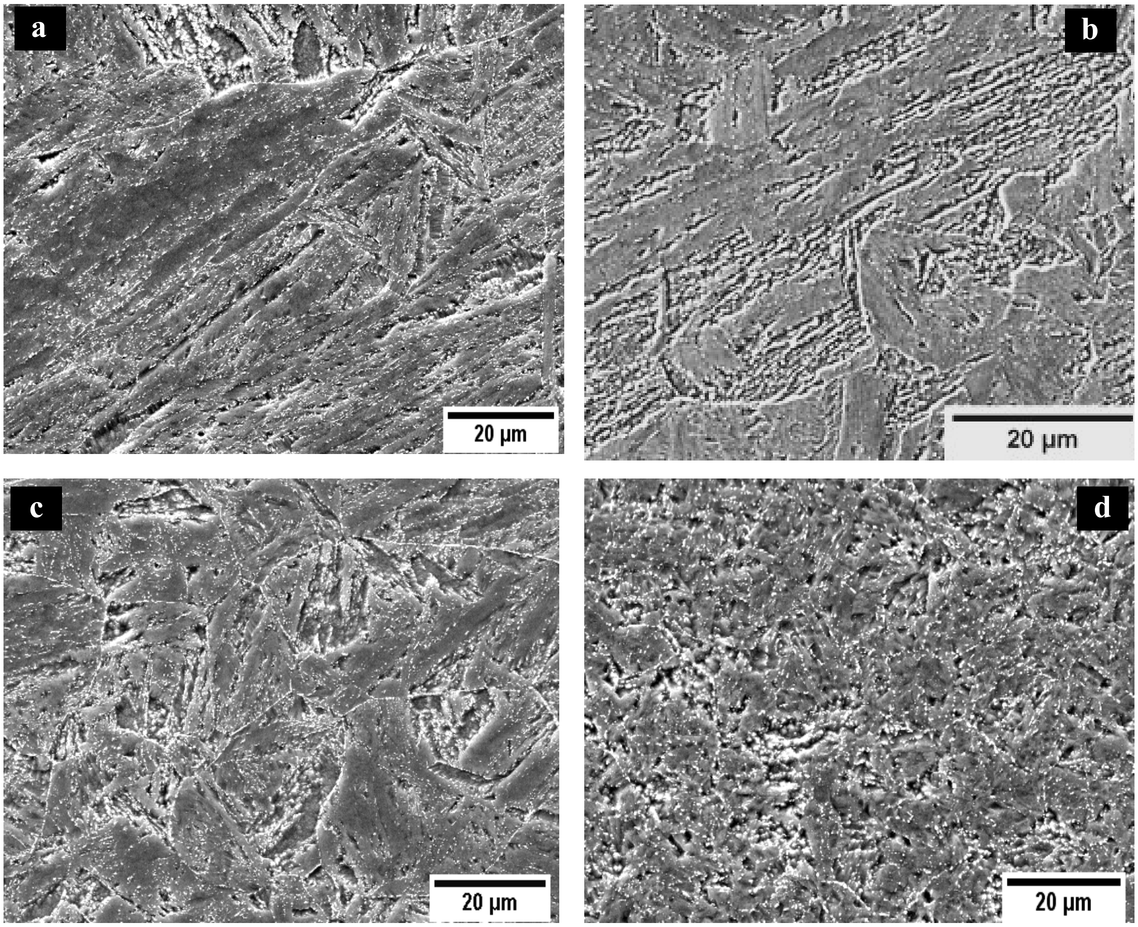

Fig.4.16: Microstructural changes in the various regions of INRAFM EB/LB weldment after PWHT (a&b) tempered martensite structure retaining the columnar morphology in weld metal of EB and LB weld (c) well defined tempered martensite structure in CGHAZ and (d) tempered ICHAZ with high amount of precipitation

undissolved carbides, transformed to tempered martensite with grain boundaries decorated by carbides (**Fig.4.16 (b)**). The ICHAZ, which showed a mixed microstructure consisting of martensite and tempered martensite in as-welded condition, shows a high amount of precipitation on PWHT. In order to understand the extent of tempering, TEM analysis on thin foils was carried out on fusion zone. **Figure 4.17 (a and b)** shows the bright field and dark field image respectively from INRAFM weld metal.

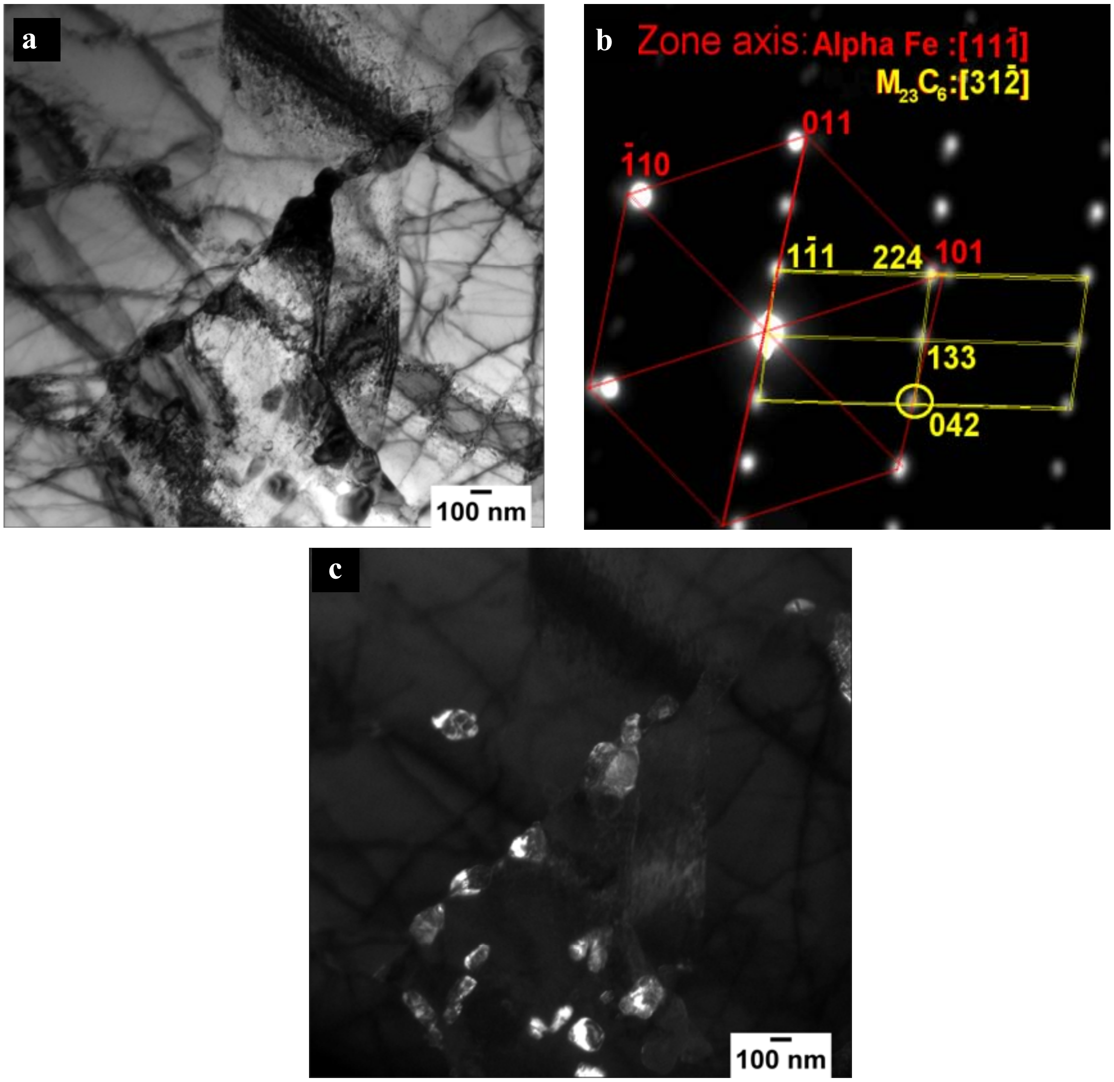

Fig.4.17: (a)TEM BF image from weld region EB weld joint showing $M_{23}C_6$ carbides (b) diffraction patterns from α-ferrite and $M_{23}C_6$ carbide along <11$\bar{1}$> and <31$\bar{2}$> zone axes respectively (c) DF image of the region in (a) using the reflection circled in (b)

Distribution of carbides along the prior austenite boundary and within the matrix is clearly seen in the dark field image. It is obvious that weld metal and HAZ have been suitably tempered and the microstructure is comparable to the one obtained after PWHT of 1033 K/2h (**Fig.4.13(d)**) in the case of 12 mm TIG welds. LB welds also exhibited a similar behavior. Based on the hardness value of weld region (250-270VHN) and the microstructures it is confirmed that a PWHT for 1h at 1033 K is adequate for 6 mm thick EB and LB welded joints.

4.3 Correlation of HAZ microstructures in INRAFM steel weld by GLEEBLE simulation

The HAZ microstructures in the previous sections, have established that there is a wide variation within this narrow zone. Hence, different zones of the HAZ were simulated specifically using GLEEBLE weld simulator as described in **Section 2.1.3** of **Chapter 2.** **Figure 4.18** gives the different thermal cycles imposed on the specimens along with the temperatures recorded by an external thermocouple attached to the specimen. Temperatures have been selected taking into account the expected increase in transformation temperatures with high heating rate experienced in welding. Microstructural examination and hardness measurements were carried out in these specimens both in the as-simulated condition and after a heat treatment is equivalent to PWHT of the weldment.

Figure 4.19 gives the hardness profile of the simulated INRAFM steel specimens as a function of distance from the centre. The measured average peak hardness at 1173 K is 280 VHN corresponds to the hardness expected in the inter-critical region of the HAZ in a weld joint and shows a small increase as compared to base metal. For the other peak temperatures of simulation the average hardness is typically above 400 VHN which corresponds to the values expected for a martensitic structure. It is observed that as the peak temperature increases the width of the zone exhibiting high hardness corresponding to the martensitic microstructure also increases, since large section of the specimen witness temperatures above Ac_3 and results in transformation to martensite during

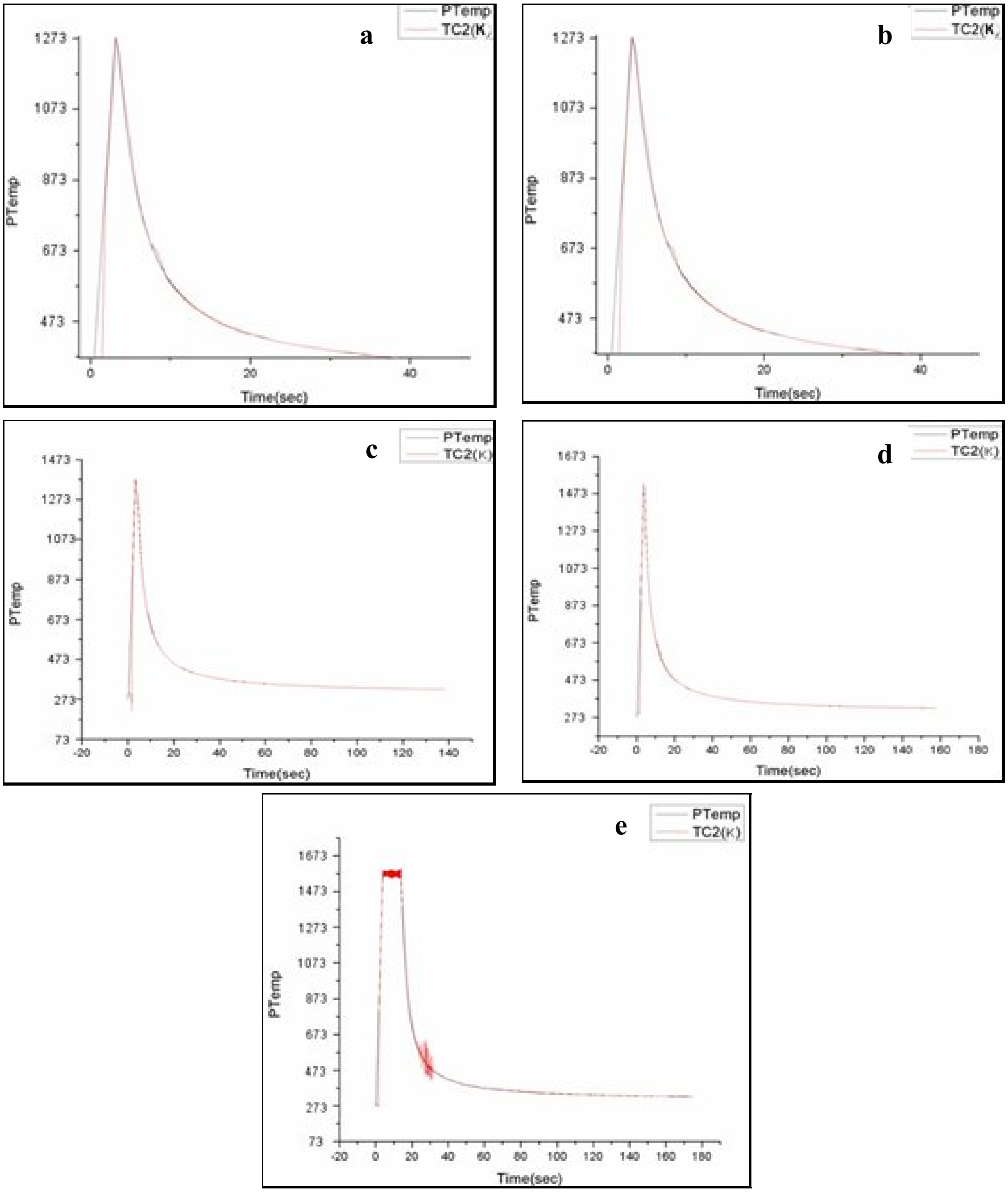

Fig.4.18: Different thermal cycles imposed on INRAFM steel (holding time in brackets) (a) 1173 K (0.33s), (b) 1273 K (0.66s), (c) 1373 K(1s) (d) 1523 K (1.5s) and (e) 1573 K (10s).

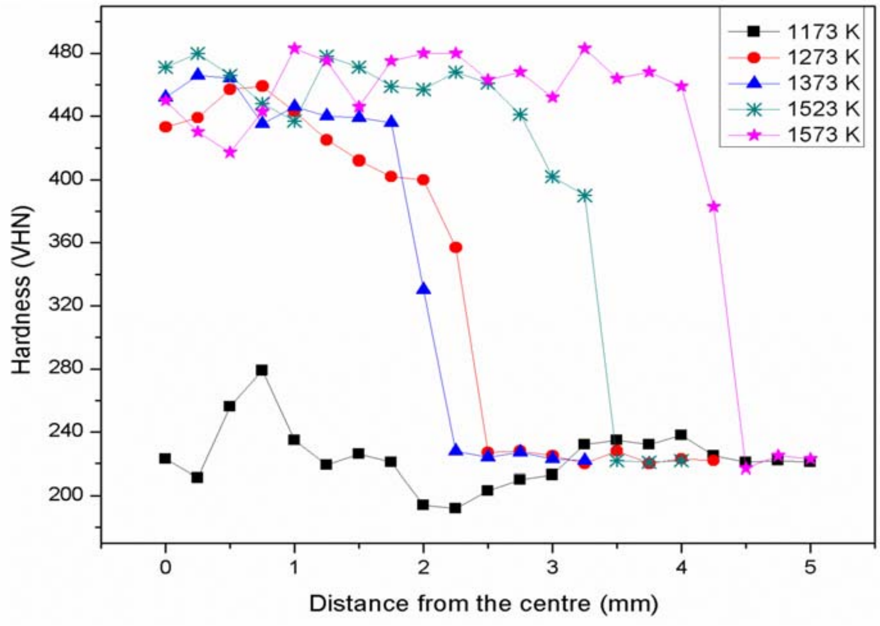

Fig.4.19: Hardness profile across the GLEEBLE tested INRAFM steel specimens.

cooling. For the microstructural studies the centre region of the specimen at a distance of 1.5 mm on either side of the location where the thermocouple was fitted was considered. The micrographs of the INRAFM steel GLEEBLE simulated at 1173, 1273 and 1523 K before and after PWHT are shown in **Fig. 4.20**. The peak hardness of ~ 280VHN, which is higher than that of the base metal, but considerably lower than that of martensite, is in agreement with the observed mixed microstructure at 1173 K. This region can be taken as a true representative structure of ICHAZ, which is hard to obtain in an actual weld, since it is difficult to differentiate ICHAZ from FGHAZ.

SEM micrograph of the specimen simulated at 1273 K is shown in **Fig.4.20(c)**. Martensitic structure with fine re-austenitized grains and undissolved carbides seen in **Fig. 4.20(c)** confirms that this structure corresponds to FGHAZ, while **Fig. 4.20(d)** reveals a microstructure typical of tempered structure after PWHT.

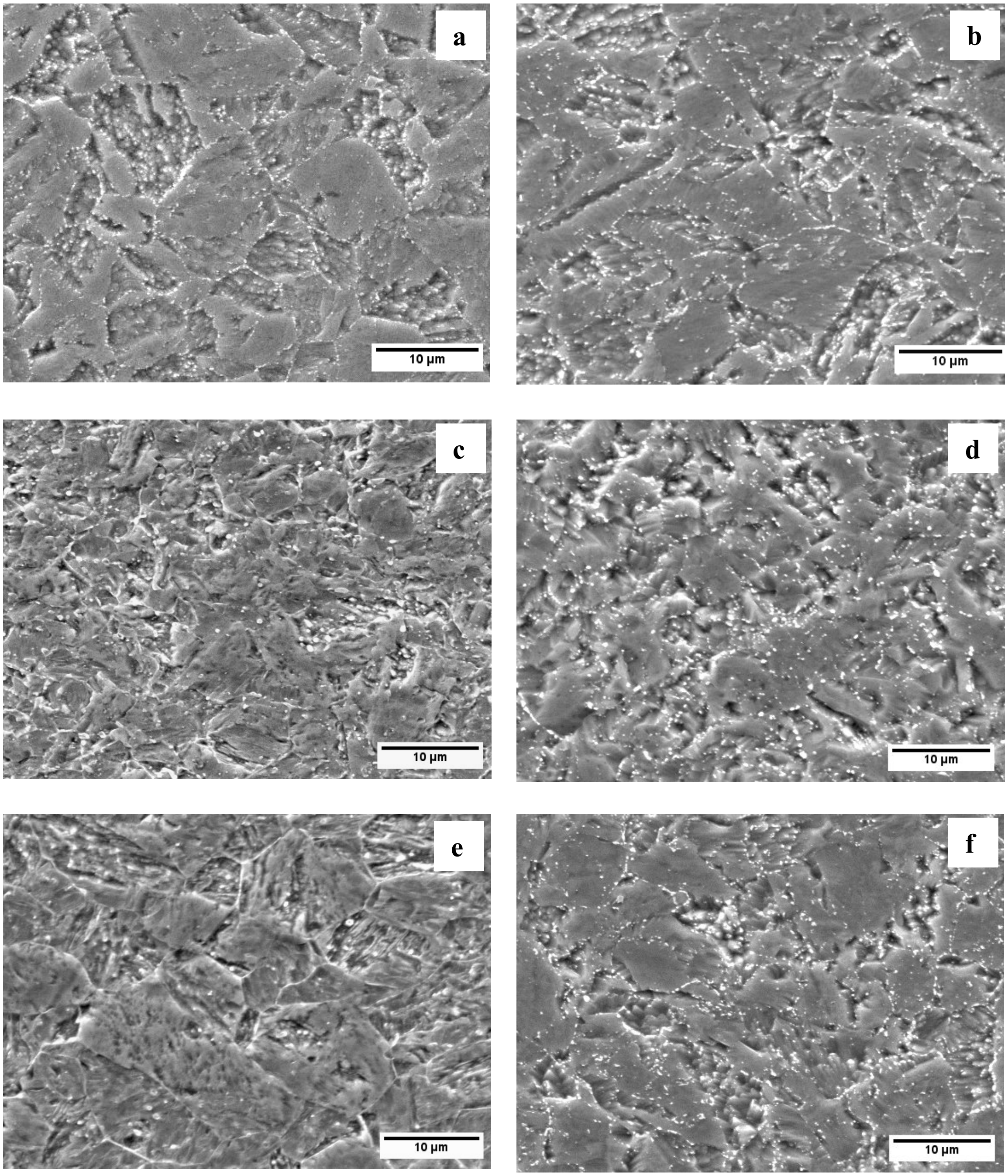

Fig.4.20: SEM micrographs of GLEEBLE simulated INRAFM steel showing martensite and tempered martensite before and after PWHT at peak temperatures of (a & b) 1173 K, (c &d) 1273 K and (e & f) 1523 K

Figure 4.20 (e and f) shows the SEM micrograph corresponding to simulation at 1523 K and after PWHT respectively. A complete martensitic structure with coarse PAGS is evident from the micrograph. It is obvious that this microstructure corresponds to the CGHAZ region referred in **Section 4.1.1**. The FGHAZ and CGHAZ show similar features except for the difference in grain size. **Figure 4.21 (a)** shows the SEM micrograph from the specimen simulated at 1573 K with the highest holding time. The microstructure was found to be significantly different from the other simulated specimens. A complete martensitic structure with large PAGS along with islands corresponding to δ- ferrite was observed. **Figure 4.21 (b)** shows that the traces of δ-ferrite are not affected by PWHT. It is to be mentioned that this experiment was carried out to know the possibility of formation of δ- ferrite by holding at 1573 K for longer duration of 10s. In actual welding the holding time would be shorter, with a lesser probability for δ- ferrite formation.

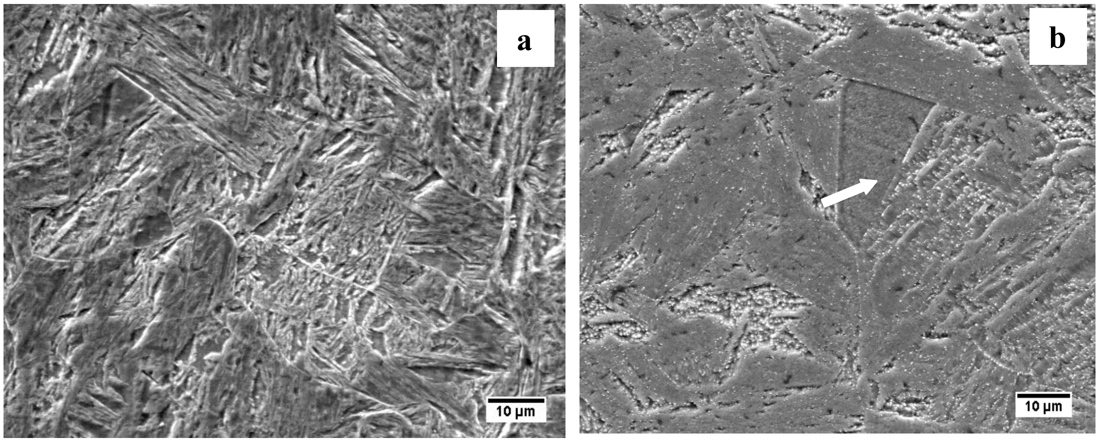

Fig.4.21: SEM micrograph of simulated (1573 K) INRAFM steel showing (a) martensite, traces of carbides and δ- ferrite grains before PWHT (b) tempered martensite and δ- ferrite grains (arrow marked) without any precipitate after PWHT

It is likely that the presence of δ-ferrite was not observed in the actual weld analysis (section 4.1) for this reason. XRD results of all simulated HAZ s are shown in **Fig.4.22**. No evidence for retained austenite was obtained.

The TEM micrograph of the 1173 K simulated specimen is given in **Fig.4.23 (a)**. The presence of ferrite with a low density of dislocations and carbides apart from lath martensite is evident. This confirms the presence of two phase structure typical of the inter-critical region as observed in the SEM micrograph (**Fig.4.20 (a)**). The TEM micrograph for the peak temperature simulation of 1173 K followed by PWHT is shown **Fig.4.23 (b)**. It clearly shows the tempered martensite with recrystallised ferrite grains with varying dislocation and carbide densities. These two distinct regions are magnified and shown in **Fig.4.23 (c)** and **(d)** respectively. The tempered martensite that formed

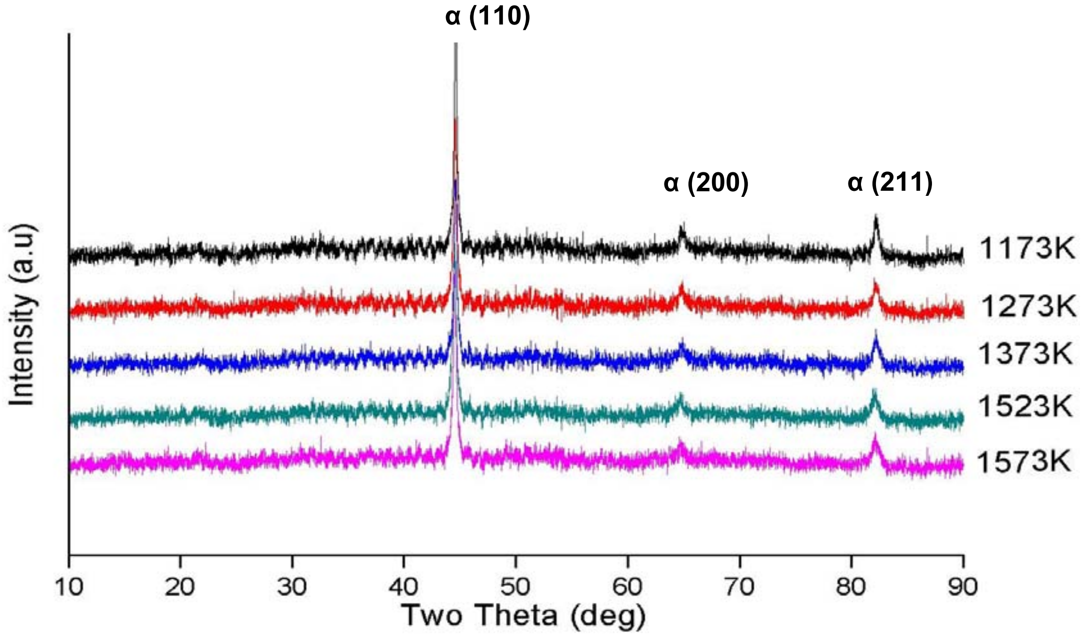

Fig.4.22: X-ray diffraction patterns of simulated INRAFM steel showing no evidence for retained austenite

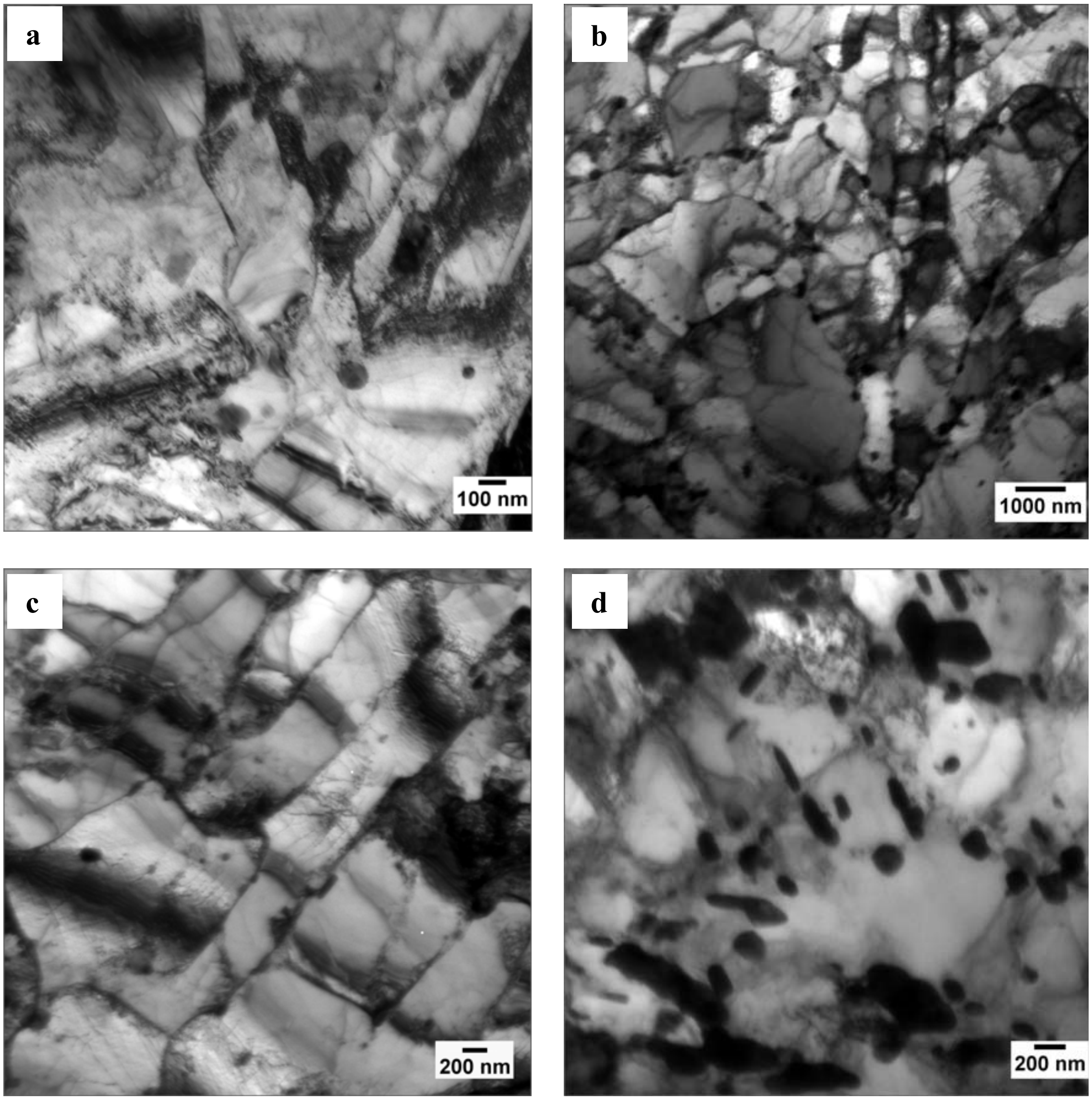

Fig.4.23: TEM micrograph from GLEEBLE simulated (1173 K) INRAM steel showing (a) lath martensite and tempered ferrite, before PWHT b) lath structure of tempered martensite over large regions after PWHT, (c) recrystallized ferrite grains with (d) low dislocation density and high density of carbides

from the martensite region formed during simulation at 1173 K is seen to retain its lath structure (**Fig.4.23(c)**) with carbides in these regions being fine sized in contrast to the coarse (>250 nm) carbides in the other region, where there was no transformation to austenite during thermal cycling (**Fig.4.23(d)**).

Figure 4.24 (a and b) shows TEM bright field images from the HAZ specimen simulated at 1523 K. A complete martensitic structure is observed with no carbides, which correlates with CGHAZ. However in a few regions, traces of undissolved carbides, is observed.

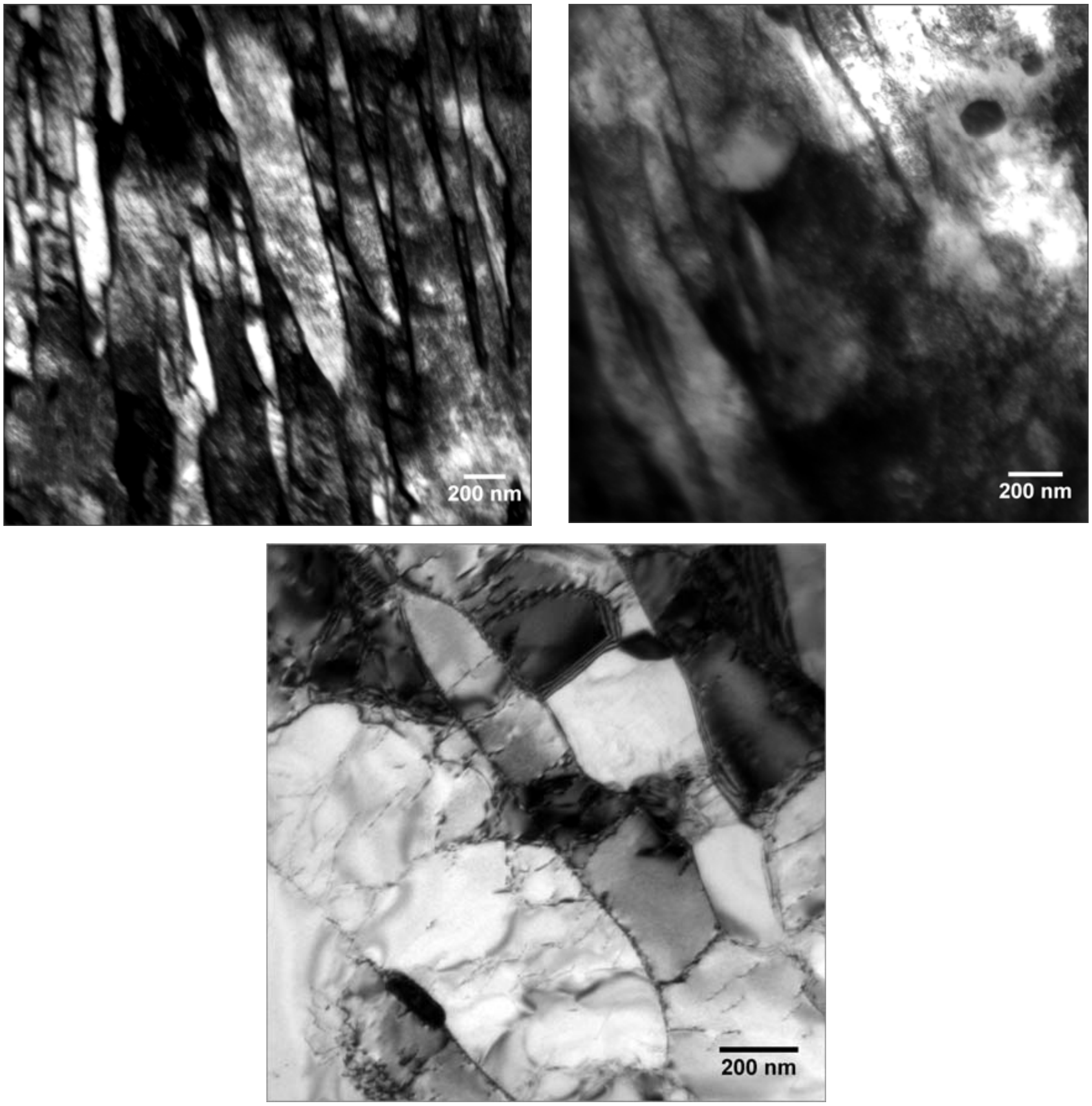

Fig.4.24: Simulated microstructures of INRAM steel showing (a) complete martensitic structure (b) lath martensite along with few undissolved carbides in simulated HAZ at 1573 K (c) tempered martensite containing carbides but retained lath structure along with dislocations in 1573 K simulation after PWHT.

The presence of carbides after exposure at 1173 K indicates that these are primary MX carbides that remain undissolved during austenitisation. In a calorimetric study of INRAFM steel, the complete dissolution of $M_{23}C_6$ and MX carbides at 1342 K and 1563 K respectively is reported [112]. The initiation of δ-ferrite formation at 1494 K is also reported. The presence of δ-ferrite (**Fig.4.21**) in INRAFM steel at 1573 K is in agreement with this. **Figure 4.24 (c)** shows a typical tempered martensitic structure obtained by PWHT of the simulated HAZ at 1573 K.

4.4 Microstructural evolution in TIG weldments of RAFM steels

PWHT is recommended for ferritic - martensitic steel weld joints in various codes and standards. However, fabrication of TBM also considers joining of RAFM steel with austenitic stainless steels using EB or Laser welding processes and for such joints PWHT may be an option. In such situations, microstructural evolution in weld joints in 'as welded' condition becomes relevant during prolonged service exposure. There are also reports of embrittlement in the vicinity of 823 K in similar joints of ferritic-martensitic steels [78, 150] which needs to be examined. Accordingly, bead-on-plate welds of both 1W and INRAFM steels produced by autogenous TIG processes were subjected to aging at 773 and 823 K for different durations and microstructural evolution in the fusion zone and different parts of the HAZ was studied. Results of this study are presented here.

The micro hardness profile of the weldment of 1W steel after aging at different temperatures and time durations is shown in **Fig.4.25**. As expected, the hardness decreased in weld and HAZ regions. However, the dip in hardness to values lower than base metal, seen in ICHAZ after PWHT is not observed when the weld is directly aged.

The equilibrium phases that formed in 1W and INRAFM steel have also been predicted by thermodynamic computations using Gibb's energy minimization routines. The sequence of evolution of secondary phases as a consequence of thermal aging at 773, 823 and 873 K for durations in the range of 1-10000 h has been computed using JMatPro. The computation predicts the type and fraction of the different phases that form as a function of aging time at different temperatures. Experimentally, the volume fraction, type and chemistry of the precipitates from different regions of the weldment have been estimated by TEM analysis on carbon extraction replica. Microstructural and microchemical changes that occur on aging are dealt in sequence in the following sections.

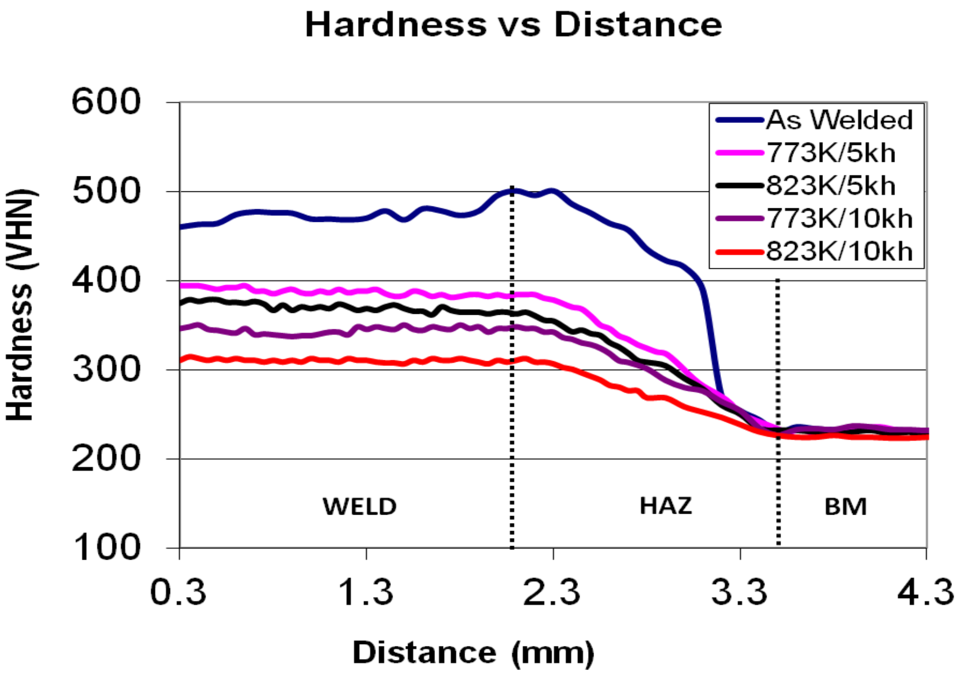

Fig.4.25: Microhardness profile of 1W RAFM steel weldment after prolonged aging

4.4.1. Computation of equilibrium phases in weld metal on thermal exposures

The type and weight percentage of the different phases that form as a function of aging time at different temperatures has been predicted using JMatPro software. The computed sequence of precipitation of secondary phases in the weld metal of 1W and INRAFM steels as a function of aging temperature for various durations is listed in **Table 4.2**.

Table 4.2: Summary of computational results showing the differences in the precipitation sequence of secondary phases in the weld metal of RAFM steels after thermal aging

Aging time (h)	1W RAFM			INRAFM		
	773 K	823 K	873 K	773 K	823 K	873 K
1	M_7C_3, $M_{23}C_6$, M_2X	$M_{23}C_6$, M_2X	$M_{23}C_6$, M_2X	M_7C_3, $M_{23}C_6$, M_2X, M_3C	$M_{23}C_6$, M_2X, M_7C_3	$M_{23}C_6$, M_2X
2	M_7C_3, $M_{23}C_6$, M_2X	$M_{23}C_6$, M_2X	$M_{23}C_6$, M_2X	M_7C_3, M_2X, $M_{23}C_6$	$M_{23}C_6$, M_2X	$M_{23}C_6$, M_2X
10	$M_{23}C_6$, M_2X	$M_{23}C_6$, M_2X	$M_{23}C_6$, M_2X	M_7C_3, M_2X, $M_{23}C_6$	$M_{23}C_6$, M_2X	$M_{23}C_6$, M_2X
100	$M_{23}C_6$, M_2X	$M_{23}C_6$, M_2X	$M_{23}C_6$, M_2X	M_7C_3, M_2X, $M_{23}C_6$	$M_{23}C_6$, M_2X	$M_{23}C_6$, MX, M_2X
1000	$M_{23}C_6$, M_2X	$M_{23}C_6$, M_2X	$M_{23}C_6$, M_2X, MX	$M_{23}C_6$, M_2X, M_7C_3	$M_{23}C_6$, M_2X	$M_{23}C_6$, Laves, MX, M_2X
5000	$M_{23}C_6$, M_2X	$M_{23}C_6$, M_2X, Laves	$M_{23}C_6$, Laves, M_2X, MX	$M_{23}C_6$, M_7C_3, M_2X	$M_{23}C_6$, Laves, M_2X	$M_{23}C_6$, Laves, MX, M_2X
10000	$M_{23}C_6$, M_2X	$M_{23}C_6$, Laves, M_2X	$M_{23}C_6$, Laves, M_2X, MX	$M_{23}C_6$, M_7C_3, M_2X	$M_{23}C_6$, Laves, M_2X	$M_{23}C_6$, Laves, MX, M_2X

Computation predicts several types of carbides namely M_7C_3, $M_{23}C_6$, M_2X, M_3C and Laves phase in the weld region. Computation of precipitate size of $M_{23}C_6$ and MX as a function of aging time and duration is already shown in **Fig.3.19**. It is predicted that$M_{23}C_6$ grows to a size of 100 and 200 nm after aging for 10000 h at 773 and 823 K respectively. In contrast to this, MX attains saturation of < 20 nm during very early stages of aging and remained unchanged even after 10000 h, due to coherency with ferrite matrix. The computed weight fraction of carbides in base metal and aged weld metal is compared in **Table 4.3.** The amount of carbides computed in aged base metal and weld metal was found to increase with temperature of aging but no increase is observed beyond 5000 h of aging. This suggests that coarsening of carbides dominates over the fresh nucleation of carbides beyond 5000h of thermal exposure.

Table 4.3: Computed amount of carbides (in weight %) in base metal and weld metal

1W steel		**773 K**		**823 K**	
		$M_{23}C_6$	MX	$M_{23}C_6$	MX
BASE METAL	1 h	0.245	-	1.525	-
	5 kh	1.676	0.068	1.708	0.078
	10 kh	1.676	0.068	1.708	0.078
WELD METAL	1 h	0.066	-	0.308	-
	5 kh	0.336	-	0.334	-
	10 kh	0.336	-	0.334	-
INRAFM steel					
BASE METAL	1 h	0.378	-	2.355	-
	5 kh	2.706	0.080	2.703	0.086
	10 kh	2.706	0.080	2.703	0.086
WELD METAL	1 h	0.025	-	0.48	-
	5 kh	0.308	-	0.5	-
	10 kh	0.308	-	0.5	-

Important inferences drawn from the computations in the weld and HAZ as compared to the base metal are as follows:

- Volume fraction of all secondary phases was lower.
- Formation of MX carbides was predicted only at high temperature of 873 K beyond 1000h of thermal exposure.
- M_3C carbides formed only in INRAFM steel for 1h of exposure at 773 K.

Laves phase precipitation was delayed in both the steels. Time required for its precipitation in INRAFM steel was found to be ≥ 5000h at 823 K and ≥1000 h at 873 K. For the same temperature-time combination laves phase volume fraction was relatively high in INRAFM as compared to 1W steel.

4.4.2. Microstructural evolution and microchemical changes during long term exposures

The hardness (macro) changes in weld metal as a function of aging time are plotted in **Fig.4.26**. The high carbon content in solution due to complete dissolution of carbides is reflected in the high initial values, but a pronounced decrease in hardness is observed as aging proceeds. In order to study the microstructural evolution of weld metal, extensive transmission microscopy studies were carried out on steels exposed to 773 and 823 K up to 10000h.

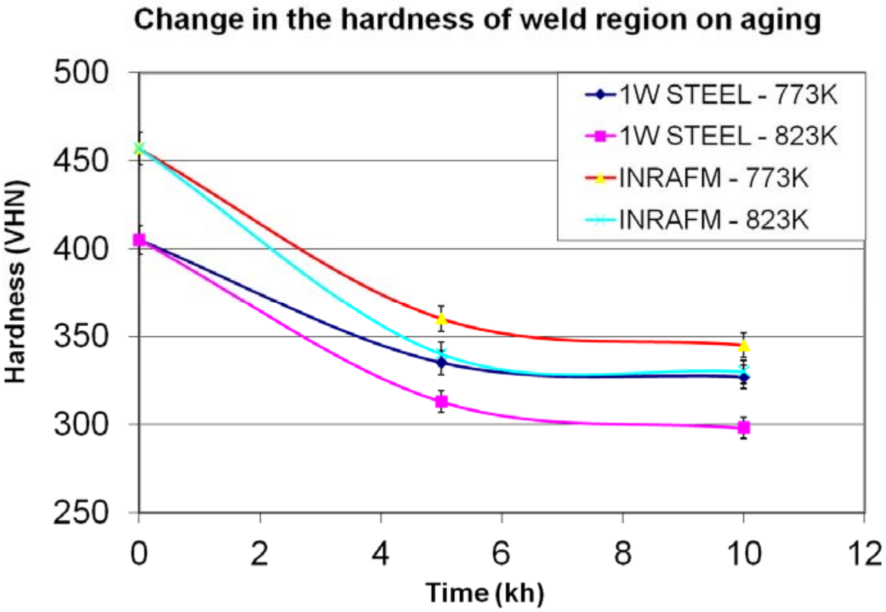

Fig.4.26: Change in hardness in the weld metal of 1W and INRAFM steel after aging at 773 and 823 K

The microstructural details of INRAFM weld metal after aging at 773 K for 5000 h and 823 K for 10000 h are shown in **Fig.4.27**. Two types of $M_{23}C_6$ carbides with distinct size and shape were observed. The very fine needle shaped carbides (circled in **Fig.4.27 (a)**) with a width of 10-15nm on exposure of weld at 773 K is unusual. These carbides have formed during aging as they were not observed in the as-welded condition. These were aligned in two perpendicular directions and had higher Cr contents of about 80wt. % as compared to other coarse carbides, which had only 60-65 wt. % Cr. This needle shaped carbides maintained their size and chemistry even after 10000h of aging. It is known that the Fe rich ($M_{23}C_6$, Epsilon-ε) carbides and Cr rich M_2X (hcp) form in the early stages [23, 79, 163] of tempering, (or lower temperature) of 9Cr steels, which subsequently transform to Cr rich $M_{23}C_6$ as tempering proceeds [164]. **Fig.4.27 (b and c)** shows the micrographs from weld metal of INRAFM steel aged at 823 K for 5000 h and 10000 h respectively. Coarsening of carbides is evident and it is found that carbides have coarsened up to a size of ~300 nm, although the average size remained at about 180 nm. The average Cr content in the carbides was found to be comparable to that of aged base metal. No evidence for MX carbides was observed in the aged steel. It has been reported by other researchers that exposure to 773-873 K is insufficient for the precipitation of MX from martensite [156].

In addition to the two types of $M_{23}C_6$ carbides, fine nano sized particles could be observed in the proximity of coarse carbides in the weld region after aging at 823 K for10000 h. SAD pattern taken from these particles is shown in the inset of **Fig.4.27(c)**. Analysis of the pattern shows that, it corresponds to the Laves phase of Fe_2W type, which was also observed in the base metal after aging at 823 K for 5000 h.

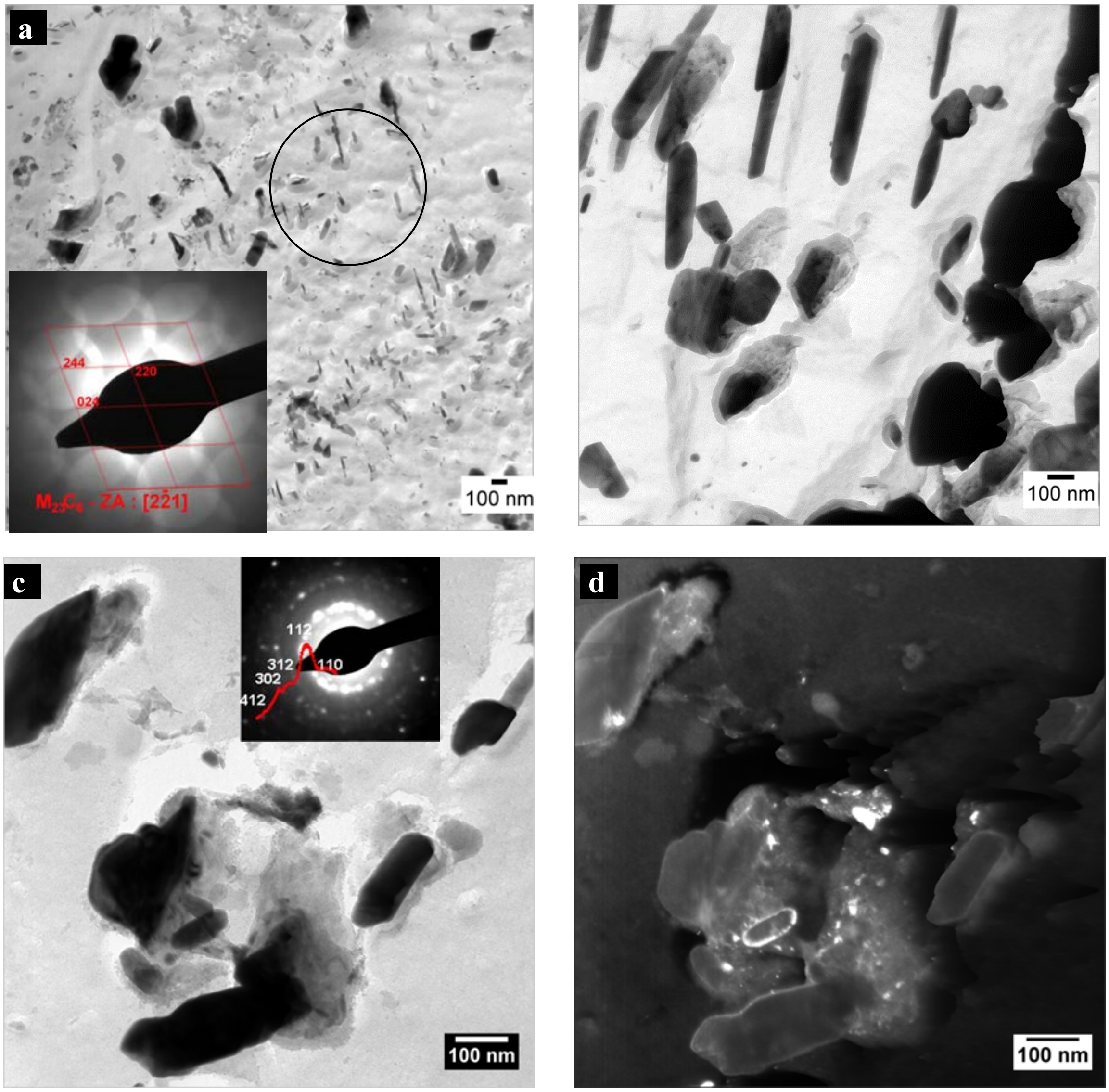

Fig:4.27: Microstructure of weld metal of INRAFM steel, (a) Presence of fine needle type precipitates, after aging at 773 K for 5000 h (inset – micro diffraction pattern from fine $M_{23}C_6$ taken along $\langle 2\bar{2}1 \rangle$) (b) Coarsened spheroidal and lenticular carbides along prior austenite boundaries and lath boundaries respectively after aging at 823 K for 5000h (c) Bright field image of coarse $M_{23}C_6$ carbides after aging at 823 K for 10000 h (inset -Diffraction pattern from nanocrystalline laves phase, super imposing the radial intensity profile) (d) Dark field image of Laves phase surrounding a coarse carbide, using one of the (112) reflections in the diffraction pattern in (c)

The spotty rings in the pattern show that these particles are very fine in size. Dark field image taken with one of the (112) reflections, given in **Fig.4.27 (d)** reveals its size, location and distribution. The delay in appearance of Laves phase in the weld metal as compared to the base metal is attributed to the initial carbide free martensite structure and the slow consumption of carbon as tempering/ aging proceeds at temperatures lower than the peak tempering temperature. The observed sharp increase in the volume fraction as well as the size of the carbide could be due to the nucleation and growth of Laves phase in the vicinity of $M_{23}C_6$ carbide.

4.4.3 Evolution of microstructure in Heat Affected Zones of 1W and INRAFM steels

The heat affected zone in the 'as welded' condition consisted of two regions namely precipitate free CGHAZ (except a few undissolved pre-existing fine MX carbides) and FGHAZ with precipitates. JMatPro computations carried out for CGHAZ showed analogous behavior as that of the weld metal due to similarity in thermal cycle and is not discussed any further. **Figure 4.28 (a)** shows low magnification micrograph of carbon extraction replica taken from CGHAZ region of INRAFM steel aged at 823 K for 10000 h. Image analysis showed a high amount of precipitates in the CGHAZ of INRAFM steel after aging at 823 K for 10000 h. **Fig.4.28 (b and c)** shows high magnification micrographs of aged CGHAZ (773 K for 5000 h) for both the steels. Diffraction and EDS studies showed that aging at 773 K for 5000 h did not result in any new phase in both the steels except coarsening of existing precipitates. Traces of MX precipitates could only be seen in CGHAZ as compared to FGHAZ. This could be due to only near complete dissolution of MX during welding at high temperatures experienced by the region while aging at 773-823 K is insufficient for the precipitation of this phase.

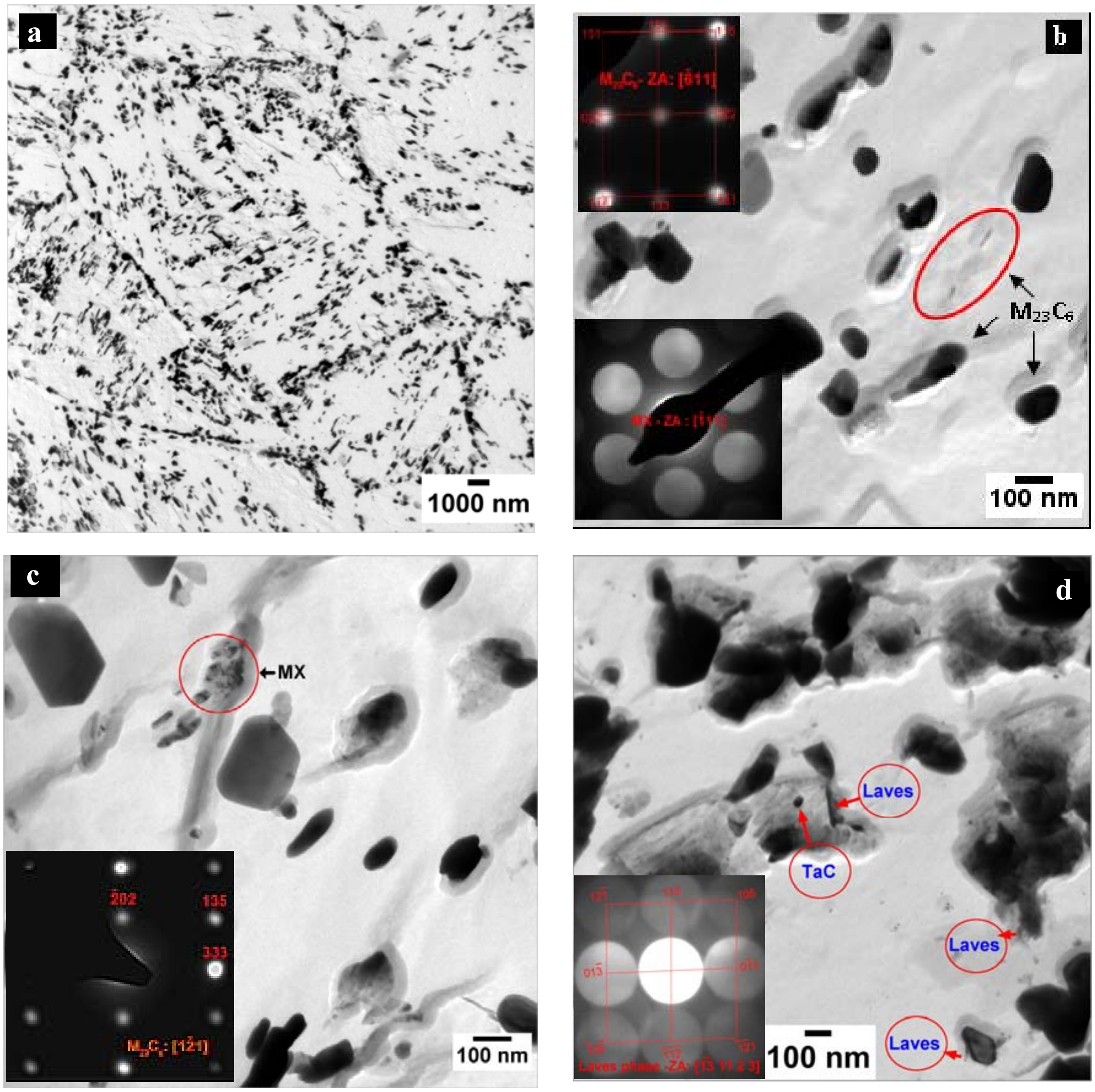

Fig.4.28: Microstructural features of CGHAZ region after aging (a) Low magnification micrograph showing high density of precipitation in INRAFM steel, after aging at 823 K/10000 h (b and c) Coarse and fine needle shaped $M_{23}C_6$ precipitates and fine MX after aging at 773 K/5000h in 1W RAFM steel and INRAFM steel respectively, (inset-(b) diffraction pattern from $M_{23}C_6$ and MX taken along zone axis $<\bar{6}11>$ and $<\bar{1}11>$ respectively and (c) SAD from $M_{23}C_6$ along $<1\bar{2}1>$) (d) Precipitation of Laves phase in INRAFM steel after 823 K/10000 h aging (inset-SAD from Laves phase along $<\bar{1}3\ 11\ 23>$

Needle shaped $M_{23}C_6$ precipitates (marked in **Fig.4.28 (b)**) were observed in CGHAZ regions of both the steels after aging at 773 K. It is worth mentioning that in 'as welded' condition CGHAZ showed a very low density of carbides (**Fig.4.4c**), similar to weld metal. So the presence of needle shaped Cr rich precipitates could be due to the reasons explained in the previous section.

Figure 4.28 (d) gives the microstructural details in CGHAZ region of INRAFM steel after aging at 823 K for 10000 h. Fine particles of Laves phase (diffraction pattern is given as inset to **Fig.4.28 (d)**) could be identified adjacent to coarser carbides in this region.

Precipitation sequence and size of the secondary phases in FGHAZ were similar to that of the base metal (**Table 3.2** and **Fig.3.10**) in both the steels, but volume fraction of the $M_{23}C_6$ carbides was found to be highest among all the other regions after aging. **Figure 4.29 (a)** shows carbon extraction micrograph from FGHAZ region of 1W RAFM steel. This region showed a high amount of MX precipitate in comparison with CGHAZ after aging. Temperature (~1050 K) experienced by this region at the time of welding could have favored the nucleation of MX. Further aging is expected to aid in the growth of already nucleated MX carbides. Coarsening of $M_{23}C_6$ carbide was found to be highest (350-400 nm) in FGHAZ after aging at 823 K for 10000 h.

Figures 4.29 (b) and (d) show extraction replica micrographs from FGHAZ region of INRAFM steel aged at 823 K for 5000 h and 10000 h respectively. Laves phase could be identified by its unique chemistry Fe_2W (EDS from Laves phase is shown as **Fig.4.29 (c)** as well as diffraction analysis (inset of **Fig.4.29 (b)**) in both the cases. Existence of independent grains of Laves phase other than the ones attached to carbides could be observed at the lath boundaries of FGHAZ region of INRAFM steel after aging at 823 K for 10000 h. The Laves phase at 5000 h is found to be fine with an average size of 40 nm, whereas it was found to be coarse (~100 nm) after 10000 h of aging. On comparing the

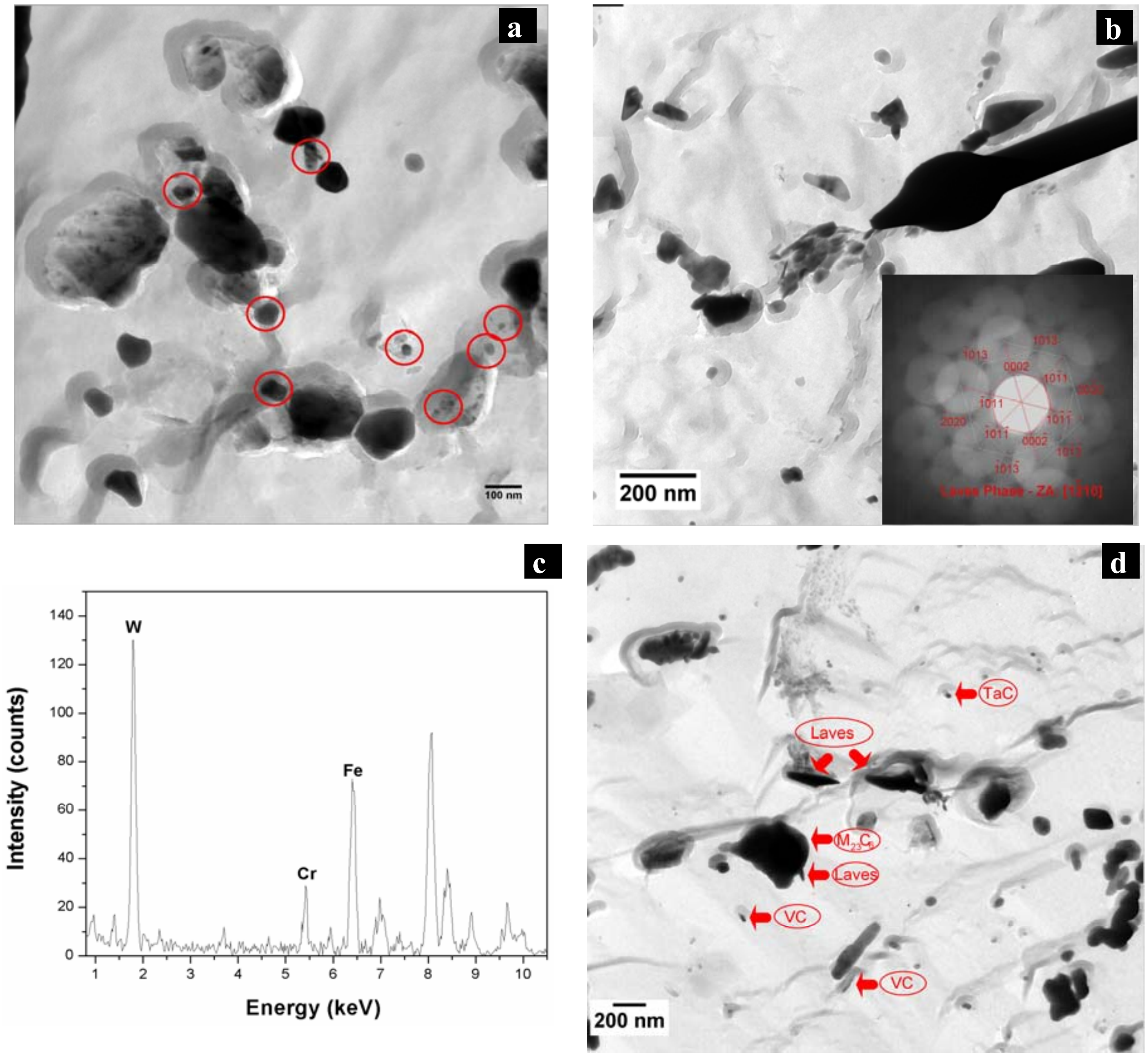

Fig.4.29: Microstructure of FGHAZ region in RAFM steels (a) Coarsened $M_{23}C_6$ carbides in 1W steel after 773 K/5Kh (fine MX precipitates circled) (b) Fine precipitates of Laves phase after aging at 823 K for 5000 h in INRAFM steel (c) EDX spectrum from Laves phase showing enrichment of W and Fe (d) coarse Laves phase after aging at 823 K for 10000 h.

size of Laves phase that formed in the base metal (**Fig.3.14**) and FGHAZ of INRAFM at 823 K/5kh, it can be deduced that Laves phase formed first at FGHAZ, but not so early as reported in F-82H steel [73], probably due to the presence of higher W and lower Ta content in the latter.

Ta in Cr-W-Fe system resists the formation and growth of Laves phase by retarding the growth of carbides resulting in stable lath boundaries which prevent release of W from the matrix [31, 165]. It is well known that the coarsening of carbides and formation of Laves phase is detrimental to fracture toughness [166-167]. Hence, it can be concluded that during thermal exposures at temperatures ≥ 823 K, FGHAZ is the weakest region in the weldment from microstructural point of view, which is in accordance with the reported creep failures in the HAZ region of similar steels [150]. No experimental evidence could be obtained for Laves phase in any region of 1W steel after aging at 823 K. The formation of Laves phase early in the HAZ of INRAFM steel during high temperature exposures in contrast to 1W steel is attributed to the higher W content in the steel and abundant precipitation of carbide which increases the availability of W and reduces the availability of supersaturated carbon in the adjacent regions.

Table 4.4 presents the summary of computational results corresponding to the FGHAZ of 1W and INRAFM steels after thermal aging for various durations. Though computations showed a relatively early onset of precipitation of Laves phase in both 1W and INRAFM steels on aging at 773 K, experimental evidence could not be obtained in both the steels, which could be due to kinetic reasons.

Table 4.4: Computational results showing differences in the precipitation sequence of secondary phases in aged FGHAZ of 1W and INRAFM steels

Aging time (h)	1W RAFM			INRAFM		
	773 K	823 K	873 K	773 K	823 K	873 K
1	M_7C_3, $M_{23}C_6$, M_3C, M_2X	$M_{23}C_6$, M_2X, M_7C_3	$M_{23}C_6$, M_2X	M_7C_3, M_3C, $M_{23}C_6$, M_2X	$M_{23}C_6$, M_2X	$M_{23}C_6$, M_2X
2	M_7C_3, $M_{23}C_6$, M_2X	$M_{23}C_6$, M_2X, M_7C_3	$M_{23}C_6$, M_2X	M_7C_3, $M_{23}C_6$, M_2X	$M_{23}C_6$, M_2X	$M_{23}C_6$, M_2X, MX
10	$M_{23}C_6$, M_2X	$M_{23}C_6$, M_2X	$M_{23}C_6$, M_2X, MX	$M_{23}C_6$, M_2X	$M_{23}C_6$, M_2X, MX	$M_{23}C_6$, MX
100	$M_{23}C_6$, M_2X	$M_{23}C_6$, MX	$M_{23}C_6$, MX	$M_{23}C_6$, M_2X, MX	$M_{23}C_6$, MX	$M_{23}C_6$, MX, Laves
1000	$M_{23}C_6$, MX	$M_{23}C_6$, MX, Laves	$M_{23}C_6$, MX, Laves	$M_{23}C_6$, MX	$M_{23}C_6$, MX, Laves	$M_{23}C_6$, MX, Laves
5000	$M_{23}C_6$, MX	$M_{23}C_6$, MX, Laves	$M_{23}C_6$, MX Laves,	$M_{23}C_6$, MX, Laves	$M_{23}C_6$, MX, Laves	$M_{23}C_6$, Laves, MX
10000	$M_{23}C_6$, MX, Laves	$M_{23}C_6$, MX Laves	$M_{23}C_6$, Laves, MX	$M_{23}C_6$, MX, Laves	$M_{23}C_6$, MX, Laves	$M_{23}C_6$, Laves, MX

4.4.4 Estimation of secondary phases across the weldment

The amount of extracted precipitates from various regions of the weldment as a function of time and temperature of aging, for both the steel is shown in **Fig.4.30**. From a large number of precipitates analyzed from extraction replica, only two types of precipitates namely $M_{23}C_6$ and MX have been identified experimentally. Computations predicted the existence of M_2X after 10000 h though the amount is very low (0.01-0.05%). Diffraction

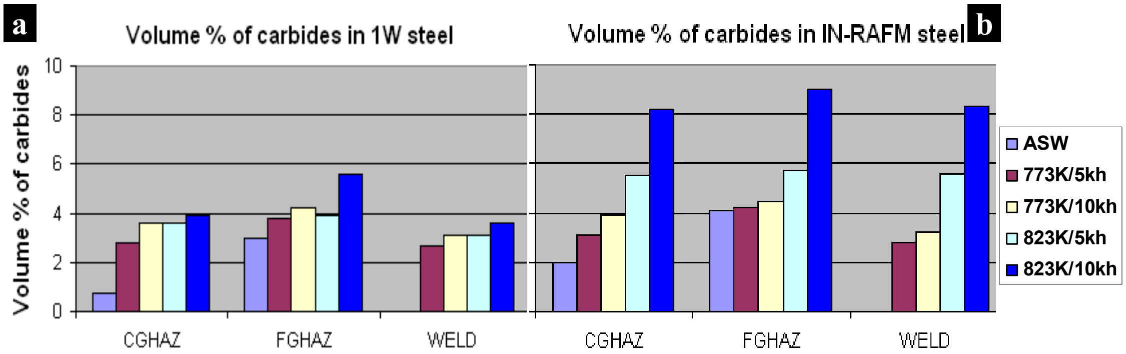

Fig.4.30: (a and b) Variation in the amount of carbides (experimental) in each region of weldment of 1W and INRAFM steels respectively, on aging at different temperatures

and EDX analysis from carbides at higher magnifications showed that size and number density of MX carbide is negligible as compared to $M_{23}C_{6,}$ which is taken as the main constituent of the precipitate fraction. It is evident that, the volume fraction of precipitates is higher in INRAFM steel than in 1W steel in all regions of the weldment. This is understood based on the higher carbon content of 0.12% in INRAFM steel as compared to 0.08 in 1W steel.

Figure 4.31 shows the change in average size of extracted carbides from different regions of the weldment in both the aged steels. On aging, the average normalized size of the carbide increased moderately from 50-60 nm to 80-100 nm except an abnormal increase in INRAFM steel after 10000 h at 823 K. This increase is due to precipitation and encapsulation of carbides by Laves phase as shown in **Fig. 4.28 & Fig.4.30**. Quantification of Cr content in $M_{23}C_6$ carbide from different regions of aged INRAFM steel weldment using EDX analysis is given in **Fig.4.32**. A steady and continuous increase in Cr content (discrepancy in the weld region is due to additional presence of high Cr rich needle shaped $M_{23}C_6$ carbides) is attributed to the evolution of metastable

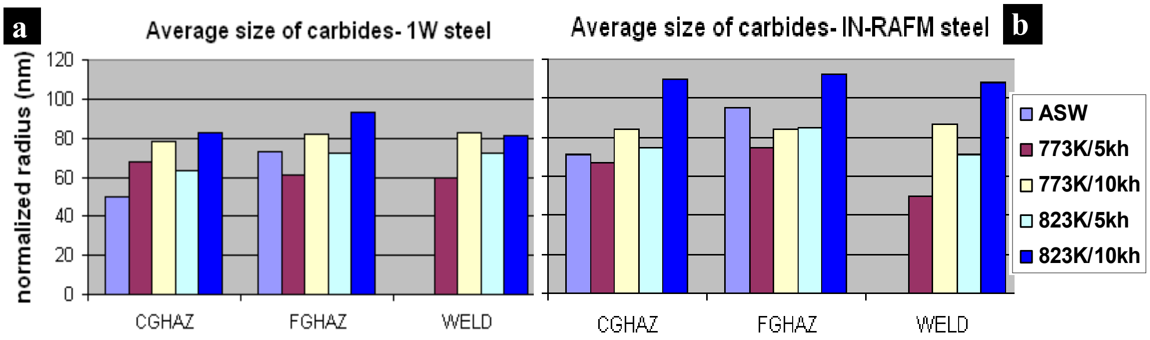

Fig.4.31: (a and b) Average normalized radius (experimental) of the carbide present in each region of the weldment of 1W and INRAFM steel respectively, on aging.

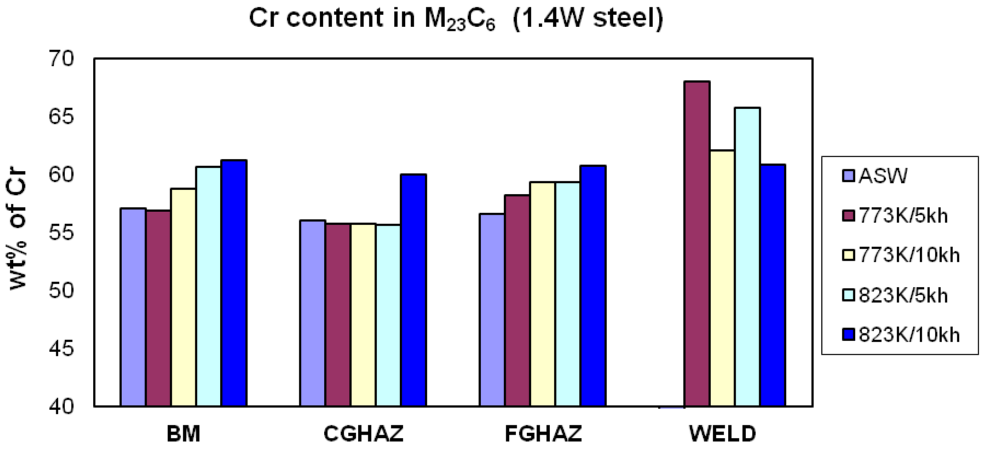

Fig.4.32: Change in the Cr content of $M_{23}C_6$ carbide on aging

$M_{23}C_6$ phase due to thermal activation driven diffusion of chromium into the carbide as it progresses towards attaining the stable configuration of $Cr_{23}C_6$. Based on the experimental and simulation studies it is evident that that thermal aging of the INRAFM weldments leads to the formation of Laves phase and coarsening of carbides mainly in the HAZ and base metal regions. The thermal cycle experienced during welding by the

HAZ favors extensive nucleation followed by the growth of a discontinuous network of carbide during service exposures especially along the lath boundaries. This condition sets off the formation of Laves phase in the vicinity of the carbides. The pre-ponderance of Laves phase in HAZ in comparison to base metal and weld metal clearly indicates that it is due to kinetic factors. Similarly, the accelerated growth of Laves phase network in the INRAFM steel in comparison to 1W steel is due to the higher tungsten content in the steel.

4.5 Summary and Conclusions

The microstructure of various regions of weldments of indigenously developed RAFM steels fabricated by three welding methods namely TIG, electron and laser beams were studied by detailed electron microscopy. Additionally, microstructural modifications on various regions of weldments of the two RAFM steels during PHWT and prolonged thermal exposure are compared. The important results of the study are summarized below:

- Prior austenite grain size in HAZ is controlled by the peak temperature and cooling rate in the region as a function of distance from the heat source.
- Variation of hardness across the HAZ is understood based on the decreasing peak temperature and cooling rate resulting in decreasing dislocation density and supersaturated carbon in the martensite. Further, in ICHAZ, during heating part of the weld thermal cycle, only partial transformation of ferrite to austenite takes place, that subsequently transforms to martensite on cooling resulting in further reduction in hardness.

- Negligible amount of carbides in CGHAZ in TIG weld is attributed to the complete dissolution of carbides at high temperatures prevailing in the CGHAZ. The higher carbon super saturation in the martensite and the high dislocation density due to high cooling rate explains for the high hardness in this region, despite the large grain size.
- Using Rosenthal's steady state solutions to heat transfer equation, thermal cycling experienced by different regions of autogenous weldment has been determined and correlated with microstructures.
- Prior austenite grain size in weld region of TIG weld was far higher than the electron and laser beam welds due to the higher residence time of the steel at temperatures above Ac_3.
- Random micro-texture was observed in all the three welds.
- Weld metal in all the cases showed comparable hardness despite finer lath size in electron and laser beam welds due to incomplete dissolution of carbide at short residence time in the high temperature regime.
- Optimum condition for PWHT is identified as 2 h at 1033 K for TIG welds of RAFM steel, while for electron and laser beam weld joints of 6mm thickness, a PWHT treatment of 1033 K/1h is sufficient.
- The activation energy of the tempering process has been evaluated and found to be matching with the activation energy for migration of carbon in ferrite matrix.
- Microstructures of CGHAZ, FGHAZ and ICHAZ have been simulated using GLEEBLE simulation and correlated with those observed in HAZ of weldments.

- $M(Cr,Fe,W)_{23}C_6$ and M(Ta,V)X carbides were the predominant precipitate phases in normalized and tempered RAFM steels, their volume fraction relatively higher in INRAFM steel. Coarsening rate of $M_{23}C_6$ carbides was much higher than that of MX.
- JMatPro based computations helped in identifying the temperature-time window for the formation of all phases as a function of temperature in various regions of RAFM steel weldments.
- Experiments carried out for few selected temperature-time combination confirmed the formation of Fe_2W type Laves phase in both FGHAZ and base metal of INRAFM steel after prolonged exposure to temperatures $\geq$823 K. Laves phase could not be detected in 1W-RAFM steel under similar experimental conditions.
- Enhanced precipitation of Laves phase observed in the FGHAZ of INRAFM steel weldments was attributed to the abundant carbide precipitations in this region leading to an increase in W and decrease in C content locally which would trigger nucleation and growth of Laves phase.
- Due to enhanced kinetics of precipitation of Laves phases, FGHAZ was identified to be the region susceptible for failure during long term service exposures of INRAFM steel weldments.

Chapter 5

Microstructural variations in a dissimilar austenitic - ferritic steel weld joint

5.0 Introduction

RAFM steel is the primary candidate material for fabrication of Test Blanket Module in ITER, whereas the vacuum vessels and several other components are being made of 316L (N) austenitic steel. Hence, dissimilar weld joint between RAFM and austenitic stainless steel is inevitable for fabrication of the structures [68, 89, 168]. Preparation of a sound dissimilar joint is challenging due to the vast differences in the chemical, structural and mechanical properties between the base metals. Electron Beam (EB) Welding is preferred considering the advantage of minimum HAZ, which is beneficial both from the irradiation and distortion point of view.

The weld joint contains a complex fusion zone, which is different both in composition and microstructure from both the base metals. Since the thermal properties are different for these alloys, thermal stresses arise during fabrication and service. PWHT is generally essential for RAFM steel to temper the martensitic microstructure formed in the HAZ of the weldment, while PHWT is not preferred for SS316L welds. Hence, it is necessary to study the microstructural changes that occur in the dissimilar weldments of RAFM and-SS. Trial welds of 1W RAFM-SS316L have been fabricated in IGCAR as a first step towards studying the feasibility of joining and understanding the behavior of the dissimilar joint. This chapter deals with the microstructural characterization of the fusion zone of ‘as welded’ 1W RAFM-SS316L steels and its modifications on PWHT and diffusion annealing at high temperatures to simulate aging treatments within shorter time durations.

5.1 Microstructural characterization of ‘as welded’ RAFM-SS316L weld joint

Detailed characterization of microstructure, micro-chemistry and micro-texture of the weld interface has been carried out in a 1W RAFM-SS316L steel dissimilar joint prepared by EB welding technique, the results of which will be discussed in sequence in this section.

5.1.1 Base metal characterization

The SEM micrographs of SS316L used for fabrication of the dissimilar EB welded joint is shown in **Fig. 5.1(a)**. The micrograph shows the predominance of equiaxed grains along with the presence of twins, shear bands and elongated inclusions. Average grain size of the steel was ~53 µm. The TEM micrograph of the steel given in **Fig. 5.1(b)** shows presence of twins in the microstructure and the diffraction pattern given as inset clearly reveals that the crystal structure is fcc. RAFM steel was used in normalized and tempered condition and the microstructural details are already discussed in **Section 3.1**

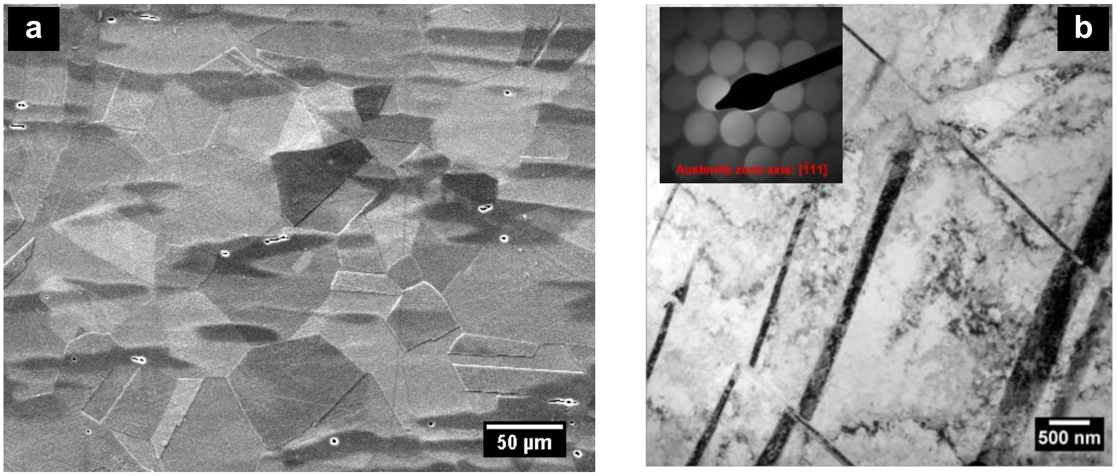

Fig.5.1: Microstructure of SS316L used in the dissimilar weld (a) SEM micrograph showing equiaxed austenitic grains (b) TEM micrograph containing twins (inset – diffraction pattern from austenite taken along <$\bar{1}$11> zone axis.

5.1.2 Macrostructure of weldment

Figure 5.2 shows the macrostructure of a dissimilar weld joint between SS316L and 1W RAFM steel. Macroscopically six different regions have been identified as shown in the figure. Region I and VI represent the base metal (BM) of SS and RAFM steel respectively. The unmixed solidified regions at the SS and RAFM weld interfaces are shown as region II and IV respectively. Region III corresponds to the mixed and solidified region in the weld metal. Microstructural details of Region I and VI have been discussed in the previous section. A detailed description of the Heat Affected Zone (region V) of RAFM steel consisting of CGHAZ, FGHAZ and ICHAZ has also been given in **Chapter 4**. Detailed characterization of regions II, III and IV will be described in the following sections. The resultant phases that form in the weld metal by fusion of

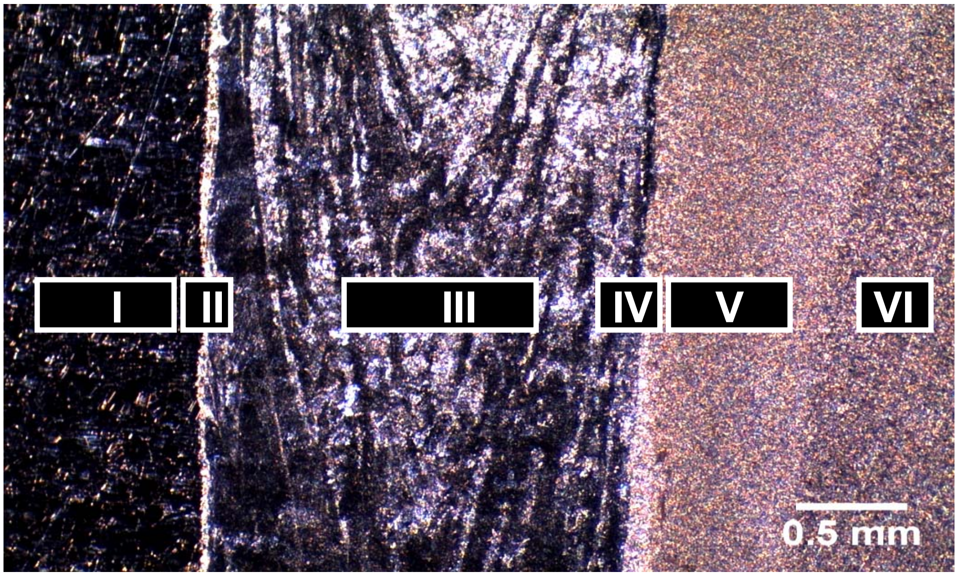

Fig.5.2: Macrostructure of cross section of SS – RAFM dissimilar weld joint showing different regions (I- SS316L base metal, II- fusion zone at SS316L side, III- mixed weld metal, IV- Fusion zone at RAFM steel side, V- HAZ of RAFM steel, VI – RAFM base metal) of interest.

two different alloys, depends on the proportion of their mixing. The chemistry of a region of the weld metal could give a measure of the extent of mixing. Microchemical analysis using Electron Probe Micro Analyzer (EPMA) was carried out to find out the distribution of elements in the weld metal. The concentration profile obtained by EPMA analysis across the weld is shown in **Fig.5.3**. A sharp decrease in Cr and Ni content is observed at the SS interface. The weld metal showed a gradient in the concentration of Ni and Cr for a typical distance of ~250 μm from either interface. But for most part of the weld metal region an average concentration of 3% Ni and 11.1% Cr was measured. Based on the chemical composition of the two alloys, the fraction of weld dilution from each alloy can be calculated by mass balance given below, since there is no filler metal addition during the welding process.

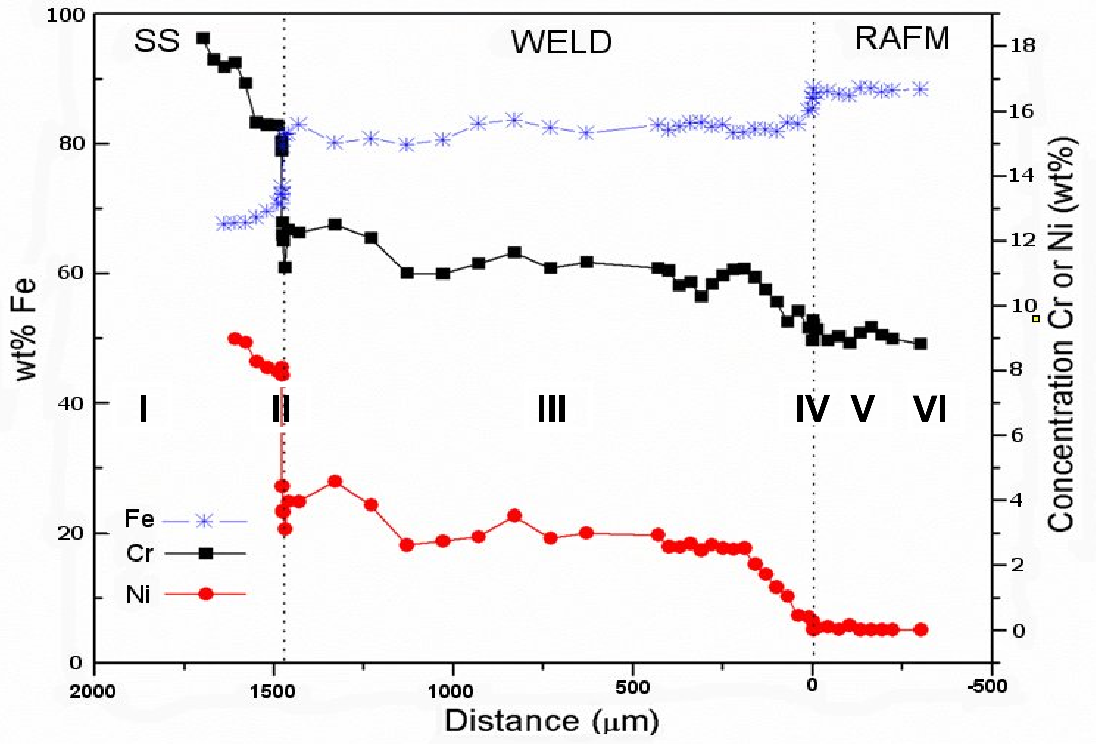

Fig.5.3: Concentration (±1%) profile of elements across the dissimilar weldment – regions of interest are marked

$$\%\text{Ni (or Cr) in SS} * x + \%\text{Ni (or Cr) in RAFM} * (1-x) = \%\text{Ni (or Cr) in WM} \qquad (5.1)$$

where ‘x’ is the SS fraction of mixing. Based on the above equation, the dilution ratio of austenitic steel to RAFM steel in the weld metal was estimated to be 1:3.

5.1.3 Phase prediction by Schaeffler-Schneider diagram

Constituents of the steel at ambient temperature following cooling from liquid may be predicted by Schaeffler-Schnieder diagram [169] **(Fig.5.4)** using nickel and chromium equivalents [13].

$$\begin{aligned}\text{Ni equivalent (wt \%)} &= (\%\text{Ni}) + (\%\text{Co}) + 0.5(\%\text{Mn}) \\ &\quad + 0.3(\%\text{Cu}) + 30(\%\text{C}) + 25(\%\text{N}) \qquad (5.2)\end{aligned}$$

$$\begin{aligned}\text{Cr equivalent (wt \%)} &= (\%\text{Cr}) + 2(\%\text{Si}) + 2(\%\text{Si}) + 1.5(\%\text{Mo}) + 5(\%\text{V}) \\ &\quad + 1.75(\%\text{Nb}) + 0.75(\%\text{W}) + 1.5(\%\text{Ti}) + 5.5(\%\text{Al}) \\ &\quad + 1.2(\%\text{Ta}) + 1.2(\%\text{Hf}) + 1.0(\%\text{Ce}) + 0.8(\%\text{Zr}) \\ &\quad + 1.2(\%\text{Ge}) \qquad (5.3)\end{aligned}$$

The $\mathrm{Cr_{eq}}$ of SS SS316L and RAFM steel are estimated as 22.0 and 11.2 respectively while the $\mathrm{Ni_{eq}}$ is 16.7 and 3.6 for the two steels. The Schaeffler diagram coordinates ($\mathrm{Cr_{eq}}$ and $\mathrm{Ni_{eq}}$) of weld metal in any proportion of mixing must position along the line joining the coordinates of RAFM and SS SS316L. A dilution of 1:3 mixing of two alloys is expected to result in a weld metal with $\mathrm{Cr_{eq}}$ and $\mathrm{Ni_{eq}}$ of 14.0 and 6.8 respectively (marked on the line in **Fig. 5.4**). These co-ordinates falls in the austenite (γ) + martensite (α') phase field of the diagram. Therefore, assuming uniform mixing in 1:3 ratio throughout the fusion zone, according to Schaeffler diagram, weld metal should have a mixture of austenite (γ) and martensite (α') phases. However, mixing is unlikely to be uniform and near the fusion boundary between weld metal and austenitic stainless, this ratio could be

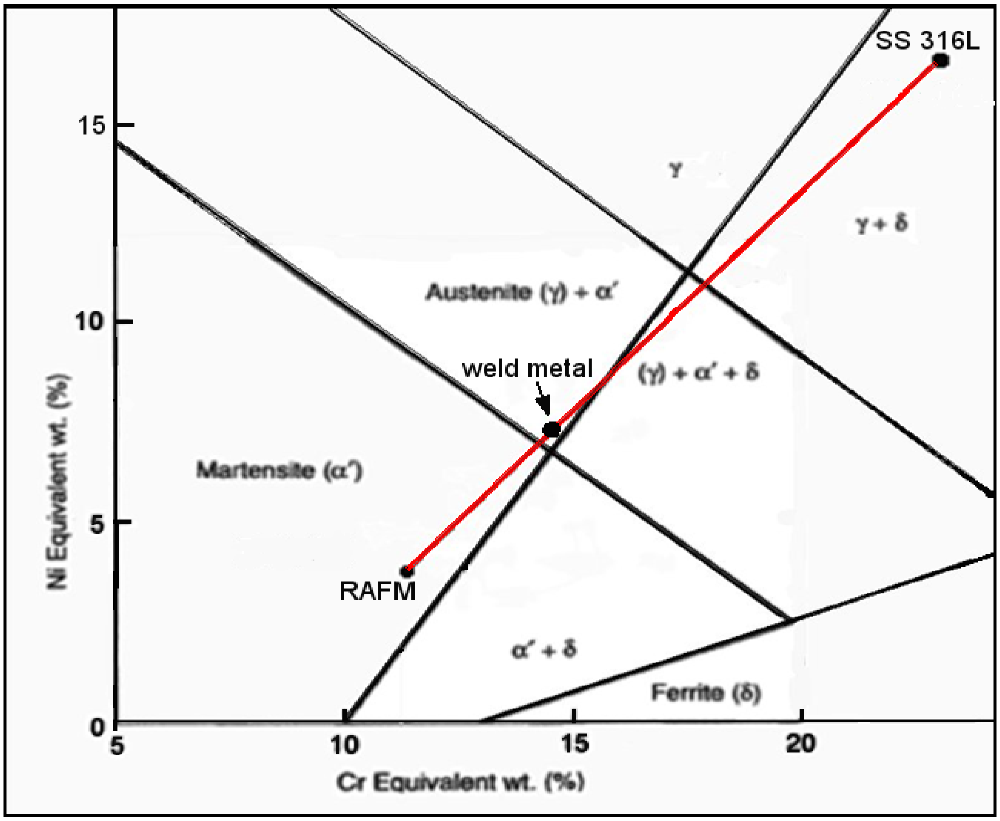

Fig.5.4: Schaeffler-Schneider diagram – Co-ordinates of weld metal with SS-RAFM steel; dilution of 1:3 is marked on the line joining RAFM steel and SS SS316L.

higher and composition of the weld metal can shift towards γ+δ+α' or even γ+δ phase fields. Similarly near the RAFMS/weld metal boundary, this ratio could be still lower with a higher contribution of RAFM steel to the weld metal composition which could make the weld metal fully martensitic. With this base line knowledge, the phases identified in region II-IV are discussed in the following section.

5.1.4 Microstructural characterization of weld metal in 'as welded' condition

Figure 5.5 shows the composite micrograph of the dissimilar weld joint. Austenitic steel base metal, fusion zone and RAFM steel base metal were separately etched for revealing the structure. Weld metal (region III) which showed a mixed composition by EPMA analysis, exhibited a martensitic structure, though the Schaeffler-Schneider diagram (**Fig**

5.4) predicted austenite also to be present in the fusion zone. The presence of delta ferrite if any could not be distinguished from the fine martensite structure in the weld metal. Average hardness of the weld metal was estimated as ~475VHN, which is in agreement with the observed martensite structure. Microstructure of the SS-Weld interface (region II) is shown in **Fig.5.6a**. It is observed that the solidification begins epitaxially from the partially melted austenite grains and mode of solidification is cellular and the cellular morphology is extended into the fusion zone up to ~200µm. EDS spectrum collected from this region showed the same composition as that of SS316L which confirmed there is little or no mixing of two base metals in this region. The cellular structure can be understood in terms of the high temperature gradient persisting in EB welds which leads to a high G/R ratio (G- temperature gradient and R- growth rate) resulting in cellular structure on solidification.

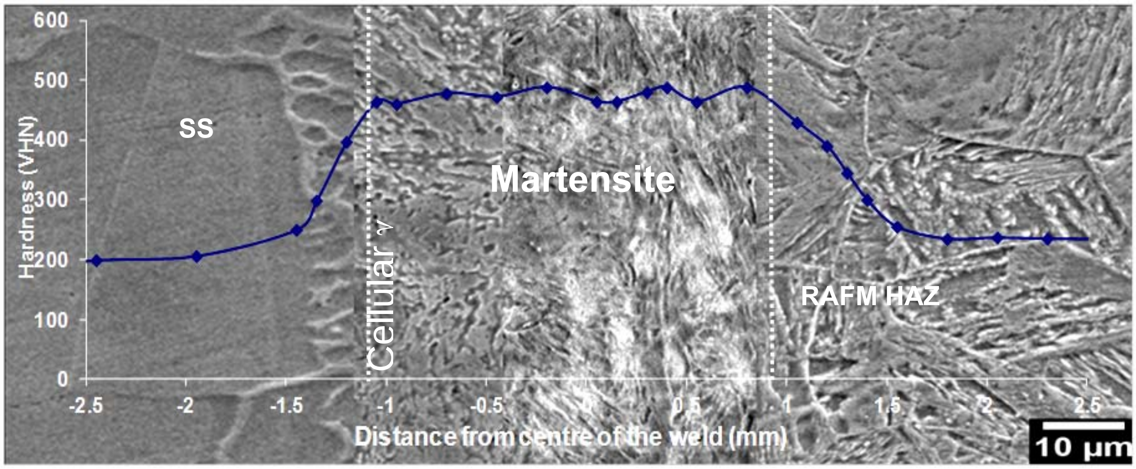

Fig.5.5: A composite micrograph of as welded RAFM-SSSS316L joint showing partly melted region of SS, weld metal consisting of dendritic austenite, dendritic martensite, partly melted region of RAFM and CGHAZ region in RAFM (all regions etched separately and micron marker is valid for microstructure only).

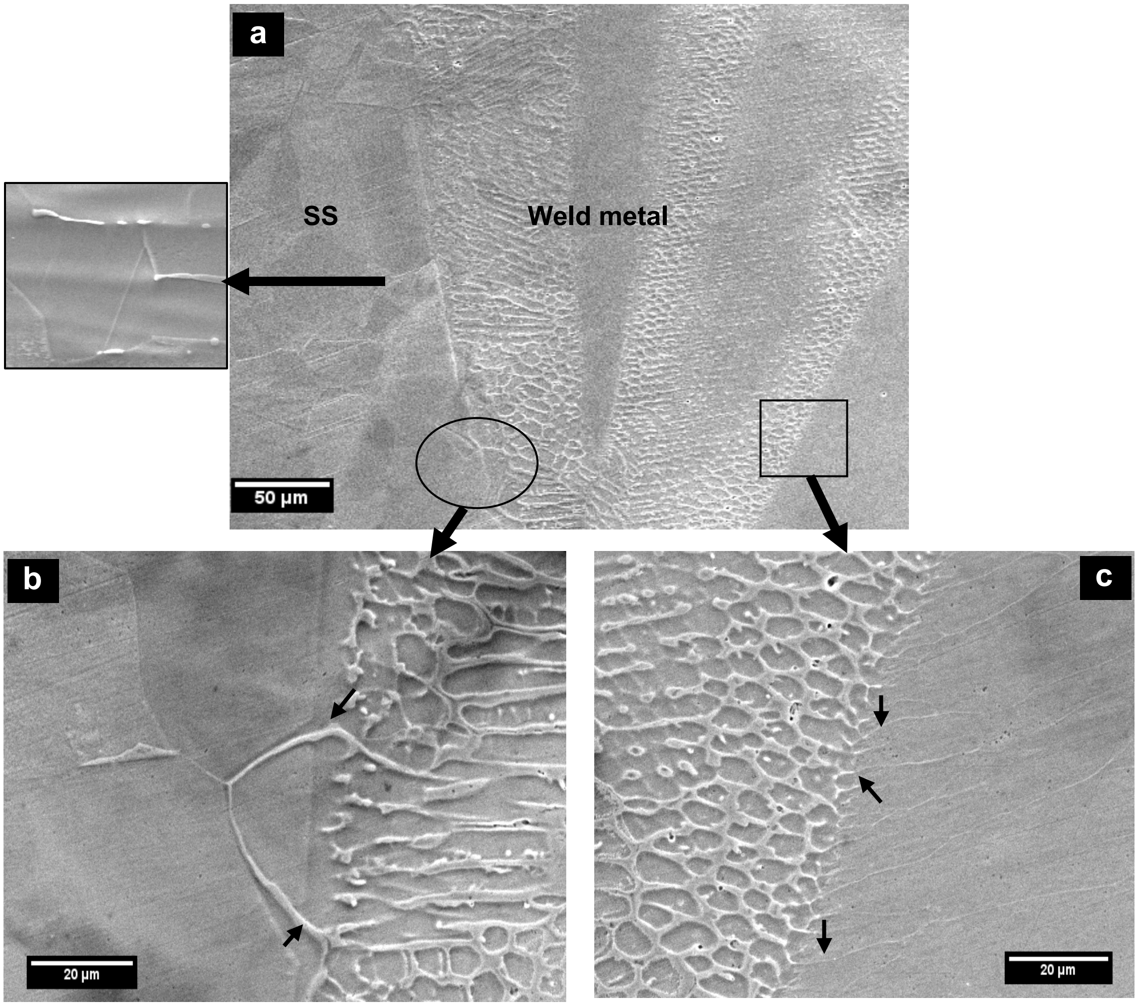

Fig. 5.6: SEM micrograph from region II of SS-Weld showing a) equiaxed austenite in unaffected base metal, delta ferrite stringers in the austenite base metal (inset) b) cellular and cellular- columnar structure in the fusion zone near the austenite stainless steel fusion boundary and c) Type I boundaries (arrow marked) formed by epitaxial growth from the partially melted grains of the base metal.

The microstructure also shows discontinuous stringers with different morphology and contrast at the austenite grain boundaries of SS-weld interface (inset of **Fig.5.6a**), resembling δ-ferrite. It is possible that there was melting of grain boundaries (partial melting) of base metal which subsequently solidified as delta ferrite. The presence of δ-ferrite was confirmed by X-ray diffraction and EBSD experiments which will be discussed in a subsequent section. Detailed studies on austenitic steels showed that solidification of SS316L is expected to occur through formation of primary austenite + δ-ferrite [170]. Delta ferrite formed during the solidification would transform to austenite either by a diffusion controlled transformation or by a massive composition invariant reaction upon cooling. Final microstructure depends on the ratio of Cr_{eq} to Ni_{eq} as described in **Table 5. 1** [171]. Assuming composition of this part of the fusion zone is same as that of the SS316L base metal, Cr_{eq}/Ni_{eq} for this composition (1.32), predicts ferrite at cell and dendrite boundaries. This rationalizes the observation of δ- ferrite in **Fig. 5.6**.

It is also reported that under rapid cooling conditions existing during welding especially in EB welding and fast growth rates aided by epitaxy, the weld structure could solidify far away from equilibrium to form δ-ferrite [172]. In dissimilar welds, two types of fusion boundaries are reported, Type I and Type II. Type I is formed when the solidification begins epitaxially from the partially melted base metal grains at the boundaries and the phases that form during solidification are the same as those in the base metal part of the boundary. Type II boundaries develop when phases formed during solidification are different from that present in the base metal and epitaxial growth from the partially melted grains is not possible. Cracking has been reported in several locations in Type II [173-174]. From **Fig. 5.6 (b and c)** it is clear that Type I boundaries are formed at both the stainless steel/fusion zone and the RAFM steel/fusion zone interfaces in the present study. **Fig.5.7 (a)** shows the SEM micrograph of the RAFM-weld interface.

The HAZ of RAFM steel immediate to the weld metal showed martensitic structure with coarse prior austenite grains followed by fine grains.

Table 5.1: Solidification modes, Cr_{eq}/Ni_{eq} ratios, reactions and final products in austenitic steel welds [171]

Solidification Mode	**Equivalent ratio**	**Reaction**	**Microstructure**
A - Fully Austenite	$Cr_{eq}/Ni_{eq}<1.25$	L→L+A	Fully austenitic
AF-Austenitic -Ferritic	$1.25<Cr_{eq}/Ni_{eq}<1.48$	L → L + A→ L + A+ $(A + F)_{eut}$ →A+ F_{eut}	Ferrite at cell and dedritic boundaries
FA- Ferritic Austenitic	$1.48<Cr_{eq}/Ni_{eq}<1.95$	L → L + F → L + F+ $(F + A)_{eut}$ →F+ A	Skeletal and/lathy ferrite resulting from ferrite to austenite transformation
F- Ferrite	$1.95< Cr_{eq}/Ni_{eq}$	L → L + F → F →F+ A	Acicular ferrite or ferrite matrix with grain boundary austenite and widmanstatten side plates

HAZ boundaries (white arrows in **Fig.5.7 (a)**) were found to be extended into the weld metal. The transition and boundaries between these regions were very smooth since HAZ as well as the weld metal showed a uniform martensitic microstructure. Near this fusion boundary, dilution of the fusion zone by the 316L base metal is less than what is predicted from Schaeffler-Schneidar diagram (**Fig. 5.4**) and hence no γ phase is found here. Fusion zone of RAFM side showed the presence of isolated grains having characteristic morphology of δ- ferrite (marked in **Fig.5.7 (a)**), but could not be unambiguously confirmed by diffraction experiments because of similar bcc crystal structure of ferrite and martensite. TEM on thin foil from CGHAZ region showed lath martensitic structure (not shown) but extraction replica showed large number of undissolved (**Fig. 5.7(b))** carbides similar to that **(Fig.4.12(c))** of EB similar weld joint described in **Chapter 4**. Presence of a large number of carbides in this region confirms that the heating cycle was rapid which is characteristic of EB welding and was not adequate for dissolution of carbides.

XRD analysis was carried out at different depths from the SS-weld interface towards SS base metal to identify the minor phase (δ-ferrite) which is observed in the partially melted region of SS. XRD plot taken from different planes parallel to SS interface at various depths is given in **Fig.5.8.** At a depth of 50µm a mixture of phases (ferrite and austenite) was obtained but ferrite phase is seen only at the austenite-weld interface.

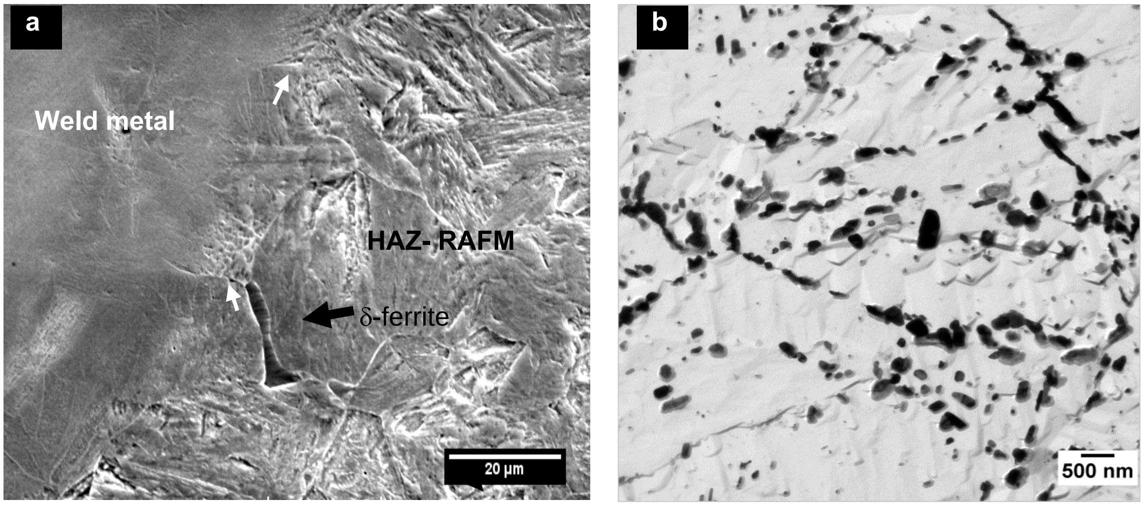

Fig.5.7: Microstructure of RAFM-weld interface showing (a) Type I boundaries (white arrow), delta ferrite at the fusion boundary and martensite in HAZ (b) large number of precipitates in grain/ lath boundaries of HAZ (from carbon extraction replica)

In order to clear the ambiguity EBSD analysis was also carried out at this interface. Figure **5.9 (a** and **b)** shows the EBSD band contrast and phase ID map of the SS-weld interface respectively. Martensitic structure of the weld and austenitic structure of the SS base metal are very much evident from these maps. Even the annealing twins in the austenite grains (**Fig. 5.9(a)** can be clearly seen. **Fig.5.9(c)** gives Inverse Pole Figure (IPF) map of austenite and ferrite together and **Fig.5.9 (d)** gives the IPF of ferrite phase only. Stringers of δ-ferrite were found to be seen in the austenitic base metal though any enrichment of this phase at the interface could not be resolved. However, this showed that the austenitic steel composition is favorable to δ- ferrite formation. Additionally, it was not possible to distinguish δ- ferrite from martensite if at all present within the weld metal due to similarity of crystal structure and lattice parameters.

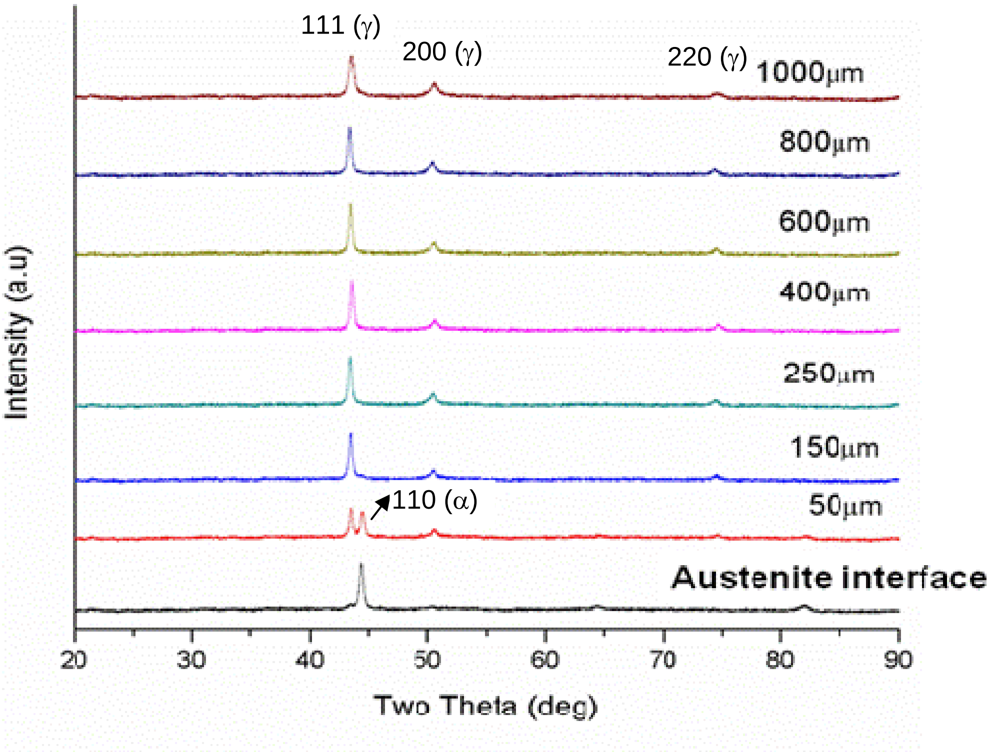

Fig. 5.8: X-ray diffraction studies at different depth from SS-weld interface, showing the presence of δ-ferrite at the austenite interface.

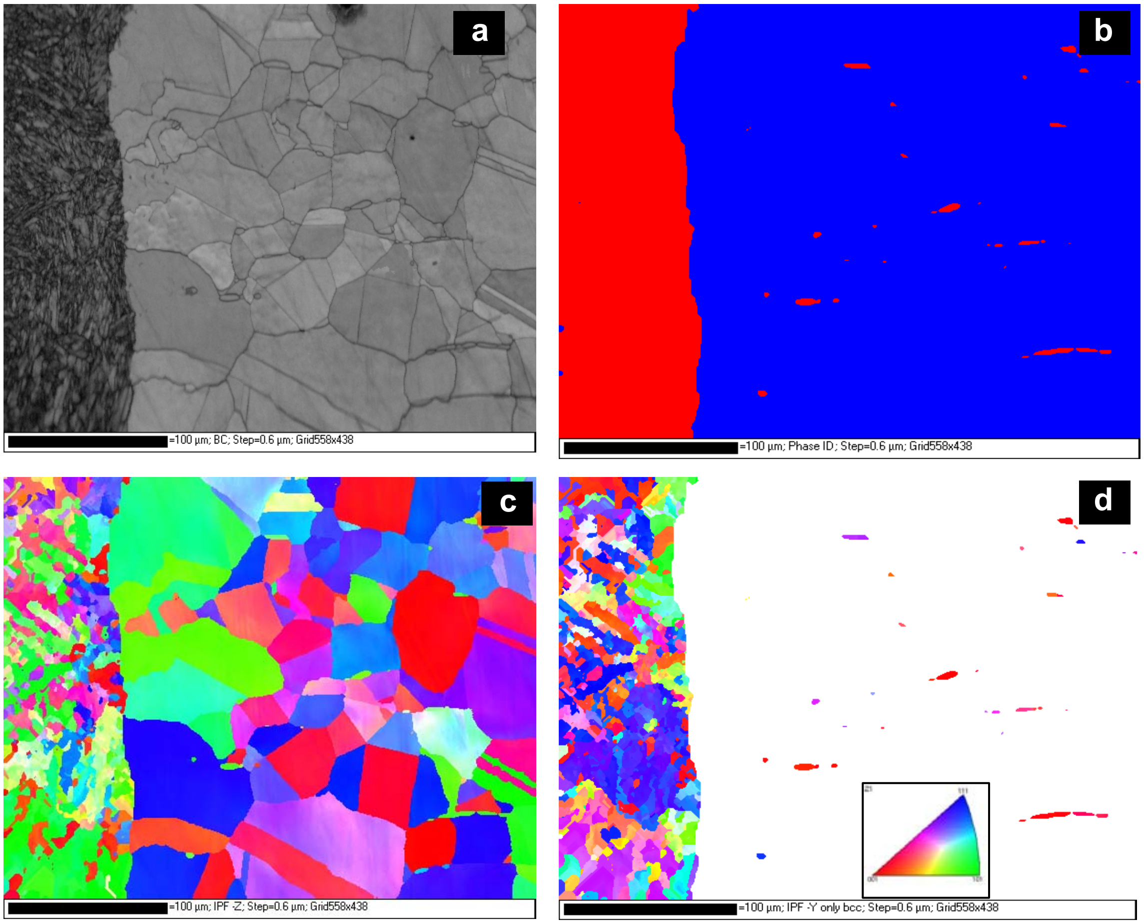

Fig. 5.9: (a) EBSD band contrast map (step size: 0.6µm) obtained from SS-weld interface, showing weld (martensite) and austenite (b) Phase ID map from interface showing presence of stringers of delta ferrite in stainless steel (c) Inverse Pole Figure map of bcc & fcc– along welding direction reveals grain growth at the austenite interface (d) Inverse Pole figure map of bcc phase only: IPF –along plate normal

A 3D EBSD map was generated to know the spatial distribution of δ- ferrite in the vicinity of the fusion line. The location from which the EBSD specimen is taken is shown in **Fig.5.10 (a)**. EBSD map from a 4µm X 4µm area was carried out up to a depth of 7.54 µm. **Fig.5.10 (b)** shows the phase identification map obtained by 3D EBSD analysis. **Fig.5.10 (b)** confirms presence of δ- ferrite phase at the interface extending up to a depth of 3-4 μm. Presence of δ- ferrite at interfaces was observed especially where width of the fusion zone was high, i.e. the entry point of the electron beam during the welding process. The appearance of high amount of δ- ferrite at the partially melted region of austenite, where no mixing or composition change is expected to take place indicates that it has formed either during the final stages of the heating part of the weld thermal cycle or during liquid to solid transformation that takes place during cooling part of the weld thermal cycle [175]. However, away from fusion boundary and well into the fusion zone, there is good mixing of the molten metal from two base metals resulting in a composition, which is lower in Chromium and Nickel than the austenitic base metal. This alloy composition is such that the austenite formed initially during cooling transforms to martensite during final part of the weld thermal cycle.

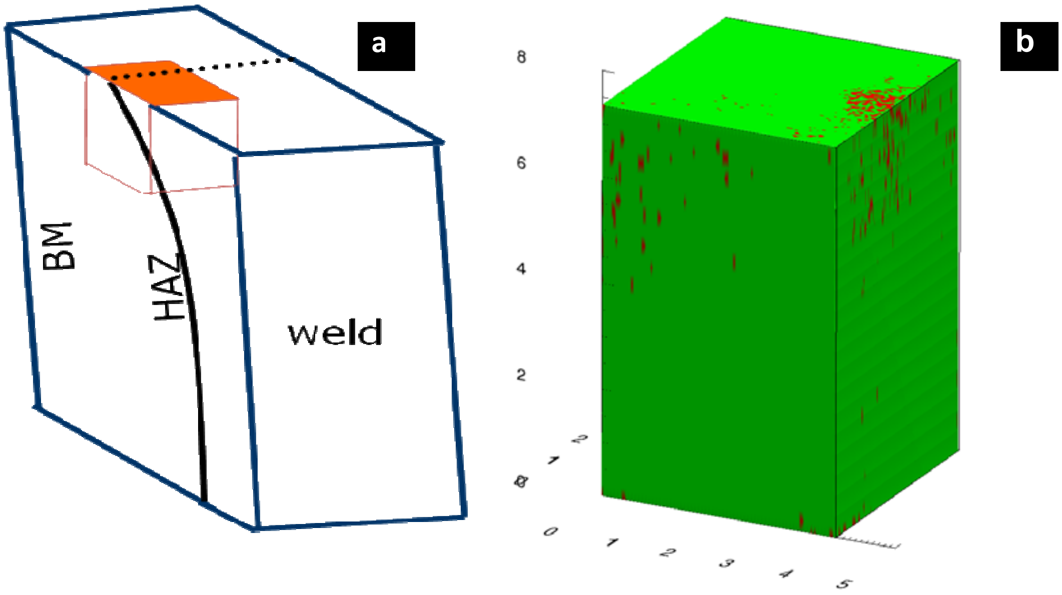

Fig. 5.10: (a) Location of specimen from weld interface for 3D EBSD b) distribution of delta ferrite in 3D showing high volume of delta ferrite at the interface.

Fig.5.11 shows the EBSD maps from fusion zone i.e weld metal Examination of the microstructure of this region and subsequent EBSD analysis of this zone revealed few islands present sporadically and possessing a different morphology.

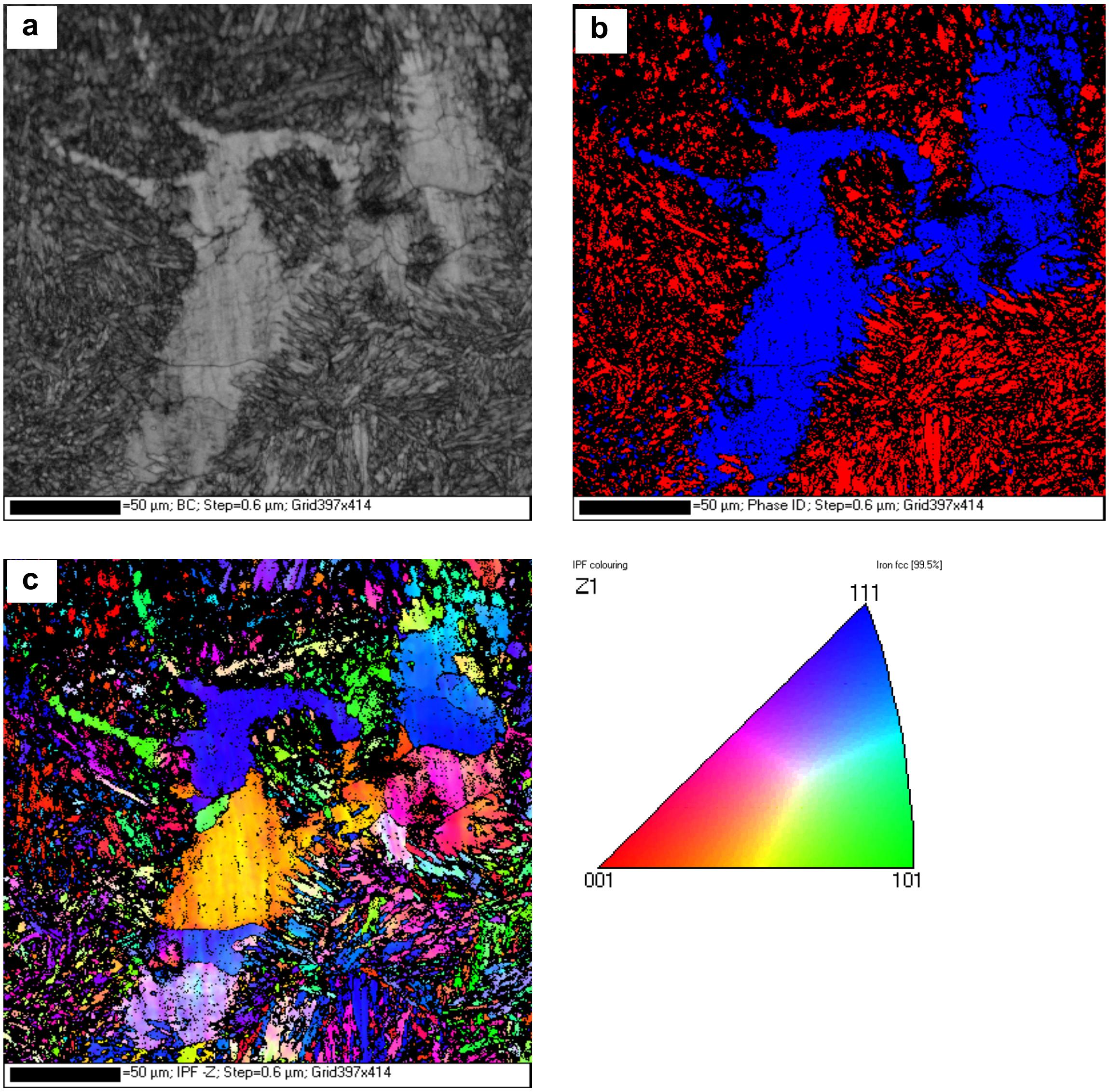

Fig.5.11: EBSD band contrast map from weld metal, (b) Phase ID map superimposed with band contrast map showing the presence of austenite phase in the weld (c) Inverse Pole Figure map of bcc and fcc, showing austenite grains at different orientations

From the band contrast and phase ID maps (**Fig.5.11 (a and b)**) this phase has been identified as austenite. It is evident that the experimental results across different regions show the co-existence of the two phases namely austenite and martensite in the fusion zone of dissimilar weld, which is in agreement with the predictions of the Schaeffler diagram discussed in **section 5.1.2**.

5.2 Effect of Post Weld Heat Treatment on the weld metal

On welding, RAFM steel undergoes a phase transformation to austenite, which transforms to hard martensite on cooling. PWHT is therefore essential for the RAFM steel weldments to regain the required toughness. A standard PWHT (1033 K for 1 h) was carried out on the dissimilar weld joint. The hardness profile of the weldment after PWHT is given in **Fig.5.12**.

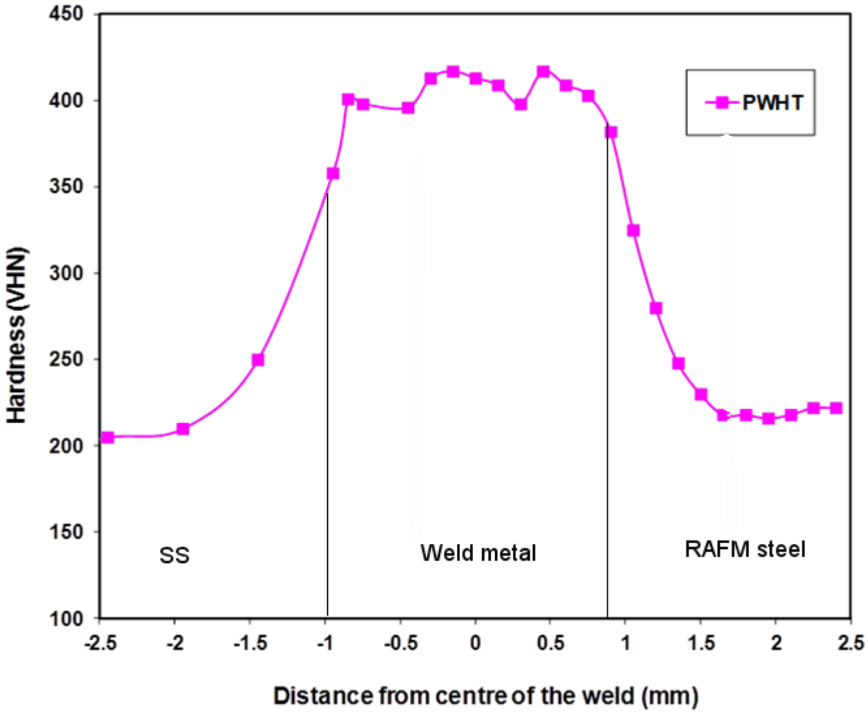

Fig.5.12: Hardness profile of the weldment after PWHT at 1033 K for 1 h

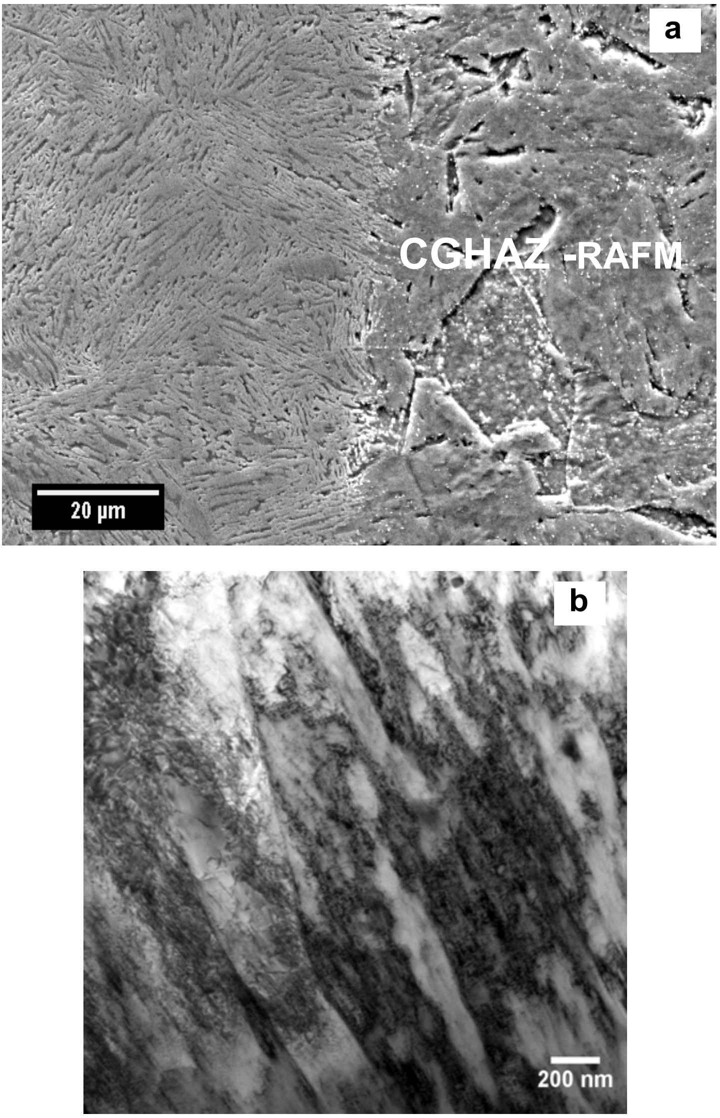

Fig. 5.13: (a) SEM micrograph of RAFM steel-weld interface after PWHT at 1033 K showing tempering of CGHAZ region but retention of martensite in weld metal (b) TEM micrograph from weld metal showing lath martensitic structure.

It is obvious that the reduction in hardness of the weld metal is insignificant, which is contrary to the observations in the case of similar welds. High hardness of the fusion zone even after PWHT could either be due to a) re-austenitisation due to exceeding lower transformation temperature during PWHT of the fusion zone or b) high resistance to tempering of martensite formed in this zone.

5.2.1 Microstructural variations during PWHT

From **Fig. 5.12** it is clear that the large decrease in hardness expected due to tempering of martensite during PWHT could not be achieved in the present study. **Fig.5.13** shows the SEM micrograph consisting of weld and RAFM interface. In comparison with the ‘as welded’ microstructure given in **Fig.5.2 & 5.7(a),** the CGHAZ region shows considerable tempering of the RAFM steel with clear evidence of carbide precipitation. TEM micrograph from the weld region is shown in **Fig.5.13 (b)**. Presence of lath martensite with high dislocation density is evident from the micrograph. The lath size was measured to be in the range of 150-300 nm. This variation is similar to that observed in the ‘as weld’ of EB welding of RAFM steel described in **Section 4.1.3**. The above results suggest that the Post Weld Heat Treatment has not been effective in tempering of the martensite which is also supported by the high value of hardness.

Fig.5.14 shows the concentration profile of dissimilar weld joint after PWHT. By comparing the profile of the weldment before (**Fig.5.3**) and after PWHT (**Fig.5.14**), it is clear that the average Cr and Ni content of the weld region has increased from 12% Cr to 13.5% and from 4% to 5.5%Ni respectively. Apart from this, the sharp change in the concentration of Ni and Cr at austenitic interface of the fusion zone has smoothened. This is due to enhanced diffusion of Cr and Ni from austenite side on PWHT at 1033 K. PWHT did not induce much change in the regions near to the RAFM fusion boundary side except for a minor enhancement of Ni at HAZ of RAFM steel. It is worthwhile to recall that during the welding process, contribution from RAFM steel to the melt is high and hence there is a less gradient in concentration across this interface in the beginning.

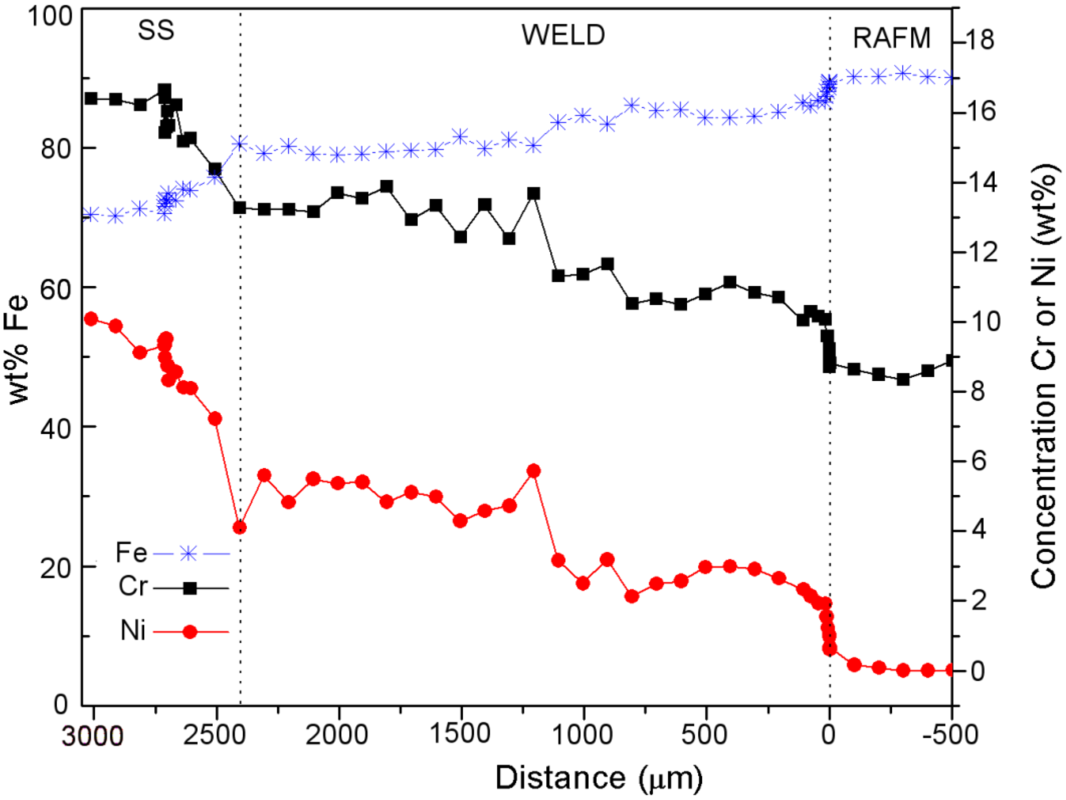

Fig.5.14: Concentration (±1%) profile of elements across the dissimilar weldment after PWHT at 1033 K

5.3 Reversion of martensite during diffusion anneal treatments

In **section 5.1.2**, it is seen that the average Ni content of the RAFM weld metal increased to ~3%. Ni being an austenite stabilizer can reduce the transformation temperature (Ac_1) to lower than PWHT temperature. Many empirical equations are available in literature for estimating Ac_1 and Ac_3. A general equation [176] for estimating $Ac1$ is given below.

$$Ac1(°C) = 723 - 10.7Mn - 16.9Ni + 29.1Si + 16.9Cr + 290As + 6.38W \qquad (5.4)$$

Such empirical equations are formulated for a range of compositions. Some of the empirical equations used specifically for ferritic type of steels are valid if the Ni content is less than 1%. Values of Cr and Ni content (wt %) were obtained from EPMA analysis and values of other elements were calculated using the weld dilution values and actual alloy contents. Using the empirical relationship A*c*1 value of the weld metal was calculated as 1130 K. An attempt has also been made to determine the Ac_1 temperature of the weld metal by designing a Calorimetry experiment. A typical Differential Scanning Calorimetry (DSC) profile obtained during heating and cooling (10 K/min) from a specific region of weld metal is given in **Fig.5.15**. Critical transformation temperatures are marked in the figure. Ac_1 and Ac_3 transformation temperatures were estimated to 1076 K and 1127 K respectively.

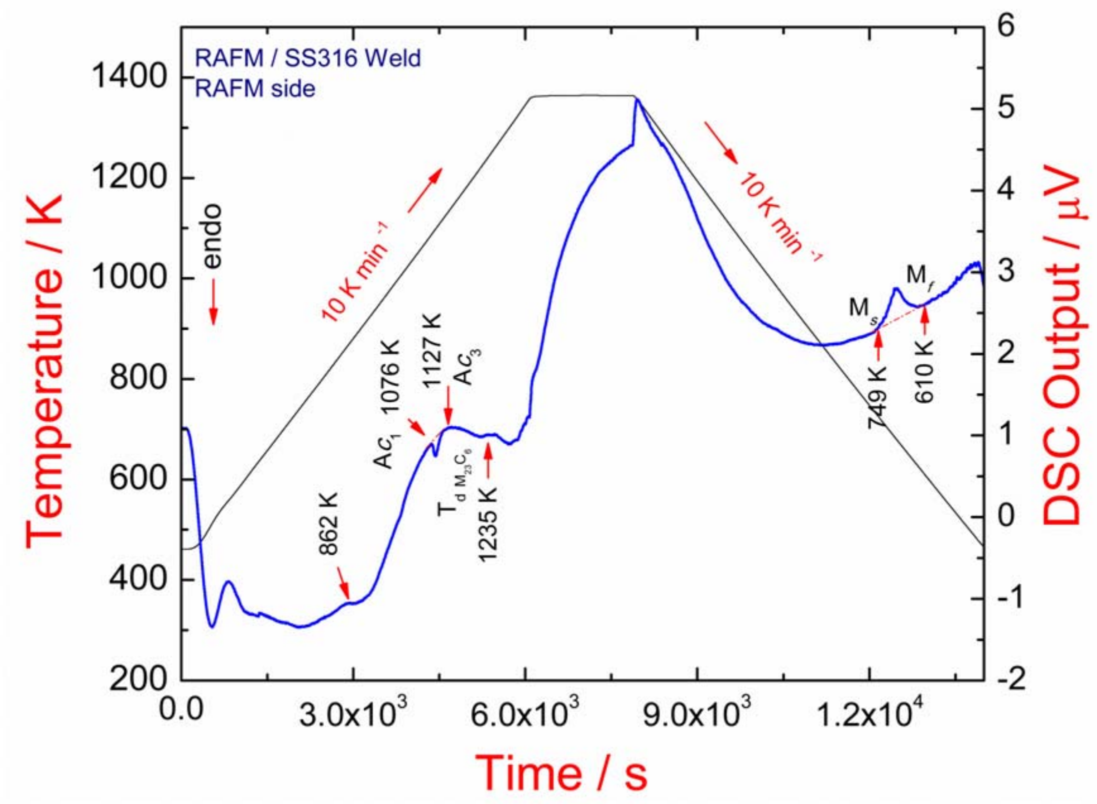

Fig. 5.15: DSC thermogram of RAFM-SS weld metal – critical transformation temperatures are marked

Calorimetry studies were carried out at a continuous heating rate of 10 K/min and hence the experimentally determined values of Ac_1 and Ac_3 may be slightly higher than the equilibrium transformation temperature. A comparison of critical transformation temperatures between base metal and weld metal are given in **Table 5.2**. Lower transformation temperature (Ac_1) value of normalized 1W RAFM steel is reported as 1104 K by Raju *et.al* [36] . It is clear that Ac_1 of the weld metal is lowered due to Ni enrichment caused by mixing with SS 316L. However, Ac_1 of weld metal obtained by both empirical and experimental methods was found to be higher than 1033 K, which is the PWHT temperature. Hence, it is natural to expect tempered martensitic structure for the weld metal after PWHT. On the contrary a predominantly martensitic structure is observed experimentally in the fusion zone after PWHT. This indicates that PWHT temperature employed is higher than the Ac_1 temperature of the fusion zone.

Table 5.2: Comparison of transformation temperatures between base metal and weld metal

Description of phase change	1W base metal (K) [36]	RAFM-SS weld metal (K)
$\alpha + MX + M_{23}C6 \rightarrow \alpha + \gamma + MX + M_{23}C_6$ (Ac_1)	1104 ± 5	1076 ± 5
$\alpha + \gamma + MX + M_{23}C6 \rightarrow \gamma + MX + M_{23}C_6$ (Ac_3)	1144 ± 5	1127 ± 5
$\gamma \rightarrow \gamma + \alpha'$ (M_s)	698 ± 5	749 ± 5
$\gamma \rightarrow \alpha'$ (M_f)	603 ± 5	610 ± 5

The small mismatch between DSC results and microstructural inference could be due to compositional variation within the weld. The minimum size requirement of the sample for calorimetry experiments also was a constraint to obtain samples with precision within the weld metal. However, this uncertainty has been clearly ruled out on the basis of the results from the high temperature exposure of the weld described in the next section.

5.4. Microstructural and micro-chemical changes during thermal exposure

In order to study the microstructural response of the various regions on thermal exposure, weldments were subjected to heat treatments at three different temperatures namely 873, 973 and 1073 K for durations up to 100 h. The choice of temperature was based on the limits of service temperature (873 K) and lower transformation temperature of weld metal (~1076 K). The change in hardness on thermal exposure at 873 and 1073K is tabulated in **Table 5.3**. The microstructural changes in the base metal and weld metal is shown in **Fig. 5.16**. The change in hardness of RAFM steel on exposure to 873 K is negligible. Since the RAFM base metal in normalized and tempered condition is not expected to have any significant change in hardness on PWHT or any treatment at lower temperature the experimental results are in agreement.

Table 5.3: Average hardness in various regions of weldment on thermal exposure

Treatment	**As welded**	**PWHT**	**873 K**				**1073 K**			
Region										
Duration			**10h**	**20h**	**50h**	**100h**	**10h**	**20h**	**50h**	**100h**
SS 316L	**185 ±2**	**185 ±2**	**187±2**	**214 ±2**	**214 ±2**	**205 ±2**	**184 ±2**	**202 ±2**	**190 ±2**	**178 ±2**
Weld metal	**476 ±15**	**405 ±10**	**376±10**	**353 ±10**	**339 ±8**	**294 ±5**	**343 ±5**	**408 ±5**	**360 ±4**	**366 ±4**
RAFM	**226 ±4**	**224 ±4**	**224±4**	**223 ±4**	**220 ±2**	**220 ±2**	**212 ±2**	**206 ±2**	**198 ±2**	**188 ±2**

Stainless steel showed a small increase in hardness on exposure at 873 K. No appreciable changes could be seen except few precipitates near the weld interface in austenitic steel (Fig.5.16a). The small increase in hardness in stainless steel at longer times could be due to precipitation of fine carbides (could not be resolved by SEM), which overrides the effect of stress relieving. From **Fig.5.16 (b)** it is seen that HAZ and base metal of RAFM steel has undergone further recovery.

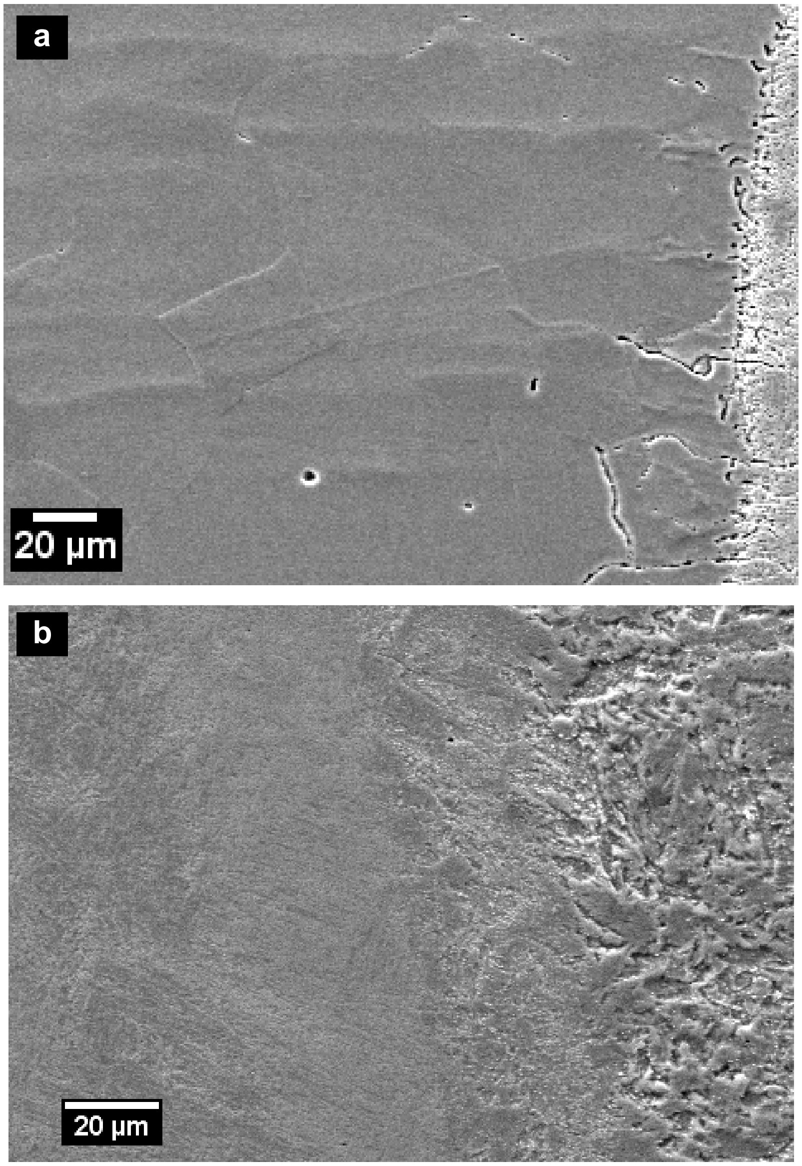

Fig. 5.16: Microstructural evolution of weld metal after thermal exposure at 873 K for 100h (a & b) microstructure of austenite and RAFM interface respectively.

Fig.5.17 shows the microstructure of SS base metal after 100 h heat treatment at 1073 K. It shows a discontinuous net work of coarse carbide along grain and twin boundaries. It is worth mentioning that the temperature 1073 K is very close to C curve of $M_{23}C_6$ and similar to PWHT temperature. A decrease in hardness at this higher temperature was observed in contrast to an increase during lower temperature treatment. This is understood on the basis of grain growth, coarsening of carbides and reduction in dislocation & twin density on prolonged heating at higher temperature. **Fig.5.18** compares the typical microstructures of the RAFM-HAZ aged at 973 K and 1073 K for 100 h. HAZ region of RAFM steel aged at 973 K showed tempered martensite microstructure, but when aged at 1073 K showed a mixed microstructure consisting of martensite and tempered martensite. This clearly indicates that this region attained temperatures exceeding Ac_1 due to increase in nickel content which transformed to austenite which further transforms to martensite during cooling.

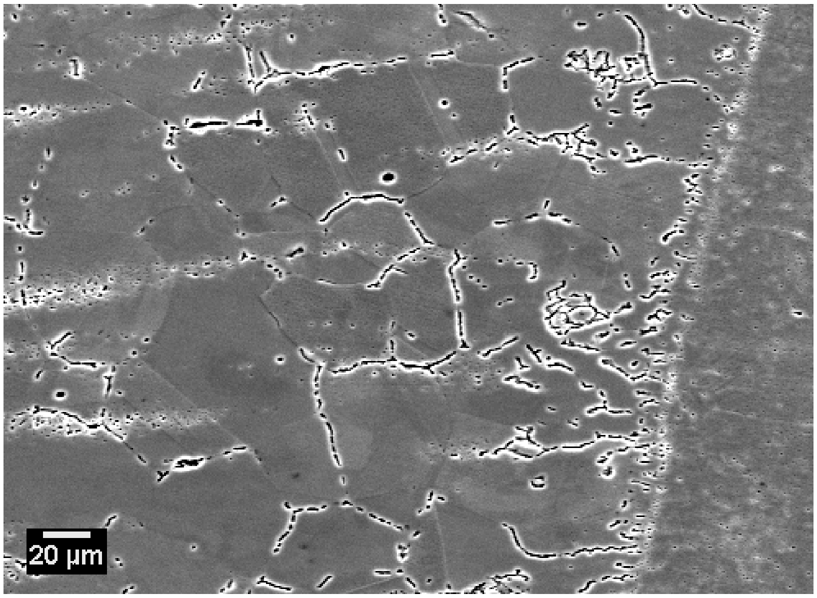

Fig. 5.17: SEM micrograph from SS base metal after exposure to 1073 K/100h, showing precipitation along grain boundaries

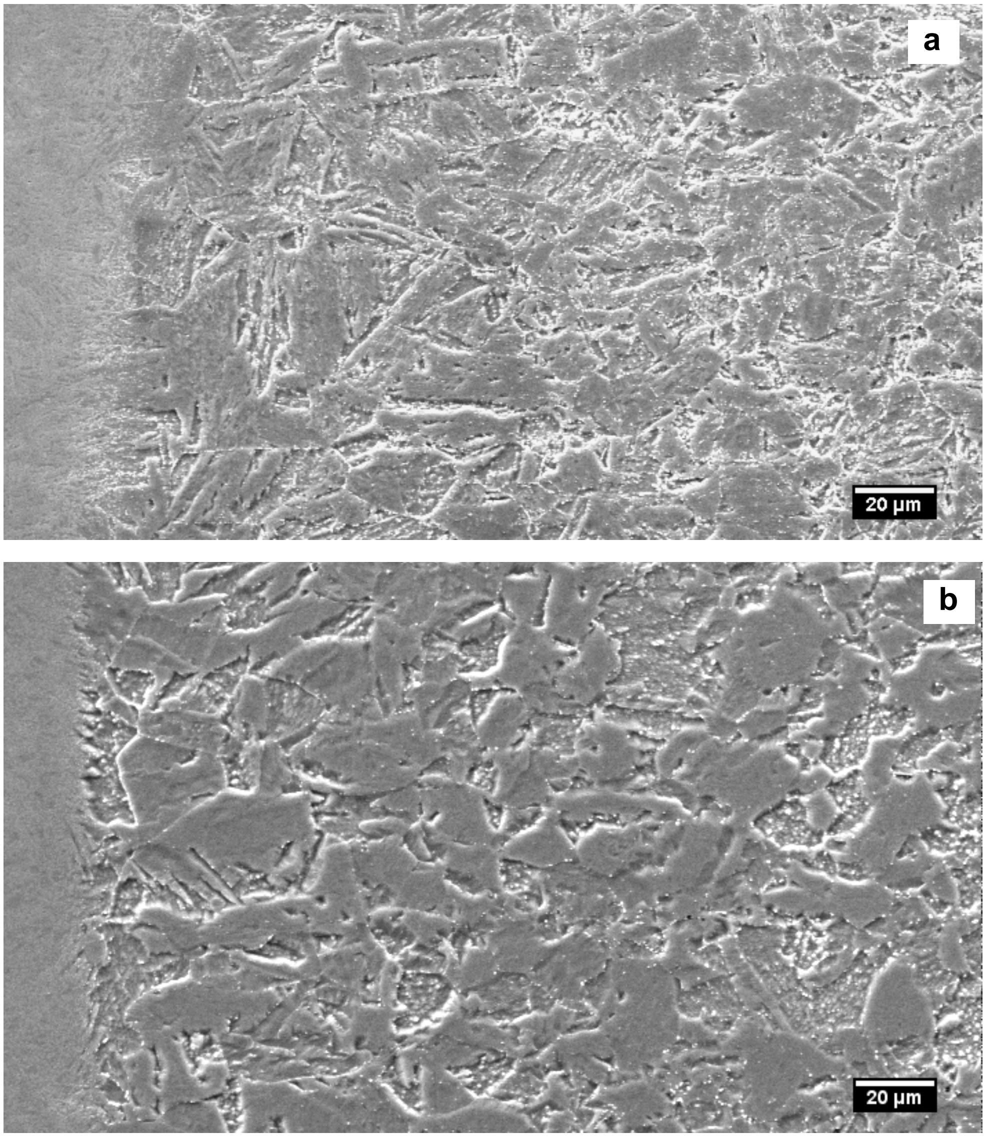

Fig.5.18: SEM micrograph of regions consisting of weld, HAZ and RAFM base metal from dissimilar weld showing (a) tempered martensite after 973 K/100 h (b) mixed microstructure consisting of martensite and tempered martensite at 1073 K/100 h

Fig.5.19 presents the elemental distribution across the weldment after aging for 100 h at 1073 K. Even after aging for 100 h the weld metal composition is not uniform. It is reasonable to assume that diffusion of nickel into HAZ of RAFM steel reduces Ac_1 of the steel, thereby producing martensite near the fusion zone.

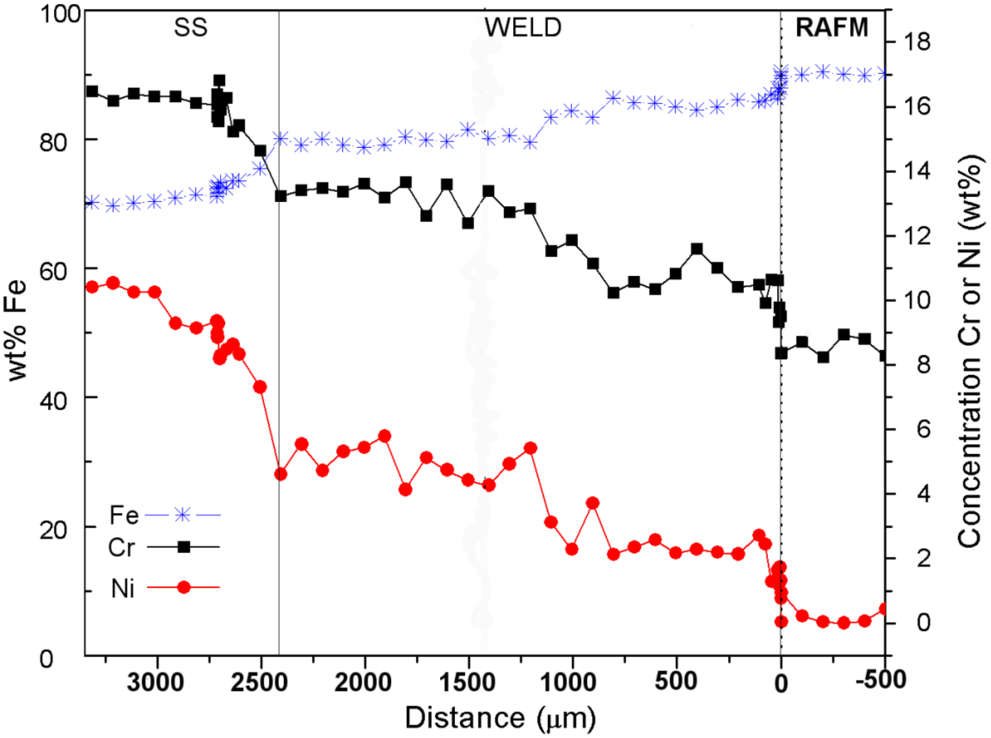

Fig.5.19: Distribution of Cr, Ni & Fe (±1%) across the dissimilar weld joint after thermal exposure at 1073 K for 100h

5.5 Evolution of phases in the SS region near to fusion zone after aging at 1073 K for 100 h

The region near to fusion zone in the austenitic steel side in 'as welded' and PWHT condition showed the presence of small amounts of δ-ferrite in the austenite matrix, while the weld metal showed a predominantly martensitic structure. The effect of thermal exposure at 1073 K for 100 h has been studied by careful preparation of the region of interest by Focused Ion Beam Technique (FIB) in FEG-SEM. **Fig.5.20 (a)** shows a montage of the microstructures from a region which includes weld metal and SS interface. Composition of the alloy at marked (A, B, C & D) regions are given in the adjacent tables. Weld metal showed lath martensite (**Fig.5.20 (b)**) with a mixed composition.

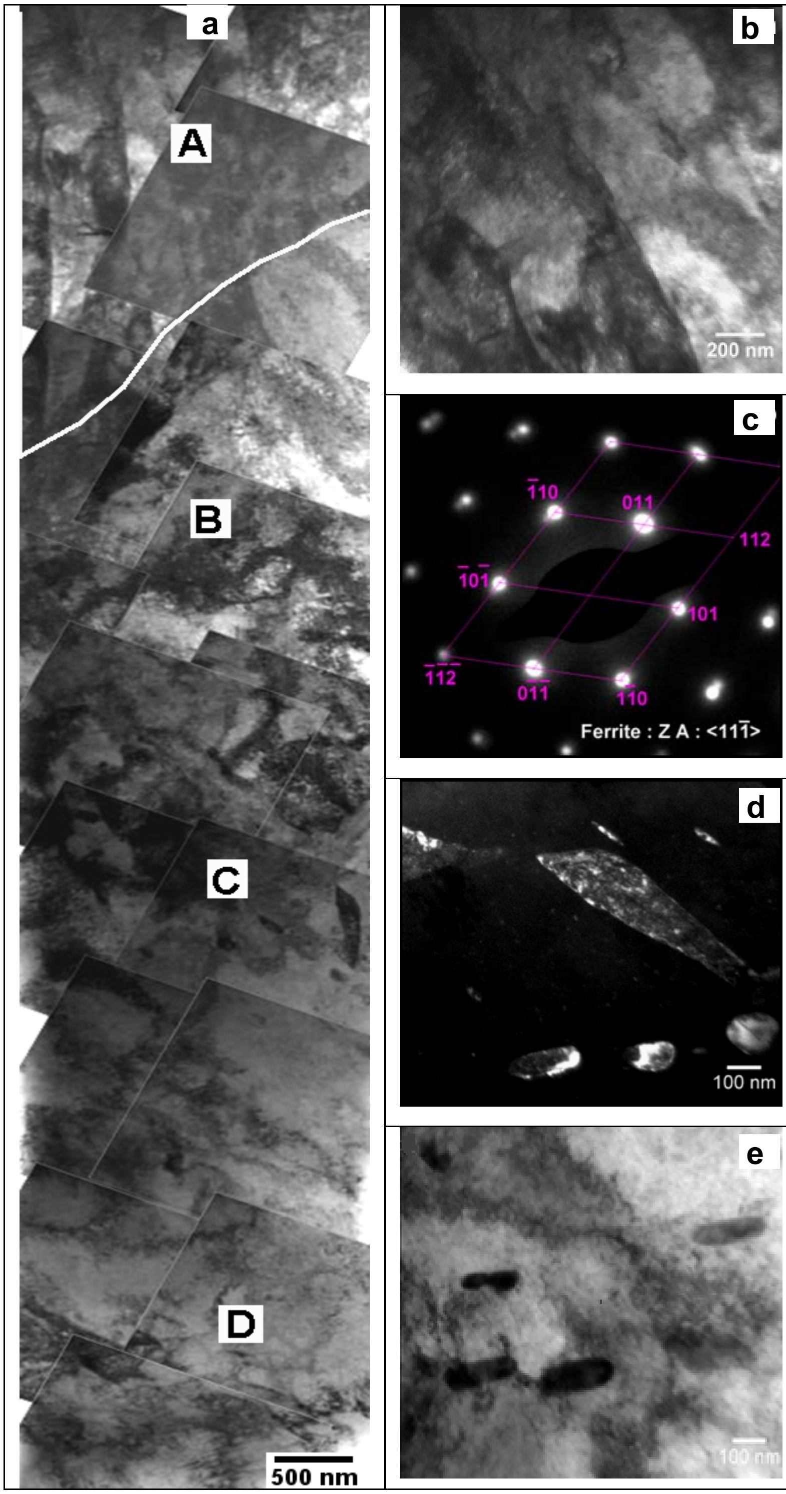

Matrix composition at respective regions marked in **Fig.5.20(a)**

A

Fe	Cr	Mn	Ni
78.3	12.9	1.09	4.07
W	Ta	Mo	
1.03	0.6	2.0	

B

Fe	Cr	Mn	Ni
78.4	13.3	1.01	4.48
W	Ta	Mo	
0.93	0	1.92	

C

Fe	Cr	Mn	Ni
77.4	13.4	1.21	5.93
W	Ta	Mo	
0	0	2.05	

D

Fe	Cr	Mn	Ni
76.3	13.8	1.52	5.61
W	Ta	Mo	
0	0	2.72	

Fig.5.20: (a) A montage of microstructure from region includes weld and SS base metal immediate to fusion zone (fusion line is marked as white line), (b) lath martensite in the weld, (c) SAD from δ-ferrite (d) DF image of δ-ferrite using (101) reflection and (e) presence of $M_{23}C_6$ in austenitic steel after aging.

On moving from fusion zone to austenitic side, concentration of W decreased, while that of Mo increased and diffusion distance of W was limited to ~500µm. But Ni and Cr continued to be same up to ~1 mm. This shows that both Ni and Cr diffused into weld metal. **Fig.5.20 (c & d)** shows diffraction pattern with zone axis $<11\bar{1}>$ and dark field image of δ-ferrite taken using (101) reflections respectively. Presence of δ-ferrite in the steel shows that this phase is stable even after exposing to 1073 K for 100 h.

Another common phase in the austenitic steel σ is formed in the temperature regime 873-1273 K, when Cr content of the steel higher than 20%. Since Cr is a ferrite stabilizer, it is expected that Cr content would be high in δ-ferrite phase, due to which σ phase formation will be promoted. In SS 316 it is reported that σ phase can precipitate after 20 h and 100 h respectively for N contents 0.03% and 0.14% respectively [177]. However, no evidence could be obtained in the present study. It is seen that Cr content at region marked C and D (15-20 µm from fusion line) is ~13.5% against 17% in the unaffected BM. The lowering of Cr content is attributed to diffusion of Cr towards weld metal. A relatively higher content of N of 0.11% and low amount of Cr in the matrix could be responsible for resisting the formation of σ phase. **Fig.5.20 (e)** shows precipitation of $M_{23}C_6$ carbides along the grain boundaries and interiors. This temperature of 1073 K is very near to the nose of TTT diagram for $M_{23}C_6$ and precipitation of carbide is rapid at this temperature. $M_{23}C_6$ is rich in Chromium (~60%) and consumption of Cr by carbide precipitation could also have restricted the formation of σ phase.

5.6 Conclusions

The microstructural characterization of dissimilar weld joints of 1W RAFM-SS316L steels has been carried out. The different regions of weldment have been characterized using SEM, TEM, XRD, DSC etc. Modification of microstructure upon PWHT and aging were studied. The important results are summarized as below:

- Weld microstructure was found to consist of very fine martensite formed through solid state transformation from austenite, which formed as dendrite during solidification.
- Diffusion of Cr and Ni into weld metal adjacent to fusion zone on aging is expected to reduce the average transformation temperatures on the RAFM side of the weldment.
- δ- ferrite was found to be stable even after aging at 1073 K for 100 h, could be due to fairly high N content of the steel and diffusion of Cr to weld metal.
- Aging leads to formation of Cr rich $M_{23}C_6$ carbides in SS316L steel.

Chapter 6

Summary and scope for future work

6. 1 Summary of the work

The present thesis entitled "EVOLUTION OF MICROSTRUCTURE AND CORRELATION WITH PROPERTIES IN WELDMENTS OF 9Cr REDUCED ACTIVATION FERRITIC / MARTENSITIC STEELS discusses the results of a study on the microstructures that evolve on prolonged exposure to near service temperature and welding in two variants of RAFM steel with different tungsten contents. The evolution of microstructures in various regions of the weldment was studied by both computation and experimental methods. Microstructural analysis and phase identification was carried out by employing a variety of techniques like TEM, SEM, EPMA and EBSD and compared with the computational results. Mechanical property evaluation was carried out using small specimen testing and correlated with the observed microstructure. A brief summary of the following three major themes are described in this chapter.

- Microstructural evolution in RAFM steels and its consequence on mechanical properties
- Comparison of different welding methods with respect to microstructural modifications
- Characterization of RAFM-316L dissimilar welds joint

The first theme dealt with the difference in the microstructural evolution of two varients of RAFM steel, emphasizing type, size and chemistry of secondary phases and its influence on mechanical properties. Analytical Transmission Electron Microscopy studies on two variants 1W and 1.4W (INRAFM)) of normalized and tempered RAFM steels showed a tempered martensitic structure with retention of lath structure. The phase fraction of secondary phases was computed using JMatPro® software and the results were supplemented by experimental studies by Analytical Transmission Electron Microscopy. The microstructural evolution on long term service temperature exposures of 1W and INRAFM steels have been studied by experiments as well as computation. The salient results of the study are as follows:

- The carbides in normalized and tempered steel were identified as Cr rich $M_{23}C_6$ and V/Ta rich MX carbides.
- Higher tungsten content in INRAFM steel delayed the coarsening of carbides and growth of laths; Coarsening of MX was negligible in both the steels.
- Computation by JMatPro® calculated the existence of M_2X carbo-nitrides only up to 4 h of heat treatment at 873 K.
- A progressive enrichment of Cr is observed in $M_{23}C_6$ upon aging, also supported by computation.
- JMatPro® predicted the nucleation of Laves phase at 773 K in 1W RAFM steel. But no experimental evidence could be obtained even after 10000 h of aging which is attributed to kinetic factors.
- Laves phase nucleates at 823 K in INRAFM steel and forms as a continuous network around ~10000 h of aging.
- Creep properties of the two steels in normalized tempered condition were compared using impression creep test.
- Change in creep rate on aging of INRAFM is estimated and correlated with coarsening of carbides and formation of Laves phase.

- DBTT measurement using small punch test showed no significant difference between the two steels. An increase in DBTT of INRAFM steel on aging was supported by the microstructural degradation caused by Laves phase distribution.

The second theme focused on detailed electron microscopy study on comparison of microstructures that formed in various regions of weldment prepared by three different welding methods namely Tungsten Inert Gas (TIG) welding, Electron Beam (EB) welding and Laser Beam (LB) welding. The optimization of PWHT conditions was carried out based on microstructure and hardness values. Role of initial microstructure, alloy composition and temperature on the kinetics of evolution of secondary phases during prolonged thermal exposure was studied by experimental and computational methods. The narrow but significant HAZ regions of weldments were physically replicated by GLEEBLE thermo-mechanical simulator and microstructures were compared with actual weldments. A brief summary of the results are given below:

- Coarse and fine PAGS in HAZ is controlled by the peak temperature and cooling rate which is dictated by distance between the region of interest and the heat source.
- Decrease in hardness across the HAZ is understood based on the decreasing peak temperature, which dictates the extent of carbon super saturation and dislocation density in the martensite.
- Negligible amount of carbides in CGHAZ in TIG weld is attributed to the complete dissolution of carbides at high temperatures prevailing in the CGHAZ.
- Thermal cycling experienced by different regions of autogenous weldment was calculated using Rosenthal's steady state solutions to heat transfer equation.

- Weld metal of TIG joint showed a coarser PAGS compared to EB and LB welds due to the higher residence time at temperatures above A_{c3}.
- No preferential texture was observed in the three welds.
- A post weld heat treatment at 1033 K for 2 h was found to be optimum for TIG welds.
- The activation energy for the tempering process was evaluated and found to be in agreement with the activation energy for migration of carbon in ferrite matrix.
- Temperature-time window for the formation of Laves phase in various regions of RAFM steel weldments have been identified by JMatPro based computations.
- Experimental results indicate the formation of Fe_2W type Laves phase in FGHAZ of INRAFM steel at an early stage of exposure to temperatures ≥823 K. Laves phase could not be detected in 1W-RAFM steel under identical experimental conditions. This is attributed to the abundant carbide precipitations in this region leading to an increase in W and decrease in C content locally which does favor nucleation and growth of Laves phase.
- FGHAZ was identified as the most susceptible region to failure in the INRAFM weld on service exposure due to enhanced kinetics of precipitation of Laves phases

The third theme consists of microstructural characterization of dissimilar weld joint between austenitic SS316L and ferritic INRAFM steel by electron beam welding. Major alloy composition of weld metal was determined by EPMA analysis. Knowing the actual Ni and Cr content in both the alloys, the fraction of weld dilution from each alloy was calculated by mass balance, since there is no filler addition in the welding. By estimating the Cr_{eq} and Ni_{eq} values of the base metals and weld dilution ratio, the position of weld metal in the Schaeffler-Schneider diagram was identified. The phase identification of weld metal was carried out by X-ray diffraction, EBSD and TEM. Further microstructural evolution was studied during PWHT and elevated temperature exposures. The shift in the transformation temperature due to mixing of the elements of the two alloys was studied by Differential Scanning Calorimetry. The effect of thermal exposure at 1073 K for 100 h has been studied by careful preparation of specific regions of interest by Focused Ion Beam Technique (FIB). The important results of the study as follows:

- The weld consisted of very fine dendritic martensite microstructure.
- The observed reduction in the transformation temperatures is due to diffusion of Cr and Ni into weld metal.
- Delta ferrite was found to be stable even after aging at 1073 K.
- The absence of σ- phase could be due to fairly high N content of the steel and diffusion of Cr to weld metal.
- Thermal exposure of HAZ region of SS316L leads to formation of Cr rich carbides.

6.2 Scope for future work

- Identification and quantification of secondary phases by elecro-chemical extraction after 20000 h of exposure at service temperatures
- Effect of irradiation on the formation and chemistry of secondary phases
- Study of fracture toughness by small punch test on irradiated INRAFM steel
- Exploring the possibility of hybrid LASER-TIG welding of INRAFM steel and its characterisation

REFERENCES:

1. https://iter.org/doc/www/content/com/.../2006_11_iter_agreement.pdf.
2. https://www.euro-fusion.org.
3. Hong, B.G., Lee, D. W., Wang,S. J., Kim, Y. H., In, W. K., Yoon, K. H. , *Basic concepts of DEMO and a design of a helium cooled molten lithium blanket for testing in ITER.* Fusion Eng. Des. , 2007. **82**: p. 2399.
4. Kohyama, A., Kohno, Yutaka., Asakura, Kentaro., Kayano, Hideo, *R&D of low activation ferritic steels for fusion in japanese universities.* Journal of Nuclear Materials, 1994. **212–215, Part 1**: p. 684-689.
5. N. Baluc., R., Schäublin., P, Spätig., M, Victoria, *On the potentiality of using ferritic/martensitic steels as structural materials for fusion reactors.* Nuclear Fusion, 2004. **44**(1): p. 56.
6. Zinkle, S.J., Busby, Jeremy T., *Structural materials for fission & fusion energy.* Materials Today, 2009. **12**(11): p. 12-19.
7. *Fusion Technology: Annual report of the association CEA/EUROATOM*. 2000. p. 199-200.
8. Giancarli, L.M., et al., *Overview of the ITER TBM Program.* Fusion Engineering and Design, 2012. **87**(5–6): p. 395-402.
9. Chuyanov, V.A., D.J. Campbell, and L.M. Giancarli, *TBM Program implementation in ITER.* Fusion Engineering and Design, 2010. **85**(10–12): p. 2005-2011.
10. Butterworth, G.J., *Objectives and prospects for low-activation materials.* Journal of Nuclear Materials, 1991. **179–181, Part 1**: p. 135-142.

11. Ian, C., W. David, and D. Sergei, *Implications of fusion power plant studies for materials requirements.* Plasma Physics and Controlled Fusion, 2002. **44**(12B): p. B121.

12. Thomas Paul V, S. Saroja, and M. Vijayalakshmi, *Microstructural stability of modified 9Cr–1Mo steel during long term exposures at elevated temperatures.* Journal of Nuclear Materials, 2008. **378**(3): p. 273-281.

13. Klueh, R.L. and D.R. Harries, *High-Chromium Ferritic and Martensitic Steels for Nuclear Applications*, ed. ASTM. Vol. ASTM MONO3. 2001, USA: pp.30.

14. Saroja, S., M. Vijayalakshmi, and V.S. Raghunathan, *Influence of cooling rates on the transformation behavior of 9Cr-1Mo-0.07C steel.* J.Mater.Sci., 1992. **27**(9): p. 2389-2396.

15. Vijayalakshmi, M., Saroja, S, Mythili, R, Paul, V Thomas, Raghunathan, VS, *Mechanisms and kinetics of tempering in weldments of 9Cr–1Mo steel.* Journal of nuclear materials, 2000. **279**(2): p. 293-300.

16. Klueh, R.L., *Reduced-activation bainitic and martensitic steels for nuclear fusion applications.* Current Opinion in Solid State and Materials Science, 2004. **8**(3–4): p. 239-250.

17. Salavy, J.F., Boccaccini, L. V., Chaudhuri, P., Cho, S., Enoeda, M., Giancarli, L. M., Kurtz, R. J., Luo, T. Y., Rao, K. Bhanu Sankara, Wong, C. P. C., *Must we use ferritic steel in TBM?* Fusion Engineering and Design, 2010. **85**(10–12): p. 1896-1902.

18. Harrelson, K.J., S.H. Rou, and R.C. Wilcox, *Impurity element effects on the toughness of 9Cr-1Mo steel.* Journal of Nuclear Materials, 1986. **141–143, Part 1**: p. 508-512.

19. Bloom, E.E., *The challenge of developing structural materials for fusion power systems.* Journal of Nuclear Materials, 1998. **258–263, Part 1**: p. 7-17.

20. Masuyama, F., *History of Power Plants and Progress in Heat Resistant Steels.* ISIJ International, 2001. **41**(6): p. 612-625.

21. Kohyama, A., Hishinuma, A., Gelles, D. S., Klueh, R. L., Dietz, W., Ehrlich, K., *Low-activation ferritic and martensitic steels for fusion application.* Journal of Nuclear Materials, 1996. **233–237, Part 1**: p. 138-147.

22. Abe, F., *Effect of fine precipitation and subsequent coarsening of Fe2W laves phase on the creep deformation behavior of tempered martensitic 9Cr-W steels.* Metallurgical and Materials Transactions A, 2005. **36**(2): p. 321-332.

23. Hong, S.G., W.B. Lee, and C.G. Park, *The effects of tungsten addition on the miocrostructural stability of 9Cr-Mo steels.* J. Nuc. Mater., 2001. **288**: p. 202-207.

24. Cermak. J, K.J., Million. B, Krumpos. J, *Self-Diffusion of Fe in the Fe-W Solid Solutions in Neighbourhood of the Curie Temperature.* Kov. Mater. , 1980. **18** p. 537.

25. Lee, J.S., Armaki, Hassan Ghassemi., Maruyama, Kouichi., Muraki, Taro., Asahi, Hitoshi, *Causes of breakdown of creep strength in 9Cr–1.8W–0.5Mo–VNb steel.* Materials Science and Engineering: A, 2006. **428**(1–2): p. 270-275.

26. Panait, C.G., Bendick, W., Fuchsmann, A., Gourgues-Lorenzon, A. F., Besson, J., *Study of the microstructure of the Grade 91 steel after more than 100,000 h of creep exposure at 600 °C.* International Journal of Pressure Vessels and Piping, 2010. **87**(6): p. 326-335.

27. Hosoi, Y., Wade, N., Kunimitsu, S., Urita, T., *Precipitation behavior of laves phase and its effect on toughness of 9Cr-2Mo Ferritic-martensitic steel.* Journal of Nuclear Materials, 1986. **141–143, Part 1**: p. 461-467.

28. Dimmler, G., Weinert, P., Kozeschnik, E., Cerjak, H., *Quantification of the Laves phase in advanced 9–12% Cr steels using a standard SEM.* Materials Characterization, 2003. **51**(5): p. 341-352.

29. van der Schaaf, B., Gelles, D. S., Jitsukawa, S., Kimura, A., Klueh, R. L., Möslang, A., Odette, G. R., *Progress and critical issues of reduced activation ferritic/martensitic steel development.* Journal of Nuclear Materials, 2000. **283–287, Part 1**: p. 52-59.

30. Klueh, R.L., Gelles, D. S.Jitsukawa, S.Kimura, A.Odette, G. R.van der Schaaf, B.Victoria, M., *Ferritic/martensitic steels – overview of recent results.* Journal of Nuclear Materials, 2002. **307–311, Part 1**: p. 455-465.

31. Tamura, M., Hayakawa, H., Yoshitake, A., Hishinuma, A., Kondo, T., *Phase stability of reduced activation ferritic steel: 8%Cr-2%W-0.2%V-0.04%Ta-Fe.* Journal of Nuclear Materials, 1988. **155–157, Part 2**: p. 620-625.

32. Abe, F., H. Araki, and T. Noda, *The effect of tungsten on dislocation recovery and precipitation behavior of low-activation martensitic 9Cr steels.* Metallurgical Transactions A, 1991. **22**(10): p. 2225-2235.

33. Klueh, R.L. and P.J. Maziasz, *The microstructure of chromium-tungsten steels.* Metallurgical Transactions A, 1989. **20**(3): p. 373-382.

34. Alamo, A., Brachet, J. C., Castaing, A., Lepoittevin, C., Barcelo, F., *Physical metallurgy and mechanical behaviour of FeCrWTaV low activation martensitic steels: Effects of chemical composition.* Journal of Nuclear Materials, 1998. **258–263, Part 2**: p. 1228-1235.

35. S Raju, G., B. Jeya, Rai, Arun Kumar, Mythili, R., Saroja, S., Mohandas, E., Vijayalakshmi, M., Rao, K. B. S., Raj, Baldev, *Measurement of Transformation Temperatures and Specific Heat Capacity of Tungsten Added Reduced Activation Ferritic - Martensitic Steel (RAFM).* J. Nuc. Mater., 2009. **389**: p. 385-393.

36. Raju, S., Jeya Ganesh, B., Rai, Arun Kumar, Mythili, R., Saroja, S., Raj, Baldev, *A study on martensitic phase transformation in 9Cr–1W–0.23V–0.063Ta–0.56Mn–0.09C–0.02N (wt.%) reduced activation steel using differential scanning calorimetry.* Journal of Nuclear Materials, 2010. **405**(1): p. 59-69.

37. Karthikeyan, T., V Thomas, Paul, Saroja, S, Moitra, A, Sasikala, G, Vijayalakshmi, M, *Grain refinement to improve impact toughness in 9Cr–1Mo steel through a double austenitization treatment.* Journal of Nuclear Materials, 2011. **419**(1): p. 256-262.

38. Armaki, H.G., Chen, Ruiping., Maruyama, Kouichi., Igarashi, Masaaki, *Creep behavior and degradation of subgrain structures pinned by nanoscale precipitates in strength-enhanced 5 to 12 pct Cr ferritic steels.* Metallurgical and Materials Transactions A, 2011. **42**(10): p. 3084-3094.

39. Kostka, A., Tak, K. G., Hellmig, R. J., Estrin, Y., Eggeler, G., *On the contribution of carbides and micrograin boundaries to the creep strength of tempered martensite ferritic steels.* Acta Materialia, 2007. **55**(2): p. 539-550.

40. Tamura, M., Shinozuka, K., Masamura, K., Ishizawa, K., Sugimoto, S., *Solubility product and precipitation of TaC in Fe–8Cr–2W steel.* Journal of Nuclear Materials, 1998. **258–263, Part 2**: p. 1158-1162.

41. Brinkman, C.R., B. Gieseke, and P.J. Maziasz, *The influence of long term thermal aging on the microstructure and mechanical properties of modified 9Cr-1Mo steel*, in *Microstructures and Mechanical Properties of Aging Material*, R.V. P.K. Liaw, K.L. Murty, E.P. Simonen and D. Frear, Editor. 1993, The Minerals, Metals& Materials Society. p. 107-116.

42. Saroja, S., M. Vijayalakshmi, and V.S. Raghunathan, *Effect of prolonged exposures of 9Cr-1Mo-0.07C steel to elevated temperatures.* Mater.Trans. JIM, 1993. **34**(10): p. 901.

43. Mythili, R., Ravikirana,, Vanaja, J., Laha, K., Saroja, S., Jayakumar, T., Mathew, M. D., Rajendrakumar, E., *Microstructural Modifications Due to Tungsten and Tantalum in 9Cr Reduced Activation Ferritic Martensitic Steels on Creep Exposure.* Procedia Engineering, 2013. **55**: p. 295-299.

44. Sawada, K., Kushima, H., Hara, T., Tabuchi, M., Kimura, K., *Heat-to-heat variation of creep strength and long-term stability of microstructure in Grade 91 steels.* Materials Science and Engineering: A, 2014. **597**: p. 164-170.

45. Tavassoli, A.A.F., *Present limits and improvements of structural materials for fusion reactors – a review.* Journal of Nuclear Materials, 2002. **302**(2–3): p. 73-88.

46. Jitsukawa, S., Tamura, M., van der Schaaf, B., Klueh, R. L., Alamo, A., Petersen, C., Schirra, M., Spaetig, P., Odette, G. R., Tavassoli, A. A., Shiba, K., Kohyama, A., Kimura, A., *Development of an extensive database of mechanical and physical properties for reduced-activation martensitic steel F82H.* Journal of Nuclear Materials, 2002. **307–311, Part 1**: p. 179-186.

47. Spatig, P., Baluc, N., *Proton Irradiation up to 1 dpa of Plate, for He Effect Testing*, in *Report on EFDA Task TW1-TTMS-001 deliverable 3*. 2001.

48. Rieth M., M., Schirra, , Falkenstein A., Graf P., Heger S., Kempe H., Lindau R., Zimmermann H, *EUROFER 97 – Tensile, Charpy, Creep and structural tests*. 2003, FZKA. p. 6911.

49. Chun, Y.B., Kang, S. H., Noh, S., Kim, T. K., Lee, D. W., Cho, S., Jeong, Y. H., *Effects of alloying elements and heat treatments on mechanical properties of Korean reduced-activation ferritic–martensitic steel.* Journal of Nuclear Materials, 2014. **455**(1–3): p. 212-216.

50. Shankar, V., Mariappan, K., Sandhya, R., Laha, K., Jayakumar, T., Kumar, E. Rajendra, *Effect of W and Ta on creep–fatigue interaction behavior of reduced activation ferritic–martensitic (RAFM) steels.* Fusion Engineering and Design, 2015.

51. Baluc, N., et al., *Status of reduced activation ferritic/martensitic steel development.* Journal of Nuclear Materials, 2007. **367–370, Part A**: p. 33-41.

52. Okubo, N., Wakai, E., Matsukawa, S., Sawai, T., Kitazawa, S., Jitsukawa, S., *Effects of heat treatment and irradiation on mechanical properties in F82H steel doped with boron and nitrogen.* Journal of Nuclear Materials, 2007. **367–370, Part A**: p. 107-111.

53. Ando, M., Wakai, E., Sawai, T., Tanigawa, H., Furuya, K., Jitsukawa, S., Takeuchi, H., Oka, K., Ohnuki, S., Kohyama, A., *Synergistic effect of displacement damage and helium atoms on radiation hardening in F82H at TIARA facility.* Journal of Nuclear Materials, 2004. **329–333, Part B**: p. 1137-1141.

54. Ando, M., Li, M., Tanigawa, H., Grossbeck, M. L., Kim, S., Sawai, T., Shiba, K., Kohno, Y., Kohyama, A., *Creep behavior of reduced activation ferritic/martensitic steels irradiated at 573 and 773 K up to 5 dpa.* Journal of Nuclear Materials, 2007. **367–370**(Part A): p. 122-126.

55. Sawai, T., Wakai, E., Jitsukawa, S., Hishinuma, A., *Phase stability and mechanical properties of irradiated Ti–Al–V intermetallic compound.* Journal of Nuclear Materials, 2002. **307–311, Part 1**: p. 389-392.

56. Klueh, R.L., Vitek J. M. , *Elevated-temprature tensile properties of irradiated 9Cr-1 MoVNb steel.* J. Nuc. Mater., 1985. **132**: p. 27-31.

57. Klueh, R.L., Vitek J. M. , *Tensile properties of 9Cr-1MoVNb and 12Cr-1moVW steel irradiated to 23dpa at 390 to 550*^{0} *C.* J.Nuc.Mater., 1991. **182**: p. 230-239.

58. Baluc, N., *The Mechanical Properties and Microstructure of the OPTIMAX Series of Low Activation Ferritic-Martensitic Steels.* Journal of Nuclear Materials, 2000. **283-287**.

59. Wong, C.P.C., Salavy, J. F., Kim, Y., Kirillov, I., Rajendra Kumar, E., Morley, N. B., Tanaka, S., Wu, Y. C., *Overview of liquid metal TBM concepts and programs.* Fusion Engineering and Design, 2008. **83**(7–9): p. 850-857.

60. Dethloff, C., et al., *Modeling of helium bubble nucleation and growth in neutron irradiated boron doped RAFM steels.* Journal of Nuclear Materials, 2012. **426**(1–3): p. 287-297.

61. Borodin, V.A. and P.V. Vladimirov, *Kinetic properties of small He–vacancy clusters in iron.* Journal of Nuclear Materials, 2009. **386–388**: p. 106-108.

62. Lindau, R., et al., *Present development status of EUROFER and ODS-EUROFER for application in blanket concepts.* Fusion Engineering and Design, 2005. **75–79**: p. 989-996.

63. Tokunaga, K.K., Akira; Araki, Kuniaki;Fujiwara, Tadashi; Miyamoto, Yoshio; Nakamura, Kazuo;Kurumada, Akira; Tokitani, Masayuki; Masuzaki, Suguru;Ezato, Koichiro; Suzuki, Satoshi; Enoeda, Mikio;Akiba,Masato, *Tungsten coatings on reduced-activation ferritic/martensitic steel by plasma spray technique : Thermal behavior of Tungsten coatings.* Transactions of JWR, 2010. **39**(2): p. 331-332.

64. Qu, D.D., W.W. Basuki, and J. Aktaa, *Numerical assessment of functionally graded tungsten/EUROFER coating system for first wall applications.* Fusion Engineering and Design, (In press).

65. Furuya, K., Wakai, E., Ando, M., Sawai, T., Nakamura, K., Takeuchi, H., Iwabuchi, A., *Microstructure and hardness of HIP-bonded regions in F82H*

blanket structures. Journal of Nuclear Materials, 2002. **307–311, Part 1**: p. 289-292.

66. P.H. Wang, J.M.C., Z.Y. Xu, *Research and development of reduced activation ferritic/martensitic steel CLF-1 at SWIP*, in *23rd IAEA Fusion Energy Conference*. 2010 Daejon, Republic of Korea.

67. Nozawa, T., Ogiwara, Hiroyuki., Kannari, Jun., Kishimoto, Hirotatsu., Tanigawa, Hiroyasu, *Torsion test technique for interfacial shear evaluation of F82H RAFM HIP-joints.* Fusion Engineering and Design, 2011. **86**(9–11): p. 2512-2516.

68. Raj, B., K.B.S. Rao, and A.K. Bhaduri, *Progress in the development of reduced activation ferritic-martensitic steels and fabrication technologies in India.* Fusion Engineering and Design, 2010. **85**(7–9): p. 1460-1468.

69. Aubert, P., Tavassoli, F., Rieth, M., Diegele, E., Poitevin, Y., *Review of candidate welding processes of RAFM steels for ITER test blanket modules and DEMO.* Journal of Nuclear Materials, 2011. **417**(1–3): p. 43-50.

70. Tanigawa, H., Hirose, T., Shiba, K., Kasada, R., Wakai, E., Serizawa, H., Kawahito, Y., Jitsukawa, S., Kimura, A., Kohno, Y., Kohyama, A., Katayama, S., Mori, H., Nishimoto, K., Klueh, R. L., Sokolov, M. A., Stoller, R. E., Zinkle, S. J., *Technical issues of reduced activation ferritic/martensitic steels for fabrication of ITER test blanket modules.* Fusion Engineering and Design, 2008. **83**(10–12): p. 1471-1476.

71. T. Jayakumar, E.R., Kumar, , *Indian Test Blanket Module in ITER - Development of RAFM Steel and Fabrication Technology* Advances in Science and Technology, 2014. **94**(Oct): p. 1-11.

72. Zhong, Z., Jung, Hun-chea., Hinoki, Tatsuya., Kohyama, Akira, *Effect of joining temperature on the microstructure and strength of tungsten/ferritic steel joints diffusion bonded with a nickel interlayer.* Journal of Materials Processing Technology, 2010. **210**(13): p. 1805-1810.

73. Arivazhagan, B., Srinivasan, G., Albert, S. K., Bhaduri, A. K., *A study on influence of heat input variation on microstructure of reduced activation ferritic martensitic steel weld metal produced by GTAW process.* Fusion Engineering and Design, 2011. **86**(2–3): p. 192-197.

74. Hirose, T., Shiba, K., Sawai, T., Jitsukawa, S., Akiba, M., *Effects of heat treatment process for blanket fabrication on mechanical properties of F82H.* Journal of Nuclear Materials, 2004. **329–333, Part A**: p. 324-327.

75. Vijayalakshmi, M., Saroja, S., Paul, V. Thomas, Mythili, R., Raghunathan, V.S., *Microstructural zones in the primary solidification structure of weldment of 9Cr-1Mo steel.* Metall. Mater. Trans. A, 1999. **30**: p. 161-174.

76. Thomas Paul V, S., Saroja., Hariharan, P., Rajadurai, A., Vijayalakshmi, M., *Identification of microstructural zones and thermal cycles in a weldment of modified 9Cr-1Mo steel.* Journal of materials science, 2007. **42**(14): p. 5700-5713.

77. Allen, D.J. and S.J. Brett. *Failure of modified 9Cr header endplate*. in *Case Histories on Integrity and Failure in Industry*. 1999. Milan, Italy: Engineering Materials Advisory Sevices Ltd, London, UK.

78. Francis, J., W. Mazur, and H. Bhadeshia, *Review Type IV cracking in ferritic power plant steels.* Materials Science and Technology, 2006. **22**(12): p. 1387-1395.

79. Jiang, Z., Ren, Litian., Huang, Jihua., Ju, Xin., Wu, Huibin., Huang, Qunying., Wu, Yican, *Microstructure and mechanical properties of the TIG welded joints of fusion CLAM steel.* Fusion Engineering and Design, 2010. **85**(10–12): p. 1903-1908.

80. Artinger, I. and Z. Rózsavölgyi, *Research and Development of New Martensitic Steels.* Materials Science Forum, 2003 **414-415**: p. 51-56.

81. C.R. Das, S.K.A., Shiju Sam, P. Mastanaiah, G.M.S.K. Chaitanya, A.K. Bhaduri, T. Jayakumar, C.V.S. Murthy, E. Rajendra Kumar, *Mechanical properties of 9Cr–1W reduced activation ferritic martensitic steel weldment prepared by electron beam welding process.* Fusion Engineering and Design, 2014. **89**(11): p. 2672-2678.

82. Samuel, E.I., B.K. Choudhary, and K.B.S. Rao, *Influence of post-weld heat treatment on tensile properties of modified 9Cr–1Mo ferritic steel base metal.* Materials Science and Technology, 2007. **23**(8): p. 992-999.

83. Hamzah, M.Z., Ibrahim, M. L., Chye, Q. H., Ahmad, B., Inayat-Hussain, J. I., Purbolaksono, J., *Evaluation on the hardness and microstructures of T91 reheater tubes after post-weld heat treatment.* Engineering Failure Analysis, 2012. **26**: p. 349-354.

84. Rensman, J., van Hoepen, J., Bakker, J. B. M., den Boef, R., van den Broek, F. P., van Essen, E. D. L., *Tensile properties and transition behaviour of RAFM steel plate and welds irradiated up to 10 dpa at 300 °C.* Journal of Nuclear Materials, 2002. **307–311, Part 1**: p. 245-249.

85. Rieth, M. and J. Rey, *Specific welds for test blanket modules.* Journal of Nuclear Materials, 2009. **386–388**: p. 471-474.

86. Allen, D. and S. Brett. *Premature failure of a P91 header endcap weld: minimising the risks of additional failures*. in *Case Histories in Failure Investigation, Milan*. 1999.

87. Chandravathi, K.S., et al., *Effect of isothermal heat treatment on microstructure and mechanical properties of Reduced Activation Ferritic Martensitic steel.* Journal of Nuclear Materials, 2013. **435**(1–3): p. 128-136.

88. Laha, K., Chandravathi, K. S., Parameswaran, P., Goyal, Sunil, Mathew, M. D., *A Comparison of Creep Rupture Strength of Ferritic/Austenitic Dissimilar Weld Joints of Different Grades of Cr-Mo Ferritic Steels.* Metallurgical and Materials Transactions A, 2012. **43**(4): p. 1174-1186.

89. Albert, S.K., Das, C. R., Sam, Shiju, Mastanaiah, P., Patel, M., Bhaduri, A. K., Jayakumar, T., Murthy, C. V. S., Kumar, Rajendra, *Mechanical properties of similar and dissimilar weldments of RAFMS and AISI 316L (N) SS prepared by electron beam welding process.* Fusion Engineering and Design, 2014. **89**(7–8): p. 1605-1610.

90. Race, J. and H. Bhadeshia, *Carbon migration across dissimilar steel welds.* International trends in welding science and technology, 1993: p. 1-5.

91. Albert, S., Gill, TPS., Tyagi, AK., Mannan, SL., Kulkarni, SD., Rodriguez, P, *Soft zone formation in dissimilar welds between two Cr-Mo steels.* Welding Journal-Including Welding Research Supplement, 1997. **76**(3): p. 135-142.

92. Saroja, S., Dasgupta, A., Divakar, R., Raju, S., Mohandas, E., Vijayalakshmi, M., Bhanu Sankara Rao, K., Raj, Baldev, *Development and characterization of advanced 9Cr ferritic/martensitic steels for fission and fusion reactors.* Journal of Nuclear Materials, 2011. **409**(2): p. 131-139.

93. Vanaja, J., Laha, K., Mythili, R., Chandravathi, K. S., Saroja, S., Mathew, M. D., *Creep deformation and rupture behaviour of 9Cr–1W–0.2V–0.06Ta Reduced Activation Ferritic–Martensitic steel.* Materials Science and Engineering: A, 2012. **533**: p. 17-25.

94. Sasmal, C.S., Chandravathi, K. S., Nandagopal, M., Selvi, S. Panneer, Parameswaran, P., Laha, K., Mathew, M. D., Jayakumar, T., Kumar, E. Rajendra, *Effect of Tungsten on Mechanical Properties of Reduced Activation Ferritic-Martensitic Steel Subjected to Intercritical Heat Treatment.* Procedia Engineering, 2013. **55**: p. 277-283.

95. Vanaja, J., Laha, K., Nandagopal, M., Sam, Shiju, Mathew, M. D., Jayakumar, T., Rajendra Kumar, E., *Effect of tungsten on tensile properties and flow behaviour of RAFM steel.* Journal of Nuclear Materials, 2013. **433**(1–3): p. 412-418.

96. T. Jayakumar., M.D., Mathew., K. Laha., S. K. Albert., S. Saroja., E. Rajendra Kumar., C. V. S. Murthy., G. Padmanabham., G. Appa Rao., S. Narahari Prasad, *Reduced Activation Ferritic Martensitic Steel and Fabrication Technologies for the Indian Test Blanket Module in ITER.* Fusion Science and Technology 2014. **65** (2): p. 171-185.

97. K.A. Gopal, S., Murugan , S. Venugopal , K.V. Kasiviswanathan, *Laser Welding of Precision Engineering Components* Indian Welding Journal, 2011. **44**(2): p. 54-59.

98. Voort, G.F.V., *Metallography Principles and Practice*. 1984, New York: Mc-Graw- Hill book Company.

99. Kenik, E.A. and P.J. Maziasz. *Application of extraction replicas and analytical electron microscopy to precipitate phase studies*. in *AnalyticalElectron Microscopy Meeting*. 1984. Bethlehem, PA (USA): Microbeam Analysis Society.

100. Mitchell, D.R.G. and S. Sulaiman, *Advanced TEM specimen preparation methods for replication of P91 steel.* Materials Characterisation, 2006. **56**: p. 49-58.

101. PDF-4+, *database*. 2013, International Centre for Diffraction Data (ICDD): USA.

102. Scott, V.D., G. Love, and S.J.B. Reed, *Quantitative electron-probe microanalysis*. 1995: Ellis Horwood Ltd, UK.

103. Joy, D.C., A.D. Romig, and J.I. Goldstein, *Principles of Analytical Electron Microscopy*. 1986, New York: Plenum Press.

104. Edington, J.W., *Practical Electron Microscopy in Materials Science*. 1976, New York: Van Nostrand Reinhold.

105. Andrews, K.W., Dyson, D. J., Keown, S. R., *Interpretation of electron diffraction patterns*. 1971, London: Adam Hilger Ltd.

106. Williams, D.B. and C.B. Carter, *Transmission Electron Microscopy*. 1996, New York: Plenum Press.

107. Mukherjee, T., W.E. Stumpf, and C.M. Sellars, *Quantitative assessment of extraction replicas for particle analysis.* Journal of materials science, 1968. **3**(2): p. 127-135.

108. Cliff, G. and G.W. Lorimer, eds. *Quantitative Microanalysis with High Spatial Resolution*. ed. M.H.J. G.W. Lorimer, P. Doigt. 1981, The Metals Society: London.

109. Kattner, U., *The thermodynamic modeling of multicomponent phase equilibria.* JOM, 1997. **49**(12): p. 14-19.

110. Lukas, H.L., J. Weiss, and E.-T. Henig, *Strategies for the calculation of phase diagrams* CALPHAD., 1982. **6**: p. 229-251.

111. Diekmann, U. *Calculation of steel data using JMatPro®*. in *COMAT 2012: Recent Trends in Structural Materials*. 2012. Plzen, Czech Republic.

112. Kirana, R., et al., *High-Temperature Phase Stability of 9Cr–W–Ta–V–C Based Reduced Activation Ferritic–Martensitic (RAFM) Steels: Effect of W and Ta Additions.* steel research international, 2015.

113. Alamo, A., et al., *Effects of thermal aging on the mechanical behavior of F82H weldments.* Journal of Nuclear Materials, 2000. **283–287, Part 2**: p. 1192-1195.

114. Anastasio, O.A., *An Approach for Impression Creep of Lead free Microelectronic System*. 2002, Master's Thesis Naval Postgraduate School , Monterey: California.

115. CEN, in *Workshop agreement CWA 15627:2006 E, 2006*. 2007, Small Punch Test Method for Metallic Materials: CEN Brussels.

116. Chu, S.N.G. and J.C.M. Li, *Impression creep; a new creep test.* Journal of materials science, 1977. **12**(11): p. 2200-2208.

117. Li, J.C.M., *Impression creep and other localized tests.* Materials Science and Engineering: A, 2002. **322**(1–2): p. 23-42.

118. Chu, S.N.G. and J.C.M. Li, *Impression creep of β-tin single crystals.* Materials Science and Engineering, 1979. **39**(1): p. 1-10.

119. Sastry, D.H., *Impression creep technique—An overview.* Materials Science and Engineering: A, 2005. **409**(1–2): p. 67-75.

120. Naveena ., V.D., Vijayanand., V. Ganesan., K. Laha., M. D. Mathew, *Evaluation of creep deformation behaviour of different microstuctural zones of 316LN SS weld joint using impression creep testing technique.* Materials Science and Technology, 2014. **30**(10): p. 1223-1228.

121. Suzuki M, E.M., Nishiyama Y, Fukaya K, Isozaki T, *Estimation of toughness degradation by microhardness and small punch tests.* In: Small specimen test techniques applied to nuclear reactor vessel thermal annealing and plant life estimation., ed. H.F. Corwin WR, Server WL. Vol. ASTM STP 1204. 1993: Philadelphia, PA: American Society for Testing and Materials.

122. Laha, K., Saroja, S., Moitra, A., Sandhya, R., Mathew, M.D., Jayakumar, T., Kumar, E. Rajendra, *Development of India-specific RAFM steel through optimization of tungsten and tantalum contents for better combination of impact, tensile, low cycle fatigue and creep properties.* J. Nucl. Mater., 2013. **439**: p. 41–50.

123. Ravikirana., R., Mythili, Raju, S, Saroja, S, Jayakumar, T, Rajendrakumar, E, *Influence of W and Ta content on microstructural characteristics in heat treated*

9Cr-Reduced Activation Ferritic/ Martensitic steels. Materials Characterisation, 2013. **84**: p. 196-204.

124. Foldyna, V., A, Jakobava., V. Vodarek., Z. Kubon *Materials for Advanced Power Engineering*. in *Proceedings of 5th conference on materials for advanced power engineering*. 1994 Liege, Belgium, p.453.
125. Jones, W.B., C.R. Hills, and D.H. Polonis, *Microstructural Evolutionof Modified 9Cr-1Mo Steel.* Metall Trans, 1991. **22A**: p. 1049-1058
126. Klueh, R.L. and A.T. Nelson, *Ferritic/martensitic steels for next-generation reactors.* Journal of Nuclear Materials, 2007. **371**(1–3): p. 37-52.
127. Schäublin, R., P. Spätig, and M. Victoria, *Microstructure assessment of the low activation ferritic/martensitic steel F82H.* Journal of Nuclear Materials, 1998. **258–263, Part 2**: p. 1178-1182.
128. Hald, J., *Metallurgy and creep properties of new 9-12% Cr steels.* Steel research, 1996. **67**(9): p. 369-374.
129. Abe, F., *Coarsening behavior of lath and its effect on creep rates in tempered martensitic 9Cr-W steels.* Mater. Sci. Eng., 2004. **387-389**: p. 565-569.
130. Kirana, R., Raju, Subramanian., Mythili, Rengachari., Saibaba, Saroja., Jayakumar, Tammana., Rajendra Kumar, Ellappan, *High-Temperature Phase Stability of 9Cr–W–Ta–V–C Based Reduced Activation Ferritic–Martensitic (RAFM) Steels: Effect of W and Ta Additions.* steel research international, 2015. **86**(9999): p. 1-16.
131. Sawada, K., Takeda, M., Maruyama, K., Ishii, R., Yamada, M., Nagae, Y., Komine, R., *Effect of W on recovery of lath structure during creep of high*

chromium martensitic steels. Materials Science and Engineering: A, 1999. **267**(1): p. 19-25.

132. Murata, Y., Koyama, Toshiyuki., Morinaga, Masahiko., Miyazaki, Toru, *Prediction of the Laves Phase Morphology in Fe-Cr-W-C Quaternary Steels with the Aid of System Free Energy Concept.* ISIJ International, 2002. **42**(12): p. 1423-1429.

133. Hald, J. and L. Korcakova, *Precipitate Stability in Creep Resistant Ferritic Steels-Experimental Investigations and Modelling.* ISIJ International, 2003. **43**(3): p. 420-427.

134. Korcakova, L., J. Hald, and M.A.J. Somers, *Quantification of Laves phase particle size in 9CrW steel.* Materials Characterization, 2001. **47**(2): p. 111-117.

135. Sawai, T., K. Shiba, and A. Hishinuma, *Microstructure of welded and thermal-aged low activation steel F82H IEA heat.* Journal of Nuclear Materials, 2000. **283–287, Part 1**: p. 657-661.

136. Vanaja, J., Laha, K., Mathew, M. D., Jayakumar, T., Kumar, E. Rajendra, *Effects of Tungsten and Tantalum on Creep Deformation and Rupture Properties of Reduced Activation Ferritic-Martensitic Steel.* Procedia Engineering, 2013. **55**: p. 271-276.

137. Bowen, A.W. and G.M. Leak, *Solute diffusion in Alpha and Gamma iron.* Metall. Trans. A, 1970. **1**(6): p. 1695-1700.

138. Ohgami, M., H. Minura, and H. Naoi. *Creep Rupture Properties and Microstructures of a New Ferritic W Containing Steel.* in *Fifth International Conference on Creep of Materials*. 1992. Lake Buena Vista, Florida.

139. Toshiei Hasegawa., Y.R., Abe., Yukio Tomita., Naoki Maruyama., Masaaki Sugiyama, *Microstructural Evolution during Creep Test in 9Cr–2W–V–Ta Steels and 9Cr–1Mo–V–Nb Steels.* ISIJ International, 2001. **41**(8): p. 922-929.

140. Abe, F., *Creep rates and strengthening mechanisms in tungsten-strengthened 9Cr steels.* Materials Science and Engineering: A, 2001. **319–321**: p. 770-773.

141. Wall, M., *A review of thermal ageing effects in high chromium ferritic steels*, in *UKAEA report R-12812*. 1987, Harwell Laboratory

142. Hippsley, C.A. and N.P. Haworth, *Hydrogen and temper embrittlement in 9Cr–1Mo steel.* Materials Science and Technology, 1988. **4**(9): p. 791-802.

143. Schaeublin, R., D. Gelles, and M. Victoria, *Microstructure of irradiated ferritic/martensitic steels in relation to mechanical properties.* Journal of Nuclear Materials, 2002. **307–311, Part 1**: p. 197-202.

144. Tanigawa, H., H. Sakasegawa, and R.L. Klue, *Irradiation Effects on Precipitation in Reduced-Activation Ferritic/Martensitic Steels.* Materials Transactions, 2005. **46**(3): p. 469 - 474.

145. Kameda, J. and X. Mao, *Small-punch and TEM-disc testing techniques and their application to characterization of radiation damage.* Journal of materials science, 1992. **27**(4): p. 983-989.

146. Abe, F., Noda, Tetsuji., Araki, Hiroshi., Okada, Masatoshi., *Development of Reduced-Activation Martensitic 9Cr Steels for Fusion Reactor.* Journal of Nuclear Science and Technology, 1994. **31**(4): p. 279-292.

147. Alexander, D.J., P.J. Maziasz, and C.R. Brinkman, *The Effect of Long-term Aging on the Impact Properties of Modified 9Cr-1Mo steels*, in *Microstructures amd*

Mechanical Properties of Ageing Materials, R.V. P.K. Liaw, K.L. Murty, E.P. Simonen and D. Frear, Editor. 1993, The Minerals, Metals and Materials Society: Warendale, PA. p. 343-349.

148. Aubert, P., Tavassoli, F., Rieth, M., Diegele, E., Poitevin, Y., *Low activation steels welding with PWHT and coating for ITER test blanket modules and DEMO.* Journal of Nuclear Materials, 2011. **409**(2): p. 156-162.

149. Zhu, Q., Lei, Yu-cheng, Chen, Xi-zhang, Ren, Wen-jie, Ju, Xin, Ye, Yi-min, *Microstructure and mechanical properties in TIG welding of CLAM steel.* Fusion Engineering and Design, 2011. **86**(4–5): p. 407-411.

150. Zheng, S., Wu, Qingsheng, Huang, Qunying, Liu, Shaojun, Han, Yangyang, *Influence of different cooling rates on the microstructure of the HAZ and welding CCT diagram of CLAM steel.* Fusion Engineering and Design, 2011. **86**(9–11): p. 2616-2619.

151. Falat, L., Svoboda, Milan., Výrostková, Anna., Petryshynets, Ivan., Sopko, Martin, *Microstructure and creep characteristics of dissimilar T91/TP316H martensitic/austenitic welded joint with Ni-based weld metal.* Materials Characterization, 2012. **72**: p. 15-23.

152. Moon, J., Lee, Chang-Hoon., Lee, Tae-Ho., Jang, Min-Ho., Park, Min-Gu., Han, Heung Nam, *Phase transformation and impact properties in the experimentally simulated weld heat-affected zone of a reduced activation ferritic/martensitic steel.* Journal of Nuclear Materials, 2014. **455**(1–3): p. 81-85.

153. Smallman, R.E. and A.H.W. Ngan, *Physical Metallurgy and Advanced Materials*. 2007: Butterworth-Heinemann, p.421.

154. Rosenthal, D., *The theory of moving source of heat and its application to metal transfer.* Transactions of ASME, 1946. **43**(11): p. 849-865.

155. Grong, O., *Metallurgical Modelling of Welding*. 1997: (The Indian Institute of Materials, II Edition, London, UK), pp.28-30.

156. Xu, Z., *Laser welding and post weld heat treatment of modified 9Cr-1VNb steel.* 2008, Report No. ANL/NE-12/12, Argonne National Laboratory, Chicago, Illinois.

157. Chen, X., Huang, Yuming., Madigan, Bruce., Zhou, Jianzhong, *An overview of the welding technologies of CLAM steels for fusion application.* Fusion Engineering and Design, 2012. **87**(9): p. 1639-1646.

158. Wu, Q., Zheng, Shuhui., Liu, Shaojun., Li, Chunjing., Huang, Qunying, *Effect of post-weld heat treatment on the mechanical properties of electron beam welded joints for CLAM steel.* Journal of Nuclear Materials, 2013. **442**(1–3): p. 512-517.

159. Silwal, B., Li, L, Deceuster, A, Griffiths, B, *Effect of Postweld Heat Treatment on the Toughness of Heat-Affected Zone for Grade 91 Steel.* Welding Journal, 2013. **92**(3).

160. Vitek, J.M. and R.L. Klueh, *Precipitation Reactions during the Heat Treatment of Ferritic Steels.* Metallurgical Transactions A, 1983. **14**(5): p. 1047-1055.

161. Raghavan, V., *Materials Science and Engineering*. 1984: Prentice-Hall, New Delhi, p.168.

162. Thomas Paul V, S., S, Albert, SK, Jayakumar, T, Kumar, E Rajendra, *Microstructural characterization of weld joints of 9Cr reduced activation ferritic*

martensitic steel fabricated by different joining methods. Materials Characterization, 2014. **96**: p. 213-224.

163. Chakraborty, G., Das, CR., Albert, SK., Bhaduri, AK., V Thomas, Paul., Panneerselvam, G., Dasgupta, Arup, *Study on tempering behaviour of AISI 410 stainless steel.* Materials Characterization, 2015. **100**: p. 81-87.

164. Thomas Paul V, C.Sudha, and S. Saroja, *Influence of Alloy Content and Prior Microstructure on Evolution of Secondary Phases in Weldments of 9Cr-Reduced Activation Ferritic-Martensitic Steel.* Metallurgical and Materials Transactions A, 2015. **46**(8): p. 3378-3392.

165. Hu, P., Yan, Wei, Sha, Wei, Wang, Wei, Guo, Zhan-li, Shan, Yi-yin, Yang, Ke, *Study on Laves phase in an advanced heat-resistant steel.* Frontiers of Materials Science in China, 2009. **3**(4): p. 434-441.

166. Duck Young Ku., O., Seungjin., Ahn, Mu-Young., Yu, In-Keun., Kim, Duck-Hoi., Cho, Seungyon., Choi, Im-Sub., Kwon, Ki-Bum, *TIG and HIP joining of Reduced Activation Ferrite/Martensitic steel for the Korean ITER–TBM.* Journal of Nuclear Materials, 2011. **417**(1–3): p. 67-71.

167. Vijayalakshmi, M., Saroja, S, Paul, V Thomas, Mythili, R, Raghunathan, VS, *Microstructural zones in the primary solidification structure of weldment of 9Cr-1Mo steel.* Metallurgical and Materials Transactions A, 1999. **30**(1): p. 161-174.

168. van der Schaaf, B., Tavassoli, F., Fazio, C., Rigal, E., Diegele, E., Lindau, R., LeMarois, G., *The development of EUROFER reduced activation steel.* Fusion Engineering and Design, 2003. **69**(1–4): p. 197-203.

169. Schneider, H., *Investment casting of high-hot strength 12% chrome steel.* Foundary Trade J., 1960. **108**: p. 562-563.

170. Lippold, J.C., *Solidification behavior and cracking susceptibility of pulsed-laser welds in austenitic stainless steels.* Welding Research Suppliment, 1994. **73**(6): p. 129s.

171. Saluja, R. and K.M. Moeed, *The embpasis of phase trasnformation of phase transformations and alloying constituents on hot ctracking susceptibility of type 304L and 316L stainless steel welds.* Int. jrl. of Engg. Sci. and Tech, 2012. **4**(05): p. 2206-2216.

172. Bhadeshia, H., S. David, and J. Vitek, *Solidification sequences in stainless steel dissimilar alloy welds.* Materials Science and Technology, 1991. **7**(1): p. 50-61.

173. Thielsch, H., *Stainless-steel weld deposits on mild and alloy steels.* Welding Journal, 1952. **31**(1): p. 37- s to 64-s.

174. Lundin, C.D., *Dissimilar Metal Welds - Transition Joints Literature Review.* welding Journal, 1982. **61**(2): p. 58s-63s.

175. Celik, A. and A. Alsaran, *Mechanical and Structural Properties of Similar and Dissimilar Steel Joints.* Materials Characterization, 1999. **43**(5): p. 311-318.

176. Andrew, K.W., *Empirical Formulae for the Calculation of Some Transformation Temperatures.* Journal of Iron and Steel Institute, 1965. **203**: p. 721-727.

177. Hsieh, Chih-Chun, and W. Weite, *Overview of Intermetallic Sigma Phase Precipitation in Stainless Steels.* ISRN Metallurgy, 2012. **2012**: p. 16.